HOW TO RECOGNIZE AND CONTROL INTERFACIAL PHENOMENA THAT HINDER THE ADVANCEMENT OF CLEAN ENERGY TECHNOLOGIES

by

Corey Michael Efaw

A dissertation

submitted in partial fulfillment

of the requirements for the degree of

Doctor of Philosophy in Materials Science & Engineering

Boise State University

December 2021

BOISE STATE UNIVERSITY GRADUATE COLLEGE

DEFENSE COMMITTEE AND FINAL READING APPROVALS

of the dissertation submitted by

Corey Michael Efaw

Dissertation Title: How to Recognize and Control Interfacial Phenomena that Prevent the Advancement of Clean Energy

Date of Final Oral Examination: 03 August 2021

The following individuals read and discussed the dissertation submitted by student Corey Michael Efaw, and they evaluated his presentation and response to questions during the final oral examination. They found that the student passed the final oral examination.

Michael F. Hurley, Ph.D.	Co-Chair, Supervisory Committee
Eric J. Dufek, Ph.D.	Co-Chair, Supervisory Committee
Hui (Claire) Xiong, Ph.D.	Member, Supervisory Committee
Paul H. Davis, Ph.D.	Member, Supervisory Committee

The final reading approval of the dissertation was granted by Michael F. Hurley, Ph.D. and Eric J. Dufek, Ph.D., Co-Chairs of the Supervisory Committee. The dissertation was approved by the Graduate College.

DEDICATION

To my partner and best friend, Mimi, who is my biggest fan, and who without I would not have been able to reach this point. You are my catalyst, giving me the driving force to overcome an energy barrier I couldn't have made by myself. You provide me with a safe space to figure out who I want to become, while simultaneously pushing me to be a better person. I hope I can constantly grow to be that better person, fighting the good fights by your side. And to my parents, Brian and Libby – you instilled in me the values of curiosity, education, and humanity. Thank you for letting me climb on your shoulders and reach heights I would have never been able to reach. Lastly, I dedicate this to all those that choose to combat the destruction we have caused to our environment. Together, we must and will take the actions necessary to preserve the beauty of this planet.

Before getting started, I would like to point out what I view as some of the major contributors to human-driven climate destruction – (1) our obsession with burning fossil fuels for the sake of upholding an excessive lifestyle, (2) our consumerist-based economy causing an overuse of non-biodegradable products and overall poor material life cycles that leads to massive waste production, (3) our overproduction and overconsumption of energy- and resource-inefficient foods along with systematic cruelty of cognitively and emotionally intelligent creatures, and (4) our destruction of natural habitats in the name of constant human territorial expansion, along with the increased infiltration of wilderness leading to increased zoonosis (transfer of disease from animal to human) like

that seen with COVID-19. There are many other key contributors to our negative impact on our planet; the beauty is that we have created these problems, therefore, we can fix them.

To correct our belief that we exist outside of nature, I call on these ideas: first, look within your own life and find your small-level, personal impacts – consume less meat and dairy; buy an electric or hybrid vehicle, or better yet bike to places that are close by; stop buying items with single-use plastics; learn about your local recycling program; spend more money on sustainable materials instead of poorly managed materials; let the thermometer get up a few degrees in the summer. There are many ways you can have an impact; however, one single person's footprint in infinitesimal when compared to the full impact of us as a species. So, speak up. Reach out to your local representatives – plead a case for why your city or state needs to uphold carbon-neutral values. Do some background research beforehand so you can touch on things that are important to your area. In Idaho for example, the ideal temperature for growing potatoes is 60-70 °F. As the planet warms, potato growth will not be sustainable in the state best known for this crop! Salmon fishing is also a famous attraction in Idaho, but their habitat has been severely affected by human action. Other pathways of focus may be to protest companies that refuse to change their practices that have a major environmental impact. In other words, fight with your dollars. Lastly, educate yourself on the key contributors to climate change – only a few are listed above.

Dr. Ayana Elizabeth Johnson, founder of the non-profit Urban Ocean Lab and advocate of conservation, often talks about how each person should decide to make their mark in the fight against climate destruction by first making a Venn diagram – in three

circles write “What are you good at?”, “What solutions are needed?”, and “What brings you joy?” Find things that connect your head and your heart, things that will be sustainable because you truly care about them. I wish to extend this wisdom on the matter of what we can do to fight our biggest threat.

And remember that as we fight against our negative environmental impact, we also fight for climate justice – for those that have been disenfranchised, mistreated, and taken advantage of for the exponential advancement of others. I hope that in my lifetime we see a truly equitable society that is prosperous for all. I will focus my ambitions to fight for that hope.

ACKNOWLEDGMENTS

The views and opinions of authors expressed herein do not necessarily state or reflect those of the U.S. Government or any agency thereof.

First, I wish to acknowledge the ancestral and unceded land of the Shoshone and Bannock tribes, on which I now receive the opportunities to learn at Boise State University and Idaho National Laboratory. It is important to recognize that our benefits as a society today came at a cost of human rights for many others throughout our history, as well as to note that the fight against negative environmental impact is also a fight for social justice – one does not exist without the other.

I acknowledge the financial support and sponsorship during my PhD work from the following sources: the NASA Idaho Space Grant Consortium EPSCoR Seed Grant; the In-Pile Instrumentation Initiative (I2) and Battelle Energy Alliance, both sponsored by the Department of Energy (DOE) Idaho Operations Office Contract DE-AC07-05ID14517; the Advanced Battery Materials Research Program (Battery500 Consortium) through the Office of Vehicle Technologies; the Assistant Secretary for Energy Efficiency and Renewable Energy; the National Science Foundation contract no. OISE-0709664 and grant no. 1727036; Boise State's Micron School of Materials Science and Engineering department.

I acknowledge the support from all members of my committee. To Dr. Paul Davis, who was the first one to show me how to be an effective researcher and has constantly given me support since. To Dr. Claire Xiong, who provided constant examples

on how to be an effective teacher, researcher, and manager with a healthy and successful working lifestyle. To Dr. Eric Dufek, who saw in me possibilities that I myself could not see and gave me the space to learn new subject-matter with boundless opportunities. And to Dr. Mike Hurley, who constantly provided positivity and emotional support while I tried to discover my interests and maintained that support during my many failures along my pathway to success.

I'd also like to acknowledge all the support I've received at Boise State during my early research career: Dr. Bill Knowlton, Dr. Amy Moll, Dr. Elton Graugnard, Dr. Megan Frary, Dr. Lan Li, Dr. Peter Müllner, Dr. Brian Jaques, Dr. Krishna Pakala, Dr. Nick Bulloss, Jasen Nielsen, Lance Patten, Katie Yocham, Kari Higginbotham, Dr. Armen Kvryan, Nick Carter, Arvin Cunningham, Robert Miner, Mike Reynolds, Olivia Maryon, Brielle Ibe, Lina Zhu, Thiago da Silva, Dr. Ember Sikorski, Dr. Matthew Lawson, German Barcenas, Jordan Vandegrift, Jennifer Watkins, Andreas Savva, Dr. Kassi Smith, Dr. Pete Barnes, Dr. Min (Haoyu) Zhu, JD Hues, Jake Soares, and so many others that were with me during my time at BSU. From Idaho National Laboratory and the Center for Advanced Energy Studies, I acknowledge Dr. Bin Li, Dr. Boryann Liaw, Dr. Tanvir Tanim, Dr. Paramesh Chinnam, Dr. Gorakh Pawar, Dr. Yuxiao Lin, Dr. Ning Gao, Dr. Yulun Zhang, Dr. Sangwook Kim, Dr. Hypo (Bor-Rong) Chen, Dr. Meng Li, Charles Dickerson, Mike Evans, Dr. Hong Hu, Dr. Yaqiao Wu, Dr. Jatuporn Burns, and Dr. Megha Dubey. There are so many others to thank that I forgot to include in this list of acknowledgements – please know I hold your efforts, support, knowledge, and friendships in high esteem. I would not be the researcher or the person I am today without all these people, along with countless others that were not named.

ABSTRACT

Nuclear energy and electrochemical energy storage, such as batteries, are key parts to the clean energy transition of critical infrastructure. This work aims to define, monitor, and modify interfacial layers that would improve the utility of materials in harsh environments seen in nuclear and energy storage applications. First, the studying of zirconium alloys, which is used as nuclear cladding, was done to better understand the degradation mechanisms within an extreme environment. High-resolution characterization techniques were used to correlate corrosion mechanisms to equivalent circuit models from novel in-pile electrochemical impedance spectroscopy sensors. Advancement in this sensor technology could provide further insight and monitoring of the complex degradation mechanisms in a harsh nuclear core environment. A novel method was developed to spatially map Raman spectral features throughout the oxide cross-section, revealing a direct correlation between tetragonal zirconia phase and compressive stress, thus supporting the theory of a stress-induced breakaway phenomenon. Additionally, a comparison of interface- and relaxed-tetragonal phase revealed a difference in stabilization mechanisms, where relaxed-tetragonal phase is stabilized solely from sub-stoichiometric contributions. Coupling Raman mapping with elemental analysis via energy dispersive X-ray spectroscopy and scanning Kelvin probe force microscopy led to a distinction of secondary-phase particles and their nobility relative to surrounding zirconium oxide and metal. Lastly, a p-n junction at the tetragonal/monoclinic zirconia interface was observed,

supporting the theory that the tetragonal layer at the metal/oxide interface provides an additional barrier to an otherwise diffusion-limited oxidation mechanism.

Other interfacial studies were conducted on next-generation battery anodes. High-capacity lithium, deemed the "Holy Grail" of battery materials, undergoes unstable interactions in most, if not all, environments. In a cell, this causes poor cycle life and/or possible safety concerns via dendritic-driven short circuiting. Novel development of lithium-metal batteries was accomplished firstly with a facile design of a closed-host, porous/dense bi-layer interfacial structure formed on lithium through a two-step *ex situ*/*in situ* process, only made possible with an electrolyte additive included in the cell. This design prevented dendrite growth, improved interfacial flexibility and ionic conduction when compared to a traditional LiF coating, reduced volume fluctuations, and prevented extensive parasitic reactions. In summary, the works presented here were done in effort to better understand and control interfacial mechanisms in both nuclear energy and energy storage fields.

TABLE OF CONTENTS

DEDICATION iv

ACKNOWLEDGMENTS vii

ABSTRACT ix

LIST OF TABLES xv

LIST OF FIGURES xvi

ABBREVIATIONS xxvii

CHAPTER 1. INTRODUCTION AND MOTIVATION 1

CHAPTER 2. INTRODUCTION TO NUCLEAR ENERGY 5

CHAPTER 3. INTRODUCTION TO BATTERIES 10

CHAPTER 4. ADVANCED CHARACTERIZATION TECHNIQUES 18

4.1 X-ray Photoelectron Spectroscopy (XPS) 18

4.2 Electron Microscopy (EM) Techniques 21

4.3 Raman Spectroscopy 27

4.4 Atomic Force Microscopy (AFM) Techniques 30

CHAPTER 5: TOWARD IMPROVING AMBIENT VOLTA POTENTIAL MEASUREMENTS WITH SKPFM FOR CORROSION STUDIES 38

5.1 Introduction 38

5.2 Experimental Methods 43

5.2.1 SKPFM Reference Sample 43

5.2.2 DFT Calculations 44

5.2.3 SKPFM Mapping 45

5.2.4 Data Evaluation 47

5.2.5 Sample Preparation 48

5.3 Results and Discussion 50

5.3.1 DFT Calculated Work Functions 50

5.3.2 Quantifying Probe Work Function 50

5.3.5 Relative Work Functions of Different Metallic Constituents 56

5.4 Conclusions 61

5.5 Acknowledgments 62

CHAPTER 6: CHARACTERIZATION OF ZIRCONIUM OXIDES PART I: RAMAN MAPPING AND SPECTRAL FEATURE ANALYSIS 63

6.1 Introduction 63

6.2 Material and Methods 65

6.3 Results and Discussion 67

6.3.1 TGA 67

6.3.2 Phase Distribution – Percent Tetragonality 69

6.3.3 Tetragonal Peak Position and HWHM 73

6.3.4 Residual Stress 77

6.3.5 Parameter Correlations 81

6.4 Conclusions 85

6.5 Acknowledgments 87

CHAPTER 7: CHARACTERIZATION OF ZIRCONIUM OXIDES PART II: NEW INSIGHTS ON THE GROWTH OF ZIRCONIA REVEALED THROUGH COMPLEMENTARY HIGH-RESOLUTION MAPPING TECHNIQUES 88

7.1 Introduction 88

7.2 Experimental methods 91

7.3 Results and discussion 94

7.4 Conclusions 111

7.5 Acknowledgments 113

CHAPTER 8 – A CLOSED-HOST BI-LAYER DENSE/POROUS SOLID ELECTROLYTE INTERPHASE FOR ENHANCED LITHIUM-METAL ANODE STABILITY 115

8.1 Introduction 115

8.2 Materials and methods 119

8.2.1 Materials Synthesis 119

8.2.2 Cathode Preparation 120

8.2.3 Electrochemical Measurements 121

8.2.4 Characterization 122

8.2.5 Computational Details 123

8.3 Results and Discussion 125

8.4 Conclusions 142

8.5 Author Contributions 143

8.6 Acknowledgments 143

8.7 Supporting Information 144

CHAPTER 9 – CONCLUSIONS AND FUTURE WORK 160

Nuclear Cladding Sensors 162

Lithium-Metal Batteries 165

Chapter 5 – SKPFM 169

Chapter 6 – Raman of Zirconium Alloys 169

Chapter 7 – Co-localization of Oxidized Zirconium 170

Chapter 8 – Bi-Layer SEI Structure 170

REFERENCES 172

LIST OF TABLES

Table 5.1. Density functional theory calculated work function values for gold over relevant planes. 49

Table 6.1. Zirconium and alloy compositions. 66

Table 6.2. Oxide thickness of each sample, pre- and post-breakaway. 68

Table 7.1. Zirconium and Zr-2.65Nb compositions. 92

Table S8.1. Resistances (electrolyte resistance, R_e; SEI resistance, R_s; charge-transfer resistance, R_{ct}) for equivalent circuit EIS fits of porous LiF symmetric cells at rest (a) without cycling, with $LiNO_3$ (Figure S8.11), (b) after cycling, with $LiNO_3$ (Figure 8.5f), and (c) after cycling, without $LiNO_3$ (Figure 8.5g) 154

LIST OF FIGURES

Figure 2.1. From Vandegrift et al. [26]: "Normalized mass gain versus isothermal oxidation time of Zr, Zry-3, Zry-4, Zr-1Nb, and Zr-2.65Nb in air and oxygen at 400-800 °C. The inset in the 800 °C is the first two hours of the isothermal oxidation showing the onset of breakaway in Zry-3, Zry-4, and Zr-2.65Nb." 7

Figure 2.2. Schematic of nuclear components and cladding interactions, including pellet-cladding interactions (PCI) and coolant-side corrosion. 8

Figure 3.1. Schematic of a battery with charge and discharge mechanisms shown.... 11

Figure 3.2. From Liu et al. [63]: "Comparing of some potential anode materials for lithium ion batteries." 12

Figure 3.3. From Mukhopadhyay et al. [67]: "Use of Li metal anodes allows high energy densities in rechargeable batteries, but Li dendrite formation leads to short-circuiting." 13

Figure 3.4. From Cheng et al. [99]: "Schematic diagrams of Li deposition. a) The routine 2D Cu foil electrode is always with an uneven surface that induces inhomogeneous electron distribution. Li ions aggregate near the protuberance on the 2D surface with a stronger field strength than the flat during continuous Li depositing. The agminated Li ions can trigger Li dendrite growth. b) GF cloth is with large quantities of polar functional groups (Si O, O H, O B), resulting in a strong interaction with Li ions. The concentrated Li ions by the protuberances on the Cu foil electrode are evenly redistributed, therefore rendering the dendrite-free Li deposits." . 17

Figure 4.1. (a) Energy diagram of XPS electron excitation. (b) Example survey spectrum acquired with XPS, observing a lithium foil. 19

Figure 4.2. (a) Depth profile example through a monoatomic layered material. (b) Experimental flow for depth profiling. 21

Figure 4.3. Visualization of different interactions between an electron beam and a sample, exemplifying the different types of data that can be collected from EM. Image provided by Thermo Scientific Fisher. 22

Figure 4.4. EM of a lithium foil cross-section after extended exposure to 1M lithium bis(trifluoromethanesulfonyl)imide (LiTFSI) in a 1:1 dioxolane (DOL):1,3 dimethoxyethane (DME) co-solvent with 2 wt. % $LiNO_3$. (a) Secondary electron image, (b) BSE image, and (c) EDS of different elements. 23

Figure 4.5. From Hu et al. [110]: "Progressive steps in the making of tips for the LEAP. (a) Before and (b) after ionized platinum deposition at metal/oxide interface. (c) OmniProbe welded to a grid for its removal from the bulk of sample. (d-e) OmniProbe with free-hanging grid. Wedge is disjointed from rest of grid and welded to a microtip post. (f) Individual wedge welded to a microtip post. (g-h) Individual wedge after annular milling, producing a tip ready for LEAP testing." Here, the LEAP is an APT tool, the Local Electrode Atom Probe, available at the Materials Characterization Suite at the CAES. Full-width of each image is (a-d) 40 μm, (e) 60 μm, (f) 12.5 μm, (g) 7.5 μm, and (h) 3 μm. 24

Figure 4.6. From Hu et al. [110]: "APT results from a pre-breakaway Zr sample, exposed for 20 hours at 700°C. (a) SEM image of ionized platinum deposition with trenches etched out on either side of Pt deposit. (b) LEAP produced elemental maps showing a distinct interface. Here, 'Volume 1' is described by a 0.5 nm binning across the interface (seen in Zr map). (c) Volume 1 elemental atom-by-atom representation, showing a transition of Zr-rich to O-rich volume. (d) Relative atomic percentages between Zr and O elements."....25

Figure 4.7. From Wang et al. [92]: Schematic images showing the processes to prepare sample, mount to grid, load on holder, and transfer into the TEM safely. (A) Sample dispersed on the substrate. (B) Mount the sample on the grid by cryo-FIB-SEM. (C) Load the grid onto the cryo transfer holder within the liquid N_2. (D)Transfer the cryo transfer into the TEM with a closed shuttle. (E) Samples directly deposited on the grid. (F) Harvest the grid in the Ar-filled glovebox. (G) Load the grid onto the cooling holder in the glovebox. (H) Transfer the cooling holder into the TEM with Ar protection. 26

Figure 4.8. From Naumenko et al. [113]: "Normal vibrations of crystal lattice of t-ZrO_2 (Raman-active modes)."....28

Figure 4.9. From Hu et al. [110]: "Raman spectra for zirconia polymorphs and other zirconium variants." 28

Figure 4.10. Raman mapping process to analyze the cross-sectioned oxide of a Zr cladding material. (a) Optical image of the Zr/ZrO_2 (right to left) interface with Raman mapped region in grey. (b) Raman spectra collected over spatial region in oxide. Peaks of focus for stress state and oxide composition are designated. (c) Rendered Raman map from spectra

processing. These images are partially published [112] and were presented at TopFuel 2019, a Light Water Reactor Fuel Performance Conference.. 29

Figure 4.11. From Xu et al. [116]: "Schematic diagram of the PFT."..... 31

Figure 4.12. From Pittenger et al. [117]: ""Force curves and information that can be attained from them: (i) Plot of force and piezo Z position as a function of time, including (B) jump-to-contact, (C) peak force, (D) adhesion. (ii) Plot of force vs. time with small peak force. (iii) A traditional force curve eliminates the time variable, plotting Force vs. Z piezo position. (iv) For fitting purposes it is more useful to plot force vs. separation where the separation is calculated from the Z piezo position and the cantilever deflection. 31

Figure 4.13. From Kvryan et al. [121]: "3D magnetic response maps with changes in height representative of differences in magnetism. Color scale ranges are 7 degress (0° = yellow, +7° = blue) for magnetic response." This work focused on the observation of different treatments of UNS S42670 martensitic stainless steel (MSS): high-temperature temper (HTT), low-temperature temper (LTT), and carbo-nitriding (CN). With MFM presented here, the purple regions indicate carbides, while yellow regions indicate steel matrix. Both types of regions exhibit out-of-plane magnetic domains, but the carbides, with increased chromium concentration, exhibit greater magnitude..... 33

Figure 4.14. Concept of SKPFM, with (a) observation of two metals (probe, P, and sample, S) in a pseudo-capacitive state of electrical contact, where a buckling voltage (V_b) is applied to determine the VPD, or relative work function between probe (ϕ_p) and sample (ϕ_s) that is intrinsically observed between the two metals. (b) Visualization of the dual-pass method, showing both readings of topography (solid black line) and VPD domains (solid blue line). (c) Cross-section of a material with different compositional domains (grey and orange) that causes differences in measured VPD (solid dark blue line) of the surface of the material..... 34

Figure 4.15. From Kvryan et al. [121]: "Time-lapse *in situ* AFM topography maps (160 nm full scale) for each of the heat-treated MSSs in 0.1M NaCl solution, with approximate exposure time at the end of each scan indicated below the corresponding map (image time was ~8.5 min)."..... 35

Figure 4.16. (Nanoscale) From Kvryan et al. [121]: "Secondary electron SEM image of Cu-Ag-Ti sample (a) followed by corresponding Scanning Kelvin Probe Force Microscopy (SKPFM surface potential image) (b). EDS elemental maps of the identical region for: Titanium (c); Copper (d); and Silver (e) are shown." The surrounding region is SS316L. (Microscale) SECM with a UME operating in feedback mode with a positive overpotential applied

to the probe while scanning across the braze (yellow) and SS316L (green) in aqueous solution of 1 mM Ferrocene Methanol (FcMeOH) and 0.1M KNO_3. (Bulk) Post-mortem optical imaging of the braze and SS316L. This is unpublished work that was presented at Materials Science & Technology Conference, 2017. 37

Figure 5.1. Crystal structures of gold oriented with (from left to right) the (100), (110), and (111) face exposed to vacuum. 45

Figure 5.2. Representative SKPFM VPD maps of the Al-Si-Au standard obtained with (a) a PFQNE-AL probe, (b) a SCM-PIT probe, and (c) a 25Pt300B probe. Note the difference in VPD color scale ranges for panels (a-c) due to differences in probe work functions. (d) Average gold VPD acquired from all SKPFM images obtained with each probe type. Left ordinate axis presents the average VPDs (with standard deviations) measured between the gold and the given probe type (PFQNE-AL in blue, SCM-PIT in orange, 25Pt300B in gray). Right ordinate axis presents the resulting average modified work function calculated for each probe type. (e) VPD and modified work function distributions of gold acquired from all SKPFM images with each probe type, with respective axes presented below and above the distributions. 95% confidence intervals are presented beside each histogram. 52

Figure 5.3 (Left) Average gold VPDs (with standard deviations) obtained from twelve SKPFM images acquired on the Al-Si-Au standard with (a) three PFQNE-AL probes, (b) three SCM-PIT probes, and (c) two 25Pt300B probes. Left ordinate axes present the average VPDs measured between the gold and the given probe. Right ordinate axes present the resulting average work function calculated for each of the probes. (Right) Distributions of measured VPDs for gold and resultant modified probe work functions obtained from twelve SKPFM images with (d) three PFQNE-AL probes, (e) three SCM-PIT probes, and (f) two 25Pt300B probes. 95% confidence intervals are presented besides each histogram. .53

Figure 5.4. Grayscale SEM image (left) and colored EDS maps (right) of the Cu-Ag-Ti brazed 316L stainless steel sample, confirming the presence of two distinct phases within the braze material: copper-rich precipitates within a silver-rich braze matrix. 55

Figure 5.5. SKPFM (VPD) maps and cross sections of the Cu-Ag-Ti braze sample acquired with a PFQNE-AL probe (500 mV scale), a SCM-PIT probe (500 mV scale), and a 25Pt300B probe (800 mV scale). Cu-rich and Ag-rich phases are called out in each map. Cross sections correspond to average data across the dotted black areas. 59

Figure 5.6. (a) VPD results for copper-rich and silver-rich regions on the braze sample obtained with the three different probe types as seen in Figure 5.5. (b) VPD results for the same three probes acquired from the gold of the Al-Si-Au standard presented on the left ordinate axis, with resulting modified probe work function values presented on the right ordinate axis, as calculated with the shown equation. (c) VPDs scaled relative to the gold of the Al-Si-Au standard imaged with the same probe prior to imaging the braze sample. The left ordinate axis (as calculated by the equation above) scales the VPD between the phases of the braze sample and the gold of the standard. The right ordinate axis (as calculated by the equation below) presents the resultant modified work function for each phase based on the modified work function of the probe in part (b). 60

Figure 5.7. SKPFM (VPD) maps and cross sections of the Cu-Ag-Ti braze sample obtained with different PFQNE-AL probes. PFQNE-AL #1 is a duplicate of Figure 5.5, while PFQNE-AL #2 (600 mV scale) is from a different region of braze sample with a different probe. Cross sections coordinate to average data across the dotted black areas. 60

Figure 5.8. (a) VPD results for copper-rich and silver-rich regions on the braze sample obtained with three different PFQNE-AL probes as seen in Figure 5.7 and from Kvryan et al. [181] (b) VPD results for the same three probes acquired from the gold of the Al-Si-Au standard presented on the left ordinate axis, with resulting modified PFQNE-AL work function values presented on the right ordinate axis, as calculated with the shown equation. (c) VPDs scaled relative to the gold of the Al-Si-Au standard imaged prior to imaging of the braze sample. The left ordinate axis (as calculated by the equation above) scales the VPD between the phases of the braze sample and the gold of the standard. The right ordinate axis (as calculated by the equation below) presents the resultant modified work function for each phase based on the modified work function of the probe in part (b). 61

Figure 6.1. Normalized mass gain during isothermal oxidation for zirconium in hours of exposure (left) and its alloys in minutes of exposure (right). Pre-breakaway samples are designated with solid lines, post-breakaway samples with dotted lines. End points are noted with large dots. 68

Figure 6.2. (a) Optical image of sectioned post-breakaway Zr sample, with metal and oxide indicated. (b) Raman spectra across line defined in (a) with individual spectra (c-e) noted. Individual spectrum for (c) monoclinic, (d) monoclinic with rich tetragonal phase near the metal/oxide interface, and (e) monoclinic with mixed tetragonal phase in the bulk of the oxide. Monoclinic (m-ZrO_2) and tetragonal (t-ZrO_2) zirconia Raman peaks are noted in each spectrum. Percent tetragonality, calculated with Equation 6.1, are included for each individual spectrum. 72

Figure 6.3. Matrix showing optical images and percent tetragonality maps for each sample, pre- and post-breakaway. Optical images reveal regions where Raman maps were collected and interfaces (oxide/epoxy and metal/oxide). Percent tetragonality for each spectrum was calculated with Equation 6.1. 73

Figure 6.4. Tetragonal (T_1) peak position of tetragonal-interface and tetragonal-relaxed phases for each alloy, pre- and post-breakaway. Shown for each sample are (left) box-and-whisker plots for the T_1 peak position of each tetragonal phase, (center) T_1 peak position as a function of the percent tetragonality calculated for each spectrum with Equation 6.1, and (right) T_1 peak position as a function of distance along the horizontal axis from the metal/oxide interface.....76

Figure 6.5. Tetragonal (T_1) HWHM of tetragonal-interface and tetragonal-relaxed phases for each alloy, pre- and post-breakaway. Shown for each sample are (left) box-and-whisker plots for the T_1 HWHM of each tetragonal phase, (center) T_1 HWHM as a function of the percent tetragonality calculated for each spectrum with Equation 6.1, and (right) T_1 HWHM as a function of distance along the horizontal axis from the metal/oxide interface. 77

Figure 6.6. Raman mapping of M_2 peak position for each sample, both pre- and post-breakaway. Scatter plots of M_2 peak position as a function of percent tetragonality are also included for each Raman map.....80

Figure 6.7. Raman mapping of M_8 peak position for each sample, both pre- and post-breakaway. Scatter plots of M_8 peak position as a function of percent tetragonality are also included for each Raman map.....81

Figure 6.8.Percent tetragonality and monoclinic peak positions, M_2 and M_8 (in cm^{-1}), as a function of distance from the metal/oxide interface for each alloy, pre- and post-breakaway.....84

Figure 6.9. Linear trends of monoclinic peak positions, M_2 (left) and M_8 (right), as a function of percent tetragonality. Pre-breakaway samples are designated with solid lines, post-breakaway samples with dotted lines. 85

Figure 7.1. Normalized mass gain during isothermal oxidation for Zr-2.65Nb (left) and Zr (right).....95

Figure 7.2. AFM results for sectioned sample of oxidized Zr. (a) Height, (b) relative Volta potential, (c) adhesion, and (d) deformation images with red lines separating metal and oxide. (e) SEM image with area where SKPFM was performed.....97

Figure 7.3. Raman mapping results for sectioned sample of oxidized Zr. (a) Percent tetragonality and (b) monoclinic (M_2) peak position maps. (c) SEM image with area where Raman mapping was performed. 98

Figure 7.4. (a) Percent tetragonality and (b) monoclinic zirconia (M_2) peak position maps of region within Raman mapped area in Figure 7.3. (c) Raman spectra across dotted line in (a-b), focusing on M_2 and tetragonal zirconia (T_1) peak positions. Spectra labeled with a blue '#' present M_2 peaks corresponding to compressive stress (i.e., notably lower peak position). Spectra labeled with an orange '*' present tetragonal peaks warranting tetragonal-rich spectra via Equation 7.1. 100

Figure 7.5. Co-localization between (a) SKPFM Volta potential map with VPD line scan of 1 V range, (b) percent tetragonality and (c) M_2 peak position maps with line scans determined via Raman mapping, and (d) SEM image with EDS elemental line scans for a sectioned sample of oxidized Zr. 103

Figure 7.6. (a) Raman spectra for partial distance across the line scan in Figure 7.5. (b) Inset of spectra with monoclinic (M) and tetragonal (T) zirconia peaks noted. 104

Figure 7.7. Co-localization between (a) height and Volta potential via SKPFM and (b) elemental analysis via SEM/EDS for a sectioned sample of oxidized pure Zr (pre-breakaway). Area where SKPFM was performed is included in SEM image. Red circles in Volta potential and EDS maps present correlations between high VPD regions and Fe-rich particles. 104

Figure 7.8. Co-localization between (a) SKPFM Volta potential map with VPD line scan of 1 V range, (b) percent tetragonality and (c) M_2 peak position maps with line scans determined via Raman mapping, and (d) SEM image with EDS elemental line scans for a sectioned sample of oxidized Zr. 109

Figure 7.9. Co-localization between (a) SKPFM Volta potential map with VPD line scan of 1.5 V range, (b) percent tetragonality and (c) M_2 peak position maps with line scans determined via Raman mapping, and (d) SEM image with EDS maps for a sectioned sample of oxidized Zr-2.65Nb. 110

Figure 7.10. Schematic summarizing the different parameters for each zirconia and zirconium phase. 111

Figure 8.1. Schematic showing the initial structure and failure mechanism for (a) Li-metal and (b) dense LiF artificial SEI, as well as (c) the plating mechanism for a bi-layer dense/porous artificial SEI. 119

Figure 8.2. (a) FESEM and EDS, (b) cross-sectional cryo-FIB-SEM, (c) fluorine and (d) iodine XPS depth profile of the mixed LiI-LiF composite film. (e)

Surface and (f) cross-sectional cryo-FIB-SEM, (g) fluorine and (h) iodine XPS depth profile of the porous LiF artificial SEI after rinse with DOL:DME. 127

Figure 8.3. (a) Schematic showing the development and retention of the bi-layer SEI structure. (b-c) Symmetric cell cycling of different anode treatments at (b) low (1 mA/cm^2, 1 mAh/cm^2) and (c) high (2 mA/cm^2, 4 mAh/cm^2) current density and areal capacity, with (d) post-mortem FESEM of 1 mAh/cm^2 lithiated electrodes at increasing cycles. 131

Figure 8.4. (a) MD energy barrier simulation of Li^+ through bulk LiF, the surface of LiF, and along a Li/LiF interface, with (b) LiF crystal and Li/LiF interface pathway schematics. (c) MD stress-strain simulation of (left) LiF crystal and (right) Li/LiF interface, with (top) stress-strain plot, (middle) potential energy-strain plot, and (d) crystal structure at 15% strain. Li and F atoms are shown as purple and red in (b) and (d), respectively. 133

Figure 8.5. (a) Symmetric cell cycling of different anode treatments without $LiNO_3$ in the electrolyte. (b, d) Surface and (c, e) cross-section cryo-FIB-SEM of porous LiF anode after a single lithiation cycle in a symmetric cell (b, c) with $LiNO_3$ and (d, e) without $LiNO_3$. (f-g) The inset in Figure (c) shows cross-section cryo-FIB-SEM of porous LiF anode after delithiation with $LiNO_3$. EIS spectra of porous LiF symmetric cells (f) with $LiNO_3$ and (g) without $LiNO_3$, as a function of time at rest after cycling (>100 cycles), with the equivalent circuit model and fits included (raw data as dashes, equivalent circuit fits as solid lines). 137

Figure 8.6. (a) Li-S cell galvanostatic cycling at C/5 rate with (b-d) charge-discharge curves for (b) Li, (c) LiF, and (d) porous LiF anode cell, as well as (e) rate performance testing. (f) Li-LFP cell galvanostatic cycling at C/2 rate with (g-i) charge-discharge curves for (g) Li, (h) LiF, and (i) porous LiF anode cell, as well as (j) rate performance testing. 141

Figure S8.1. A temporal evolution of PVDF in DMF solution with snapshots taken at (a) 0 ps, (b) 500 ps, and (c) 1000 ps. A temporal evolution of PVDF in DMA solution with snapshots taken at (d) 0 ps, (e) 500 ps, and (f) 1000 ps. The simulation box size in all simulations is $24.5703 \times 24.5703 \times 30$ $Å^3$. 144

Figure S8.2. (a, c, e) High-resolution XPS with peaks labeled and (b, d, f) FESEM and EDS of (a, b) polished Li, (c, d) LiF artificial SEI, and (e, f) LiI-LiF composite layer. 146

Figure S8.3. (a) LiF structure and (b) a pairwise distribution function of LiF structure after 25 ps. (c) LiI structure and (d) a pairwise distribution function of LiI

structure after 25 ps. (e) LiF–LiI structure and (f) a pairwise distribution function of LiF–LiI structure after 500 ps. 147

Figure S8.4. (a) Surface and (b) cross-section cryo-FIB-SEM of dense LiF artificial SEI 148

Figure S8.5. (a) 3C and (b) 5C rate symmetric cell cycling at low areal capacity (1 mAh/cm^2) for bare Li, dense LiF, and porous LiF treatments. 149

Figure S8.6. XPS survey scan of (a) untreated, rolled Li foil and (b) polished Li foil, with peak identifications presented. Weight percentages for each identified element is included. 150

Figure S8.7. AFM techniques of polished Li, with (top) QNM of (a) topography and (b) log DMT Modulus, as well as (bottom) SKPFM of (c) topography and (d) Volta potential, showing a correlation of peaks and valleys, as well as chemical heterogeneities, to variations in mechanical and electronic properties, respectively by technique. 150

Figure S8.8. Sulfur XPS spectra of lithiated porous LiF electrode (left) with and (right) without $LiNO_3$ in the electrolyte, examined after (a-b) 2 cycles as a function of depth profiling in minutes of sputtering, and (c-d) the electrode surface after 100 cycles. 151

Figure S8.9. Post-mortem FESEM of different anode treatments (all lithiated electrodes) in a symmetric cell over increasing cycles operating at low current density (1 mA/cm^2) and areal capacity (1 mAh/cm^2) without $LiNO_3$ in the electrolyte (1M LiTFSI in 1:1 DOL:DME). 153

Figure S8.10. Cross-section cryo-FIB-SEM of porous LiF artificial SEI electrode after (a) first stripping cycle, revealing retention of porous structure, and after (b) second stripping cycles, revealing formation of dense top layer, with semi-porous inner layer visible. 153

Figure S8.11. EIS spectra of a symmetric porous LiF cell as a function of time at rest, without any cycling, with the equivalent circuit model and fits included (raw data as dashes, equivalent circuit fits as solid lines). 154

Figure S8.12. (a) Symmetric cell cycling of varied LiF porosity, as correlated to iodine concentration in the precursor solution. (b) Voltage hysteresis (i.e., cell potential range for each cycle) for each symmetric cell. 155

Figure S8.13. Cyclic voltammograms for (a) sulfur cathode and (b) LFP cathode, with different anode treatments. 156

Figure S8.14. (a) FESEM of as-prepared sulfur cathode with sulfur EDS map. Post-mortem FESEM with sulfur EDS map for (b, d, f) anode and (c, e, g) sulfur cathode, respectively with anode treatment of (b, c) polished Li, (d, e) dense LiF artificial SEI and (f, g) porous LiF artificial SEI. Sulfur weight percentages are included for the EDS maps on the anode side. ..157

Figure S8.15. (a) FESEM of as-received LFP cathode. Post-mortem FESEM of anode and LFP cathode, respectively, of (b, c) polished Li (d, e) LiF artificial SEI, and (f, g) porous LiF artificial SEI cells. 158

Figure 9.1. From ahssinsights.org, "Vehicle Life Cycle Assessment (LCA) encompasses all phases of the product cycle, from raw material extraction to end of life recycling and disposal." 161

Figure 9.2. Adapted from Reynolds [297]: Correlation of EIS and post-mortem SEM oxide thickness measurement for Zry-4 alloy exposed to 700°C simulated air (80% N_2 + 20% O_2). (a) Thermogravimetric analysis with oxidation states (OS) increasing from 1 to 4 with increasing exposure time. (b) EIS Bode plots at each OS. (c) post-mortem cross-sectional SEM at OS1-4, from a-d respectively. (d) Comparison of oxide thickness from EIS and SEM at each OS. 163

Figure 9.3. From Hu et al. [110]: "(a) Dimensional rendering of the HT Raman sample holder, via Harrick. (b) Raman HT Raman sample holder, with arrow pointing out sample cup and circle noting availability for gas or electrolyte inlet and outlet. (c) BSU's HT Raman stage set-up, including high temperature controller (HTC) and coolant. (d) HT Raman sample holder mounted on stage and set up for Raman spectroscopy with a 20x objective." 164

Figure 9.4. Raman spectra of different electrolytes and their components. From bottom to top: (orange) common solvent with peaks between 800-860 cm^{-1}, (purple) diluent cosolvent with peaks between 830-850 cm^{-1}, (gold) mixed solvent with primary peaks dominated by the diluent, (red) LCE electrolyte, with cation-anion interactions (SSIP and CIP) between 710-730 cm^{-1} and Li^+-solvent interaction at 875 cm^{-1}, (blue) HCE electrolyte with a blue-shift of cation-anion interactions to 730-750 cm^{-1} (SSIP, CIP, and AGG), (green) LHCE electrolyte with a further blue-shift of cation-anion interactions to 740-760 cm^{-1} (CIP, AGG, and AGG+), and (black) solid salt with prominent peak at ~775 cm^{-1}. 165

Figure 9.5. (Left) From Tang et al. [94]: "Time-lapsed digital photos to show the polishing process of lithium foil by naphthalene in tetrahydrofuran." (Right) Same process of time-lapse photos of lithium foil by 0.1M naphthalene in tetrahydrofuran. 167

Figure 9.6. Comparison of charge-transfer mechanisms of lithiation for (a) liquid and (b) solid electrolytes. (a) For liquid electrolytes, transport is driven by (electro)chemical potential gradients. Upon approach of the SEI, desolvation occurs, followed by Li^+ transport through SEI by vacancy and interstitial "hopping" mechanism. At the electrode surface, another charge-transfer step occurs. (b) For solid electrolytes, transport is driven by charge mobility and concentration. In the electrolyte, transport of Li^+ occurs by vacancy and interstitial "hopping", followed by a charge-transfer at the electrode surface. 168

ABBREVIATIONS

NASA	National Aeronautical and Space Administration
I2	In-Pile Instrumentation Initiative
DOE	Department of Energy
NSF	National Science Foundation
GHG	Greenhouse Gases
IEA	International Energy Agency
SKPFM	Scanning Kelvin Probe Force Microscopy
SEM	Scanning Electron Microscopy
EBR-I	Experimental Breeder Reaction No. 1
PCI	Pellet-Cladding Interactions
PIE	Post-Irradiation Examination
EIS	Electrochemical Impedance Spectroscopy
SEI	Solid Electrolyte Interphase
SHE	Standard Hydrogen Electrode
CE	Coulombic Efficiency
HCE	High-Concentration Electrolyte
LHCE	Localized High-Concentration Electrolyte
EDL	Electrical Double Layer
LCE	Low-Concentration Electrolyte
PAH	Polycyclic Aromatic Hydrocarbon
XPS	X-ray Photoelectron Spectroscopy

KE	Kinetic Energy
BE	Binding Energy
EM	Electron Microscopy
TEM	Transmission Electron Microscopy
BSE	Backscattered Electron
EDS	Energy Dispersive X-ray Spectroscopy
FIB	Focused Ion Beam
APT	Atom Probe Tomography
LOCA	Loss-of-Coolant Accident
HWHM	Half-Width at Half-Maximum
LEAP	Local Electrode Atom Probe
AFM	Atomic Force Microscopy
PFT	PeakForce Tapping
QNM	Quantitative Nanomechanical Mapping
EC-AFM	Electrochemical Atomic Force Microscopy
SECM	Scanning Electrochemical Microscopy
MFM	Magnetic Force Microscopy
MSS	Martensitic Stainless Steel
HTT	High-Temperature Temper
LTT	Low-Temperature Temper
CN	Carbo-Nitriding
VPD	Volta Potential Difference
UME	Ultramicroelectrode

DFT	Density Functional Theory
XRD	X-Ray Diffraction
VASP	Vienna Ab initio Simulation Package
PAW	Projector Augmented Wave
PBE	Perdew-Burke Ernzerhof
GGA	Generalized Gradient Approximation
FM	Frequency Modulation
DC	Direct Current
AM	Amplitude Modulation
UHP	Ultrahigh Purity
TGA	Thermogravimetric Analysis
CPD	Contact Potential Difference
TREAT	Transient Reactor Test Facility
SPP	Secondary-Phase Precipitate
HCP	Hexagonal Closed Packed
LMB	Li-Metal Battery
LAM	Loss of Active Material
CNT	Carbon Nanotubes
ETD	Everhart-Thornky Detector
RPT	Rate Performance Test
LAMMPS	Large-scale Atomic/Molecular Massively Parallel Simulator
MD	Molecular Dynamics
LJ	Lennard-Jones

MEAM	Modified Embedded-Atom Method
NVT	Number Volume Temperature
EIM	Embedded Ion Method
NPT	Number Pressure Temperature
FESEM	Field Emission Scanning Electron Microscopy
CPE	Constant Phase Element
OS	Oxidation State
HT	High-Temperature

CHAPTER 1. INTRODUCTION AND MOTIVATION

Since the Industrial Revolution of the 19th century, humans have exponentially developed, leading to an increase in life expectancy, improved quality of life, and advancement in technology and understanding of our world. Overall, many people on Earth today have established access to basic needs such as food, shelter, and access to advanced medical care, as well as higher-level needs like access to energy, technology, and information. However, other drastic changes we are witnessing include an increase in global temperature, extreme weather patterns, and species extinction [1-5]. The correlation between human activity and these negative effects on our environment has been well established. The recognition of carbon dioxide's ability to trap heat and how that could change our environment is credited to Eunice Newton Foote's published work in 1856, which states "An atmosphere of that gas (CO_2) would give to our earth a high temperature" [6]. The rate at which our environment is changing is atypical, correlating to a high output in greenhouse gases (GHG) such as CO_2, formed from processes that have afforded the advancement of society. In our technological and social advances, the cost has been destruction of non-renewable resources that are necessary for our continued prosperity. We are seeing the extreme cases of what climate change can mean for our future existence on this planet; for example, increasing rates in extreme weather such as hurricanes, fires, and winter storms have exposed instability in our energy infrastructure, leading to destruction seen especially in our most vulnerable countries and communities

[7]. The transition to a reduced environmental impact while maintaining our level of security is of the upmost importance.

Many leaders have taken verbal action to combat climate destruction, such as the signing of the Paris Agreement of 2015 by 196 countries to limit global warming to below 2°C compared to pre- industrial levels (with a preferred goal of being below 1.5°C). Efforts to back verbal agreements like this must happen in a drastic manner. The largest sector to make changes is energy, which according to the International Energy Agency (IEA) is the greatest source of GHG emissions. The IEA has published a roadmap for future global energy modifications to reach net-zero emissions by 2050, which many experts have identified as the point to reach the lofty goal of limiting global warming below 1.5°C increase [8, 9]. Therefore, in just three decades we need to advance cleaner energy technologies, such as improved energy-efficiency, carbon capture usage and storage/sequestration [10], replacement of gas and oil with cleaner energy producers [11], and securing cleaner supply chains throughout the existence of material and energy lifecycles (i.e., holistic decarbonization along material extraction, manufacturing, usage, and reuse/recycling methods) [12-15].

Two major utilities of a decarbonized energy transition are nuclear energy and energy storage. According to the Nuclear Energy Institute, nuclear energy generates nearly 20% of all electricity in the United States, accounting for more than half of the country's clean energy generation. Energy storage, such as batteries, is commonly coupled with intermittent, non-dispatchable wind and solar energy resources to align with peak energy demands. Batteries are also replacing gas-dependent combustion engines in our vehicle fleet, reducing GHG emissions in the transportation sector. In order to expand

the feasibility of both nuclear and storage technologies in the energy sector, the electrochemical degradation of crucial materials during operation needs to be addressed. For instance, extreme conditions in a nuclear reactor cause degradation of the material that encapsulates the uranium-based fuel, i.e., cladding, thus restricting long-life energy production in an efficient manner. In a battery, the degradation of electrodes, such as lithium metal, causes rapid fade in capacity, as well as dendrite growth that can lead to dangerous short circuiting.

The surface of a material can be thought of as an interfacial defect, where reduced coordination and increased free energy initiates reactions with a surrounding environment, driving eventual operational failure [16]. For example, electrochemical degradation (i.e., corrosion) occurring at the interface leads to reduced material sustainability. The economic costs (e.g., material loss, overdesign, reduced efficiency, etc.) of corrosion is massive, where a conservative estimate of over $100B is spent each year in the United States on corrosion [17]. Estimates also rarely incorporate newer energy technologies, such as batteries, where material degradation prevents reaching lifetime competitiveness with traditional technologies such as combustion engines or coal-fired plants. Overall, the failure of materials through electrochemical degradation is a limiting factor to advancing many cleaner energy technologies. This work will discuss the two major topics of nuclear energy and batteries, focusing on advances in methods to reduce degradation of critical materials, along with advanced characterization of these materials.

The rest of this dissertation starts with a general introduction of nuclear energy (Chapter 2) and batteries (Chapter 3). Chapter 4 provides an introduction and insight into

different characterization tools that were used throughout my PhD efforts. Chapters 5-8 are my first-author publications. Chapter 5 discusses the improved repeatability and enhanced measurement of the scanning Kelvin probe force microscopy (SKPFM) technique. With the use of an inert gold standard, a reduction in Volta potential deviation for a CuSil brazed stainless-steel system was observed across different SKPFM probes used, pointing to a direction of better technique usage in order to have direct comparison to other's works throughout many fields, such as corrosion and energy storage. Chapter 6 focuses on Raman spectroscopy as a tool to map different characteristics of zirconium cladding and its alloys, such as stress state and oxide make-up. These parameters were related to better understand the oxidation mechanism and cladding stability. Chapter 7 expands on this work by co-localizing Raman mapping with SKPFM and scanning electron microscopy (SEM) to further the understanding of the oxidation mechanism for zirconium cladding. Here, it was shown that tetragonal zirconia stabilized nearest the metal interface is an additional barrier to an otherwise diffusion-limited oxidation mechanism. Chapter 8 discusses a novel treatment of lithium metal anode in a battery, where a porous LiF-rich layer was produced on the lithium metal surface prior to exposure to electrolyte. With the support of $LiNO_3$ as an additive in the electrolyte, a bi-layer structure was formed that improved ionic flux and maintained structural integrity over cycles when compared to both standard lithium foil and dense LiF coating. Chapter 9 summarizes all this work, along with possible directions for future research in these fields.

CHAPTER 2. INTRODUCTION TO NUCLEAR ENERGY

The utilization of atomic, or nuclear, energy was first realized as a viable electrical energy source in 1951, when INL's Experimental Breeder Reactor No. 1 (EBR-I) supplied this form of energy to illuminate four 200-watt light bulbs. Four years later, Argonne National Laboratory progressed the results from EBR-I to power the city of Arco, Idaho, making it the first city to be powered by nuclear energy. Since that time, nuclear energy has been recognized around the world as an effective and low carbon-emission energy source. Outside of the United States, other countries such as France, Slovakia, Ukraine, and Hungary utilize nuclear energy to supply more than half of their total electricity generation, according to the Nuclear Energy Institute. The future outlook of a diverse decarbonization of energy should incorporate nuclear energy, as its superior energy density supports both baseline and peak loading points of the grid's energy, as well as produces electricity without carbon or other air-pollutant byproducts. However, nuclear energy is deemed a non-renewable resource, due to the need for long-term waste storage of dangerous radioactive byproducts. Beyond the issue of waste storage, nuclear reactors are susceptible to intense radioactive exposure from reactor failure, which, though low in probability, has potentially severe consequences, such as those seen after the Chernobyl disaster, or the near disaster accidents at Three Mile Island and Fukushima Daiichi.

Nuclear energy functions by uranium-based fuels releasing multiple high energy neutrons by fission that causes a chain reaction, heating neighboring water coolant into

steam that in turn spins a turbine and generates electricity. To allow a fission chain reaction to occur unperturbed and generate energy efficiently, a cladding material encapsulates the fuel, preventing highly radioactive fission products from escaping into the surrounding coolant. Zirconium is a viable material choice for cladding due to its low neutron absorption cross-section, high mechanical strength, and strong corrosion resistance while in an extreme environment [18]. Alloying of zirconium has been shown to increase cladding performance by improving mechanical properties while maintaining corrosion resistance in high-temperature water [19-23].

The general high-temperature coolant-side corrosion of zirconium cladding is similar regardless of its primary media (oxygen, water, or steam) [24]. Initial formation of the oxide film on zirconium is passivating according to its Pilling-Bedworth ratio of ~1.6 [25], thus slowing the rate of oxidation to follow the empirical power-law with parabolic to sub-parabolic characteristics (exponent, $n \leq 0.5$, Figure 2.1) [26]. Here, the oxidation rate is limited by diffusion of corrosion species (e.g., oxygen anions) to the metal/oxide interface [27]. With subsequent oxidation, cracks develop within the oxide, providing pathways for species to reach the base metal at an increased rate. This is observed as a transition in mass growth, progressing to a near-linear to linear oxidation rate [26-30]. This is commonly termed as the "breakaway phenomenon" [29]. Depending on alloy composition, some elements support cyclic transition between passivation and oxidation, while others do not support re-passivation and the alloy fails to recover from the first breakaway. Some alloys in specific environments, such as Zr-2.65Nb in 700 °C air, show minimal passivation and degrade at a rapid rate (Figure 2.1). Continuous oxidation of the metal eventually leads to failure of the cladding material, albeit at

different rates [26]. Having a better grasp on the state of a cladding material in-pile could provide insight into when it is necessary to shut down a nuclear reactor safely.

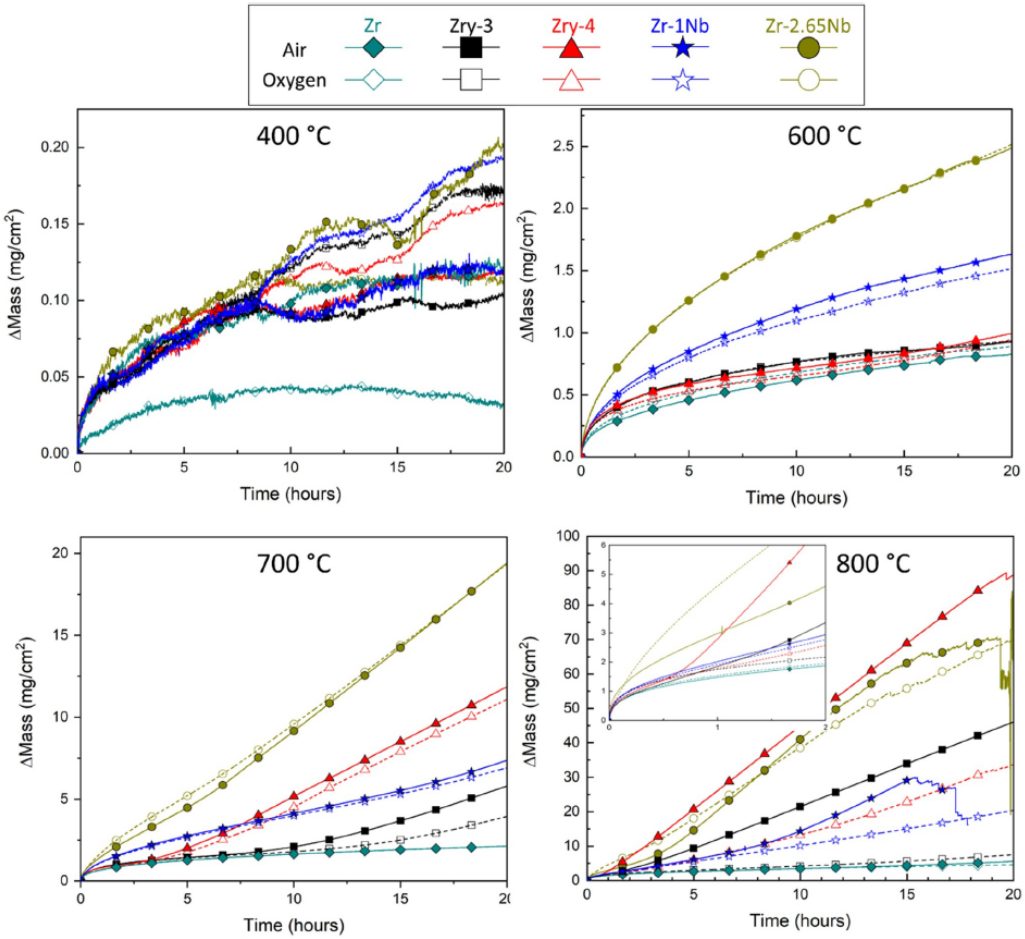

Figure 2.1. From Vandegrift et al. [26]: "Normalized mass gain versus isothermal oxidation time of Zr, Zry-3, Zry-4, Zr-1Nb, and Zr-2.65Nb in air and oxygen at 400-800 °C. The inset in the 800 °C is the first two hours of the isothermal oxidation showing the onset of breakaway in Zry-3, Zry-4, and Zr-2.65Nb."

In addition to the breakaway phenomenon, there are other effects that contribute to cladding failure. Addition of hydrogen species in the coolant has been shown to cause cladding embrittlement by dendrite-like precipitation in the metal [19, 31]. Inclusion of nitrogen species has been found to advance the breakaway phenomenon by creating defects and lattice mismatch in the oxide or at the metal interface, thus permitting

increased oxygen diffusion to the base metal [32-35]. High compressive stresses [30, 36-41], zirconia phase content [38, 42-45], sub-stoichiometry of the oxide [24], operating temperature and environment [46-49], and alloying dopants [23, 27, 28, 50] have all been shown to play a role in cladding lifetime and failure mechanisms. Additional contributions from the fuel/cladding interface (i.e., pellet-cladding interactions (PCI)), such as fuel swelling [51], fuel fracture [52], and stress corrosion cracking [53] lead to unpredictable cladding lifetimes as well as decreased energy efficiency. The complexity of differing effects presents a difficult problem to predict and monitor cladding failure, and thus has been a major focus of nuclear research (Figure 2.2).

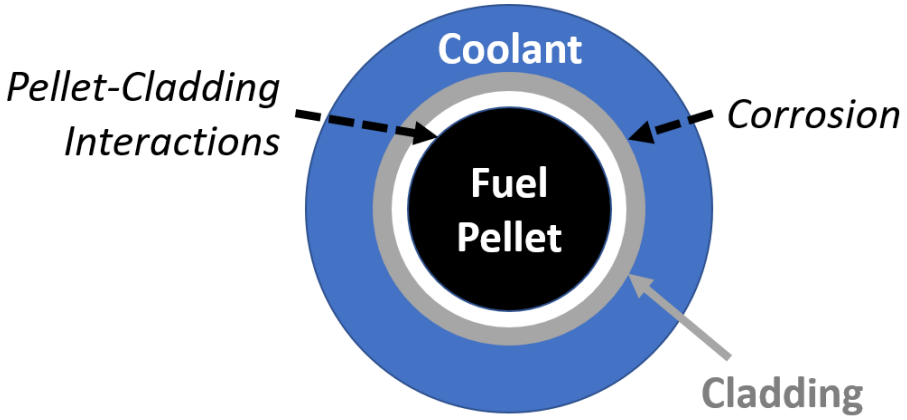

Figure 2.2. Schematic of nuclear components and cladding interactions, including pellet-cladding interactions (PCI) and coolant-side corrosion.

Presently, chemical evolution over the lifetime of the fuel and cladding inside a nuclear reactor can only be inferred using post-irradiation examination (PIE) [54]. Due to the adverse environment created from harsh ambient conditions and irradiation, the corrosion mechanisms of cladding are difficult to observe in-pile or effectively mimic through experimentation. This limitation presents a significant obstacle for achieving a comprehensive and unified understanding of cladding degradation mechanisms. Progress

is being made to establish a new sensing technique by monitoring cladding in-pile with an electrochemical impedance spectroscopy (EIS) sensor. In order to improve EIS sensor accuracy through the fitting parameters of equivalent circuit models, high-resolution characterization of materials has been utilized to better understand the degradation mechanisms of zirconium alloys on the coolant-side. The objective of the work presented herein on nuclear energy is to develop an in-pile measurement technique, with initial focus on utilizing high-resolution materials characterization techniques to better understand the degradation mechanisms (seen in Chapters 6 and 7). From there, the "blind" in-pile EIS technique will have an improved accuracy of equivalent circuit modeling (seen in Chapter 9).

CHAPTER 3. INTRODUCTION TO BATTERIES

Batteries convert acquired energy to stored energy; this is done through an electrochemical mechanism, where the conversion between electrical and chemical energy allows high-density energy storage and utilization. The basic system of a battery with lithium metal as anode is shown in Figure 3.1. The electrodes (i.e., cathode and anode) are the physical collectors of transferring ionic species (i.e., i^{+}). The separator is used to prevent physical contact between cathode and anode, while providing a barrier to particle transfer outside of the desired ionic species. Between the electrodes is the electrolyte, which provides a low resistance pathway for ionic transport. This has commonly been a salt-in-solvent-based liquid solution; however, recent advances in solid-state electrolyte design have provided a new generation for plausible large-scale battery production [55-60].

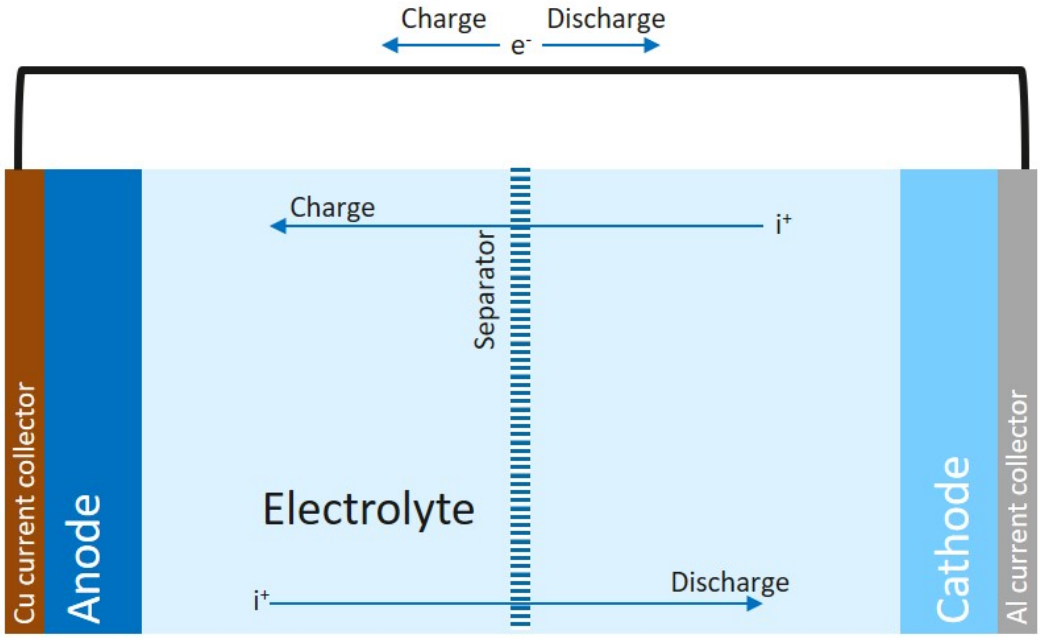

Figure 3.1. Schematic of a battery with charge and discharge mechanisms shown.

Alessandro Volta is credited as the first person to develop an effective battery when he designed the voltaic pile around 1800. From there, batteries were developed and modified with materials that supply higher energy densities. Around 60 years ago, effort into designing lithium-based batteries was initiated by both governmental and military entities, as lithium provides vastly superior theoretical capacity (3,860 mAh/g, 2,061 mAh/cm^3) and low electrochemical reduction potential (-3.04 V vs. SHE) compared to other materials (Figure 3.2) [61-64]. These measurables matter due to the amount of energy that can be stored into a battery's unit space or mass. Equation 3.1 shows that energy (E) of an electrode is dependent on cell voltage (V) and capacity (Q), of which lithium-metal provides advantageous amounts [65].

$$E\left(\frac{mWh}{cm^3, g}\right) = \int V\,(V)\,dQ\,\left(\frac{mAh}{cm^3, g}\right)$$

Equation 3.1

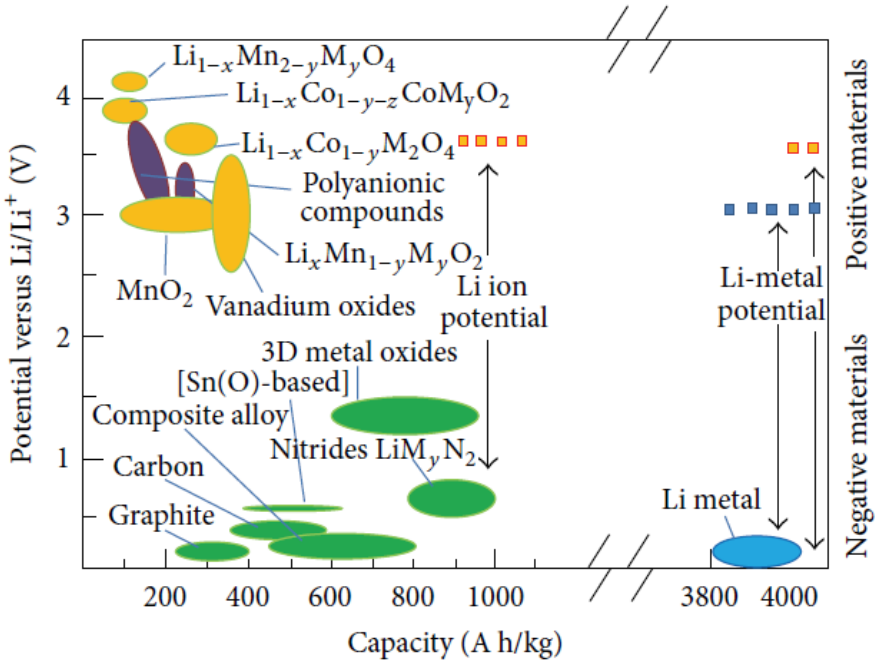

Figure 3.2. From Liu et al. [63]: "Comparing of some potential anode materials for lithium ion batteries."

However, due to lithium's high reactivity, these batteries are susceptible to dendrite growth, a needle-like or tree-like structure that rapidly grows and eventually contacts the cathode, causing short-circuiting (Figure 3.3). The safety concerns with short-circuiting in a flammable electrolyte, along with poor cycle life and low Coulombic efficiency (CE, i.e., efficiency of charge transfer) caused by Li/electrolyte side reactions, are the major barriers to commercialization of secondary lithium-metal batteries [62]. Changing the anode to materials where lithium ions can be stored in interstitial sites reduced the danger and low cycle life seen with lithium metal as the anode. This led to a technology revolution, where portable electronics became a reality and worked their way into our everyday lives. Additionally, the electrification of long-range electric vehicles and storage support of non-dispatchable renewable energy sources gave lithium-ion batteries a role in the efforts to decarbonize our energy.

The difference between the lithium-ion and the lithium-metal battery is the mechanism of insertion and removal of lithium ions at the anode. For current lithium-ion anodes, such as graphite, lithium (de)intercalate (out of) into graphite's interstitial spaces, whereas lithium is plated and stripped from the lithium-metal anode. This (de)intercalation of lithium-ion batteries reduces the possibility of dendrite formation and short-circuiting, as well as loss of capacity over shortened cycle life. However, the capacity ceiling of Li-ion batteries (upwards of 340 mAh/g) is incapable of meeting new demands [66]. Due to the fact that lithium metal can supply a theoretical capacity approximately ten times greater than common lithium-ion anodes, as well as a more negative reduction potential, lithium metal has reemerged as a candidate anode with attempts to better understand and reduce the mechanisms that cause its failure.

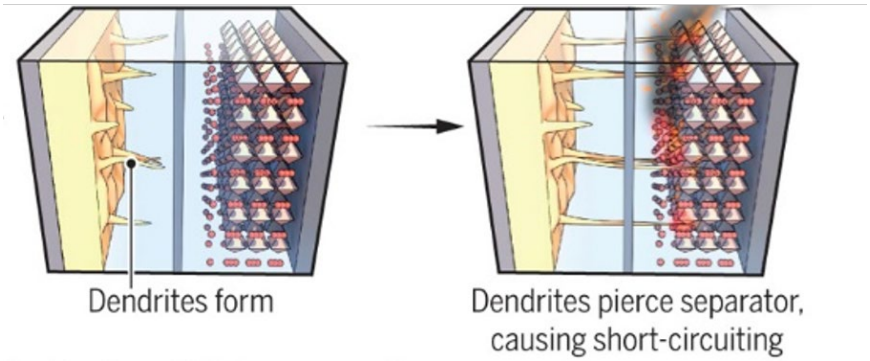

Figure 3.3. From Mukhopadhyay et al. [67]: "Use of Li metal anodes allows high energy densities in rechargeable batteries, but Li dendrite formation leads to short-circuiting."

The core of these mechanisms is rooted in poor interfacial stability. When exposed to nearly all environments, lithium metal will act as a strong reducing agent of the environmental species, forming a surface film on lithium. An example is the native film, which forms when trace gases in an inert environment (e.g., O_2, CO_2, hydrogen and nitrogen species, etc.) reduce on the lithium surface, forming various organic and

inorganic species (e.g., Li_2CO_3, Li_2O, LiOH, etc.) [68]. This non-uniform native film starts a waterfall effect of heterogeneity for progressive interfacial instability. This initial heterogeneity is exacerbated when the anode is immersed in an electrolyte. The electrochemical potential of lithium is outside the stability window for most electrolytes (hydrous or anhydrous), and thus the electrolyte will reduce at the lithium surface to form a solid electrolyte interphase (SEI) made up of a complex mixture of organics and inorganics (e.g. ROLi, $ROCO_2Li$, LiF, Li_2O, Li_2CO_3, etc.). This is one of the originally predicted and observed SEI structures, commonly referred to as mosaic [69]. Another predicted pathway for SEI formation is a multi-layered structure, where the amount of inhomogeneity is reduced for each individual layer, where inorganic material is commonly seen nearest the anode and organic material nearest the electrolyte [70, 71]. Beyond simple variations in chemical make-up, other heterogeneities, such as topographical roughness (e.g., “tip” effect) and micro- to nanoscale crystallographic defects like grain boundaries lead to non-uniform SEI formation and eventual ionic flux during (dis)charge [72]. Regardless, the SEI is believed by many to be the key to harnessing the Li-metal battery, as its instability is the common reason for battery failure through issues such as dendrite formation, active material consumption, and poor interfacial charge-transfer. Much discussion has been suggested as to the desirable SEI structure, and how that can vary the preferential pathways for mass and charge-transfer [71]. Efforts to produce an ideal SEI have been placed in intermingling fields of electrolyte engineering [73-76], interface engineering [72, 77-79], and 3-D architecture [80-84], all of which are centered around stabilizing the interphase.

For electrolytes, recent focus on the solvation structure has given rise to advanced electrolyte designs such as high-concentration electrolyte (HCE) or localized high-concentration electrolyte (LHCE) [85-88]. With these new designs, the Li^+ cation in the bulk electrolyte maintains high interaction with the salt anion in its primary solvation shell, rendering a salt-derived interphase upon desolvation within the electrical double layer (EDL) near the anode surface. This is contrary to a common low-concentration electrolyte (LCE), where the solvation shell is primarily comprised of the solvent, leading to an organic-rich, porous, and unstable SEI. Interestingly, the results presented in literature have shown some variance, where the key parameters as to why a particular electrolyte presents improved performance are still not completely understood. Continued effort into this work is ongoing, with further expansion of electrolytes for harsher ambient environments [89, 90], along with increased efforts in fundamental characterization analysis [91-93].

Interfacial engineering is another interesting topic in the battery world, where a design of the interface prior to exposure to electrolyte is done to initiate SEI properties that are deemed as ideal. One way of producing an ideal SEI is through pre-treatment, with the intention of minimizing chemical, topographic, and crystallographic variations on the surface. These methods can vary in complexity, from simple polishing [84] or polycyclic aromatic hydrocarbon (PAH) treatments [94] to melting and rolling lithium foil [72]. Others have produced what is called an “artificial SEI”, which can be viewed as a coating that inhibits the instability of lithium metal. LiF is a common artificial SEI choice, as it provides electrochemical stability and low solubility [79, 95-98]. However, the rigidity of LiF causes SEI fracture upon the semi-infinite volume fluctuations that

lithium metal can undergo [84]. A more complex surface treatment design is a three-dimensional anode matrix that conducts both electrons and ions (i.e., mixed ionic electronic conductor). This design reduces the “tip” effect, where (electro)chemical potential gradient of topographical heterogeneities is reduced, which in turn reduces local volume fluctuations and dendrite propagation (Figure 3.4) [99]. However, with this open-host design, the rendered SEI is still driven by Li/electrolyte reactions; thus it is susceptible to continuous parasitic reaction that consumes active material over a shortened cycle life.

There are many different pathways being taken in an attempt to stabilize the lithium-electrolyte interface, with much discussion as to what the idealized SEI structure should be to extend capacity utilization and cycle life. Advances are necessary in two identified routes – first, a fundamental understanding of ionic pathways and materials stability, and second, expansion of current cell designs into large-scale batteries, such as multi-layer pouch cells. To advance the efforts of decarbonizing the energy grid and transportation sector, higher energy density and safer battery chemistries must be designed through advanced fundamental techniques, with a mindset of expanding to large-scale efforts.

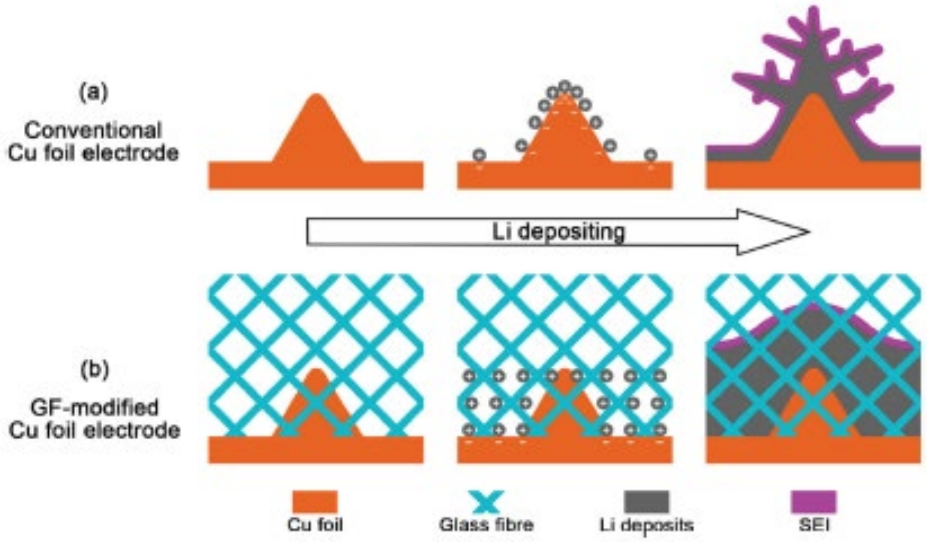

Figure 3.4. From Cheng et al. [99]: "Schematic diagrams of Li deposition. a) The routine 2D Cu foil electrode is always with an uneven surface that induces inhomogeneous electron distribution. Li ions aggregate near the protuberance on the 2D surface with a stronger field strength than the flat during continuous Li depositing. The agminated Li ions can trigger Li dendrite growth. b) GF cloth is with large quantities of polar functional groups (Si O, O H, O B), resulting in a strong interaction with Li ions. The concentrated Li ions by the protuberances on the Cu foil electrode are evenly redistributed, therefore rendering the dendrite-free Li deposits."

CHAPTER 4. ADVANCED CHARACTERIZATION TECHNIQUES

4.1 X-ray Photoelectron Spectroscopy (XPS)

Based on the photoelectric effect, XPS is a surface to sub-surface characterization technique that provides chemical information of materials. Elemental composition and chemical states can be measured with XPS, providing insight into the make-up of the material. This is accomplished by irradiating a solid surface with a monochromatic X-ray beam of a specific photon energy ($h\nu$) to excite material electrons while simultaneously measuring these excited electrons' kinetic energy (KE). A photoelectron spectrum of binding energy (BE) is produced from these collected electrons (Equation 4.1, Figure 4.1), equating to chemical and oxidation state(s) of the material structure. Reference spectra are utilized to define peak positions in a spectrum, basing the value upon the photoelectron energies defined by the host atoms and their interactions. In general, there is a direct trend between higher host atom binding energy to more electronegative element interaction. In other words, the breaking of a more electronegative bond requires more energy [100]; for example, LiF (~56-57.5 eV [101-104]) is observed as a higher binding energy peak than Li_2O (~53-54 eV) [102]. Further, increasing the number of bonds also increases the bond energy. An example can be seen in a carbon spectrum, where C=O (~288-290 eV) [88, 105, 106] is higher in binding energy than C-O (~286-287 eV) [88, 101, 105, 106]. Alternatively, when observing the more electronegative oxygen species as host atom, binding energy is less for C=O (~532-532.5 eV) than C-O

(~533.5-534 eV). [105, 106] Therefore, XPS can provide chemical information like the oxidation state of elements in the material of interest.

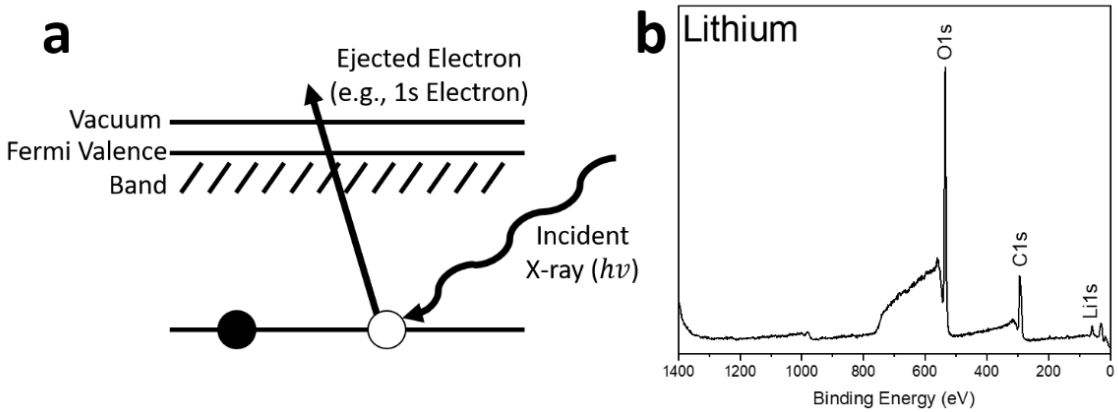

Figure 4.1. (a) Energy diagram of XPS electron excitation. (b) Example survey spectrum acquired with XPS, observing a lithium foil.

$$KE = hv - BE$$

Equation 4.1

Difficulty in peak deconvolution and defining peaks has been greatly discussed, causing frequent misinterpretation by novice users and variable results presented [107]. Herein are some thoughts on interpreting XPS spectra. The C1s hydrocarbon (C-C/C-H) peak signal at ~284.8 eV is a common peak to calibrate spectra, due to its nearly universal presence. Knowledge of other peaks could be utilized when poor carbon signal is seen, air exposure is prevented (as almost all air-exposed surfaces are contaminated with adventitious carbon), or overall differentiation of the C-C peak is difficult [100]. Since electrons can only travel a short distance in solids, the surface characterization acquired from the energy spectra is defined by the top 1-10 nanometers of the material [100]. Sub-surface analysis can be accomplished with depth profiling, where an ion beam is used to etch layers of a material away, allowing analysis of underlying layers with XPS (Figure 4.2). This is a common tool for monoatomic materials (i.e., layering of single

materials), where etch rates should be equal across the collection area. When a material is more complex, etch rates may spatially vary, and therefore quantitative analysis with depth profiling is at best difficult to interpret. Therefore, supporting analysis with other techniques should be used to analyze depth profiling data; an example is using SEM to observe surface morphology (e.g., surface porosity, roughness, etc.). Additionally, relative comparisons between samples could be used to observe trends seen with a change in conditions; an example would be forming a coating/interphase on a material at different temperatures and seeing how spectral peaks or elemental concentration transition as a function of sputtering time. Another major issue with depth profiling of complex structures is the damage done to the material by impacting ions, therefore causing shifts in energy spectra when analyzed after sputtering. Again, though quantitative analysis is not easily rendered, comparative analysis between different samples could provide insight into how a controlled variable could affect the sub-surface make-up of the material of interest.

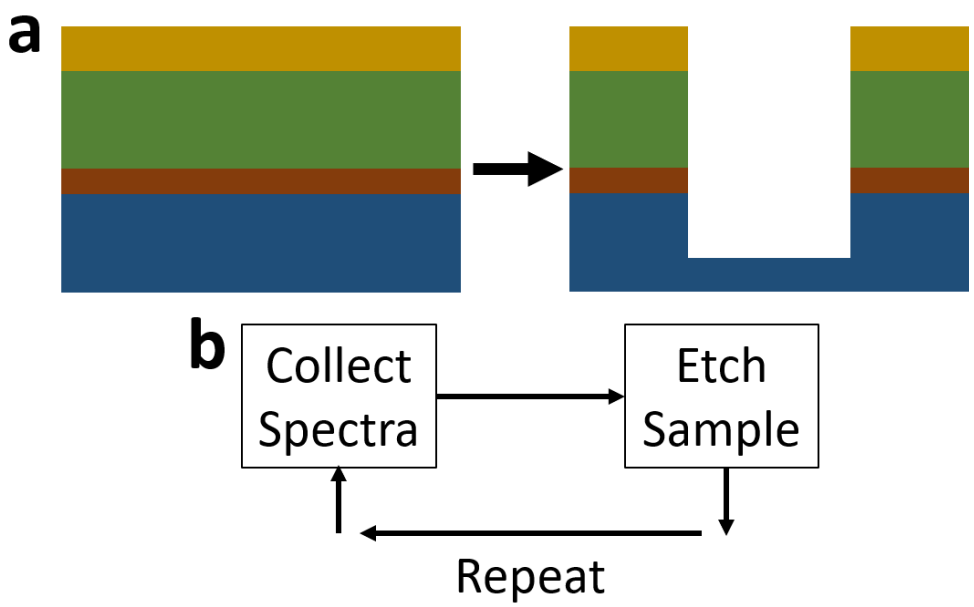

Figure 4.2. (a) Depth profile example through a monoatomic layered material. (b) Experimental flow for depth profiling.

4.2 Electron Microscopy (EM) Techniques

EM is a surface analysis technique with magnification that far surpasses the ability of visible light photons. With EM, focused, accelerated wave-like electrons carry kinetic energy through a vacuum space until they bombard the surface of a material, where interactions with the surface (e.g., scattering, reflection, or transmission) reach a detector, providing the user visualization of the sample. Varied methods of analysis can provide different information about the material of interest (Figure 4.3). Transmission electron microscopy (TEM) is used to observe ultra-thin foils with an electron beam that passes through the material, providing detailed diffraction patterns. Contrast observed in a TEM image or diffraction pattern can correlate to material density, atomic make-up, crystal structure or orientation, and the presence of defects (e.g., dislocations). SEM uses raster scanning with low-energy secondary electrons to analyze an area, collecting

reflected energy. The depth of field of SEM is useful to investigate surface morphology, giving the user a visualization of three-dimensional roughness and defects. High-energy backscattered electron (BSE) detection can be utilized to contrast areas of different compositions. Energy dispersive X-ray spectroscopy (EDS) can align its elemental analysis with contrast seen in BSE and structure in SEM secondary electron imaging (Figure 4.4) [16].

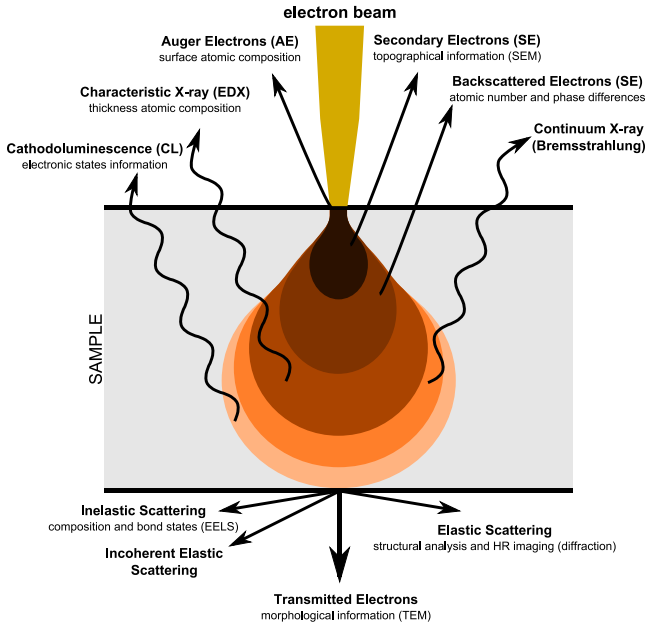

Figure 4.3. Visualization of different interactions between an electron beam and a sample, exemplifying the different types of data that can be collected from EM. Image provided by Thermo Scientific Fisher.

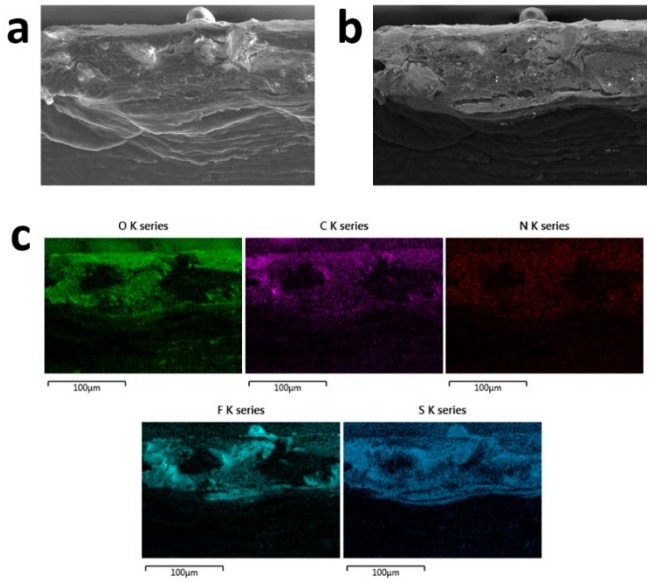

Figure 4.4. EM of a lithium foil cross-section after extended exposure to 1M lithium bis(trifluoromethanesulfonyl)imide (LiTFSI) in a 1:1 dioxolane (DOL):1,3 dimethoxyethane (DME) co-solvent with 2 wt. % $LiNO_3$. (a) Secondary electron image, (b) BSE image, and (c) EDS of different elements.

With the inclusion of a high-energy focused ion beam (FIB), the user can etch away material, making it possible to observe sub-surface features. This is especially useful for those that wish to view material density, interfaces (e.g., SEI in batteries [84, 91], metal/oxide networks [108], etc.), layer thickness, and differentiation of consumed (i.e., oxidized or insulating) from active (i.e., metallic) material [109]. Additionally, with the help of a micromanipulator (e.g., OmniProbe) and platinum gas injection system, etched out material can be removed in a conical shape to be analyzed with an atom probe tomograph (APT, Figure 4.5). APT acquires 3-D imaging with atomistic composition that allows observation along metal/oxide boundaries, compositional gradients, or other minor variations/defects in a material. In the nuclear field, APT has revealed evident differences in phase distribution for oxidized cladding. This was accomplished by examining a metal/oxide interface of pure Zr cladding after exposure to a LOCA (loss-of-coolant accident)-simulated high-temperature air (Figure 4.6). Here, a thin $Zr(O)_{ads}$ region is seen

(i.e., approximately 50/50 Zr/O) interfaced by zirconium and oxygen-rich regions [110], providing evidence in agreement with the cladding oxidation model that states that oxygen diffusion through ZrO_2 forms a metastable sub-stoichiometric ZrO_{2-x} region at the interface [27]. With the use of other characterization techniques, this sub-stoichiometric region is stabilized as a tetragonal phase, in contrast to monoclinic ZrO_2 further from the metal interface [111, 112].

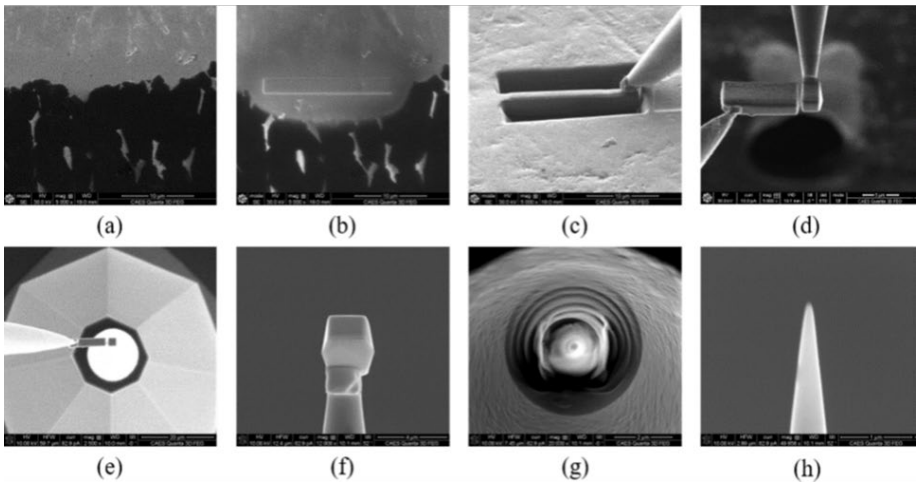

Figure 4.5. From Hu et al. [110]: "Progressive steps in the making of tips for the LEAP. (a) Before and (b) after ionized platinum deposition at metal/oxide interface. (c) OmniProbe welded to a grid for its removal from the bulk of sample. (d-e) OmniProbe with free-hanging grid. Wedge is disjointed from rest of grid and welded to a microtip post. (f) Individual wedge welded to a microtip post. (g-h) Individual wedge after annular milling, producing a tip ready for LEAP testing." Here, the LEAP is an APT tool, the Local Electrode Atom Probe, available at the Materials Characterization Suite at the CAES. Full-width of each image is (a-d) 40 µm, (e) 60 µm, (f) 12.5 µm, (g) 7.5 µm, and (h) 3 µm.

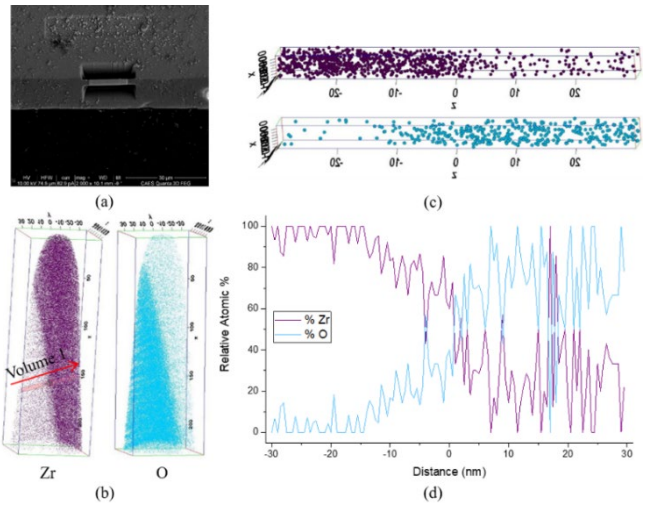

Figure 4.6. From Hu et al. [110]: "APT results from a pre-breakaway Zr sample, exposed for 20 hours at 700°C. (a) SEM image of ionized platinum deposition with trenches etched out on either side of Pt deposit. (b) LEAP produced elemental maps showing a distinct interface. Here, 'Volume 1' is described by a 0.5 nm binning across the interface (seen in Zr map). (c) Volume 1 elemental atom-by-atom representation, showing a transition of Zr-rich to O-rich volume. (d) Relative atomic percentages between Zr and O elements."

Placing samples in a cryogenic atmosphere maintains the structure and composition of materials without radiation damage from the beam, providing even better analysis with FIB or TEM (Figure 4.7) [84, 92, 93]. Similar to the ion beam with XPS depth profiling, incident electrons ionize the surface, breaking bonds and causing a cascading effect of secondary damage; cooling the sample, along with limiting beam exposure, can drastically reduce sample damage. Originally developed in 1974 for the biological community, cryo-EM has been utilized to visualize metal-organic frameworks, battery materials, and many other systems [92]. In the battery field, cryo-EM has provided intriguing results, such as showing an amorphous phase nucleating during initial plating on a lithium metal anode [93]. It has also been used to observe coatings (i.e., artificial solid electrolyte interphases) and redox-driven interphases on electrodes [84].

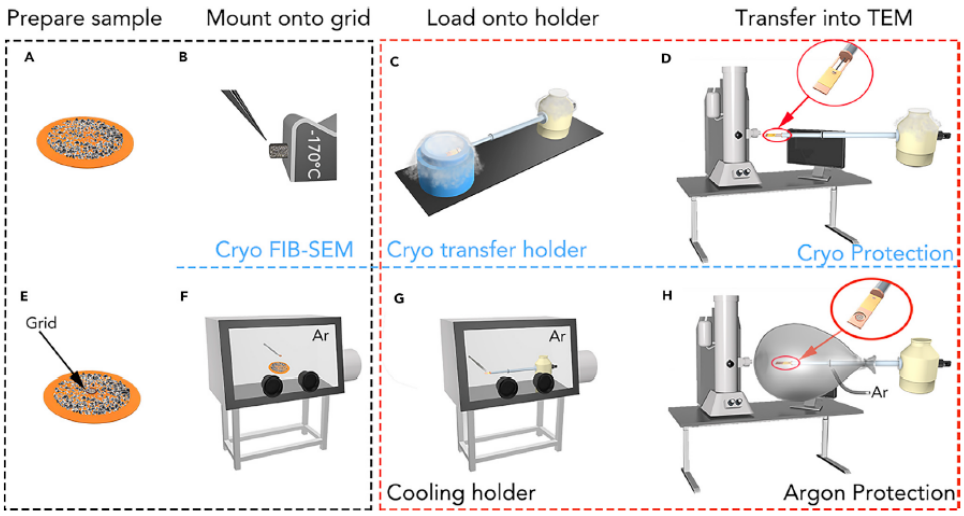

Figure 4.7. From Wang et al. [92]: Schematic images showing the processes to prepare sample, mount to grid, load on holder, and transfer into the TEM safely. (A) Sample dispersed on the substrate. (B) Mount the sample on the grid by cryo-FIB-SEM. (C) Load the grid onto the cryo transfer holder within the liquid N_2. (D)Transfer the cryo transfer into the TEM with a closed shuttle. (E) Samples directly deposited on the grid. (F) Harvest the grid in the Ar-filled glovebox. (G) Load the grid onto the cooling holder in the glovebox. (H) Transfer the cooling holder into the TEM with Ar protection.

There are some limitations to EM techniques beyond ion-beam damage that lessen the quality of imaging or the materials that can be analyzed. If the sample is insulating, then the surface will pool with charged particles and cause issues in achieving pristine images. Sputtering carbon or other conductive materials onto the insulating surface will help prevent surface charge; however, the ability to conduct elemental analysis is now drastically less reliable, as carbon will flood the EDS spectrum. Light elements, like hydrogen or lithium, are also not detectable with EDS, limiting the amount of elemental analysis that is possible, such as elemental confirmation of metal-hydrides.

In summary, the EM suite of techniques is incredibly useful for understanding the structure of a sample from the macro to the atomic scale. Many advanced research fields rely on EM methods to provide insight into material structure and composition. Specifically, this suite of EM tools is useful in examining both battery and nuclear

materials. EM techniques are often used to observe materials after processing, post-exposure to a corrosive environment, or post-mortem after operation. Materials synthesis and their survival in an extreme environment are observed with EM to better predict or observe the mechanisms at which these materials degrade.

4.3 Raman Spectroscopy

Raman spectroscopy utilizes monochromatic light to interact with a material, where the light is transiently adsorbed and scatted. Alternative to the same frequency re-emittance seen with elastic Rayleigh scattering, Raman scattering is inelastic, where scattered light shifts in its energy after interaction with matter ($v_o \pm v_m$). Herein, peaks are observed at measurable shifts from the Rayleigh scattering and observed as spectra. Each peak correlates to vibrational modes of molecules or collective modes (e.g., phonons or lattice vibrations) in the material system; tetragonal zirconia (t-ZrO_2) is displayed in Figure 4.8 [113], while Raman spectra of different zirconia crystal structures is shown in Figure 4.9 [110]. Raman spectroscopy can therefore be used to determine crystallographic structure [38, 45, 114], stress-state [40, 41, 111, 112], and defects in solids, as well as solvent-salt interactions in liquids [88, 89, 115]. However, pure metals are not Raman active, as they do not show a change in polarizability during molecular vibrations; therefore, ceramics, polymers, and liquids are the common materials observed with Raman spectroscopy.

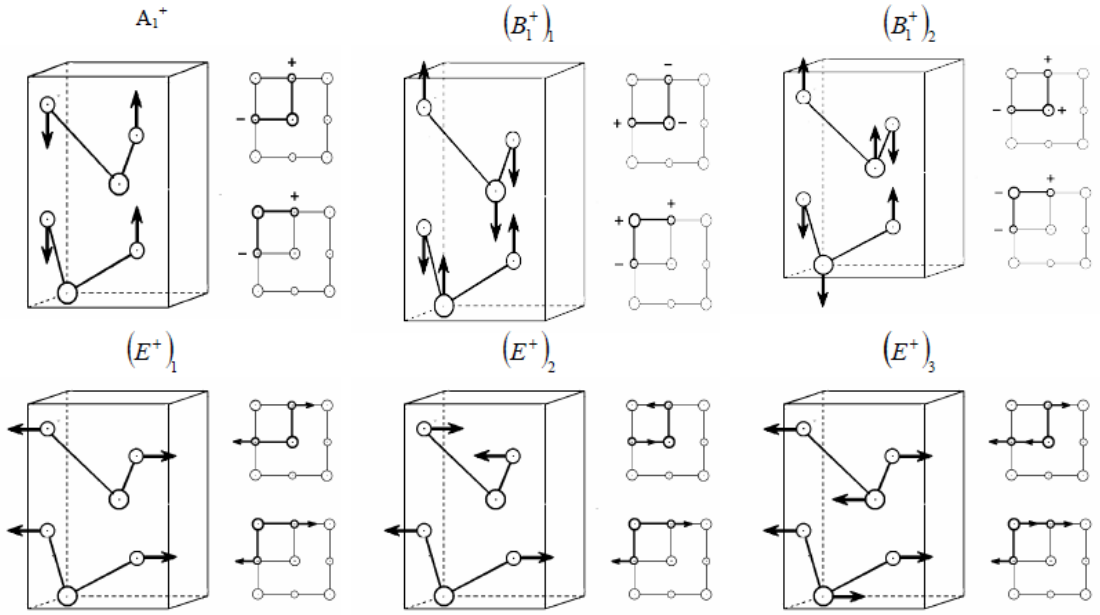

Figure 4.8. From Naumenko et al. [113]: "Normal vibrations of crystal lattice of t-ZrO_2 (Raman-active modes)."

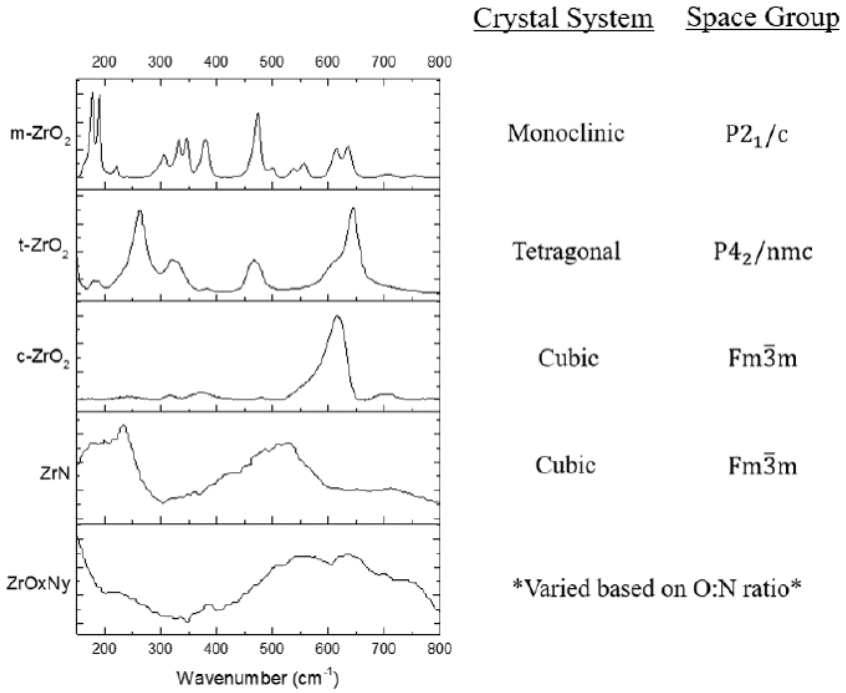

Figure 4.9. From Hu et al. [110]: "Raman spectra for zirconia polymorphs and other zirconium variants."

Mapping with Raman can provide spatial insight into different crystallographic features [42, 43]. This is particularly useful when examining gradient structures, such as the cross-section across a metal/oxide interface. An example is shown in Figure 4.10, where Raman spectra were collected in an X-Y spatial region along the oxide of a corroded zirconium sample. With the collection of spectra, different forms of analysis such as peak heights, peak positions, half-width at half-maximum (HWHM), or peak area can be quantified to correlate to differentiating structural features. From there, a map may be rendered to spatially analyze these features. This is further discussed in Chapter 6.

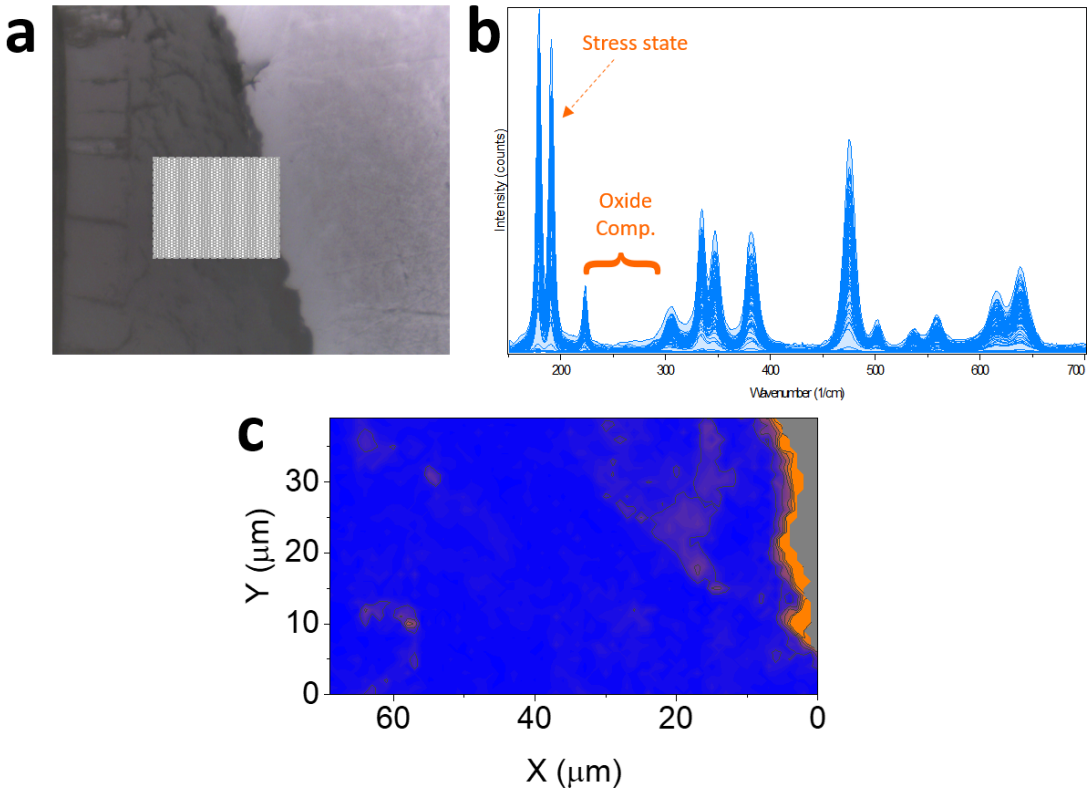

Figure 4.10. Raman mapping process to analyze the cross-sectioned oxide of a Zr cladding material. (a) Optical image of the Zr/ZrO_2 (right to left) interface with Raman mapped region in grey. (b) Raman spectra collected over spatial region in oxide. Peaks of focus for stress state and oxide composition are designated. (c) Rendered Raman map from spectra processing. These images are partially published [112] and were presented at TopFuel 2019, a Light Water Reactor Fuel Performance Conference.

4.4 Atomic Force Microscopy (AFM) Techniques

Invented in 1985 at IBM, AFM measures van der Waals interactions between a highly resolved probe and the surface of a material. Thanks to advanced processing of the probe tip and design of piezoelectric feedback electronics, this non-destructive method of characterization can achieve spatial resolution on the nanoscale. The simplest task accomplished with AFM is the acquisition of topography. Here, the probe will raster while going across the material, collecting data in a line-by-line process. An advanced mechanism recently developed by Bruker called PeakForce Tapping (PFT) employs 2-8 kHz force curve acquisition with an incredibly low and controllable force setpoint (10s-100s nN) between probe and surface for the feedback mechanism (Figure 4.11). Along with the sinusoidal drive, a set interaction rate allows low force control, as well as reduces parasitic deflection signal, thus providing better resolution. In addition to acquiring topography, probe-surface interactions with PFT also provide mapping of quantitative nanomechanical (QNM) properties – modulus, adhesion, deformation, and dissipation (Figure 4.12). With this, the user can observe both surface roughness and differences in mechanical properties that correlate to differences in material composition, nanoscale defects, or other structural information [116].

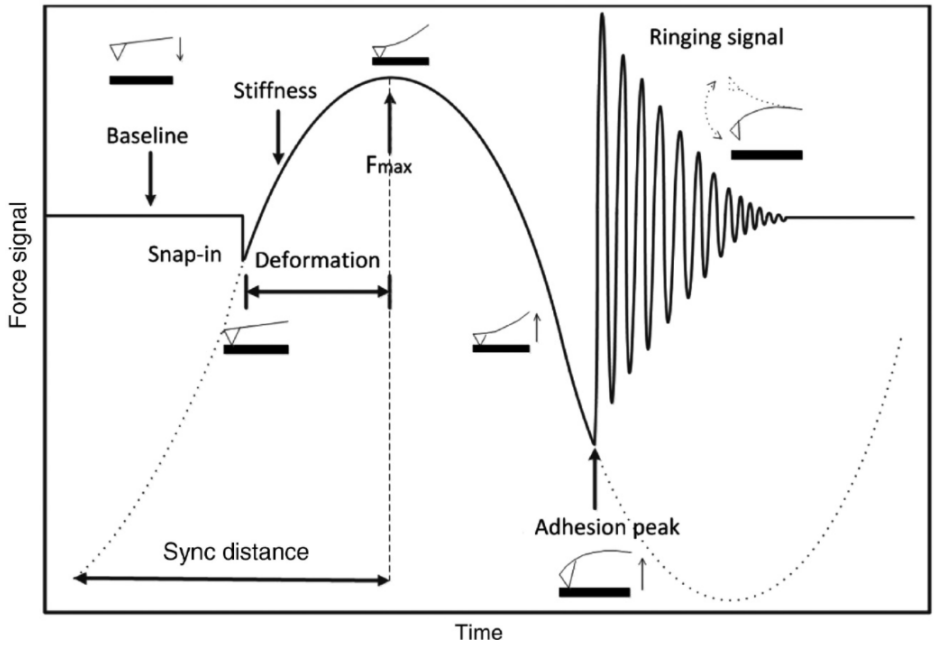

Figure 4.11. From Xu et al. [116]: "Schematic diagram of the PFT."

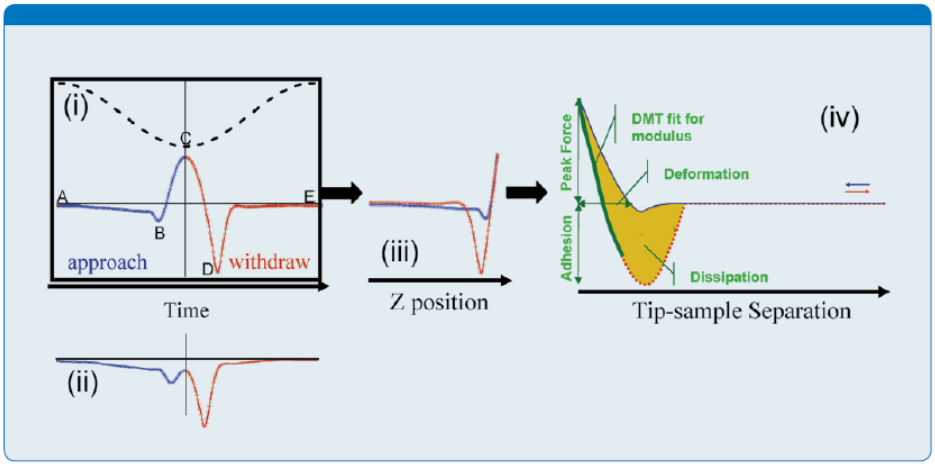

Figure 4.12. From Pittenger et al. [117]: ""Force curves and information that can be attained from them: (i) Plot of force and piezo Z position as a function of time, including (B) jump-to-contact, (C) peak force, (D) adhesion. (ii) Plot of force vs. time with small peak force. (iii) A traditional force curve eliminates the time variable, plotting Force vs. Z piezo position. (iv) For fitting purposes it is more useful to plot force vs. separation where the separation is calculated from the Z piezo position and the cantilever deflection.

Variants of the basic AFM technique within the scanning probe microscopy suite allow additional measurement of many different properties of a material surface, such as conductivity, magnetic fields, or electrical responses. Additionally, immersing a material

into a new environment allows the opportunity to observe kinetic properties *in situ*/*in operando* with methodologies such as electrochemical AFM (EC-AFM) or scanning electrochemical microscopy (SECM). The diverse suite of AFM techniques allows users to observe many different features of a material system to help connect large-scale mechanisms with high-resolution phenomena. A few AFM methods will be described in more detail below.

Magnetic force microscopy (MFM) is a method of probing a sample to observe spatial magnetic response, allowing the observation of features such as magnetic domains or moment orientation. A magnetized tip is used to image the material, commonly in a dual-pass method, where the first pass collects topography, and the second pass collects magnetic response between the probe and material surface. This technique is primarily used to examine different nanomaterials and devices to better understand material response and defect distribution [118-120]. However, MFM is also useful in the corrosion field, where ferromagnetic metals such as stainless-steels are observed to differentiate magnetic domains, and thus differences in phase composition and microgalvanic corrosion response (Figure 4.13) [121].

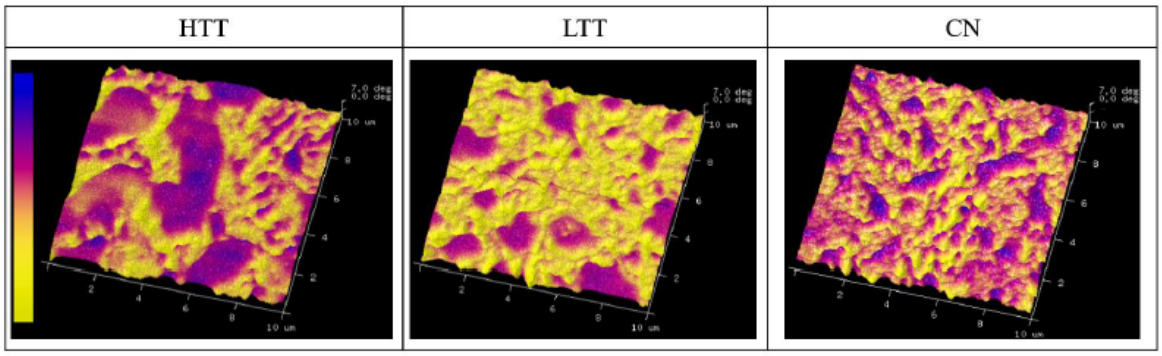

Figure 4.13. From Kvryan et al. [121]: "3D magnetic response maps with changes in height representative of differences in magnetism. Color scale ranges are 7 degress (0° = yellow, +7° = blue) for magnetic response." This work focused on the observation of different treatments of UNS S42670 martensitic stainless steel (MSS): high-temperature temper (HTT), low-temperature temper (LTT), and carbo-nitriding (CN). With MFM presented here, the purple regions indicate carbides, while yellow regions indicate steel matrix. Both types of regions exhibit out-of-plane magnetic domains, but the carbides, with increased chromium concentration, exhibit greater magnitude.

SKPFM measures the difference in work function, or energy required to remove an electron from the Fermi level to the vacuum level, between the material surface and the probe. This technique utilizes the concept of work function difference (directly correlated to the Volta potential difference, VPD) [122] first observed by Lord Kelvin in the late 1800s, where metals physically close together in a capacitor-like alignment undergo an energy and charge shift when placed in electrical contact (Figure 4.14a). Miniaturizing this design with an AFM probe leads to high spatial resolution of the VPD. Here, the probe interacts with the sample in a dual-pass manner, measuring topography first, followed by a user-defined lift off the surface to measure VPD in a pseudo-capacitor method, where the probe traces the topography to maintain the same probe-sample distance across the surface (Figure 4.14b). SKPFM is a highly surface sensitive technique that provides spatially resolved information on the electronic state of the material surface such as galvanic coupling (Figure 4.14c). This technique is commonly used in many

fields, including semiconductors [123, 124], solar cells [125, 126], corrosion detection and prevention [111, 121, 127-134], and batteries [135-140]. More information on this technique is available in Chapter 5.

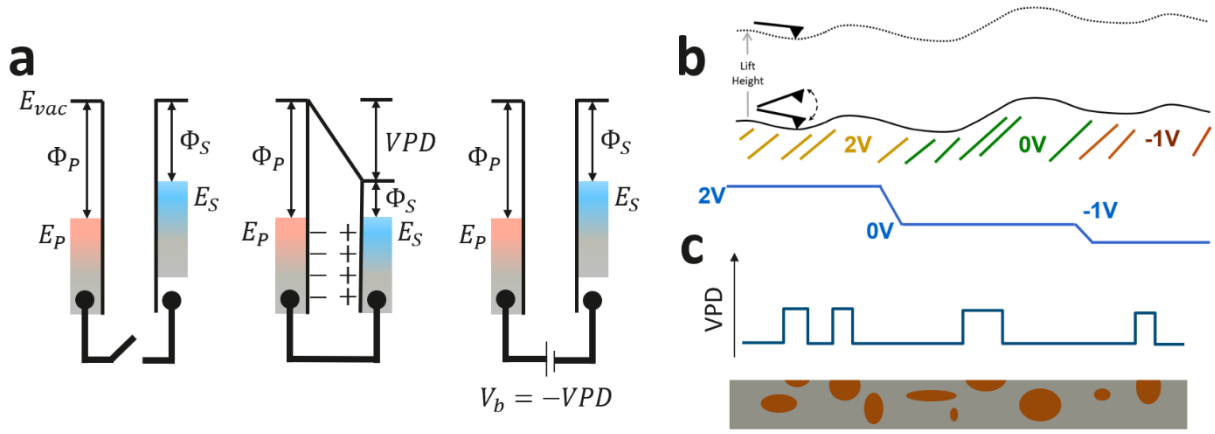

Figure 4.14. Concept of SKPFM, with (a) observation of two metals (probe, P, and sample, S) in a pseudo-capacitive state of electrical contact, where a buckling voltage (V_b) is applied to determine the VPD, or relative work function between probe (ϕ_p) and sample (ϕ_s) that is intrinsically observed between the two metals. (b) Visualization of the dual-pass method, showing both readings of topography (solid black line) and VPD domains (solid blue line). (c) Cross-section of a material with different compositional domains (grey and orange) that causes differences in measured VPD (solid dark blue line) of the surface of the material.

In situ AFM imaging allows the user to observe reaction mechanisms in real-time. The key benefit to *in situ* over *ex situ* or post-mortem techniques is the ability to observe reaction pathways on a micro- to nanoscale, providing further understanding of material stability in an active environment. In the corrosion field, *in situ* AFM has provided insight into how materials processing methods can affect the corrosion mechanism. For example, differently treated MSSs were observed with *in situ* AFM (Figure 4.15). A CN treatment produced many matrix-carbide interfaces that drove localized microgalvanic corrosion, whereas a HTT treatment reduced the density of these interfaces (Figure 4.13)

and therefore underwent more uniform corrosion. LTT performed in the middle of these two, showing some localized attack, but not to the extent of CN [121].

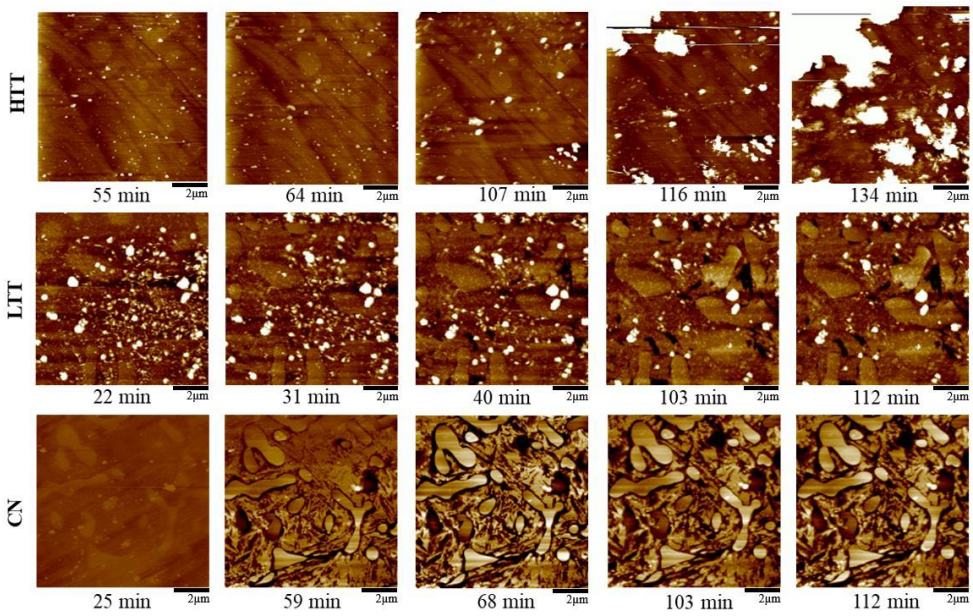

Figure 4.15. From Kvryan et al. [121]: "Time-lapse *in situ* AFM topography maps (160 nm full scale) for each of the heat-treated MSSs in 0.1M NaCl solution, with approximate exposure time at the end of each scan indicated below the corresponding map (image time was ~8.5 min)."

Electrochemical, or EC-AFM, is a useful *in situ* technique to drive and observe reactions such as SEI formation or (de)lithiation mechanisms of electrodes used in a battery. Much has been accomplished with EC-AFM, observing both plating and insertion-based battery materials. Kitta and Sano showed through the support of QNM analysis during *in situ* imaging of lithium metal that regions of low adhesion had a higher growth rate during a galvanostatic plating, revealing the initiation steps of dendritic growth. Additionally, these locations of higher growth rate were observed as having a thinner SEI formed prior to plating than other regions, revealing them as "hot spots", sites of lower energy barriers and thus increased ionic flux [141].

SECM is another *in situ*, *in operando* technique used to provide insight into active behavior of a material. Developed in the late 1980s, SECM has been used to study adsorption rates, metabolism and other biological reactions, surface patterning, as well as many other charge-transfer reactions [142-146]. In contrast to EC-AFM, where the sample is the only working electrode, SECM activates the probe as another working electrode to prompt faradaic current flow to collect electrochemical information about the sample surface. This tool is commonly utilized on the microscale with an ultramicroelectrode, or UME, operating with a spatial resolution of 10-25 μm. Comparing to a nanoscale technique, such as SKPFM, the ability to resolve differences in phases is limited. However, some insight can be drawn to make a connection between nanoscale *ex situ* measurements and microscale *in situ* electrochemical data. For example, observing a Cu-Ag-Ti (CuSil) braze used to join a stainless-steel alloy (SS316L) revealed that the theoretical driving force of corrosion predicted with SKPFM is misleading to the actual corrosion response (Figure 4.16). The ability of stainless steel to form a passivation layer in a neutral pH salt solution caused a change in the mechanism, showing preferential attack on the braze material, contrary to the prediction of the SKPFM results, which showed a lower VPD (i.e., more active or anodic) of the steel when compared to the higher VPD (i.e., more inert or cathodic) of the binary braze components. Additional difficulty is seen in confirming inner-braze mechanisms, where a possible Cu-rich phase is showing less reactivity than the surrounding Ag-rich matrix of the braze. However, post-mortem presented a difference in mechanism, where extensive attack is observed at the Cu-rich regions (Figure 4.16c). The incorporation of a high-resolution optical microscope during the acquisition of SECM is therefore necessary to

provide visual confirmation of separate phases. The complicated effect of surface roughness is also difficult to mitigate with microscale SECM, as the UME does not trace surface topography, therefore providing possibly misleading results that are topographically driven rather than compositionally driven. Miniaturizing SECM to the nanoscale with AFM is a difficult task to accomplish due to frequent issues in probe design and handling. Although limited in recent accomplishments, continued efforts into higher resolution SECM will help advance the fields of both corrosion science and energy storage.

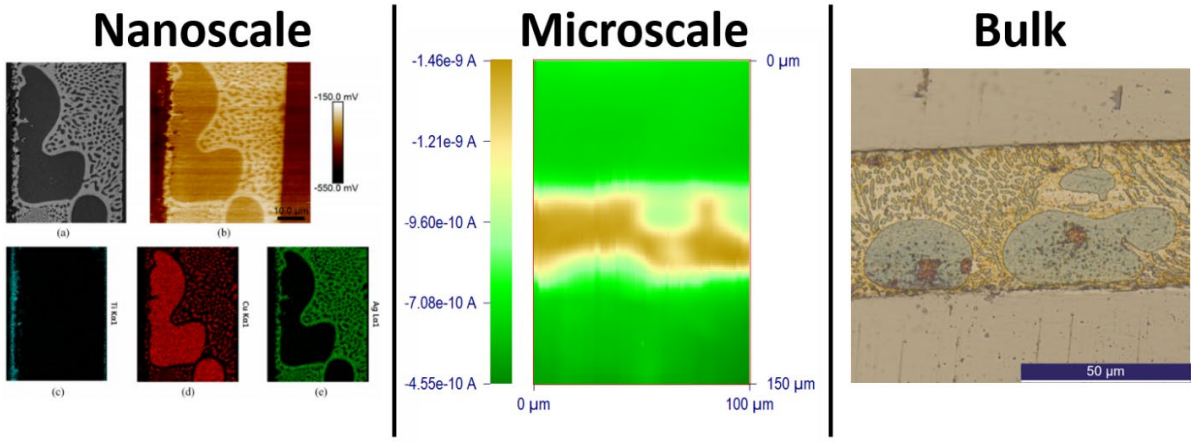

Figure 4.16. (Nanoscale) From Kvryan et al. [121]: "Secondary electron SEM image of Cu-Ag-Ti sample (a) followed by corresponding Scanning Kelvin Probe Force Microscopy (SKPFM surface potential image) (b). EDS elemental maps of the identical region for: Titanium (c); Copper (d); and Silver (e) are shown." The surrounding region is SS316L. (Microscale) SECM with a UME operating in feedback mode with a positive overpotential applied to the probe while scanning across the braze (yellow) and SS316L (green) in aqueous solution of 1 mM Ferrocene Methanol (FcMeOH) and 0.1M KNO_3. (Bulk) Post-mortem optical imaging of the braze and SS316L. This is unpublished work that was presented at Materials Science & Technology Conference, 2017.

CHAPTER 5: TOWARD IMPROVING AMBIENT VOLTA POTENTIAL MEASUREMENTS WITH SKPFM FOR CORROSION STUDIES

5.1 Introduction

The traditional Kelvin probe is a conductive vibrating capacitor-like plate used in vacuum to measure the contact potential difference, which correlates to the work function difference between the probe and the sample of interest. By reducing the size of the Kelvin probe to the nanoscale and combining it with an atomic force microscope (AFM) [147, 148], the resulting SKPFM produces simultaneous maps of surface topography and relative Volta potential that correspond to microstructural heterogeneities on the material's surface. Employed under either ambient, inert, or electrolytic environments, SKPFM can spatially resolve features at the nanoscale [123, 126, 149], and has therefore found use in a wide range of diverse applications, including semiconductor [123, 124, 126, 150] and electrical device characterization [125, 136, 151-153], as well as corrosion studies [130, 131, 154-159].

SKPFM produces nanoscale maps of Volta potential differences (VPD or $\Delta\psi$), which can be calculated theoretically from the difference in work function between the sample surface and the probe (which acts as a pseudo reference), as shown below in Equation 5.1 [149, 160-162].

$$\Delta\psi_P^M = \psi^M - \psi^P = (\varphi^M - \varphi^P)/e \qquad \text{Equation 5.1}$$

In Equation 5.1, ψ is Volta potential, φ is work function, and e is the elementary charge carried by an electron, while the scripts M and P refer to the (metallic) surface and probe, respectively. Volta potential and work function are surface properties, related to each other by Equation 5.1 in vacuum conditions. Outside of vacuum, the redefined "modified" work function and Volta potential are measured from the interfaces of the two surfaces and the environment. This recognition of environmental factors having an effect on Volta potential maps has been well established [131, 149, 159, 163-173]. Making the assumption that the interactions between metals M and P and the surface layers from environment are identical, then Equation 5.1 holds true for non-vacuum conditions [174].

Further, it is important to note that according to Equation 5.1, the measured VPD is dependent on the choice of probe and its structural factors. Even the smallest change in the probe, such as degree of structural order (i.e., percent crystallinity), will change the material's work function, and therefore change the measurable VPD [149]. Thus, quantification of the probe's work function in theory can provide repeatable work functions of the features observed from VPD measurements. Though the calculation of the probe's work function is simple in theory, there are many parameters that may influence the probe's work function, especially when mapping Volta potentials at the nanoscale with SKPFM. Most of these parameters are difficult to quantify, including probe wear, aging effects (e.g., oxide growth, hydroxylation, and atmospheric corrosion), reconstruction or relaxation of the probe, and contamination. As a result, comparisons of experimental VPDs derived from SKPFM measurements have been limited to either a pseudo or semi-quantitative scale (e.g., relative nobility in corrosion studies), resulting in large variations in reported VPD values for similar features [127, 160]. As a result,

alternate routes are used to reliably determine accurate work function values. The overwhelming benefit of SKPFM, however, is that it can provide spatial resolution into the nanoscale. Thus, recent efforts have been made for SKPFM to become a usable technique in highly quantitative spatial mapping of work functions [126, 151, 160, 161, 175].

Though the techniques presented in this work can be used to interpret SKPFM data in many different fields, this work is driven by the desire to further improve the value of SKPFM results in corrosion studies. The Kelvin probe was originally used to observe corrosion properties while the sample was covered with thin electrolyte layers [176-179], and was increasingly used to study metal alloys with the development of SKPFM. The technique was introduced to the corrosion community when a direct correlation between VPDs and open circuit potentials of metal/electrolyte interfaces was demonstrated [133, 166, 180]. This was accomplished by comparing Volta potentials of pure metals post-immersion in electrolytic solution to the corrosion potential of the same metal/electrolyte systems. However, the observations between SKPFM measurements and the actual corrosion mechanisms of the material is not directly correlated, as mapping freshly polished metals with the Kelvin probe does not provide direct correlation to corrosion behavior [149]. Electrolyte factors, such as pH and ion concentration, play a major role in the kinetics, which are not addressed when observing fundamental electronic properties of the material in ambient conditions. SKPFM has therefore been utilized for predicting (in ambient or inert conditions) microgalvanic couples as localized corrosion initiation sites for a variety of pristine complex metallic systems [127, 162, 165, 167-170, 181-188], *ex situ* measurements of such systems following periods of

exposure to corrosive environments [131, 134, 189-191], and *in situ* measurements of VPD changes under non-ambient conditions [161, 162, 164, 192-197]. While much of the previously reported work has focused on distinguishing relative nobility within individual SKPFM maps, comparisons to other work are not direct. Accordingly, a notable lack of reproducibility in measured VPDs has been observed and discussed for different alloy series [127, 160]. This lack of repeatability and an inability to connect to bulk electrochemical testing has led to contradictory conclusions when investigating the corrosion behavior in various metal alloys [127, 160, 161, 198].

For one route to address this challenge, comparison of calculated work function values for a particular material with the resulting VPDs measured via SKPFM can provide improved predictability of corrosion behavior. Computational chemistry calculations have provided experimentalists with a database of theoretical work function values for various elements. Of recent interest is the ability to increase such a database to microconstituents within complex metal alloys [160, 161, 199, 200]. DFT-based computational simulations [201, 202] can show that the crystallographic orientation, as well as the terminating atom of the material surface, can drastically affect the work function [160, 199]. Notable shifts in relative VPDs measured via SKPFM have also been linked to metal passivation and/or adsorbed species. This has been confirmed both experimentally [203, 204] and by linking experimentation to DFT simulations [161].

Although DFT simulations can help explain some of the variations seen in measured VPDs, they have only just recently started to address systems that are not perfectly pristine. In reality, following polishing of a material, the surface is actively changing. There are a multitude of factors that can cause this activity, most of which are

difficult to quantify, as well as control while doing SKPFM in ambient conditions. Thus, standardization of the SKPFM technique has not been established. This work attempts to control one particular variable for ambient-based SKPFM by directly addressing probe choice and how that contributes to the variability and uncertainty observed in experimentally determined VPDs. Many probe factors, as previously described, will ultimately affect the measured VPD, regardless if active changes are occurring on the surface of the sample. It can thus be seen that the SKPFM probe also likely accounts for some of the variability present in VPDs reported in the literature. However, probe choice, as well as progressive usage of the probe, is commonly removed from SKPFM results by comparing microstructural heterogeneities on the surface to one another.

Recently, redesign of SKPFM probes has been undertaken to address variability in VPD as it is linked to the probe. The redesign is completed by applying a coating only to the backside of the probe cantilever, while the tip is left uncoated. The uncoated tip minimizes work function change from tip wear and tip shape. With this redesign, enhanced reproducibility of results has been able to address some of these uncertainties, showing consistent initial VPD results from many probes of the same type [205].

Though improvements in probe design have resulted in greater consistency during initial probe usage, this work hopes to also address variability in the probe work function from uncontrollable structural variations of probes by utilizing an inert reference material prior to imaging a material of interest. A practice has been presented for SKPFM, wherein the pseudo reference probe is calibrated by comparing Volta potential of the material of interest to the Volta potential of a relatively inert material (e.g., gold) [129, 133, 134, 149, 206]. Expanding on this approach, the observed work functions of

heterogeneities on the surface of metal alloys can be better quantified and ultimately compared to theoretical calculations from DFT. A remarkable agreement between resulting modified work functions of microconstituents calculated using different probes is seen, and thus highlights the utility of this broadly applicable method.

5.2 Experimental Methods

5.2.1 SKPFM Reference Sample

The inert reference sample employed for this study was a Bruker PFKPFM-SMPL (Santa Barbara, CA), which consists of an n-doped silicon wafer patterned with 50 nm thick rectangular islands of aluminum surrounded by a 50 nm thick interconnect of gold, with small sections of the underlying wafer exposed between the aluminum and gold regions (hereinafter referred to as the Al-Si-Au sample). The abrupt step-wise shifts in VPD from aluminum to silicon to gold can be used to track both inter- and intra-probe consistency, as well as determine SKPFM spatial resolution limitations arising from Volta potential averaging at boundaries by observing the slope of the measured VPD at the transitions between elements of the standard.

Both aluminum and silicon are highly reactive and form passive films when exposed to an ambient environment, thus increasing their surface work functions. [161, 203, 204] This uncertainty in the physical nature of the aluminum and silicon surfaces of the Al-Si-Au sample could contribute to notable differences between the calculated work functions of the pure materials and the work functions measured experimentally via SKPFM of their oxides. In contrast, gold is a relatively inert metal with expected long-term stability in oxygen-enriched environments (i.e., ambient conditions) [207], and thus should exhibit reasonable agreement between theoretical calculations and experimental

measurements. Additional factors such as relative humidity and adsorption of other species will cause changes to the gold surface, which will be assumed to be minimal in ambient air over time. Therefore, work function values of gold were derived using first-principles density functional theory to compare with SKPFM results. X-ray diffraction (XRD) of the Al-Si-Au standard was accomplished using a Rigaku Miniflex 600 X-ray Diffractometer (Tokyo, Japan) to accurately specify the crystallographic orientation of the gold on the standard.

5.2.2 DFT Calculations

Initial atomic structures of gold were built in an FCC crystal structure (space group $Fm\bar{3}m$) with lattice parameters of 4.07 Å [208]. Atomic and electronic structures were calculated using the Vienna ab initio simulation package (VASP) [209] with the projector augmented wave (PAW) method [210]. The Perdew-Burke Ernzerhof (PBE) [211] form of the generalized gradient approximation (GGA) [212] was used for the exchange-correlation potential to address electron-electron interactions. Plane-wave expansion of the wave function was performed with the PAW method and a cutoff energy of 450 eV. Brillouin zone integration was performed on a 9 x 9 x 1 gamma-centered mesh for all the slab structures. Periodic slabs of these structures were built large enough for convergence of the calculated work function and separated by a vacuum of 20 Å to avoid unphysical interactions with neighboring slabs (Figure 5.1) [213]. The vacuum energy level (Ev) and Fermi energy level (E_F) were obtained for each structure, and the theoretical work function (φ) was calculated using Equation 5.2 below.

$$\varphi = E_v - E_F$$

Equation 5.2

Work function values for gold were obtained for the (100), (110), and (111) planes to utilize in Equation 5.1 in quantifying the modified work function of the probe.

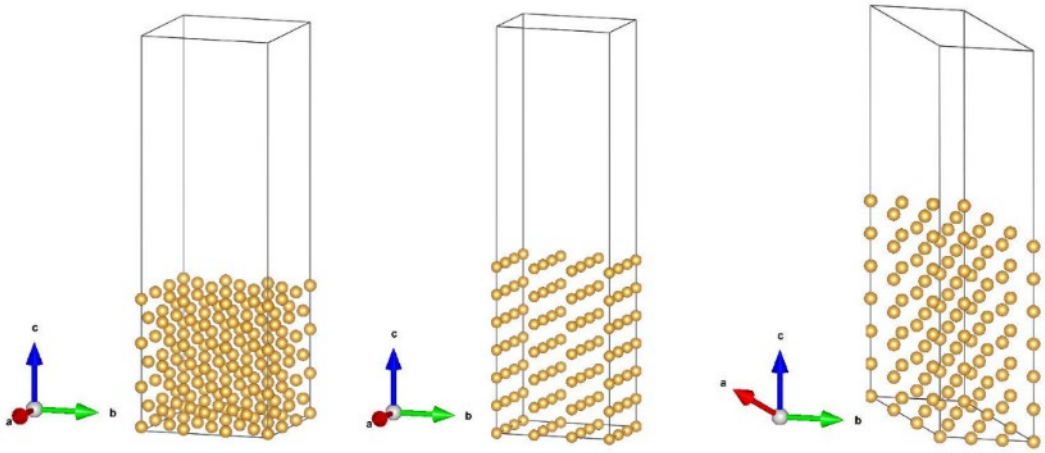

Figure 5.1. Crystal structures of gold oriented with (from left to right) the (100), (110), and (111) face exposed to vacuum.

5.2.3 SKPFM Mapping

SKPFM was carried out using a Bruker Dimension Icon AFM equipped with a 64 bit NanoScope V controller. Depending upon the precise design characteristics of the probe used for imaging (i.e., spring constant, k, and natural resonance frequency, f_0), two different implementations of SKPFM were employed. Stiffer AFM cantilevers (k on the order of 10s of N/m) utilized single pass tapping mode frequency modulation Kelvin probe force microscopy (FM-KPFM). In this single-pass method, both sample topography and Volta potential are acquired simultaneously. To accomplish this, the probe is mechanically oscillated at or near its natural resonance frequency f_0 (typically 100s of kHz) by a dither piezo while simultaneously a much lower frequency (2 kHz) AC bias is applied to the probe. Variations in the oscillation amplitude at f_0 are used to track changes in the sample topography. Meanwhile, variations in the electric force gradient between the probe and surface, which is modulated at the 2 kHz AC bias frequency,

produce sidebands at $f_0 \pm f_{AC}$, with the amplitude of the sidebands proportional to the magnitude of the tip-sample VPD. By applying a variable DC bias to null the sidebands, it becomes possible to measure the tip-sample VPD [205]. Potential inversion is not required when the nullifying bias is applied to the sample, and thus the Volta potential of the sample relative to the probe ($\Delta\psi_P^M$) is directly measured. Although the signal-to-noise ratio is lower in FM than in amplitude modulation (AM) technique, it has been shown that the resolution of electric force gradient signal FM surpasses that of AM, and thus was chosen as the method of VPD collection in this work [205, 214]. One drawback of FM-KPFM is that the single pass nature is more susceptible to phase cross-talk driven by strong phase contrast [205].

A second technique, peak force frequency modulation KPFM, or FM PF-KPFM, was employed for softer AFM cantilevers (k on the order of few to tenths of N/m). As the name implies, FM PF-KPFM also utilizes frequency modulation to acquire VPD maps [205]. However, in this implementation the probe conducts a dual pass over the sample surface, wherein line-by-line topography and VPD values are sequentially acquired. In the first pass, sample topography is scanned and recorded using Bruker's proprietary PeakForce tapping mode, which employs rapid (2 kHz) force curve acquisition with a user-defined peak force (5-20 nN in this study) as the setpoint for feedback. Upon completion of each individual trace and retrace line of topography, the probe lifts off the surface and retraces the topography at a user-defined lift height. During the second trace and retrace, VPD measurements are acquired by the frequency modulation method described above for FM TM-KPFM. The lift height has drastic effects on the VPD measurement [205], and thus a constant lift height (i.e., tip-sample separation) of 100 nm

was used throughout this work. Additionally, this lift height will sufficiently avoid artifacts caused by sudden tip-sample contact arising from high aspect ratio features [175].

SKPFM imaging was performed with three different types of probes: PFQNE-AL (Bruker, k = 0.8 N/m, f_0 = 300 kHz, 5 nm radius of curvature highly doped silicon tip with an aluminum-based conductive coating on the backside of a silicon nitride cantilever), SCM-PIT (Bruker, k = 2.8 N/m, f_0 = 75 kHz, 20 nm radius n-doped silicon tip with a conformal platinum/iridium coating covering the cantilever backside and tip), and 25Pt300B (Rocky Mountain Nanotechnology, k = 18 N/m, f_0 = 20 kHz, 20 nm radius solid platinum probe connected to a conductive gold bonding pad via conductive epoxy). Due to their relatively low spring constants, the PFQNE-AL and SCM-PIT probe types were well-suited to operate in FM PF-KPFM mode, while the solid platinum 25Pt300B probe operated best in the FM-KPFM mode due to its significantly higher spring constant [205]. Temperature was held in the range 68-72 ^{o}F, while relative humidity was observed between 5-20%. Variations in VPD results caused by relative humidity and temperature were not accounted for in this work.

5.2.4 Data Evaluation

Image processing and analysis were conducted using NanoScope Analysis V1.8 (Bruker). Threshold analysis, which analyzes the Volta potential channel's data above or below a user-defined value, was implemented as part of the "Roughness" tool in determining VPDs of the heterogeneities in the sample.

Statistical analysis of SKPFM probes was performed by imaging the Al-Si-Au sample to observe variations between probes of both differing and nominally identical

composition. SKPFM data on the Al-Si-Au sample were collected and sorted into equidistant VPD "bins", where a higher amount of bins provides higher resolution of data. For all acquired data, 512 bins were used to collect data from each map. The bins collected for each image were placed into populations for each probe type (PFQNE-AL, SCM-PIT, and 25Pt300B), which were each distributed into 512 bins equally dispersed between the maximum and minimum values observed in the population. The population sets for PFQNE-AL, SCM-PIT, and 25Pt300B probes were normalized for variations in data points collected per map, as well as total maps acquired with each probe type. Skewness and 95% confidence interval limits were calculated for each data set. Skewness is a descriptor of the symmetry of a distribution plot, and can quantify the shape of the distribution curves. A symmetric distribution would present a skewness of 0, whereas right and left leaning distributions result in positive and negative skewness values, respectively.

5.2.5 Sample Preparation

Proof of concept SKFPM was performed on a commercial 316L stainless steel coupon separated and thermally re-joined with an active brazing Cu-Ag-Ti alloy (further description of the sample is provided elsewhere) [181]. The effect of polishing and sample preparation on VPDs has been previously observed and reported [203]. To minimize effects such as metal passivation and/or adsorbed species on the variability of acquired VPD values, the sample was prepared using the same steps for each map acquisition. To create a fresh, smooth surface for SKPFM, the sample was mechanically ground with progressively finer silicon carbide abrasive pads to US 1200 grit. Following SiC grinding, the sample was polished with 1 μm and 0.05 μm alumina slurries.

Following each polishing step, the sample was sequentially rinsed with DI water and non-denatured 190-proof ethanol, then dried with compressed air. Following polishing and immediately prior to SKPFM imaging, the sample was cleaned by ultrasonication in ethanol, then dried with compressed ultrahigh purity (UHP) nitrogen gas (99.999%, Norco). An electrical connection between the sample surface and the AFM stage was then established using colloidal silver paint (PELCO®) and verified with a digital voltmeter. The Al-Si-Au sample was mapped both prior to and following mapping of the braze sample to ensure consistency of the probe for the entirety of the imaging session, as well as provide calculation of the work functions of the constituents seen on the braze surface.

The elemental distribution of the Cu-Ag-Ti brazed stainless steel sample was determined by a Hitachi S-3400N-II scanning electron microscope (SEM) equipped with energy-dispersive X-ray spectroscopy (EDS) capabilities (Oxford Instruments Energy+, Oxford Instruments, Abingdon, United Kingdom) operated at 10 keV and a 10 mm working distance. Due to the residual effects of electron beam irradiation and carbon pyrolysis, all SEM/EDS mapping was performed after SKPFM measurements [127, 184, 215].

Table 5.1. Density functional theory calculated work function values for gold over relevant planes.

Material	Face	Vacuum Energy E_v	Fermi Energy E_F	Work Function φ	Ref. (Approx.)
Gold	(100)	4.770 eV	-0.324 eV	5.09 eV	5.0-5.2 eV [216-218]
	(110)	2.590 eV	-2.410 eV	5.00 eV	
	(111)	3.357 eV	-1.759 eV	5.12 eV	

5.3 Results and Discussion

5.3.1 DFT Calculated Work Functions

The work functions of three different possible exposed faces of pure gold were determined via DFT calculations. Table 5.1 summarizes the results, which are in agreement with those reported in the literature [216-218]. XRD results from the Al-Si-Au standard showed a dominant peak of gold in the (111) orientation. From these results, 5.12 eV was used as the calculated work function of the gold on the standard.

5.3.2 Quantifying Probe Work Function

Prior to utilizing the described method to quantify the work functions of the constituents present in the braze sample, an experiment was conducted to quantify statistical differences between probe types, as well as between probes of the same design. To accomplish this, mapping of the Al-Si-Au sample was done twelve times (in a successive manner so as to minimize drastic variations in temperature and relative humidity during testing) with eight different probes (three PFQNE-AL, three SCM-PIT, and two 25Pt300B), for a total of 96 SKPFM maps of the Al-Si-Au sample. Representative VPD maps of the standard obtained with each probe type are shown in Figure 5.2a-c.

5.3.3 Variability Between Probe Types

Figure 5.2d presents the average VPDs (with standard deviations) obtained from all data for each of the three probe types relative to the gold standard. From Equation 5.1, the VPD between the probe and gold ($\Delta\psi_P^{Au}$) measured via SKPFM is equivalent to the difference in work function between the gold surface (φ^{Au}, calculated by DFT to be 5.12 eV, Table 5.1) and the probe (φ^P). By multiplying the VPD, $\Delta\psi_P^{Au}$, by a negative

magnitude of electron charge and then adding the work function of gold, the modified work function of the probe can be found. For the population results for each probe type, the average modified work function of each probe type can be found (right ordinate axis in Figure 5.2d).

For ambient air SKPFM, the results show that the PFQNE-AL and SCM-PIT probes exhibit relative precision for a large population of data, with lower standard deviations (246 mV and 106 mV, respectively) combined with low skewness values of +0.18 and +0.47. The 25Pt300B probe also shows a relatively symmetric distribution (skewness of -0.29), but produces a much larger range of VPD values (standard deviation >700 mV, Figure 5.2d). This may be due to the use of the single-pass tapping mode that the 25Pt300B probe employs, as well as the conflation caused by interactions between the surface and the entirety of the probe, which is composed entirely of platinum. Confidence intervals at 95% for each set are provided in Figure 5.2e, and show that the three probe types exhibit statistically significant differences in VPD versus gold, and therefore statistically different average probe modified work functions. The probe types exhibiting different modified work functions is as expected, given their differing material compositions. Thus, VPDs measured via SKPFM on the same alloy with these different probe types will be offset by the corresponding differences in probe work function.

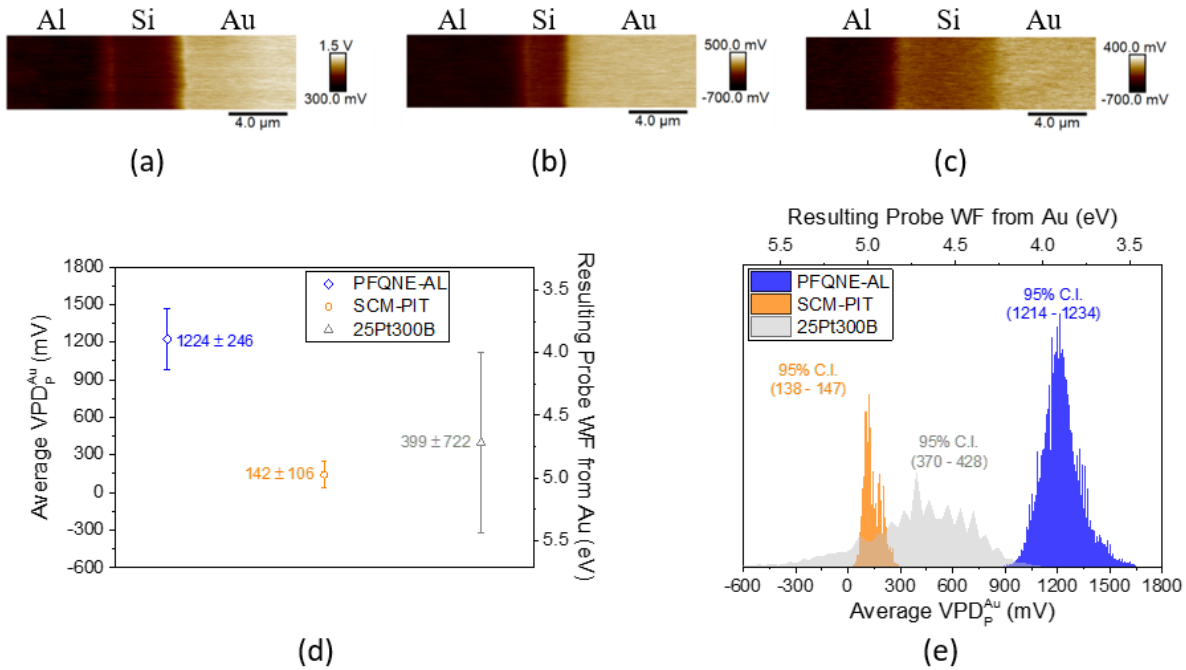

Figure 5.2. Representative SKPFM VPD maps of the Al-Si-Au standard obtained with (a) a PFQNE-AL probe, (b) a SCM-PIT probe, and (c) a 25Pt300B probe. Note the difference in VPD color scale ranges for panels (a-c) due to differences in probe work functions. (d) Average gold VPD acquired from all SKPFM images obtained with each probe type. Left ordinate axis presents the average VPDs (with standard deviations) measured between the gold and the given probe type (PFQNE-AL in blue, SCM-PIT in orange, 25Pt300B in gray). Right ordinate axis presents the resulting average modified work function calculated for each probe type. (e) VPD and modified work function distributions of gold acquired from all SKPFM images with each probe type, with respective axes presented below and above the distributions. 95% confidence intervals are presented beside each histogram.

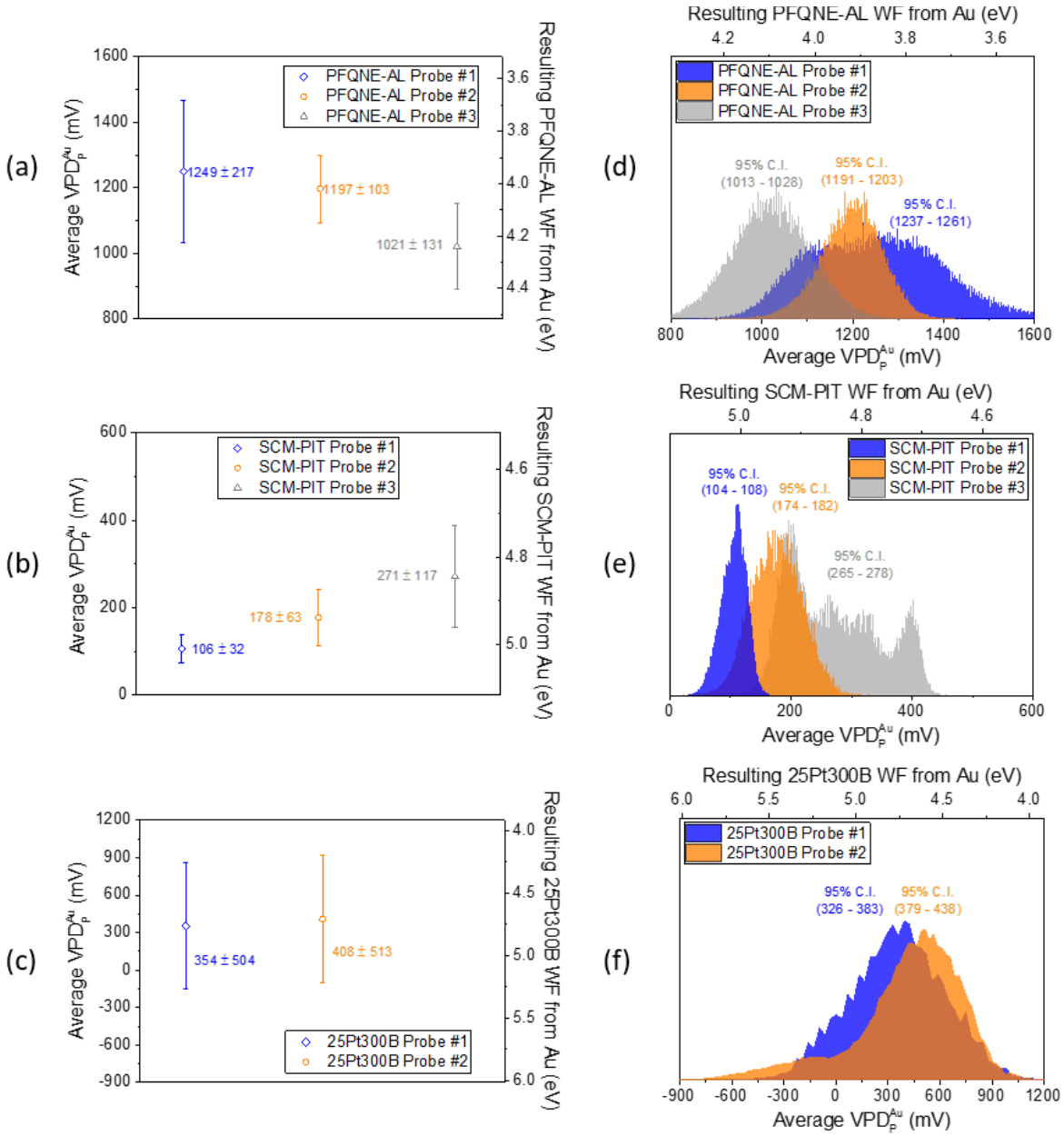

Figure 5.3 (Left) Average gold VPDs (with standard deviations) obtained from twelve SKPFM images acquired on the Al-Si-Au standard with (a) three PFQNE-AL probes, (b) three SCM-PIT probes, and (c) two 25Pt300B probes. Left ordinate axes present the average VPDs measured between the gold and the given probe. Right ordinate axes present the resulting average work function calculated for each of the probes. (Right) Distributions of measured VPDs for gold and resultant modified probe work functions obtained from twelve SKPFM images with (d) three PFQNE-AL probes, (e) three SCM-PIT probes, and (f) two 25Pt300B probes. 95% confidence intervals are presented besides each histogram.

5.3.4 Variability of Individual Probes by Type

The data obtained from the twelve images collected with each of the eight individual probes tested (i.e., 8 data sets made by the 12 SKPFM images acquired by the individual probes) were further statistically analyzed and compared to each other to determine the distribution of intra-probe variability. Figure 5.3 presents variations between individual probes of the same type, both as averages (with standard deviations) in Figure 5.3a-c and as histograms in Figure 5.3d-f. Similar statistical analyses were performed on the data for each individual probe as described above for the aggregate data for each probe type (i.e., observation of 'Probe A' in the previous section, observation of 'Probe A1', 'Probe A2', and 'Probe A3 in this section). The data from each of the eight individual probes exhibited relatively symmetric distributions, with skewness values for all distributions <|0.75|. There is one distinct probe showing either bimodal (PFQNE-AL Probe #1) or multimodal (SCM-PIT Probe #3) histograms. These probes are still useful for collecting semi-quantitative or qualitative VPD results of individual maps (e.g., relative nobility). However, if improved accuracy of work function calculations are desired, these probes lack consistent, predictable use. Also, confidence intervals for the PFQNE-AL and the SCM-PIT probes are not overlapping (Figure 5.3d-e). The confidence intervals for the two 25Pt300B probes do overlap (Figure 5.3f); however, their standard deviations are vastly larger (Figure 5.3c) than for the other two probe types. This suggests a larger range of VPDs could be measured on a given sample with the 25Pt300B probe type, and thus it is less reliable for repeatable work function calculations. In addition, the statistically significant differences observed between probes of the same make-up and design highlights the need for probe quantification prior to

SKPFM imaging of a material of interest to enable comparison of VPD measurements made with different probes, even of the same type. The bimodal and multimodal behavior of specific probes also suggests shifting in probe work function over time and usage, driven by other factors such as environmental changes over time (e.g., relative humidity and temperature) and structural changes of the probe as previously described. SKPFM still has validity in the corrosion field (e.g. semi-quantitative analysis, relative nobility, effects of environment, etc.) as proven by the number of works done by others. However, greater control of outside parameters will be needed to further the improved standardization of the technique, as well as improve the precision of work function calculations. Though many other parameters are not precisely controlled, this statistical study still shows that the constant monitoring of probe work function is required, particularly when used in ambient conditions.

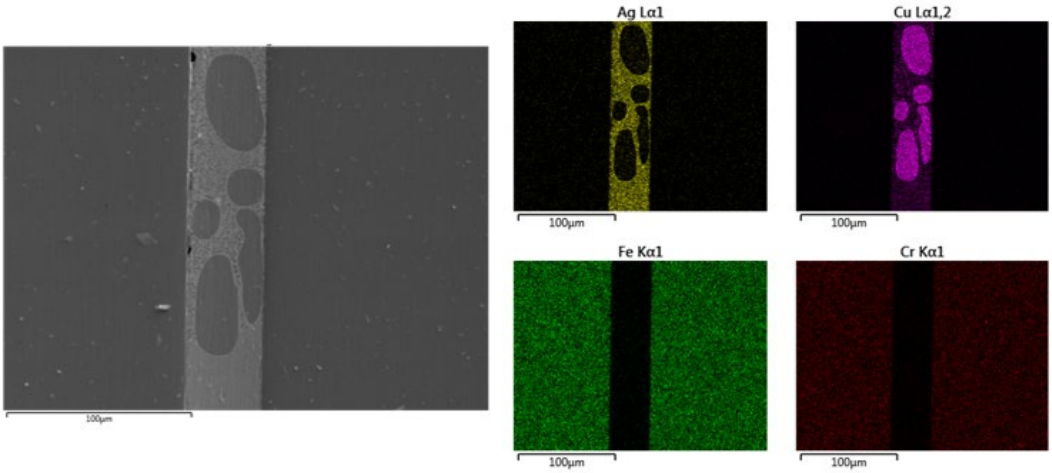

Figure 5.4. Grayscale SEM image (left) and colored EDS maps (right) of the Cu-Ag-Ti brazed 316L stainless steel sample, confirming the presence of two distinct phases within the braze material: copper-rich precipitates within a silver-rich braze matrix.

5.3.5 Relative Work Functions of Different Metallic Constituents

Once the probe's work function has been quantified by mapping the inert gold portion of the Al-Si-Au sample, the SKPFM data acquired from the sample of interest (in this case, a Cu-Ag-Ti braze sample) can be placed on an absolute scale. Elemental mapping of the Cu-Ag-Ti braze region with SEM/EDS revealed a two-phase eutectic structure of copper-rich regions embedded within a silver-rich matrix, with titanium (a wetting agent) diffusing to the braze-steel interface (Figure 5.4) [181]. Thus, two distinct phases can be readily distinguished on the surface of the sample – a copper-rich phase (Cu-rich) and a silver-rich phase (Ag-rich). Note that micro-segregation is still evident in this sample, meaning that each phase is rich in a certain element, but is still alloyed. This brazing material presents near-pure metals to validate to well-known elemental work function values, but exhibits enough complexity as an alloy to show expansion from pure material observations. Thus, SKPFM mapping is done within the Cu-Ag-Ti braze material to observe differences between the two phases.

Figure 5.5 shows VPD maps acquired with the three different probe types, all of whose modified work functions were quantified using the inert gold of the Al-Si-Au sample immediately before imaging the braze sample. It is notable that the results acquired by the different probe types show differing lateral resolution, in order of superiority (least to highest) from 25Pt300B to SCM-PIT to PFQNE-AL probe type. This can be attributed to a combination of the technique used (single pass tapping mode versus dual pass PF- FM KPFM), as well as probe design and resultant resolution (i.e., contributions from both the tip and the cantilever causing a decrease in lateral resolution for the 25Pt300B and SCM-PIT relative to the PFQNE-AL, which is only coated on the

backside). All images acquired on the braze alloy have pixel resolution between 24-28 nm. However, regardless of resolution, the SKPFM maps obtained with all three probe types present consistent relative nobility within the braze area, wherein the silver-rich braze matrix is noble relative to the copper-rich regions. This confirms the utility of SKPFM for assessing relative nobility of the sample's constituents. From this, a microgalvanic couple is distinguished, and atmospheric corrosion behavior can be predicted. To expand SKPFM use toward acquiring consistent modified work functions of the two phases in the sample, probe quantification relative to an inert material is needed. As shown in Figure 5.6a, the resulting VPD values for each phase vs. probe are notably different.

Figure 5.6b-c presents the method quantifying the probe relative to gold as a reference prior to imaging the braze sample. Figure 5.6b presents the average VPD of gold from the Al-Si-Au sample versus each probe. Utilizing Equation 5.1, the resulting probe modified work function can be calculated, as shown on the right ordinate axis and the equation below Figure 5.6b. In Figure 5.6c, displayed on the left ordinate axis (as well as the equation above Figure 5.6c) is the VPD of each phase relative to the VPD of gold mapped with the probes just prior to mapping the braze sample. Another way to display the results can be seen on the right ordinate axis, where each phase's absolute modified work function is calculated via the equation shown below Figure 5.6c. In this case, the gold from the Al-Si-Au sample is used as reference to quantify the work function of the operating probe, as previously described. Following quantification of probe work function, Equation 5.1 can again be used to calculate the work function of each phase present on the braze sample, where the average VPD between the specific

phase and probe ($\Delta\psi_P^M$) is found from the potential map, and probe modified work function (φ^P) is found in Figure 5.6b. From this, the distribution of plausible results for each of the phases has been reduced from a range of >800 mV (Figure 5.6a), to a range of <150 mV (or alternatively <0.15 eV in modified work functions, Figure 5.6c).

Since probes of the same type can also exhibit differences in their modified work function, the same process was used to analyze images acquired with different probes of the same type. The PFQNE-AL probe was chosen for this experiment. Figure 5.7 presents SKPFM images (VPD maps) captured by two different PFQNE-AL probes on different dates at different locations within the braze sample. For further comparison, a third VPD map has been presented in a previous publication [181] and is analyzed here as well. Parameters for these acquired data were similar to parameters described in this work. Figure 5.8a displays the VPD of each phase determined from the three separate SKPFM images. Again, although the relative nobility is consistent, the three separate tests conducted on this material by probes of the same nominal composition result in three vastly different measured VPD values. Using the method outlined in this work, the resulting distribution for the Cu-rich and Ag-rich regions reduces the average VPD range from >700 mV (Figure 5.8a) to <55 mV (or alternatively <0.055 eV, Figure 5.8c), thereby demonstrating the power and utility of this method.

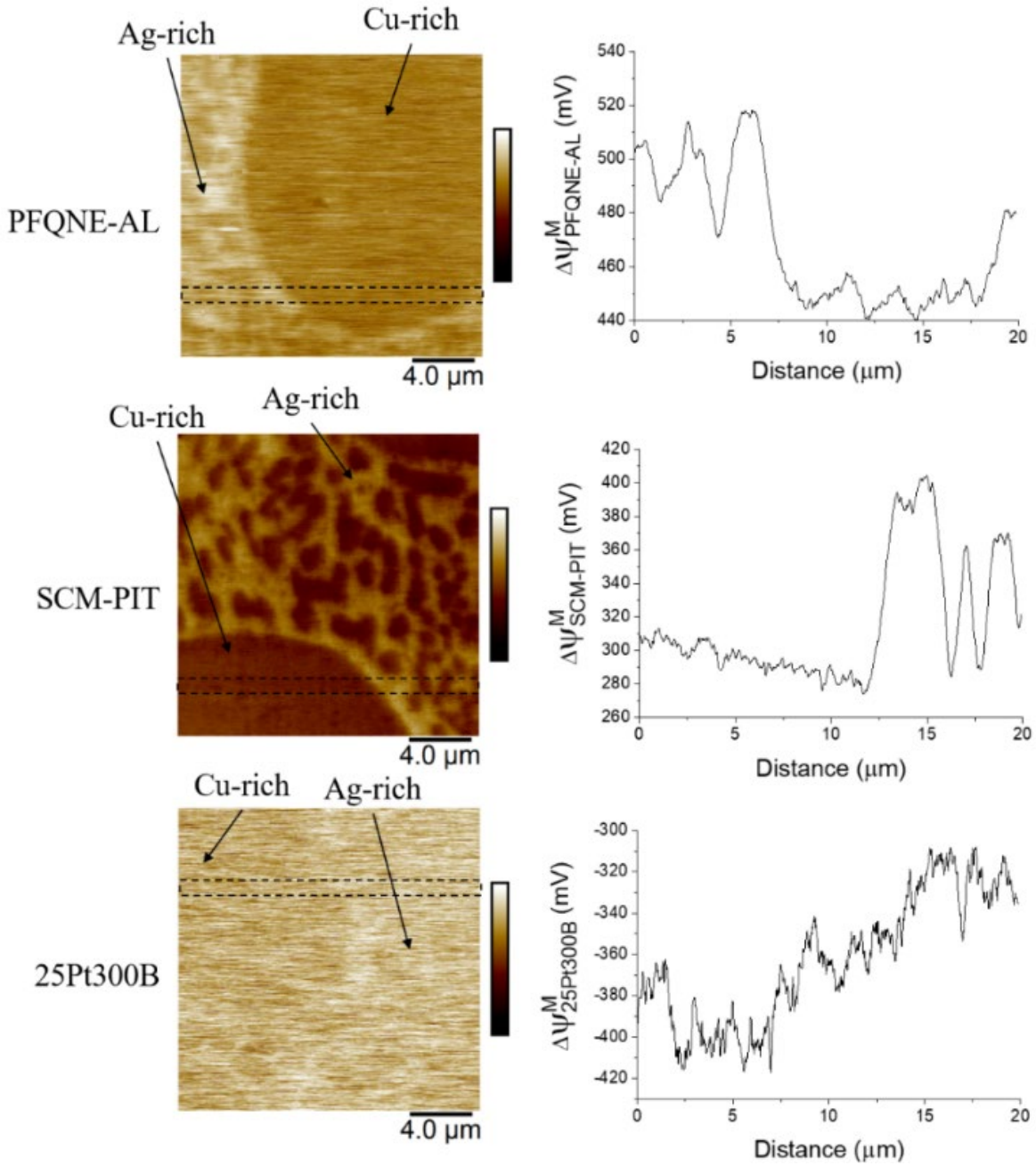

Figure 5.5. SKPFM (VPD) maps and cross sections of the Cu-Ag-Ti braze sample acquired with a PFQNE-AL probe (500 mV scale), a SCM-PIT probe (500 mV scale), and a 25Pt300B probe (800 mV scale). Cu-rich and Ag-rich phases are called out in each map. Cross sections correspond to average data across the dotted black areas.

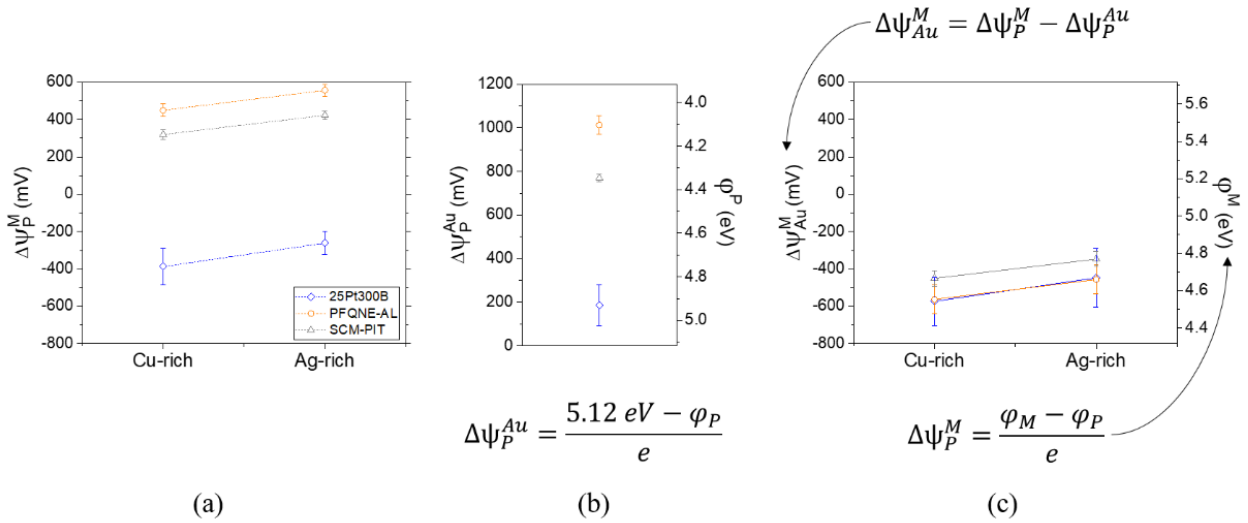

Figure 5.6. (a) VPD results for copper-rich and silver-rich regions on the braze sample obtained with the three different probe types as seen in Figure 5.5. (b) VPD results for the same three probes acquired from the gold of the Al-Si-Au standard presented on the left ordinate axis, with resulting modified probe work function values presented on the right ordinate axis, as calculated with the shown equation. (c) VPDs scaled relative to the gold of the Al-Si-Au standard imaged with the same probe prior to imaging the braze sample. The left ordinate axis (as calculated by the equation above) scales the VPD between the phases of the braze sample and the gold of the standard. The right ordinate axis (as calculated by the equation below) presents the resultant modified work function for each phase based on the modified work function of the probe in part (b).

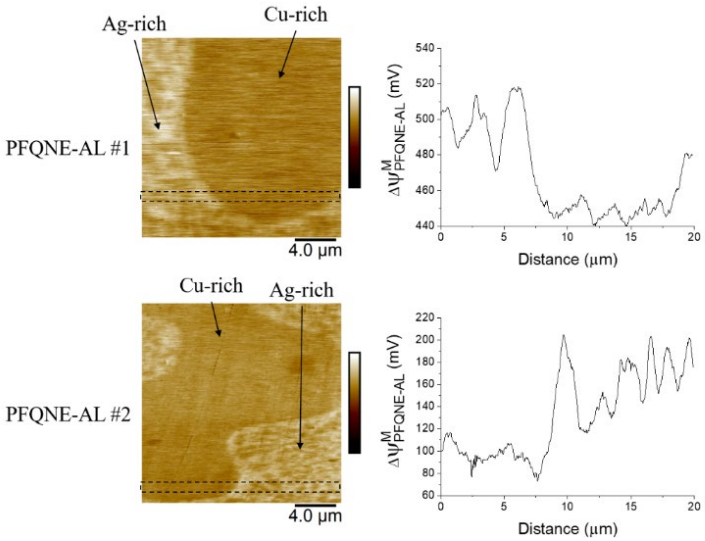

Figure 5.7. SKPFM (VPD) maps and cross sections of the Cu-Ag-Ti braze sample obtained with different PFQNE-AL probes. PFQNE-AL #1 is a duplicate of Figure 5.5, while PFQNE-AL #2 (600 mV scale) is from a different region of braze sample with a different probe. Cross sections coordinate to average data across the dotted black areas.

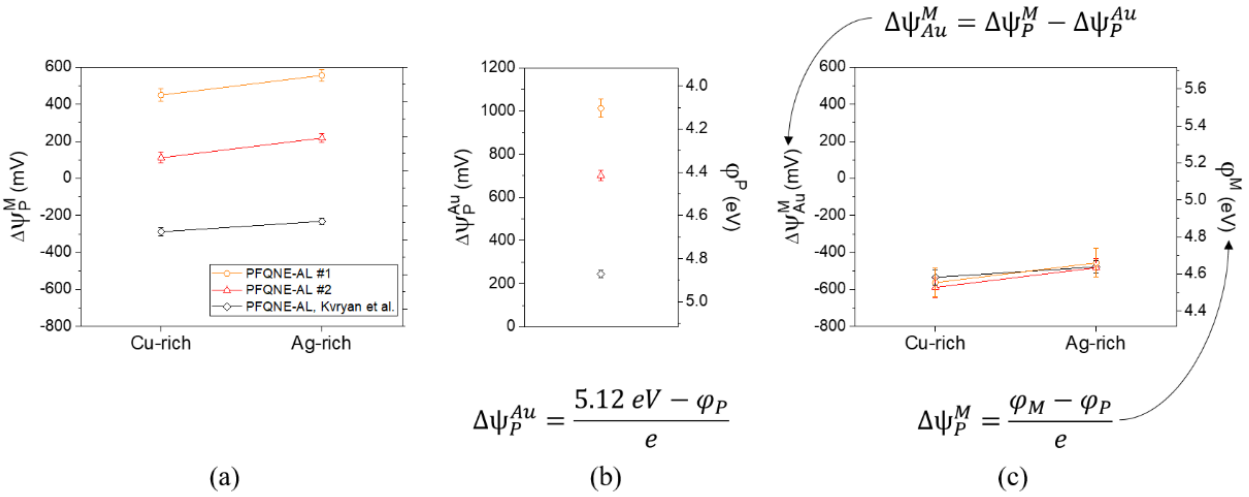

Figure 5.8. (a) VPD results for copper-rich and silver-rich regions on the braze sample obtained with three different PFQNE-AL probes as seen in Figure 5.7 and from Kvryan et al. [181] (b) VPD results for the same three probes acquired from the gold of the Al-Si-Au standard presented on the left ordinate axis, with resulting modified PFQNE-AL work function values presented on the right ordinate axis, as calculated with the shown equation. (c) VPDs scaled relative to the gold of the Al-Si-Au standard imaged prior to imaging of the braze sample. The left ordinate axis (as calculated by the equation above) scales the VPD between the phases of the braze sample and the gold of the standard. The right ordinate axis (as calculated by the equation below) presents the resultant modified work function for each phase based on the modified work function of the probe in part (b).

5.4 Conclusions

This work proposes a methodology for presenting SKPFM VPD results by utilizing a relatively inert reference material (gold) to enable determination of the absolute modified work function of materials, as opposed to merely the relative difference in Volta potential between the sample and non-equilibrated, pseudo-reference probe. Implementing this simple addition to standard SKPFM practice could greatly reduce the notable variation in reported VPDs for heterogeneities seen in metallic alloys that can arise from differences in probe type/composition, variability between individual probes of a given type, and/or changes in probe work function over time.

The utility of this method was demonstrated by quantifying the statistically significant differences in VPDs and work functions between probes of different types and among probes of the same type, as well as changes in VPD over time for a given probe. Using the Cu-Ag-Ti braze sample as an example, the spread of measured VPDs was greatly reduced regardless of probe used for the testing. With the support of DFT calculations, SKPFM can provide nanoscale spatially resolved work functions. With knowledge of the operating probe's relative work function, various heterogeneities seen on common metal alloys can be cataloged and compared to DFT modeled predictions. By advancing DFT efforts to more complex multicomponent systems, as well as improving the repeatability and standardization of SKPFM, a connection between theory and experimentation can start to form. By bridging the gap between these two regions of focus, an improved understanding of materials beyond single element make-up can occur. Additionally for corrosion studies, the improved standardization of SKPFM will enable a greater understanding of the driving force behind corrosion initiation and progression on the nanoscale.

5.5 Acknowledgments

CME, and MFH acknowledge funding from the NASA Idaho Space Grant Consortium EPSCoR Seed Grant. Computing facilities (TdS and LL) were provided by Boise State University's R1 and R2 computing clusters as well as Idaho National Laboratory's high performance computing center. The authors thank the Boise State Center for Materials Characterization and Surface Science Laboratory staff for experimental assistance and access to their instrumentation resources.

CHAPTER 6: CHARACTERIZATION OF ZIRCONIUM OXIDES PART I: RAMAN MAPPING AND SPECTRAL FEATURE ANALYSIS

6.1 Introduction

Zirconium alloys are used for fuel cladding in nuclear reactors due to their low neutron absorption cross-section, high mechanical strength, and strong corrosion resistance while in typical water reactor conditions [18]. Alloying of zirconium has been shown to increase cladding performance by improving mechanical properties and corrosion resistance, while maintaining a low neutron cross section during operation [20-23, 27]. Research of high temperature degradation of zirconium cladding is of high interest in the nuclear field, and thus has been extensively studied for over 50 years [20, 27].

The general high-temperature coolant-side corrosion of zirconium cladding is similar regardless of oxidizing media (oxygen, water, or steam) [20, 27]. Initial formation of the oxide film provides a passivation layer, thus slowing the rate of subsequent oxidation to empirical power-law kinetics with parabolic to sub-parabolic characteristics (i.e., exponent ≤ 0.5) [27]. During this stage, the kinetics are limited by Fick's law phenomena, where oxygen diffusion is proportional to concentration gradient. With continued oxidation, cracks develop within the oxide, providing dynamic pathways for electrolyte species to reach the base metal at an increased rate. This transition is observed by an increase in mass gain rate, with kinetics evolving to a near linear oxidation rate. Oxide growth behavior at this transition is commonly termed the "breakaway

phenomenon" [20, 21]. Depending on alloy composition, some elements support a cyclic transition between passivation and oxidation, while others do not support re-passivation and the alloy fails to recover from the first breakaway [20, 27]. Regardless, continuous oxidation of the zirconium-alloys eventually leads to failure of the cladding material, albeit at different rates [26, 27].

In addition to the breakaway phenomenon, there are other structure and chemistry factors that contribute to cladding failure during reactor operation. The addition of hydrogen species in the coolant has been shown to cause cladding embrittlement by dendrite-like phase precipitation in the metal [18]. Inclusion of nitrogen species accelerates oxidation kinetics, attributing to initial nitride formation followed by oxidation that causes a volume expansion and increased oxide porosity [26, 38, 42, 43, 47, 48]. Additional effects such as interfacial stresses [30, 36, 37, 39-41, 219], temperature [47, 48], and alloying elements [22, 220] are all believed to play a role in cladding degradation. Furthermore, contributions from the fuel/cladding interface lead to an unpredictable cladding lifetime, as well as decreased reactor production efficiency [221]. Though the general degradation mechanisms have been well described, there are still questions regarding the predictability of cladding failure inside a nuclear reactor. The complexity of various, simultaneous degradation processes presents a difficult problem in predicting cladding failure, and thus has been a major focus of nuclear research [27].

Improved characterization of the zirconia scale is a critical link needed to advance the fundamental understanding of cladding degradation. Raman spectroscopy has been utilized as a characterization technique of the zirconia scale, both for *in situ* and post-exposure cross-section analysis [37, 38, 40-45, 219, 222-224]. Raman spectroscopy

provides qualitative to semi-quantitative information on composition, (sub) stoichiometry, order disorder, elastic strain, and plastic deformation [30, 38, 225]. Specifically, for zirconia the distinction between monoclinic and tetragonal phase has been well established in oxides grown in varying temperatures and environments [44, 45, 222-224]. Raman spectroscopy has supported the correlation between metastable tetragonal phase formation and high compressive stress in the oxide, oxygen vacancies, grain size, and alloying elements [36-38, 40, 225]. Utilization of Raman mapping provides spatial information regarding these properties with sub-micron resolution [38, 42, 43], and thus is a useful technique for understanding zirconium cladding degradation mechanisms. However, little works have provided mapping of Raman spectral features [38]. More so, there are no known efforts using Raman mapping differences between zirconium alloys or at different points in the corrosion mechanism.

In this work, interest has been given to particular spectral parameters to distinguish key properties of zirconia oxide. New insights on positioning of peaks, relative peak intensities between phases, and half-width at half-maximum (HWHM) of Raman peaks across the oxide and at the oxide/metal interface were used to further distinguish the nature of oxide evolution. Spatially resolved Raman mapping of oxides that were grown to points before and after the onset of breakaway on Zr, Zr-2.65Nb, Zry-3, and Zry-4 allowed for correlations between Raman spectral parameters and materials performance.

6.2 Material and Methods

Zirconium (Goodfellow) and alloys Zr-2.65Nb (ATI Metals), Zry-3, and Zry-4 (Idaho National Laboratory) were chosen for the current work (Table 6.1) due to their

wide nuclear applications [27]. Samples were isothermally oxidized, with thermogravimetric analysis (TGA) used to monitor mass gain rate, as described elsewhere [26]. Samples were exposed to 80% N_2, 20% O_2 environment at 700 °C. After oxidation, samples were sectioned and mounted in epoxy. They were then ground with SiC up to 1200 grit, followed by polishing up to 0.05 μm alumina slurry. Following polishing, samples were cleaned with heated Alconox solution on a soft pad, rinsed with ultrapure water, and then air dried. The approximate oxide thickness of each sample was examined with a Leica DM6000 M Materials optical microscope.

Raman mapping was accomplished using a Horiba LabRAM HR Evolution (Horiba Scientific) equipped with a 50 mW monochromatic 532 nm doubled Nd:YAG laser with ~0.3 cm^{-1} spectral resolution. Samples were mounted on a motorized stage with ±1 μm X-Y repeatability and accuracy. Spatial resolution depended upon objective lens magnification, and thus ranged from 721 nm to 1.18 μm. Maps of various sizes were acquired with 1 μm spacing between collected spectra. Spectral range of 150-700 cm^{-1} was used to examine peaks of interest. Spectra were processed and analyzed with LabSpec V6.3.x (Horiba). Spectral arrays underwent a baseline correction to remove background noise. Convolution of Gaussian and Lorentzian peak fitting was collected for spectral arrays. Peak position, amplitude, and HWHM were collected for different peaks in each spectrum and formed into X-Y maps. Spectra collected in metal were observed with low collection counts and large relative noise, and thus were excluded from analysis.

Table 6.1. Zirconium and alloy compositions.

	Sn	Fe	Cr	Nb	C	Hf	O	N	H	Zr
Zr (ppm)	-	200	200	-	250	2500	1000	100	10	bal.
Zr-2.65Nb (wt. %)	-	0.061	-	2.62	-	-	0.106	-	-	bal.
Zry-3 (wt. %)	0.25	0.25	-	-	-	-	-	-	-	bal.
Zry-4 (wt. %)	1.4	0.2	0.1	-	-	-	0.12	-	-	bal.

6.3 Results and Discussion

6.3.1 TGA

The TGA data provided an observable mass gain rate during oxidation of zirconium and alloy samples. Pre- and post-breakaway samples were produced based on the time of parabolic-to-linear transition confirmed with TGA (Figure 6.1). Approximate oxide thickness of each sample is included in Table 6.2.

According to the TGA results, pure zirconium greatly outperformed the alloyed samples. This is contradictory of waterside corrosion results, where alloys provide greater resistance to corrosion and oxide breakaway when compared to pure zirconium [27]. In addition, the effect of other degradation mechanisms such as hydrogen ingress provide motivation for alloying of zirconium [27]. However, in the case of this study, high-temperature air simulates transients of different accident scenarios. Nitrogen supports faster oxidation kinetics and increased porous oxide formation than seen in pure oxygen or steam. Further description of the corrosion mechanism of zirconium cladding materials in air is described elsewhere [26].

Amongst the samples in the Zircaloy family (i.e., zirconium-tin based system), Zry-3 resisted breakaway for a longer period of time than Zry-4. With regards to oxidation rate, the Zircaloys experienced similar mass gain rates in the pre-breakaway regime. The zirconium-niobium sample experienced breakaway at a point between the Zry-4 and Zry-3 samples. Additionally, Zr-2.65Nb experienced a greater mass gain rate than all other samples. Though breakaway could be distinguished, the oxidation rate before breakaway is nearly linear.

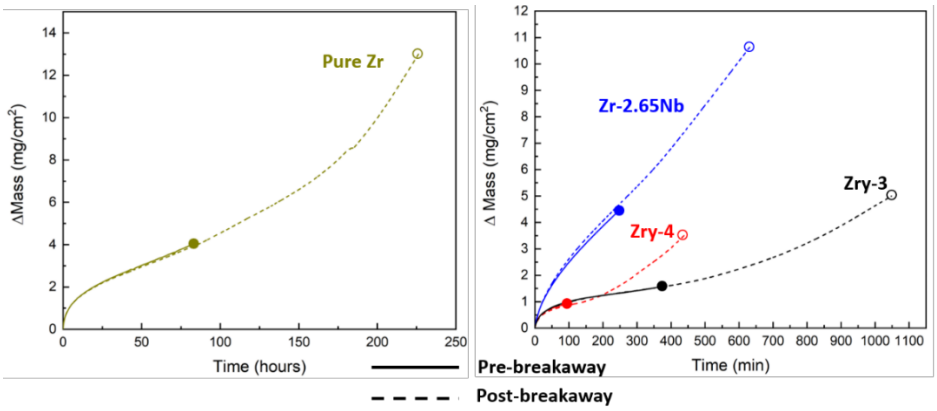

Figure 6.1. Normalized mass gain during isothermal oxidation for zirconium in hours of exposure (left) and its alloys in minutes of exposure (right). Pre-breakaway samples are designated with solid lines, post-breakaway samples with dotted lines. End points are noted with large dots.

Table 6.2. Oxide thickness of each sample, pre- and post-breakaway.

	Oxide Thickness (μm)			
Alloy	Zr	Zr-2.65Nb	Zry-3	Zry-4
Pre-break	20 ± 3	30 ± 4	17 ± 2	7 ± 1
Post-break	110 ± 30	60 ± 7	40 ± 8	32 ± 2

Cross-sectioned oxides were further observed with Raman mapping. In particular, some characteristic spectral parameters were spatially resolved to analyze changes in the oxide structure. Phase distribution, specifically monoclinic and tetragonal zirconia, were studied by calculating the percent tetragonality of each spectrum within a map. The positioning of a tetragonal peak was determined and correlated to different mechanisms of tetragonal phase formation. HWHM of a tetragonal peak was analyzed to determine degree of sub-stoichiometry of the tetragonal phase. Finally, residual stress, as it relates to shifts in monoclinic peak positions, was determined on a relative scale versus non-stressed expected peak positions. The specifics of these Raman parameters are described in the following sections to establish trends and relate those trends to sample performance.

6.3.2 Phase Distribution – Percent Tetragonality

The Raman spectra of common zirconium-based polymorphs have been extensively studied. Specifically, distinct vibrational spectra have been well established for both monoclinic and tetragonal zirconia [44, 45, 222]. Tetragonal zirconia is thermodynamically stable above 1205 °C [226]; however, tetragonal phase has been observed in zirconia grown on zirconium at lower temperatures [44]. Two different stabilization mechanisms of tetragonal phase have led to distinct naming of tetragonal phases. First, the "interface-tetragonal" phase is stabilized by high compressive stress and sub-stoichiometry, driven by metal/oxide lattice mismatch and low oxygen availability near the metal/oxide interface [227]. Second, stabilization of the "relaxed-tetragonal" phase in the bulk or external part of the oxide has solely been linked to stoichiometry of the oxygen sub-lattice, evidenced by a shift in position and increased disorder of the Raman peak [38]. A spectrum for each of these tetragonal phases, as well as bulk monoclinic zirconia phase, can be seen in Figure 6.2. For tetragonal phase near the metal/oxide interface, two large tetragonal peaks are seen in the 267-282 cm^{-1} (T_1) and 439-456 cm^{-1} (T_2) ranges, whereas only the T_1 peak is seen in the relaxed-tetragonal spectrum. Additionally, the tetragonal phase content for each spectrum is included in Figure 6.2, of which defines these three different phases.

Tetragonal phase content within zirconia (i.e., percent tetragonality, %T) is estimated as a volume fraction of tetragonal Raman peak intensity versus monoclinic peaks (Equation 6.1). Different forms of volume fraction have been used in literature to determine percent tetragonality [30, 40, 45]. The T_1 peak is seen for both interface- and relaxed-tetragonal phases, and thus was chosen versus the adjacent monoclinic peaks (M_3

and M_4) for calculating percent tetragonality in this work. Because of the peak collection methodology, where local maximums were collected within expected spectral ranges, single phase oxide cannot be calculated with Equation 6.1 (i.e., due to spectral noise, 100% and 0% tetragonality are not possible). For convenience, the threshold for monoclinic-rich oxide phase was defined as %T < 19.5%, where tetragonal contributions to the calculation arise from spectral noise. From this approximation, accounts of tetragonal and monoclinic phase are made. Distinction between relaxed- and interface-tetragonal phases are made by observing the X-Y location of the collected tetragonal-rich spectra with respect to the metal/oxide interface.

$$\%T_{ZrO_2} = \frac{I(T_1)}{I(M_3) + I(T_1) + I(M_4)}$$

Equation 6.1

Spatially resolved percent tetragonality of each sample, pre- and post-breakaway, is shown in Figure 6.3. A highly tetragonal phase can be seen near the metal/oxide interface, while the majority of the bulk oxide displays monoclinic-rich characteristics. Evidence of the relaxed-tetragonal phase is seen in many of the Raman maps. With regards to pre- versus post-breakaway samples, a greater amount of relaxed-tetragonal phase is seen in post-breakaway samples than in pre-breakaway samples. In addition, the thickness of the interface-tetragonal phase is thinner after breakaway than before breakaway for the three alloys, indicating that the occurrence of martensitic phase transformation from tetragonal to monoclinic zirconia increases after the onset of breakaway. This supports the theory that the tetragonal phase acts as a barrier to oxygen diffusion [23].

Although the relaxed-tetragonal phase is apparent for Zr samples, the bulk monoclinic oxide displays lower relative tetragonality than the alloys. This lack of tetragonal phase mixing in the oxide bulk could correlate to the superior performance of pure Zr versus the alloys in high temperature O_2/N_2 environment. The lattice mismatch between tetragonal and monoclinic zirconia could contribute to greater porosity and increased pathways for oxygen diffusion to the base metal, thus increasing oxidation rate and instability of the oxide. Further, via the Pilling-Bedworth ratio, alloying elements can be categorized based upon their oxidation volume compared to the zirconium matrix. Elements that oxidize at slower rates, in this case Fe, Nb, and Cr, could preferentially initiate cracking in the oxide [22]. Though there are concentrated areas of relaxed-tetragonal phase in the pure Zr samples, the rest of the bulk oxide is predominantly monoclinic zirconia, showing little to no tetragonal phase.

Finally, Zr and Zry-3 have thinner interface-tetragonal phase than the Zry-4 and Zr-2.65Nb samples. This corresponds with sample performance in Figure 6.1, where Zr and Zry-3 show superior resistance to degradation and breakaway than Zry-4 and Zr-2.65Nb. A thicker tetragonal phase could be expected to correlate with increased corrosion resistance. However, the results indicated differences in tetragonal phase stability between the samples, where the lower performing alloys transition from tetragonal to monoclinic zirconia from large stress gradients, driven by lattice mismatch at the metal/oxide interface [23]. For the better performing alloys, the stabilization of the tetragonal phase is additionally supported by reduced epitaxial growth of tetragonal grains, thus preserving an interface-tetragonal phase that is more resistant to oxygen diffusion to the metal.

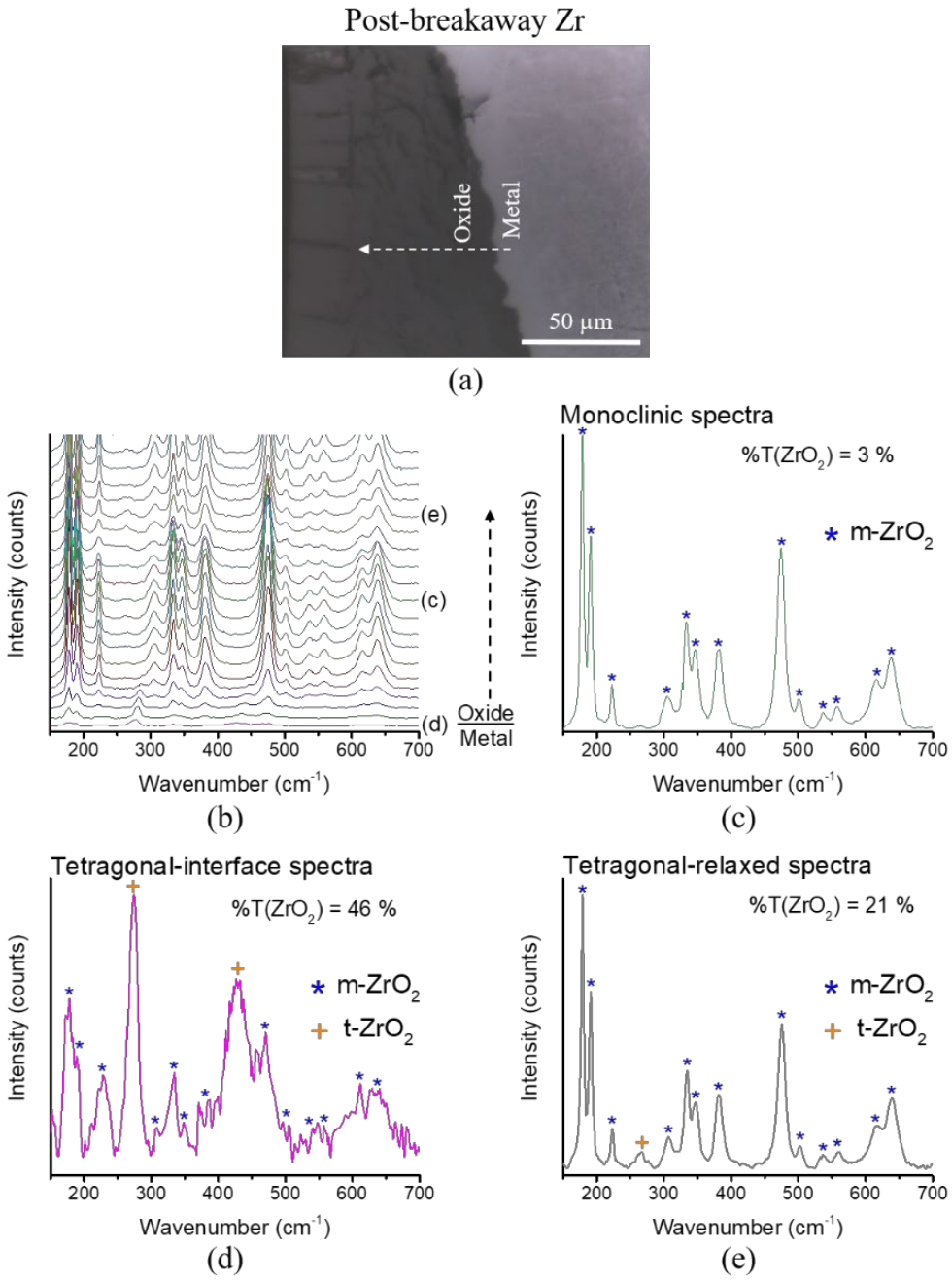

Figure 6.2. (a) Optical image of sectioned post-breakaway Zr sample, with metal and oxide indicated. (b) Raman spectra across line defined in (a) with individual spectra (c-e) noted. Individual spectrum for (c) monoclinic, (d) monoclinic with rich tetragonal phase near the metal/oxide interface, and (e) monoclinic with mixed tetragonal phase in the bulk of the oxide. Monoclinic (m-ZrO_2) and tetragonal (t-ZrO_2) zirconia Raman peaks are noted in each spectrum. Percent tetragonality, calculated with Equation 6.1, are included for each individual spectrum.

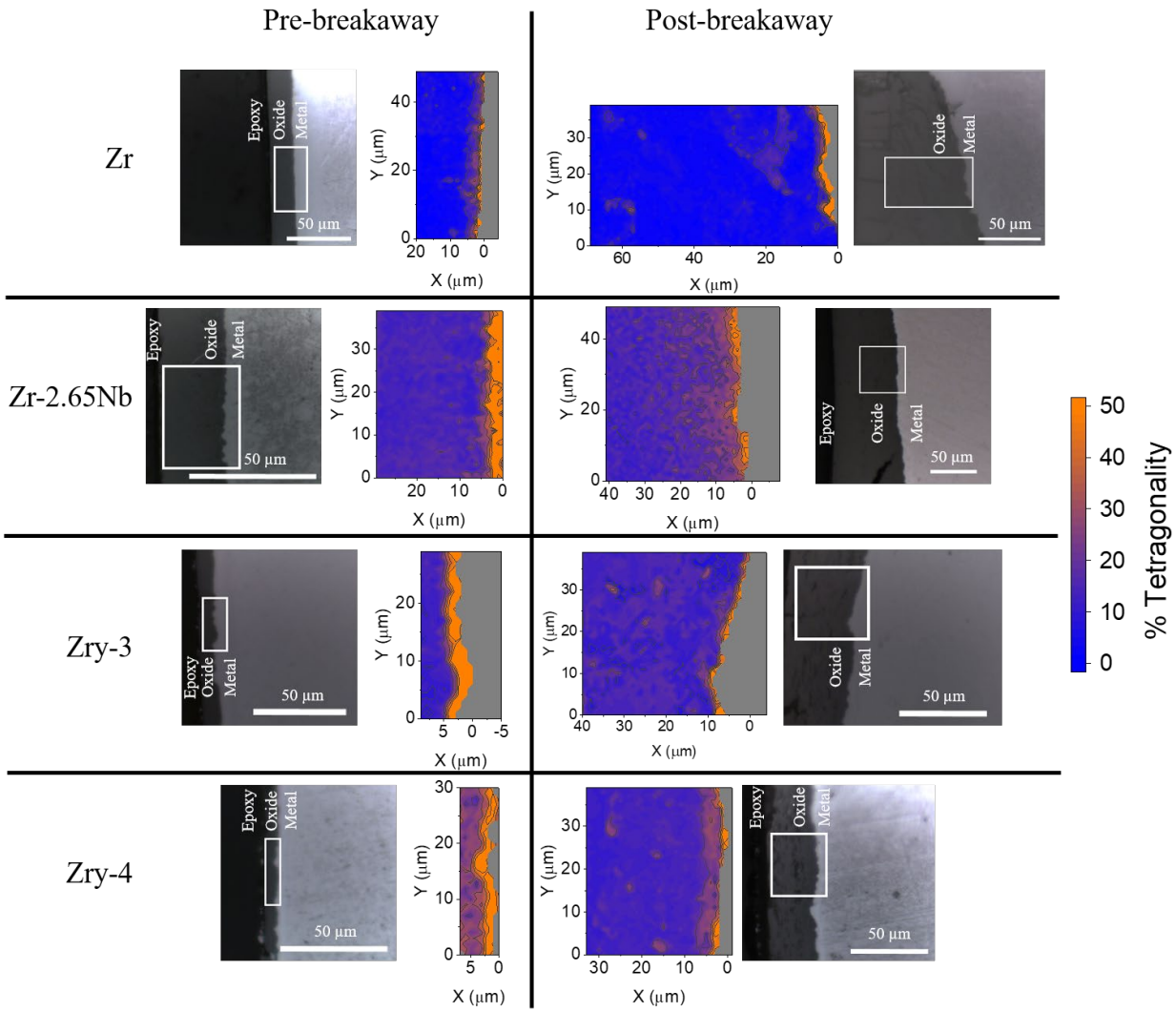

Figure 6.3. Matrix showing optical images and percent tetragonality maps for each sample, pre- and post-breakaway. Optical images reveal regions where Raman maps were collected and interfaces (oxide/epoxy and metal/oxide). Percent tetragonality for each spectrum was calculated with Equation 6.1.

6.3.3 Tetragonal Peak Position and HWHM

The large variation of the first tetragonal Raman peak position (262-287 cm^{-1}) has been attributed to differing stabilization factors, leading to the two different tetragonal phases being defined. [38, 40, 42, 45] The tetragonal phase that is stabilized with the support of compressive stress is correlated to a higher positioned tetragonal peak (i.e., wavenumber $\geq$ 275 cm^{-1}). When high amounts of stress are not evident, as would be seen

in the bulk of the oxide, relaxed-tetragonal phase is evidenced by a lower tetragonal peak position (i.e., wavenumbers ≤ 270 cm^{-1}). As for determining stoichiometry in the oxygen sub-lattice, the HWHM ratio has been used for the tetragonal peak [38, 40]. The HWHM increases with an increasing lattice disorder, driven by factors such as defects, doping cations, and/or oxygen sub-stoichiometry [38, 228]. Thus, the peak position and HWHM of the tetragonal peak were found for each spectra in all Raman maps, as summarized in Figure 6.4 and Figure 6.5. Spectra meeting the monoclinic-rich zirconia criteria (i.e., %T < 19.5%) were excluded from the tetragonal phase analysis.

For tetragonal phase with lower percent tetragonality (i.e., near 20% tetragonality), there is a notably large scatter in the T_1 peak position (Figure 6.5). As percent tetragonality increases, the T_1 peak position tends to stabilize around 275 cm^{-1}. Spectra deemed as relaxed-tetragonal zirconia phase do not show high relative intensities versus the nearest monoclinic peaks – all spectra fall between 20-30% tetragonality. The tetragonal peak position of relaxed-tetragonal spectra is also scattered. For Raman maps where a notable amount of relaxed-tetragonal phase is evident (all post-breakaway samples, as well as pre-breakaway Zr-2.65Nb), the interface-tetragonal phase statistically have higher tetragonal peak position than relaxed-tetragonal phase (Figure 6.4).

As for HWHM results (Figure 6.5), tetragonal phase with low percent tetragonality have large scatter in HWHM. As the tetragonal peak increases in relative intensity, the HWHM trends toward low values, revealing highly ordered oxygen sub-lattice in the tetragonal-rich zirconia. This trend is rather consistent over all alloys, both before and after breakaway has occurred. The large scatter for lower tetragonal phase could be driven by the sub-stoichiometry in the oxygen sub-lattice. This is particularly

key for zirconia at the metal/oxide interface, where others have shown that the highest sub-stoichiometry is greatest near the metal interface [38, 229]. For Zr, Zry-3, and Zry-4 post-breakaway samples, the HWHM of relaxed-tetragonal phase is statistically greater than the interface-tetragonal phase. Alternatively, there is no notable distinction between the two tetragonal phase types in terms of order/disorder for the Zr-2.65Nb pre- and post-breakaway samples. This correlates to the performance of the Zr-2.65Nb alloy seen with TGA, where mass gain rate is near linear before and after breakaway.

Focusing on the Zircaloys, the relaxed-tetragonal phase displayed statistically lower peak positions and higher HWHM than seen from the interface-tetragonal phase. This supports the differences in stabilization mechanisms between the two tetragonal phase types. Relaxed-tetragonal phase is stabilized via sub-stoichiometry, while interface-tetragonal phase is additionally supported by the high compressive stresses near the metal/oxide interface. The greater presence of relaxed-tetragonal phase with Zircaloys compared to elemental Zr could be related to the inclusion of elements with greater Pilling-Bedworth ratios (iron and chromium). It has been shown that inclusion of trivalent dopants, which is available for iron and chromium, compete with zirconium ions for oxygen vacancies, resulting in stabilization of tetragonal phase [230]. This increase in relaxed-tetragonal phase is seen only after breakaway occurs. However, the oxide scales of Zry-3 and Zry-4 before breakaway were relatively thin (< 10 μm), and thus an ability to distinguish between interface- and relaxed-tetragonal phase is unclear.

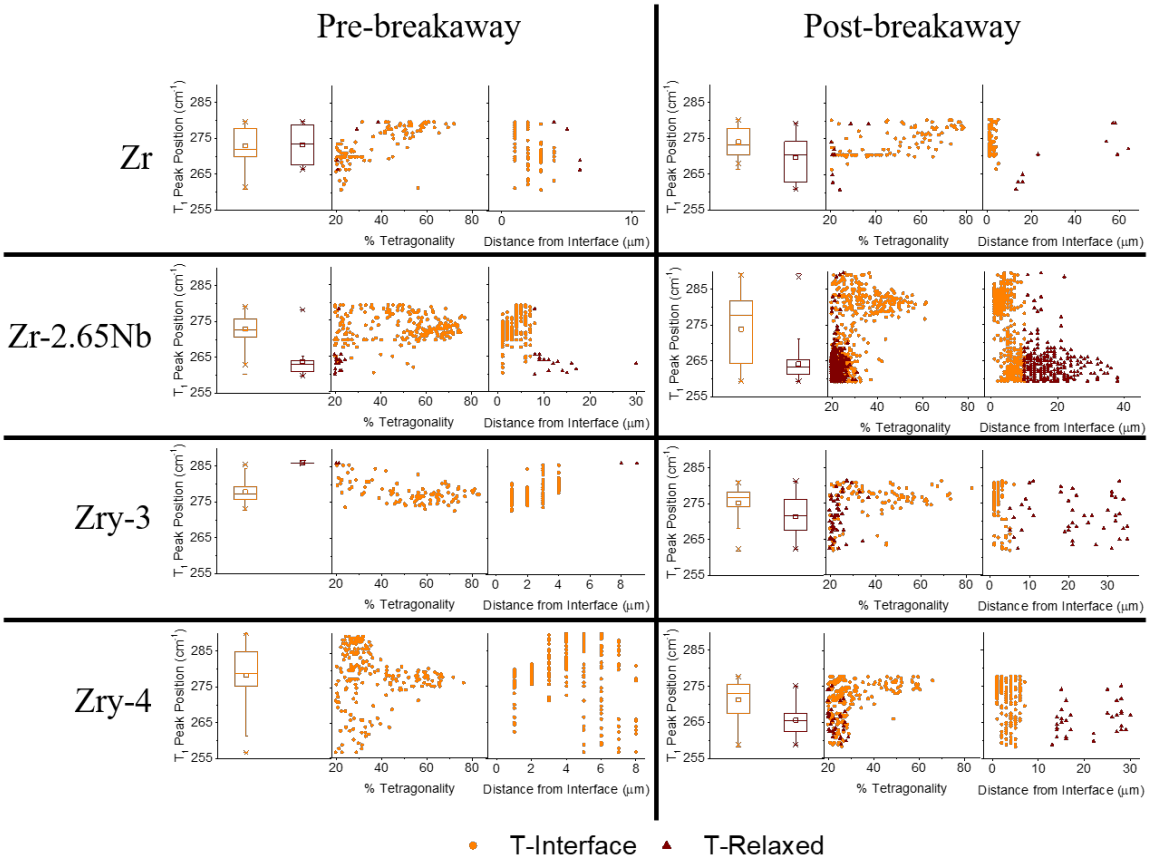

Figure 6.4. Tetragonal (T_1) peak position of tetragonal-interface and tetragonal-relaxed phases for each alloy, pre- and post-breakaway. Shown for each sample are (left) box-and-whisker plots for the T_1 peak position of each tetragonal phase, (center) T_1 peak position as a function of the percent tetragonality calculated for each spectrum with Equation 6.1, and (right) T_1 peak position as a function of distance along the horizontal axis from the metal/oxide interface.

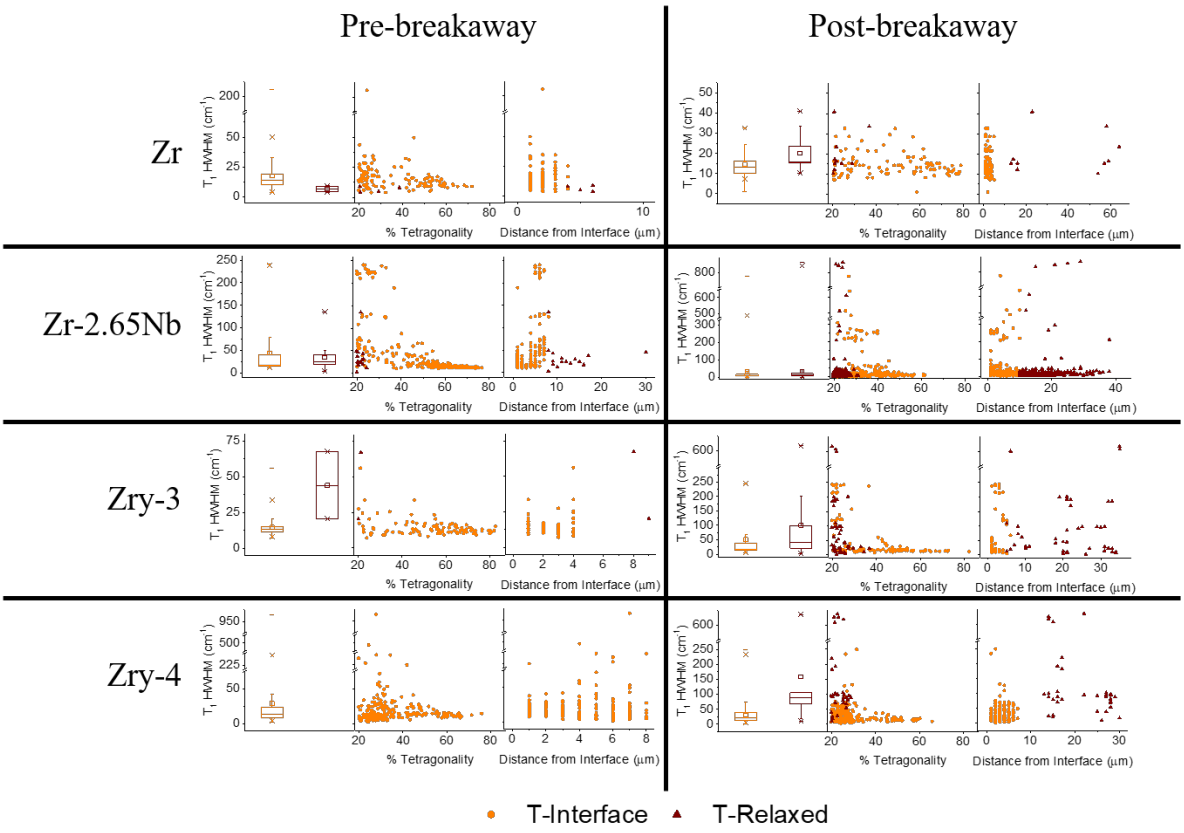

Figure 6.5. Tetragonal (T_1) HWHM of tetragonal-interface and tetragonal-relaxed phases for each alloy, pre- and post-breakaway. Shown for each sample are (left) box-and-whisker plots for the T_1 HWHM of each tetragonal phase, (center) T_1 HWHM as a function of the percent tetragonality calculated for each spectrum with Equation 6.1, and (right) T_1 HWHM as a function of distance along the horizontal axis from the metal/oxide interface.

6.3.4 Residual Stress

There has been much discussion about the relationship between the presence of tetragonal zirconia and stress state. As previously stated, zirconia is thermodynamically stable as monoclinic phase below 1205 °C. However, tetragonal zirconia grown on zirconium is stabilized at lower temperatures; specifically, the interface-tetragonal phase stabilizes near the metal/oxide interface by high compressive stresses [227]. Therefore, oxide with high tetragonal concentration near the metal/oxide interface should coincide with high compressive stresses. The understanding of this correlation is important, as

prior efforts have led to a belief that the interface-tetragonal phase relates to alloy passivity, porosity, and crack formation [23, 225].

As for the stress-state, stress development of zirconia has been studied for more than 50 years [29, 30, 36, 37, 39-41, 219]. In particular, Raman spectroscopy has been utilized to observe stress development during sample heating [37, 39, 219], as well as residual stress from post-exposure examination of sectioned oxides [36]. The residual stress seen with post-exposure examination is comprised of growth, thermal, and relaxation stress [36]. With Raman, residual stress is observed by shifts from non-stressed peak positions, where the rate of stress as a function of peak shift is calibrated via uniaxial compression [30, 37, 38, 41, 44]. Using Raman, residual stress has been calculated between hundreds of MPa to more than 5 GPa of compression at the metal/oxide interface [36]. In general, a direct correlation between shift from expected peak position and residual stress has been shown [30]. For this work, residual stress is qualitatively observed as a shift from expected peak positions, where a positive peak shift aligns with tensile stress and a negative peak shift aligns with compressive stress. Two monoclinic peaks were used to observe residual stress state – the M_2 (189 cm^{-1}) and the M_8 (475 cm^{-1}) peaks.

Figure 6.6 and Figure 6.7 provide X-Y maps of the M_2 and M_8 peak positions, respectively. The bulk of the oxide for each sample tend to show peaks near the expected, or non-stressed, positions. As the distance from the metal/oxide interface decreases, the monoclinic peak positions decrease, coordinating to compressive stress. This is further evidenced in Figure 6.6 and Figure 6.7 when looking at the monoclinic peak positions as a function of percent tetragonality. As the percent tetragonality increases, the peak

position trends below non-stressed peak position. The exception is the thin Zry-4 sample before breakaway. Here, it appears that even the epoxy-side oxide reveals lower positions than non-stressed peaks, and thus some compressive stress is evident throughout the entire oxide. This correlates with the tetragonality maps seen in Figure 6.3, where highly tetragonal spectra also demonstrate large shifts in monoclinic peak positions, and thus high compressive stress.

Zry-3 before breakaway does not have this high compressive stress in the bulk of its thin oxide. This supports why Zry-3 resisted breakaway for a longer period of time than Zry-4. Interface-tetragonal phase in Zry-3 is driven by a stabilization of a thinner tetragonal phase via grain size in addition to compressive stress, while Zry-4's thick, unstable tetragonal phase forms primarily by compressive stress. As for Zr-2.65Nb, a consistency of stress distribution before and after breakaway correlates to the performance seen from TGA, where the kinetics behaved similar before and after breakaway. However, for the post-breakaway Zr-2.65Nb, the scatter of the M_8 peak position is notable, as well as no notable trend correlating compressive stress to increasing tetragonality.

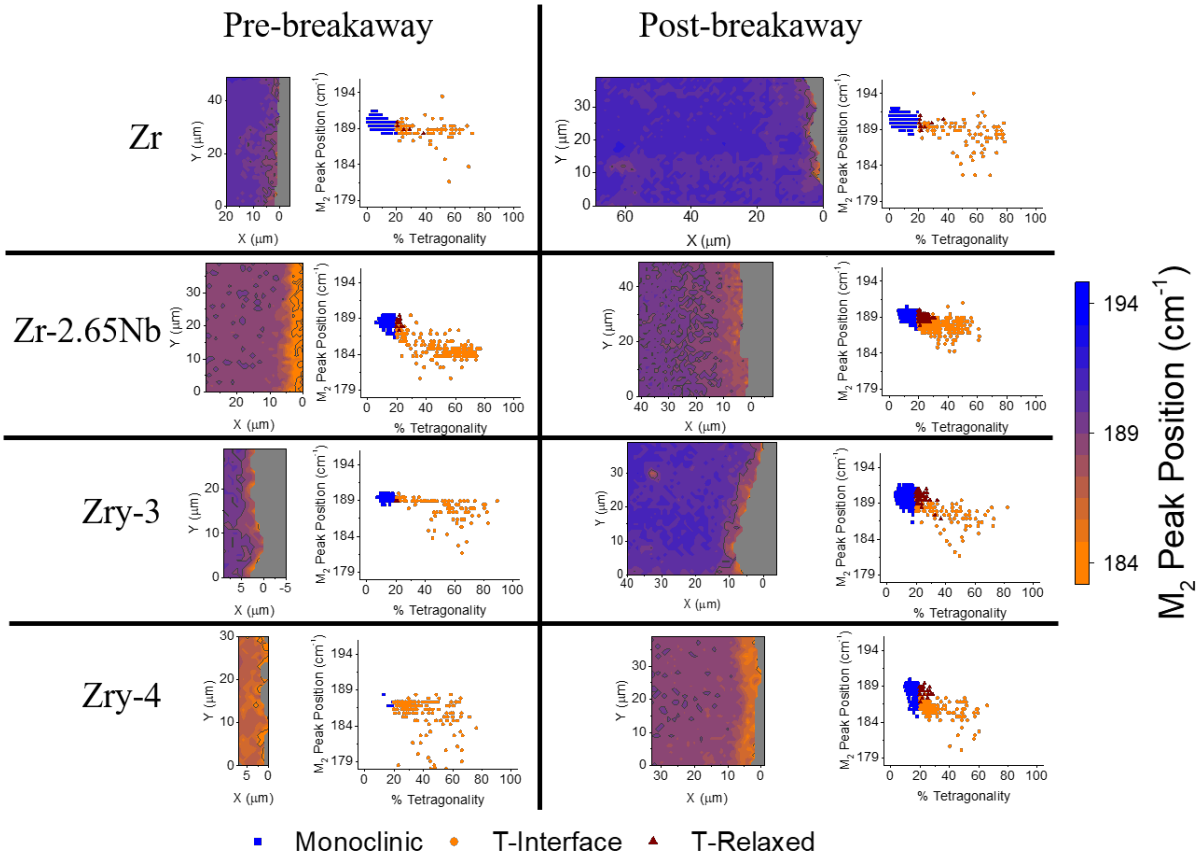

Figure 6.6. Raman mapping of M_2 peak position for each sample, both pre- and post-breakaway. Scatter plots of M_2 peak position as a function of percent tetragonality are also included for each Raman map.

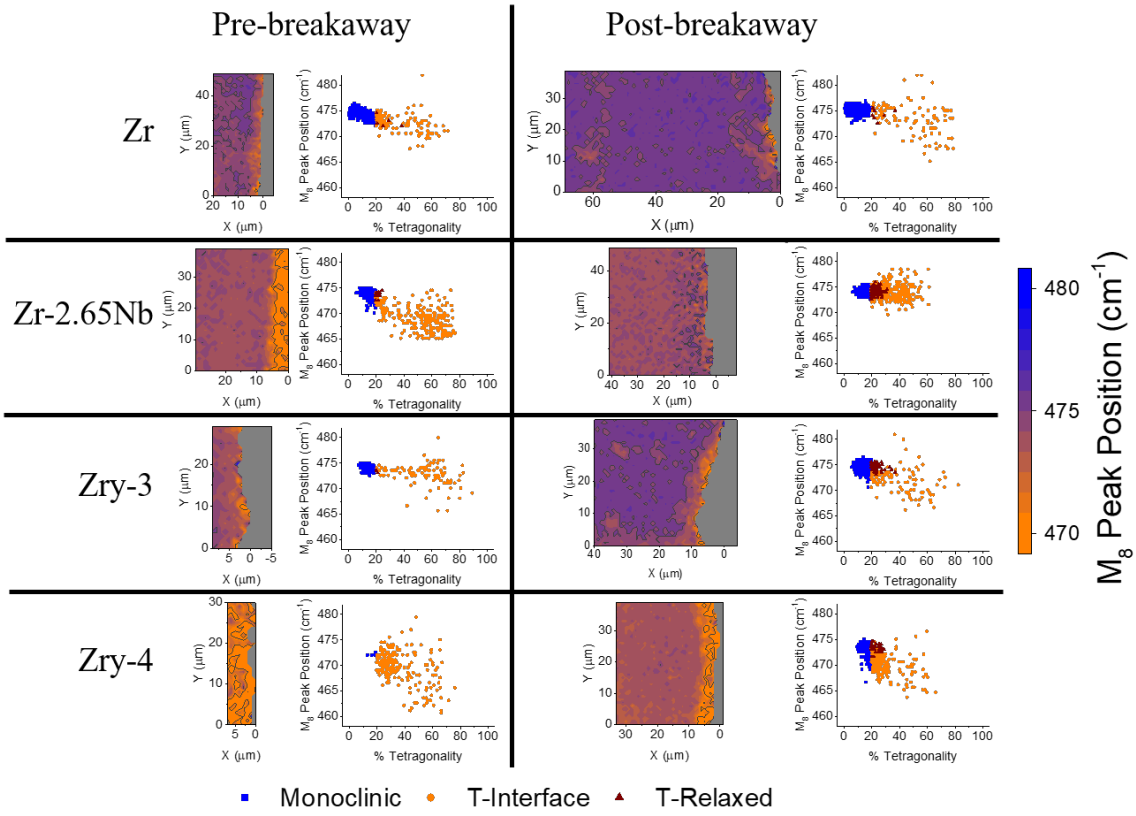

Figure 6.7. Raman mapping of M_8 peak position for each sample, both pre- and post-breakaway. Scatter plots of M_8 peak position as a function of percent tetragonality are also included for each Raman map.

6.3.5 Parameter Correlations

A correlation between the stabilization of tetragonal phase at the metal/oxide interface and compressive stress has been investigated and established. Similar trends between these two factors as a function of distance from the metal/oxide interface can be inferred from Figure 6.8. The shape of these plots display asymptotic characteristics, where evidence of tetragonal phase approaches zero, and monoclinic peaks approach non-stressed positions as distance from the metal/oxide interface increases. Near the interface, high tetragonal phase coincides with large decreases in monoclinic peak positions (i.e., compressive stress). Also of note is how the relaxed-tetragonal data closely follows the trend of monoclinic peak positions. This supports the theory that

relaxed-tetragonal phase is not stabilized with contribution from compressive stress, and rather is stabilized from sub-stoichiometric contributions.

Due to the similar trends that percent tetragonality and monoclinic peak positions present as a function of distance from metal/oxide interface, a linear correlation between percent tetragonality and monoclinic peak positions were assumed (Figure 6.9). Referring to Figure 6.6 and Figure 6.7, all of the spectra with high percent tetragonality are recognized as interface-tetragonal phase, and thus should also possess the highest compressive stress in the oxide. From this, a correlation between the performance of each material, as seen with TGA in Figure 6.1, and the amount of stress observed near the metal/oxide interface, can be made. Zry-4, which experienced breakaway the quickest during the isothermal oxidation, also reveals some of the highest Raman shifts in monoclinic peaks at the metal/oxide interface. This same trend between shortest time to breakaway and highest stress-level at the metal/oxide interface is seen, in order Zry-4, Zr-2.65Nb, Zry-3, and pure Zr. The outlier again is the post-breakaway Zr-2.65Nb sample when looking at the M_8 trend line. The slope of this trend is relatively flat, showing no correlation between M_8 peak position (i.e., compressive stress) and percent tetragonality.

As for comparing pre- to post-breakaway, no observable trend can be distinguished for the high percentage tetragonality end of the linear fits. However, pre-breakaway samples consistently display greater shifts in monoclinic peak positions at the monoclinic-rich side of the linear fits (i.e., near zero percent tetragonality). In theory, this means there is more compressive stress within the bulk of the oxide prior to breakaway than there is after breakaway, confirming the theory that stress builds up until breakaway initiates to relieve the stress in the oxide. This difference in monoclinic peak position is

especially evident for Zry-4, where the oxide thickness of the pre-breakaway sample is under 10 μm in thickness. The Raman spectra collected for this sample is majority tetragonal-present phase, as well as under high compressive stress throughout the entire oxide. This is in agreement with work done by Kurpaska et al., where *in situ* Raman provided evidence of monoclinic peak shifts to less stressed wavenumbers as a function of exposure time. [219] Thus, the early onset of oxide growth should display lower monoclinic peak positions, and transition to higher values as the oxide grows and stress of the surface oxide declines. As for Zr-2.65Nb, there is little difference in M_2 peak position before and after breakaway, supporting the minimal transition of mass gain rate and stress state before and after breakaway.

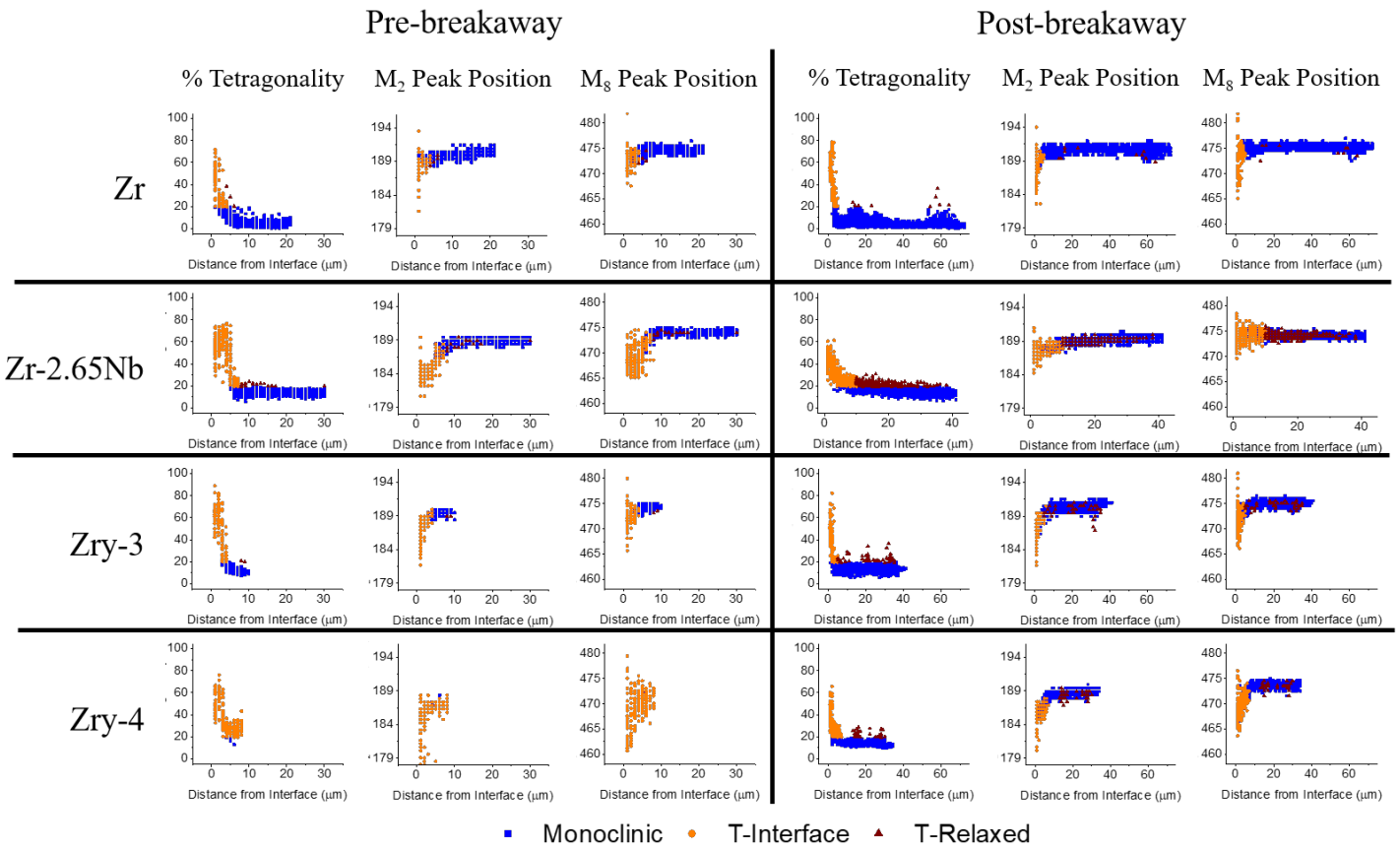

Figure 6.8.Percent tetragonality and monoclinic peak positions, M_2 and M_8 (in cm^{-1}), as a function of distance from the metal/oxide interface for each alloy, pre- and post-breakaway.

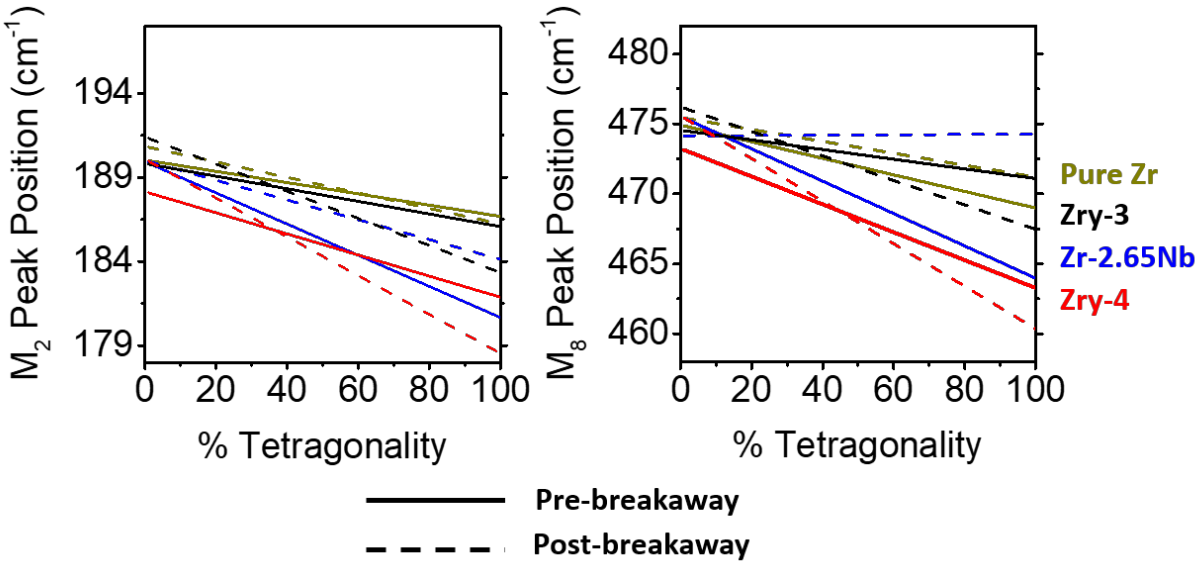

Figure 6.9. Linear trends of monoclinic peak positions, M_2 (left) and M_8 (right), as a function of percent tetragonality. Pre-breakaway samples are designated with solid lines, post-breakaway samples with dotted lines.

When comparing the Zircaloys, Zry-3 outperformed Zry-4 in regards to resisting breakaway. In Figure 6.9, Zry-4 displays lower peak positions for monoclinic-rich phase (i.e., higher compressive stress in the bulk of the oxide) as well as more intense slopes, leading to higher compressive stress of interface-tetragonal phase. This supports the differences in stabilization between Zry-3 and Zry-4 proposed by Wei et al., where a decrease in tin content improves corrosion resistance. [23] Tetragonal phase of Zry-4 theoretically stabilizes mainly by compressive stress, whereas tetragonal phase of Zry-3 stabilizes with support by tetragonal grain size. The stress-stabilized, tetragonal grains of Zry-4 undergo a martensitic transformation to monoclinic zirconia rapidly, thus causing damage in the oxide and supporting breakaway sooner than for Zry-3.

6.4 Conclusions

This work utilized Raman mapping to resolve spectral features as a function of X-Y location for different zirconium alloys after exposure to 700 °C mixed N_2 and O_2

environment, reaching points before and after breakaway. Raman mapping of sectioned oxides provides utility of correlating spatially-resolved spectral peak positions and shape to both performance and oxide properties.

Tetragonal phase volume fraction was calculated (Equation 6.1) and mapped for each spectrum, revealing a tetragonal-rich phase near the metal/oxide interface, as well as a relaxed-tetragonal phase stabilized in the bulk of the oxide. The better performing Zr and Zry-3 samples had thinner tetragonal phase at the metal/oxide interface than Zry-4 and Zr-2.65Nb. This supports the theory that differences in tetragonal phase stability, in addition to the mechanism behind the martensitic phase transition to monoclinic zirconia, play a role in oxide stability and diffusion-limited kinetics. The stable Zry-3 and Zr tetragonal phase may be driven by low or absence of tin and niobium inclusion, thus resulting in the tetragonal phase being stabilized via grain size rather than solely by interfacial stress.

The tetragonal Raman peak was compared between interface- and relaxed-tetragonal phases, revealing higher peak position and lower HWHM for the interface-tetragonal phase. In this case, the Raman data indicated that the contribution of highly compressive stress stabilized formation of tetragonal phase at the metal/oxide interface. This was further supported by certain monoclinic peak positions seen at lower wavenumbers for spectra nearest the metal/oxide interface. This decline in monoclinic peak position correlates to highly compressive stress, while the bulk of the oxide revealed nearly non-stressed peak positions.

Finally, a linear correlation between tetragonal phase fraction and stress state was made. A trend showing decrease in monoclinic peak position with increase in tetragonal

phase content was revealed. The monoclinic peak positions for monoclinic-rich zirconia were consistently lower in pre-breakaway oxides than seen in post-breakaway oxides, supporting the theory of stress-induced breakaway. A higher amount of residual stress is seen in Zry-4 than in Zry-3, supporting the stabilization of low-tin content alloys via grain size rather than stress stabilization. This methodology of mapping Raman spectral features has revealed these trends, providing greater insight into the mechanisms that cause failure of zirconium alloy cladding in nuclear reactors.

6.5 Acknowledgments

This work was supported in part through the Department of Energy (DOE) In-Pile Instrumentation program under DOE Idaho Operations Office Contract DE-AC07-05ID14517. Paul H. Davis of Boise State University is thanked for his support with the Horiba Raman system. The authors also acknowledge the departmental support from Boise State's Micron School of Materials Science and Engineering. The views and opinions of authors expressed herein do not necessarily state or reflect those of the U.S. Government or any agency thereof. The raw/processed data required to reproduce these findings can be shared upon request to corresponding author at coreyefaw@u.boisestate.edu.

CHAPTER 7: CHARACTERIZATION OF ZIRCONIUM OXIDES PART II: NEW INSIGHTS ON THE GROWTH OF ZIRCONIA REVEALED THROUGH COMPLEMENTARY HIGH-RESOLUTION MAPPING TECHNIQUES

7.1 Introduction

The adverse environment created from irradiation and variable conditions within a nuclear reactor core induces complex degradation processes of cladding. Zirconium alloys are a viable material choice for fuel cladding, due to its low neutron absorption cross-section and strong corrosion resistance while in a nuclear reactor environment. Dynamic material effects and the extreme environment make it difficult to predict or monitor cladding condition in-core and present significant obstacles for achieving a comprehensive and unified understanding of cladding degradation mechanisms [20, 27, 221, 231].

Currently, chemical evolution over the lifetime of cladding can only be inferred using post-irradiation examination (PIE) [54], or mimicking the coolant-side conditions with *in situ* characterization [19, 37, 38, 219, 232]. Progress is being made to establish new sensing techniques; for instance, electrochemical impedance spectroscopy (EIS) is becoming established as a cladding degradation sensing technique [19, 54, 232]. However, in order to develop accurate EIS models and advance current sensor technology, high-resolution characterization techniques must be used to translate degradation processes along the cladding pathway to equivalent circuit models. This work utilizes scanning Kelvin probe force microscopy (SKPFM), Raman spectroscopy,

and scanning electron microscopy (SEM) with energy-dispersive X-ray spectroscopy (EDS) to provide high-resolution co-localized characterization of zirconium oxide and metal/oxide interface.

Raman spectroscopy provides qualitative to semi-quantitative information on ceramic material composition. This technique has been extensively used for both *in situ* and post-exposure sectioned analysis of zirconium alloys [30, 37, 38, 42, 43, 219]. Raman provided evidence of a bilayer oxide structure grown on zirconium after extended thermal oxidation [45, 225]. The inner layer is a metastable tetragonal phase that has been considered on both ends of the spectrum with regards to being either a protective barrier or a non-participant in the corrosion mechanism of the cladding [27]. The metastable tetragonal phase is believed to be stabilized by a combined effect of interfacial compressive stress, oxygen sub-stoichiometry, and grain size [37, 38]. Via a martensitic phase transformation, tetragonal zirconia transitions to a columnar grained and more porous monoclinic zirconia outer layer. A region of mixed, transient tetragonal-monoclinic zirconia exists between these layers. Raman spectra also provide insight into the stress distribution within the oxide, where high compressive stress is seen in the small, equiaxed tetragonal grains near the metal/oxide interface. With support by oxide porosity, this high compressive stress is believed to reach a critical value that is followed by a rapid transition to a less stressed state. The stress relief, termed the breakaway phenomenon, is allowed by vertical fracturing in the oxide, providing a pathway for increased oxidation rate [27, 30].

SKPFM is a non-destructive atomic force microscopy (AFM) variant that resolves nanoscale features on the material surface. The traditional Kelvin probe utilizes the

capacitive nature between conductors in electrical contact to determine the contact potential difference (CPD), or Volta potential difference (VPD). When applied to a nanoscale and mobile probe, SKPFM spatially resolves local relative Volta potentials that correspond to microstructural heterogeneities on the material's surface. The VPD between two metals in electrical contact directly relates to the difference in their electron work functions [233]. While in an inert environment with minimum surface adsorbates, the Kelvin probe can theoretically acquire the work function difference between probe and sample surface. It is a useful surface characterization technique for specifying phase nobility (i.e., microgalvanic coupling) [165, 168-170, 184, 215], hydrogen precipitation detection [234-238], characterization of semiconductors [239, 240], and co-localization with elemental makeup from SEM/EDS [127]. However, SKPFM has yet to be utilized for characterizing nuclear cladding zirconium alloys. The thermally grown zirconia is an n-type semiconductor, where oxide growth at the cladding's metal/oxide interface is limited by oxygen anion diffusion [27]. With the existence of an electric field driving spontaneous high-temperature corrosion, the flux of oxygen anions to the metal is balanced by a flux of electrons to the oxide/coolant boundary via hopping mechanism, thus netting zero current [20, 27]. The ionic conductivity of zirconia is ultimately driven by crystal lattice defects, such as Frenkel defects, Schottky disordering, dislocations, and grain boundaries [20, 241]. A region of oxide bordering the metal substrate, stabilizes as tetragonal zirconia due to high compressive stress and oxygen sub-stoichiometry [37, 38, 219, 242], making it a viable electron acceptor (i.e., p-type semiconductor). This thin tetragonal phase is theorized to be a barrier layer to increased oxide growth [27]. Additionally, distribution of other species in zirconia produces spatial heterogeneities in

electronic properties, and thus provide a driving force for microgalvanic reactions to occur [243]. Given these notable variabilities in the oxide structure, the nanoscale resolution capabilities of SKPFM can provide spatial mapping of ionic/electronic pathways that regulate the corrosion mechanism. SKPFM can provide new insight into the electronic properties of the zirconia layering, oxygen stoichiometry, and metal/oxide interface. Additionally, SKPFM could be utilized to detect heterogeneities such as secondary-phase precipitates, hydrides, and nitrides. The electronic structure of both oxide and metal has great effect on the catalytic activity at the metal/oxide interface. Also, the inclusion of alloying elements plays a role in catalytic activity and selectivity of metals [244]. An ensemble of carefully selected complementary characterization techniques enables new correlations between electronic properties, microstructural heterogeneities, and elemental composition. These correlations provide an insight of zirconia growth mechanisms yet to be observed with individual techniques. With an improved knowledge of cladding degradation, accurate EIS equivalent circuit models can be used for in-core monitoring of cladding degradation.

7.2 Experimental methods

Zirconium (Goodfellow) and Zr-2.65Nb (ATI Metals) were chosen for the current work (Table 7.1). Plate samples were isothermally oxidized, with thermogravimetric analysis (TGA) used to monitor mass gain rate, as described elsewhere [26]. Samples were exposed to 80 % N_2, 20 % O_2 environment at 700 °C. After oxidation, samples were sectioned and mounted in epoxy. They were then ground with SiC up to 1200 grit, followed by polishing with 1 and 0.05 μm alumina slurries. Following polishing, samples were cleaned with heated Alconox solution on a soft pad, rinsed with ultrapure water, and

air dried. Samples were then immediately transferred to the glovebox AFM for SKPFM analysis.

Table 7.1. Zirconium and Zr-2.65Nb compositions.

	Fe	Sn	Cr	Nb	C	Hf	O	N	H	Zr
Zr (ppm)	200	-	200	-	250	2500	1000	100	10	bal.
Zr-2.65Nb (wt. %)	0.061	-	-	2.62	-	-	0.106	-	-	bal.

SKPFM was done with a Dimension Icon AFM (Bruker) in an argon filled glovebox (MBraun,<0.1 ppm O_2 and H_2O). PFQNE-AL probes were used to acquire results, operating under a dual-pass method called FM PF-KPFM [122]. In addition to topography, quantitative nanomechanical (QNM) properties were simultaneously acquired from probe/material interactions. Volta potential differences were acquired when the probe was lifted to a user-defined lift height of 100 nm above the surface, creating a nanoscale scenario synonymous to the traditional Kelvin probe. Prior to SKPFM acquisition of the cladding samples, probes were calibrated by imaging a Bruker PFKPFM-SMPL, consisting of an n-doped silicon substrate with patterned islands of aluminum surrounded by a gold interconnect. This sample was utilized to ensure relative consistency of probes by providing a step-wise VPD map from aluminum to silicon to gold [122]. Image processing and analysis were conducted using NanoScope Analysis V1.8 (Bruker). Topography maps underwent a flattening process to remove sample tilt. Raman spectroscopy was accomplished using a Horiba LabRAM HR Evolution (Horiba Scientific) with a monochromatic 532 nm doubled Nd:YAG laser with 50 mW power and ~0.3 μm spectral resolution. Samples were mounted on a motorized stage with ±1 μm X–Y repeatability and accuracy. Spatial resolution depended upon objective lens magnification, ranging from 721 nm to 1.18 μm, and thus Raman maps were acquired

with 1 μm spacing between collected spectra. Spectral range of 150–700 cm^{-1} was used to examine peaks of interest. Spectra were processed and analyzed with LabSpec V6.3.x (Horiba). Spectral arrays underwent a baseline correction to remove background noise. Convolution of Gaussian and Lorentzian peak fitting was collected for spectral arrays. Peak position and amplitude were collected for different peaks in each spectrum and formed into X–Y maps. Distinction of zirconia phase, particularly monoclinic and tetragonal, has been well established [43]. Tetragonal phase, which is thermodynamically stable above 1205 °C [226], is stabilized at lower temperatures in the grown oxide. The stability of tetragonal phase near the metal/oxide interface is driven by high compressive stress and oxygen sub-stoichiometry [38]. Phase content (i.e., volume fraction) of tetragonal and monoclinic zirconia is estimated to calculate the named percent tetragonality. The first tetragonal peak (T_1) versus neighboring monoclinic peaks (M_3 and M_4) was decidedly used to calculate percent tetragonality (Equation 7.1). Also analyzed from Raman spectra was relative residual stress, where shifts in monoclinic peak positions directly correlates to relative stress [30]. The M_2 peak was chosen to observe relative residual stress, where a decrease in this peak's position correlates with increasingly relative compressive stress. A calibration is commonly done in order to quantify stress – however, a calibration was not conducted for this work. Rather, the relative stress state was observed to show trends as a function of percent tetragonality and distance from the metal/oxide interface.

$$\%T_{ZrO_2} = \frac{I(T_1)}{I(M_3)+I(T_1)+I(M_4)}$$

Equation 7.1

SEM/EDS with a Hitachi S-3400N-II (Oxford Instruments Energy+) at 10-15 keV and 10 mm working distance to provide elemental distribution of each sample. Due to the

inherent sample damage that occurs during Raman (laser beam damage [245]) and SEM/EDS (carbon pyrolysis and electron beam irradiation [170, 184, 240]), these techniques were done in corresponding order after SKPFM. In addition, samples were carbon-coated prior to SEM/EDS to provide a conductive layer over the epoxy mount and inhibit charge build-up.

7.3 Results and discussion

TGA provided observable mass gain rate for the zirconium samples (Figure 7.1). Samples were held to points either before or after breakaway was observed. Breakaway was identified by a transition of mass gain rate from parabolic to linear kinetics. Faster kinetics and breakaway are induced much earlier in air than seen in oxygen or steam environments, due to the inclusion of nitrogen in the mechanism. Nitride formation and subsequent oxidation of those nitrides leads to increased porosity of the oxide [26]. The post-breakaway pure Zr sample was oxidized for ~226 h, while the post-breakaway Zr-2.65Nb was oxidized for ~10.5 h. An additional pure Zr sample was oxidized for 20 h, being removed prior to breakaway occurring. The vast superiority of Zr over Zr-2.65Nb in resisting corrosion and breakaway is opposite of waterside corrosion performance, where inclusion of niobium improves corrosion and breakaway resistance, as well as mechanical properties when compared to pure zirconium [27]. In the case of this study, exposure to high temperature mixed nitrogen/oxygen environment presents different possible scenarios mimicking an air-cooled core (such as with Transient Reactor Test Facility (TREAT) at Idaho National Lab) or air ingress and rapid increase in temperature during a nuclear reactor loss-of-coolant accident (LOCA). Corrosion mechanisms in this particular environment are described elsewhere [26].

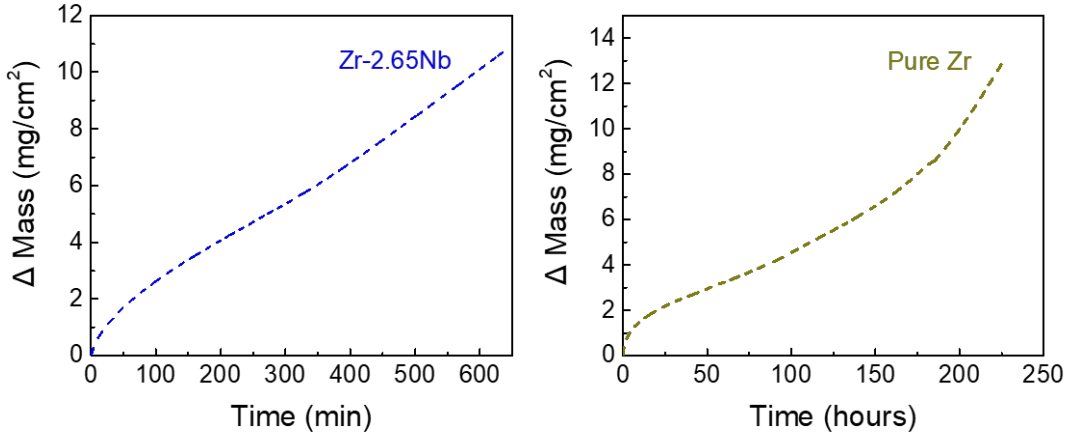

Figure 7.1. Normalized mass gain during isothermal oxidation for Zr-2.65Nb (left) and Zr (right).

Post-oxidation analysis was done on cross sectioned samples. Being the least destructive technique, SKPFM in an argon filled glovebox was done first. Co-localization of SKPFM with the other techniques was accomplished by establishing fiducial marks, such as distinct crack morphology in the oxide or variation in oxide/metal profile.

For SKPFM, relative Volta potentials (i.e., Volta potential difference, VPD), as well as QNM properties were mapped and used to identify the exact metal/oxide boundary. Figure 7.2 presents height, VPD, adhesion, and deformation acquired for the oxidized Zr sample. The metal/oxide interface is noted with red lines. A clear boundary is seen between the metal and oxide, where the average metal Volta potential is ~160 mV higher than the average oxide Volta potential (Figure 7.2b). Differences in surface morphology (Figure 7.2a), as well as changes in adhesion (Figure 7.2c) and deformation (Figure 7.2d) support that the transition point between metal and oxide correspond with the boundary in the Volta potential channel. In addition, a large particle is seen at the metal/oxide interface, displaying higher Volta potential than the surrounding oxide and metal. Based upon the size and location of the particle, as well as the exposing

environment, it is likely either a secondary-phase precipitate (SPP) or a nitride. During breakaway in a mixed nitrogen/oxygen environment, nitride particles form at the metal/oxide interface [26]. The difference in lattice density between Zr, ZrO2, and ZrN causes lattice mismatch, driving cracking and formation of porous oxide following the oxidation of the nitride particle, leading to pathways for increased cladding degradation [32, 33, 48]. On the other hand, elements such as chromium and iron can form SPPs that tend to oxidize at a slower rate than the surrounding zirconium matrix. These slow oxidizing SPPs may support microgalvanic corrosion of the surrounding zirconium, as well as provide pathways via lattice mismatch to cause cracking of the oxide [27]. At higher temperatures, the mobility of iron and chromium should increase, allowing possible formation of SPPs, even when low in concentration. The higher measured Volta potential of the particle seen in Figure 7.2 supports the theory that it acts as a local cathode relative to the surrounding oxide.

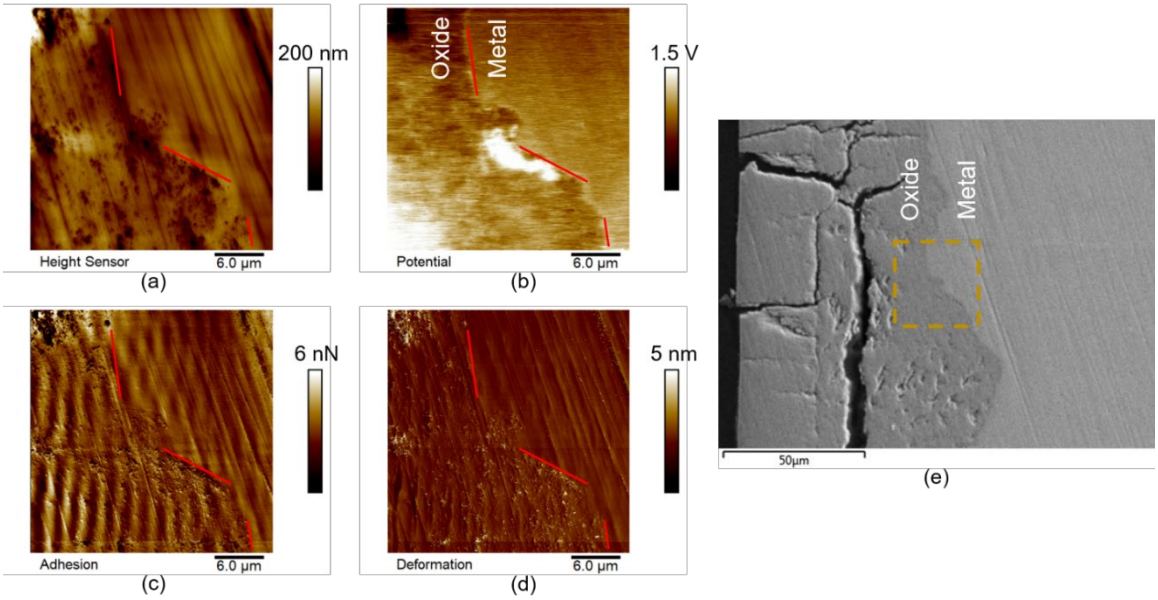

Figure 7.2. AFM results for sectioned sample of oxidized Zr. (a) Height, (b) relative Volta potential, (c) adhesion, and (d) deformation images with red lines separating metal and oxide. (e) SEM image with area where SKPFM was performed.

Raman mapping of the same area provided insight into the separation of oxide phases. Figure 7.3 shows maps of both percent tetragonality (i.e., phase content) and monoclinic peak position (i.e., relative stress state). At the metal/oxide interface (metal is gray in color), tetragonal- rich phase is evident, as are shifts to lower monoclinic peak position that corresponds to increasing compressive stress. As the distance from the interface increases, relative stress decreases, as does the concentration of tetragonal phase. There are notable regions in the bulk oxide with higher percent tetragonality, which may correspond to the "relaxed-tetragonal" phase. It has been shown that this other tetragonal phase stabilizes in the bulk of the oxide via sub-stoichiometry, absent of compressive stress supporting its formation. However, in the case of a few of the tetragonal-rich regions in the bulk of the oxide, a notable correlation between high tetragonality and compressive stress is seen. Looking at the SEM image showing the

collected Raman map (Figure 7.3c), these regions appear to be near a large horizontal crack, along with highly porous oxide.

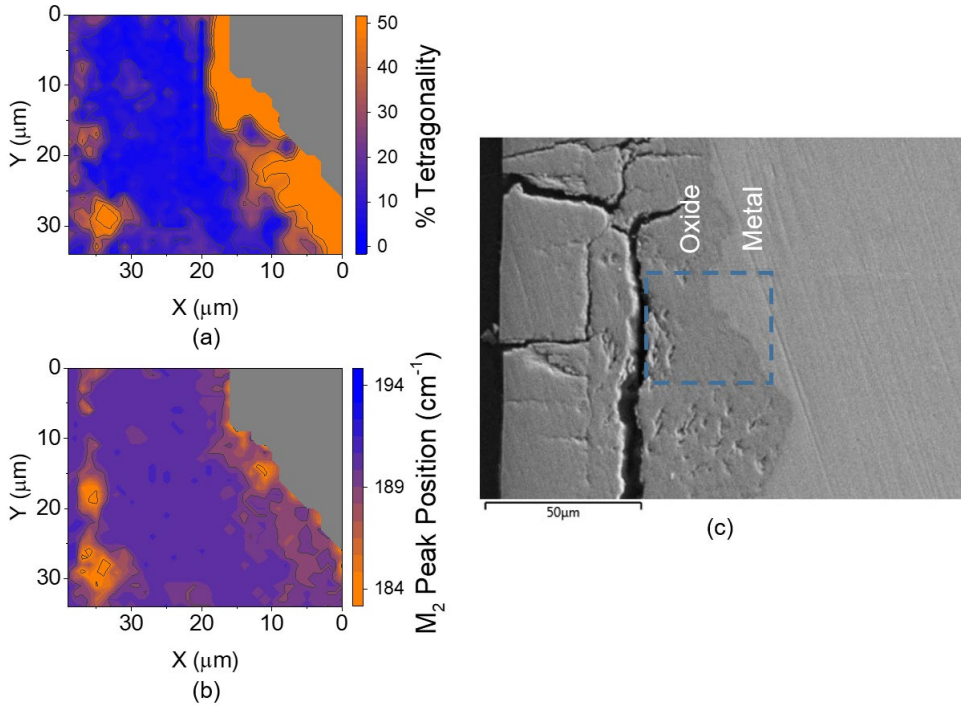

Figure 7.3. Raman mapping results for sectioned sample of oxidized Zr. (a) Percent tetragonality and (b) monoclinic (M_2) peak position maps. (c) SEM image with area where Raman mapping was performed.

A particular region in the bottom left of the Raman map in Figure 7.4 was further investigated to determine the reason for high compressive stress in the bulk of the oxide. Considering the spectra along the line in Figure 7.4, a few observations can be made. The spectra that have lower monoclinic peak position and tetragonal-rich peaks are noted in Figure 7.4c. A majority of spectra with high compressive stress (i.e., low monoclinic peak position) correlate with the presence of tetragonal-rich phase. Two spectra contradict this correlation at X =30 μm and 38 μm. For the former, the tetragonal peak is near 265 cm^{-1}, which is different than tetragonal peak positions seen in the other spectra (275−285 cm^{-1}). Additionally, there is a lessened presence of compressive stress, as the

monoclinic peak is positioned at a higher wavenumber. These factors correspond with the relaxed-tetragonal phase, where relaxed-tetragonal peak position is lower than peak position of tetragonal phase stabilized by compressive stress [38]. For the X =38 μm spectra, it appears that high compressive stress is present, but no tetragonal peak is observed. This appears to be the transition point from the tetragonal-rich region to monoclinic-rich, even though there is still high compressive stress. These observations support the theory that oxygen sub-stoichiometry must be present with notable compressive stress to stabilize tetragonal phase [38]. For all other spectra with noted tetragonal phase (X=32–37 μm), the location of the tetragonal peaks are at 275–285 cm^{-1}, corresponding with what is typically seen for stress-stabilized tetragonal phase. Additionally, the M_2 peak position for these spectra supports presence of a relative compressive stress with lower peak positions. Therefore, the stabilization of this tetragonal zirconia is driven by both oxygen sub-stoichiometry and compressive stress, much like the tetragonal phase present near the metal/oxide interface. The presence of the large crack close to this zirconia may support the change in stress state and thus stabilization of tetragonal phase.

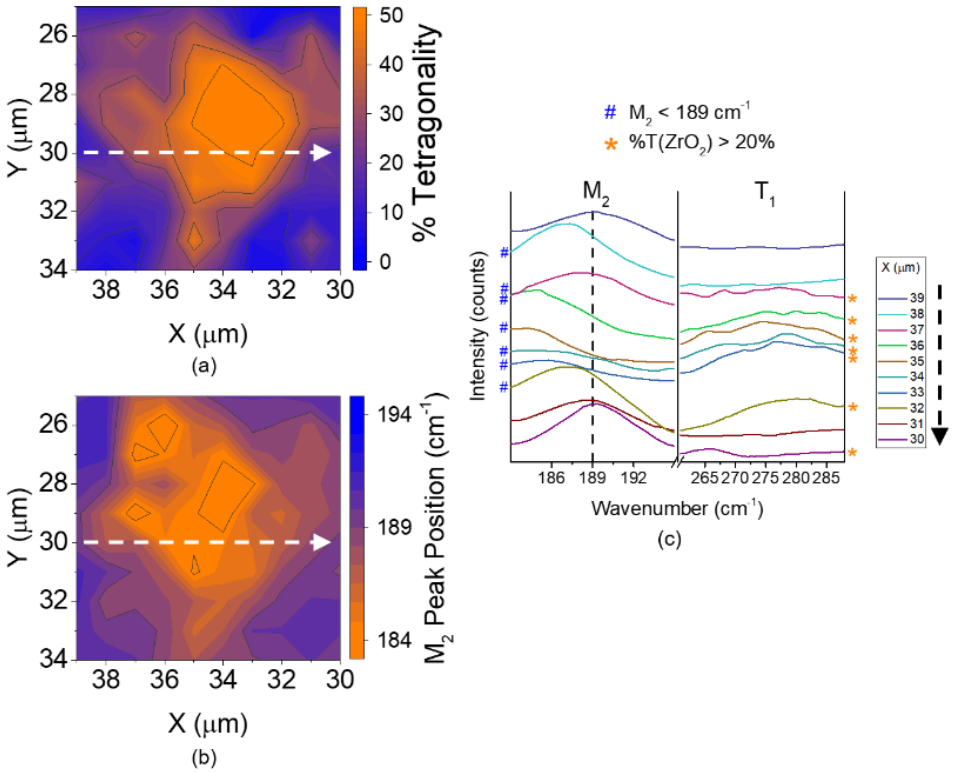

Figure 7.4. (a) Percent tetragonality and (b) monoclinic zirconia (M_2) peak position maps of region within Raman mapped area in Figure 7.3. (c) Raman spectra across dotted line in (a-b), focusing on M_2 and tetragonal zirconia (T_1) peak positions. Spectra labeled with a blue '#' present M_2 peaks corresponding to compressive stress (i.e., notably lower peak position). Spectra labeled with an orange '*' present tetragonal peaks warranting tetragonal-rich spectra via Equation 7.1.

Correlations between the SKPFM and Raman maps were also made. Within the Raman tetragonality map (Figure 7.3a), at the metal/oxide interface there is an area of lower percent tetragonality with similar shape and size to the cathodic particle seen with SKPFM (Figure 7.2b). A closer look at this particle is seen in Figure 7.5. The data acquired via SKPFM (Figure 7.5a), Raman mapping (Figure 7.5b-c), and SEM/EDS, (Figure 7.5d) follow a line that crosses the cathodic particle. Co-localization of X–Y position for each technique was done by aligning the distance from the metal/ oxide interface to other notable features. The Volta potential for the particle is ~600 mV greater than the neighboring metal, displaying relative cathodic nature (Figure 7.5a). This

particle's Volta potential maximum is at the same point as the largest decrease in M_2 peak position, and thus largest relative compressive stress (Figure 7.5c). Additionally, this occurs when percent tetragonality is increasing, but is still below its maximum value (Figure 7.5b). The end of the oxide, where percent tetragonality and M_2 peak position lines abruptly end, is where the particle ends.

Further evidence of either nitride or iron-enrichment for this particle can be seen in Figure 7.6, showing individual Raman spectra across a portion of the noted line scan in Figure 7.5. Spectra nearest the metal/oxide interface (i.e., near X =8 μm) reveal a high relative tetragonal peak around 280 cm^{-1}. As the distance from the metal/oxide interface increases, evidence of a broad peak around the 200−250 cm^{-1} range is seen. The broad peak in this region can help explain why the percent tetragonality map revealed a particle of lower tetragonality with similar shape to the high Volta potential particle. It is likely due to the M_3 monoclinic peak being used to support calculation of percent tetragonality (Equation 7.1). Since the broad peak arises in this spectral range, it is recognized as the 'M_3 peak', when in actuality a different compositional feature is revealed. Further away from the metal/oxide interface, this broad peak is slowly lost (Figure 7.6), and the sharp M_3 peak is revealed (i.e., X=17–19 μm). The broad peak shows similar spectral features as those seen in ZrN, [43] as well as hematite (Fe_2O_3) [246]. For ZrN, a sharp peak is seen in the 230−235 cm^{-1} range, with a broad shoulder to the left to ~170 cm^{-1}. For hematite, the A_{1g} mode at 225 cm^{-1} and its shouldering E_g mode at 247 cm^{-1} are similar to the spectral features of the broad peak. Due to the shape of this broad peaks seen in Figure 7.6, it is reasonable to conclude that the particle is an iron-rich SPP. The shouldering that is visible to the right of the broad peak likely correlates to the E_g mode

of hematite, while ZrN has a shouldering to the left of its peak. In addition, the Fe-rich SPP is likely highly metallic, thus producing Raman spectra with high amounts of noise. The oxidation of cathodic SPPs are slow relative to Zr, thus leaving a heavily metallic particle in an oxidized matrix [27].

For compositional correlation, a line scan of EDS measurements is included (Figure 7.5d). There is no discernable evidence of concentrated iron or nitrogen counts near the metal/oxide interface. A possible reason for this lack of secondary element response may be due to the damage inflicted upon the sample from the 50 mW Raman laser. When laser power is increased, there is a tradeoff between maximizing signal and increasing surface damage. Damage to the sample surface from the Raman laser makes it difficult to resolve particles even a few microns in size with SEM/EDS. Further evidence of this effect can be seen in Figure 7.7, where a Zr pre-breakaway sample correlates high Volta potential particles and iron-rich SPPs. Raman mapping was excluded in the analysis of this sample, thus excluding the possible effect of Raman laser damage prior to SEM/EDS. This provides evidence of SPP formation in the Zr sample, regardless of the low concentration of iron in pure Zr (Table 7.1). Therefore, the absence of iron in the EDS line scan in Figure 7.5d does not restrict iron from being the contributing element to the cathodic behavior of the particle.

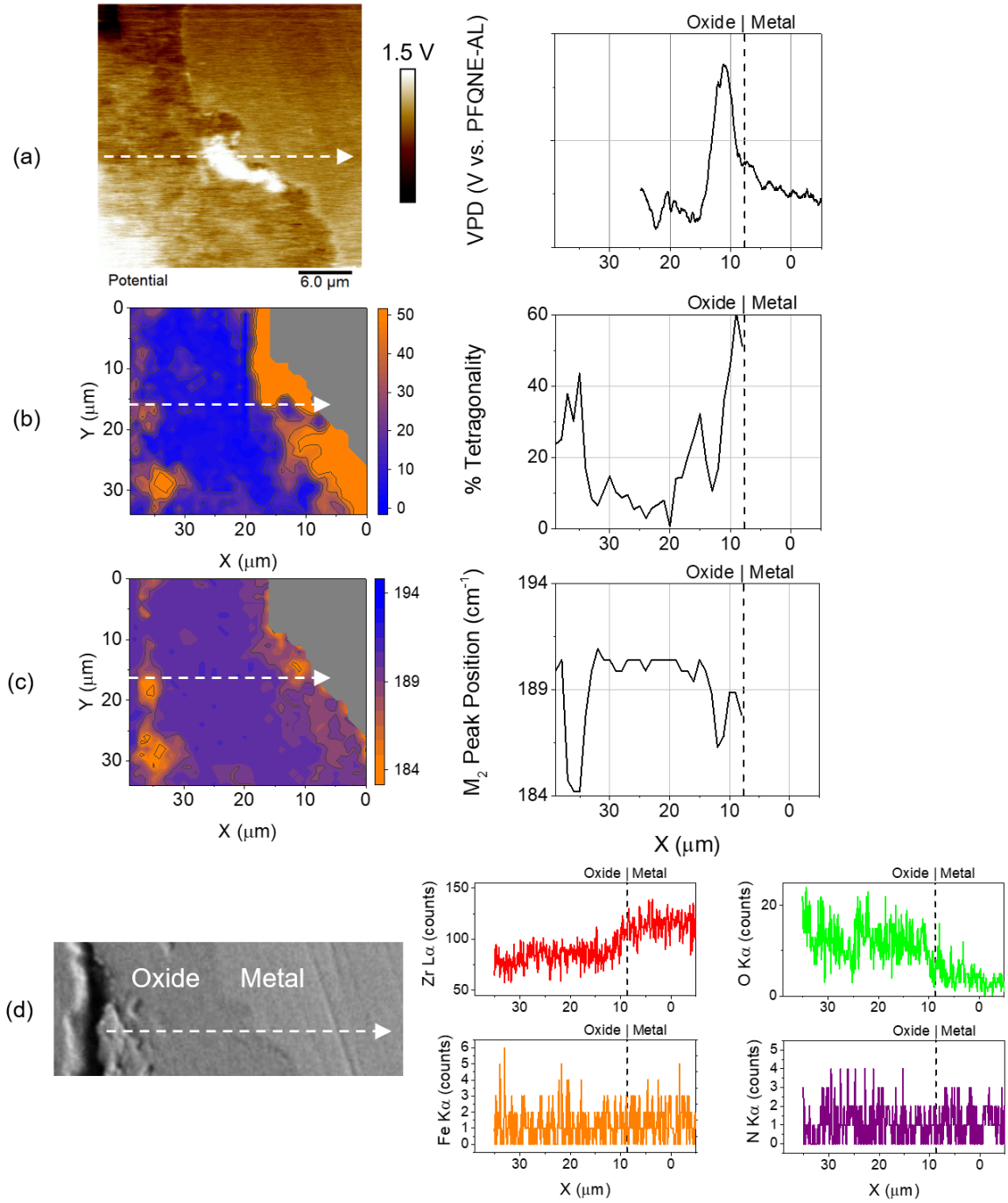

Figure 7.5. Co-localization between (a) SKPFM Volta potential map with VPD line scan of 1 V range, (b) percent tetragonality and (c) M_2 peak position maps with line scans determined via Raman mapping, and (d) SEM image with EDS elemental line scans for a sectioned sample of oxidized Zr.

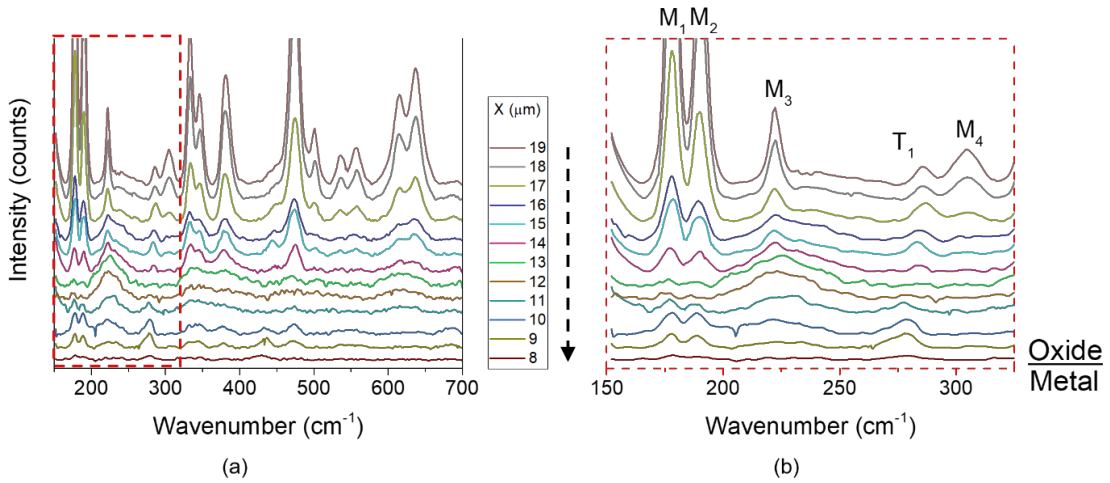

Figure 7.6. (a) Raman spectra for partial distance across the line scan in Figure 7.5. (b) Inset of spectra with monoclinic (M) and tetragonal (T) zirconia peaks noted.

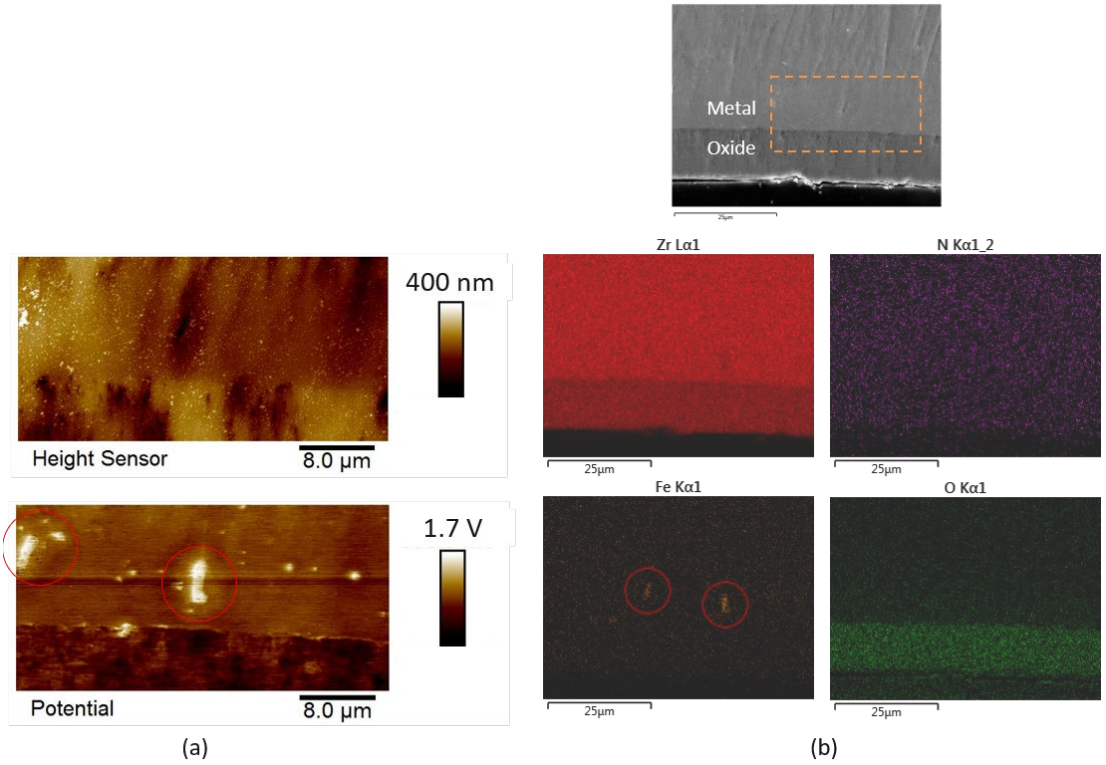

Figure 7.7. Co-localization between (a) height and Volta potential via SKPFM and (b) elemental analysis via SEM/EDS for a sectioned sample of oxidized pure Zr (pre-breakaway). Area where SKPFM was performed is included in SEM image. Red circles in Volta potential and EDS maps present correlations between high VPD regions and Fe-rich particles.

To observe the metal/oxide interface and similarities between features, Figure 7.8 shows co-localized maps with corresponding line scan data plots for each technique. In this case, a direct transition between metal and oxide is seen at X ≈ 8 μm. This occurs where the Raman spectra ends, as well as where a sharp transition in Volta potential is seen. The tetragonal-rich region can be distinguished in the X = 8–20 μm range (Figure 7.8b). A drop in Volta potential is visible in this range, providing evidence that the tetragonal-rich region nearest the metal/oxide interface is relatively anodic versus the metal. In fact, the only region within the captured SKPFM image that shows a higher relative Volta potential is in the bottom left area of the image (Figure 7.8a). This region likely correlates to monoclinic-rich zirconia, while the rest of the zirconia mapped in the SKPFM image is tetragonal-rich, and thus lower in relative Volta potential.

Co-localized SKPFM, Raman mapping, and SEM/EDS was also performed on the sectioned Zr-2.65Nb sample (Figure 7.9). Contrary to Zr, the average Volta potential of the oxide is ~685 mV greater than that of the metal, revealing relative cathodic behavior for the oxide and relative anodic behavior for the metal (Figure 7.9a). The Raman map reveals a tetragonal-rich region at the metal/oxide interface, while the bulk of the oxide is monoclinic-rich (Figure 7.9b). Similarly, compressive stress is seen in the form of lower M_2 peak position for zirconia nearest the metal/oxide interface, while the bulk of the oxide is relatively close to the expected M_2 peak position of 189 cm^{-1} (Figure 7.9c). Looking at the line scans across the metal/oxide interface, correlations between phase content and VPD can be made. A rapid decline in Volta potential is seen at the same position as an increase in percent tetragonality and decrease in M_2 peak position. In the VPD line scan, there is a thin trench that corresponds to the tetragonal-rich zirconia seen

in Figure 7.9b. After this trench, the VPD slightly increases, coordinating to the Zr-2.65Nb metal. This supports the evidence seen from Zr, where tetragonal-rich zirconia has a lower Volta potential than both the monoclinic-rich zirconia and the metal. A clear metal/oxide boundary is seen in the EDS maps. Due to the substitutional mechanism of Nb in zirconium, no SPPs were seen with EDS. Similarly, no discernible particles were seen in the SKPFM or Raman maps.

The tetragonal phase zirconia at the metal/oxide interface has been recognized as a protective barrier, providing a dense layer that limits the oxidation mechanism by diffusion of oxygen anions. The porous monoclinic zirconia layer is theorized to provide an easy pathway for coolant media diffusion through the pores and columnar grain boundaries. Once the corrosive media reaches the tetragonal-rich layer, the small, equiaxed tetragonal grains create an oxidation barrier, forcing transport of oxygen anions via vacancy mechanism to reach the metal and form new oxide. A correlation between tetragonal phase stability and oxygen sub-stoichiometry has already been established [219]. Diffusion resistance of the barrier layer correlates with resistance to charge transfer. Moreover, the lower Volta potential for the tetragonal phase implies that it is in fact more active than the surrounding monoclinic zirconia. Here oxidation is supported by the increased oxygen vacancies near the metal/oxide interface. Oxygen concentration gradients have been seen at the metal/oxide interface prior to the martensitic transition to monoclinic phase. This includes a $Zr(O)_{sat}$ region of a few hundred nanometers at the metal/oxide interface, followed by a shallow sub-stoichiometric region (ZrO_{1-x} to ZrO_{1+x}) prior to the stable ZrO_2 zirconia [27]. This coordinates with the stability of tetragonal phase, where both compressive stress and oxygen sub-stoichiometry support its

formation. The stable monoclinic bulk zirconia has a balanced stoichiometry (ZrO_2), whereas the tetragonal zirconia is substoichiometric (ZrO_{1-x} to ZrO_{1+x}). This establishes a p-n junction between the n-type monoclinic zirconia and the p-type sub-stoichiometric tetragonal zirconia. This junction provides an additional barrier for anion transfer to the metal substrate [247]. In addition, the high concentration of holes in this p-type, tetragonal-rich, sub-stoichiometric region causes a reduction in Volta potential relative to the neighboring metal. This provides further support to the barrier layer theory, where diffusing oxygen anions will need to overcome the p-n junction barrier to progress to the oxide/metal interface.

All metal/oxide parameters discussed are summarized schematically in Figure 7.10. The percent tetragonality, stress, Volta potential, and oxygen concentration are shown for different phases of zirconia and zirconium metal. For the metal, the crystal structure is hexagonal closed packed (HCP), under tensile stress, and has minimum oxygen concentration [20]. Crossing the metal/oxide interface, the p-type tetragonal-rich region of zirconia is shown with small, equiaxed grains, high in percent tetragonality, under high compressive stress, and sub-stoichiometric of oxygen. Further from the metal interface the oxide then undergoes the martensitic phase transformation to an n-type monoclinic zirconia phase, where percent tetragonality is at a minimum, compressive stress is lessened, and the lattice is stoichiometric. Additionally, two small grains of relaxed-tetragonal phase are presented in the bulk of the monoclinic oxide. Here, the percent tetragonality slightly increases and oxygen concentration decreases; however, the stress does not deviate from the rest of the bulk oxide. In this region the oxygen sub-stoichiometry supports stabilization of isolated relaxed-tetragonal phase regions, void of

compressive stress. A theoretical representation of a decrease in Volta potential of relaxed-tetragonal phase is included. Based upon the measured anodic behavior of the interface-tetragonal phase, the relaxed-tetragonal phase should also hold relative anodic coupling to the neighboring monoclinic phase with a higher Volta potential. Future studies are needed to further understand the electronic properties and micro-galvanic interactions between oxide phases, secondary particles, and the metal of degraded zirconium cladding.

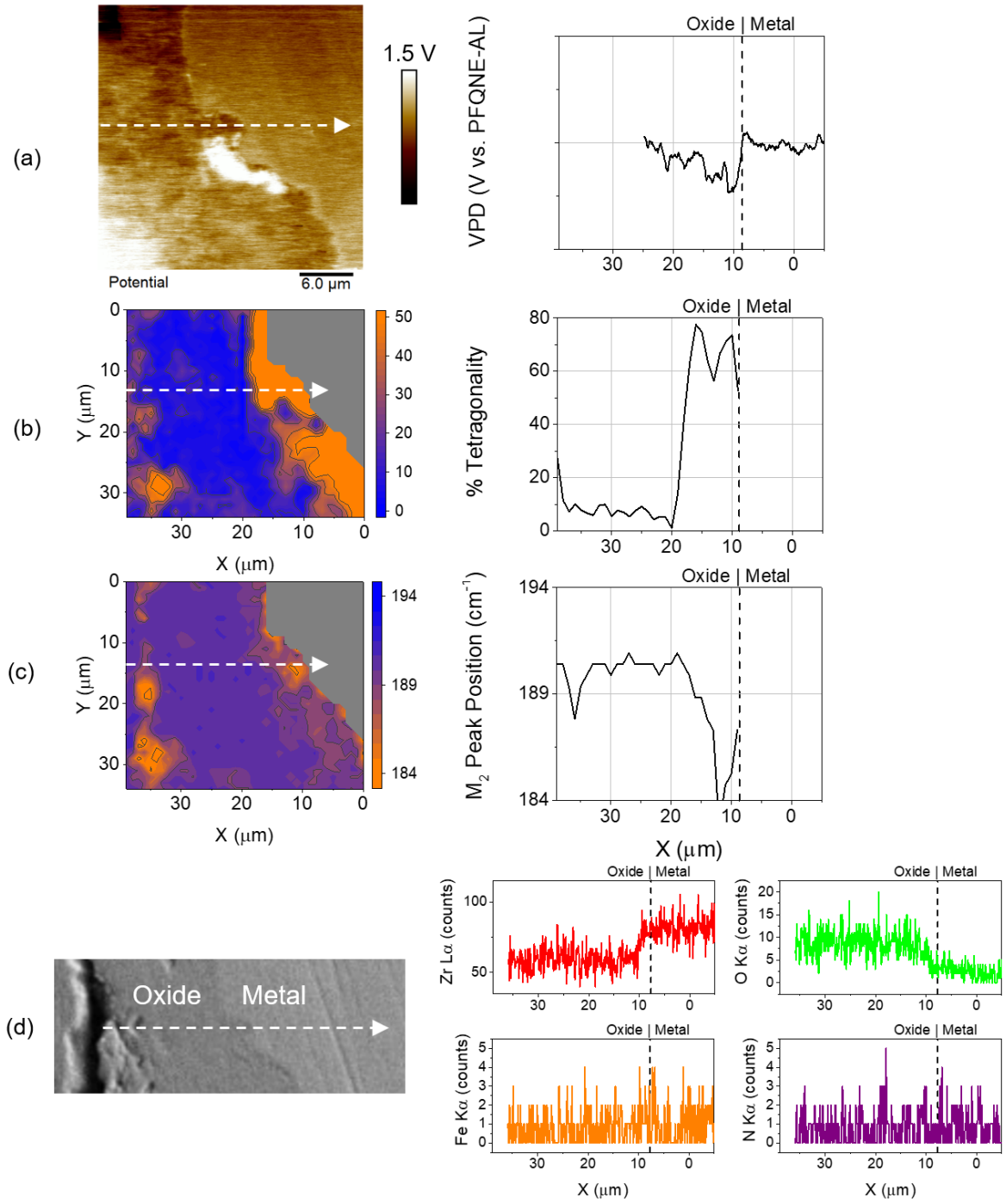

Figure 7.8. Co-localization between (a) SKPFM Volta potential map with VPD line scan of 1 V range, (b) percent tetragonality and (c) M_2 peak position maps with line scans determined via Raman mapping, and (d) SEM image with EDS elemental line scans for a sectioned sample of oxidized Zr.

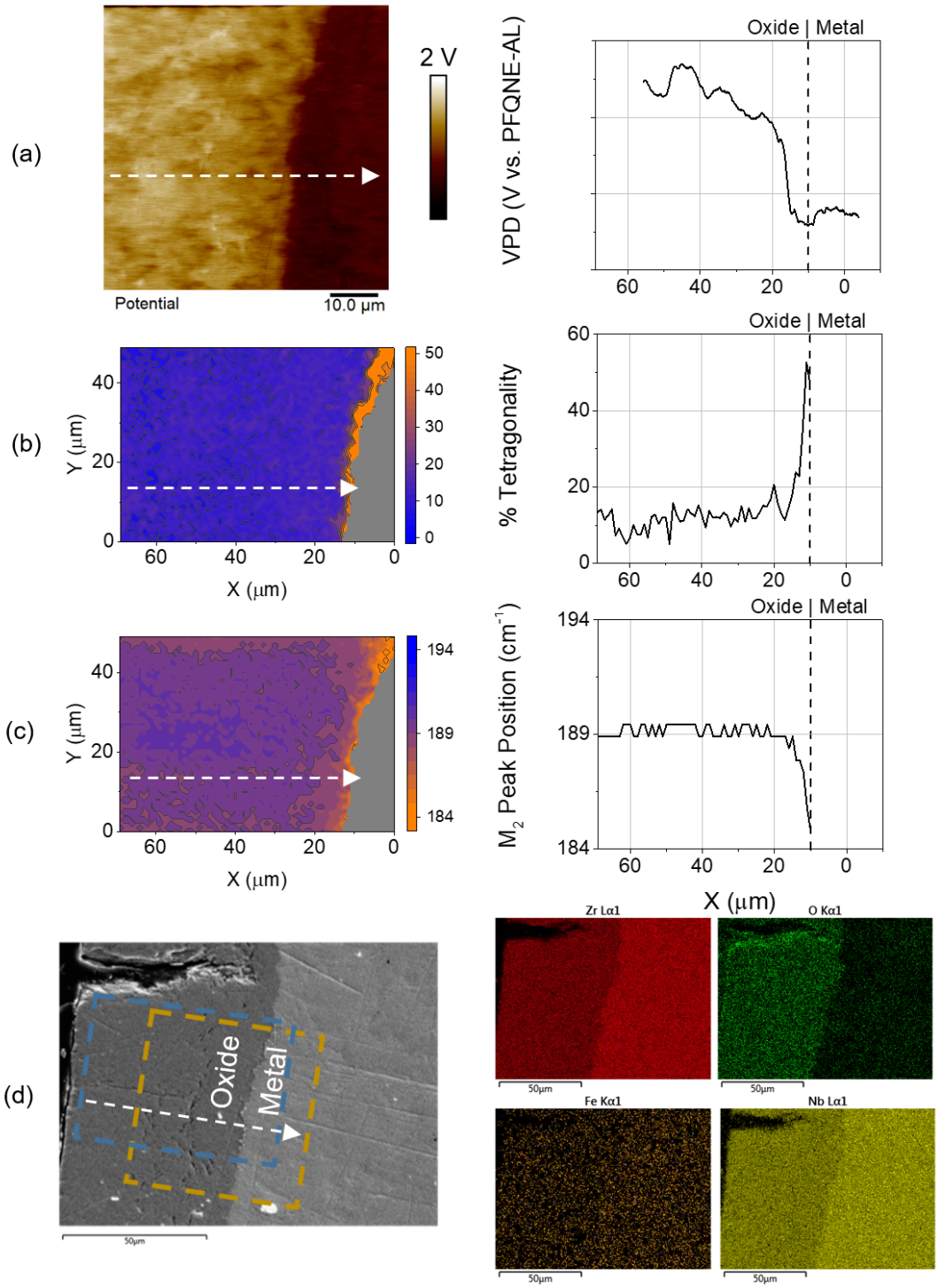

Figure 7.9. Co-localization between (a) SKPFM Volta potential map with VPD line scan of 1.5 V range, (b) percent tetragonality and (c) M_2 peak position maps with line scans determined via Raman mapping, and (d) SEM image with EDS maps for a sectioned sample of oxidized Zr-2.65Nb.

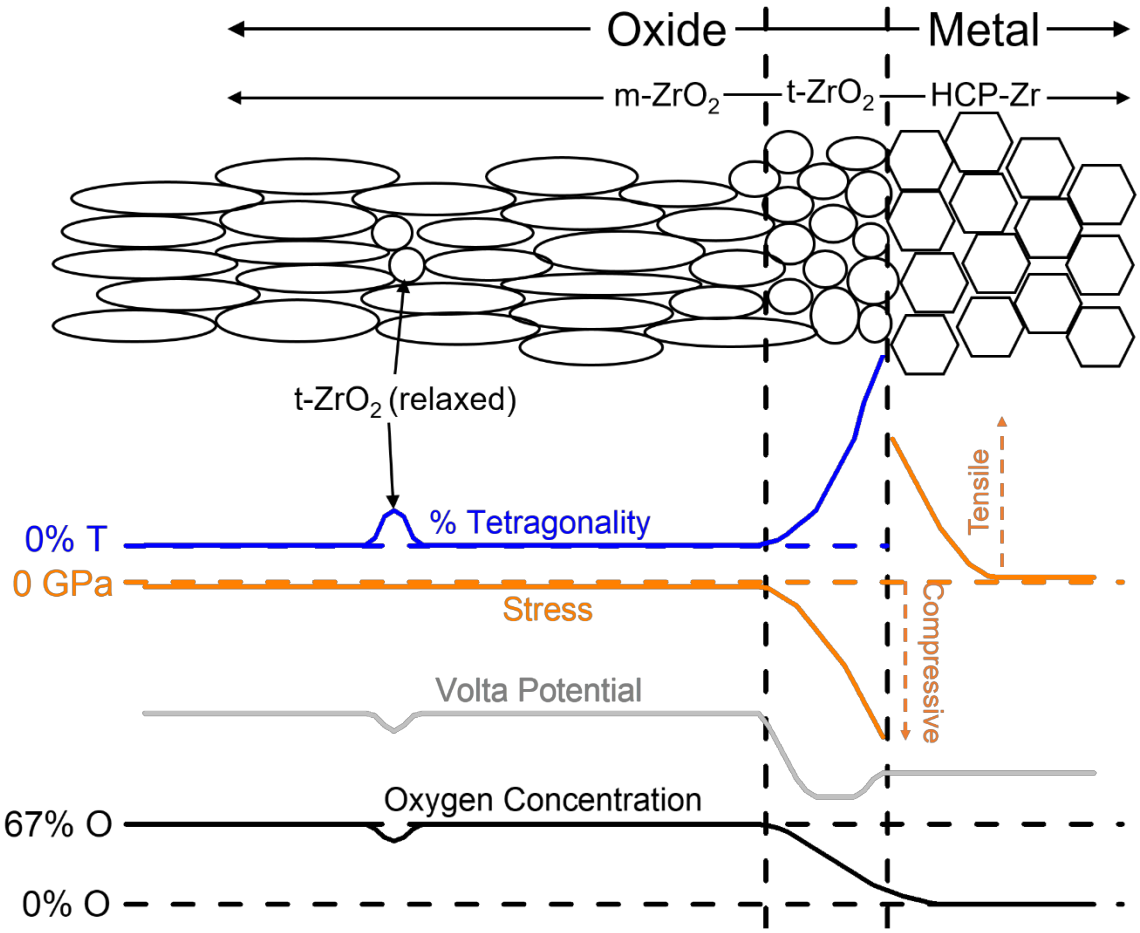

Figure 7.10. Schematic summarizing the different parameters for each zirconia and zirconium phase.

7.4 Conclusions

SKPFM was used to characterize sectioned Zr and Zr-2.65Nb metal/oxide interfaces. SKPFM provided electronic properties for microstructural heterogeneities across these interfaces. For Zr, the average VPD of the oxide near the metal/oxide interface was lower than the average VPD of the metal. A cathodic particle was seen at the metal/ oxide interface in the post-breakaway Zr sample. For all samples (pre- and post-breakaway Zr, as well as post-breakaway Zr-2.65Nb), the oxide nearest the metal was lower in VPD than the metal; for the post-breakaway Zr-2.65Nb, oxide further from this interface was much higher in VPD.

Raman mapping provided phase and stress distributions for post breakaway Zr and Zr-2.65Nb. Tetragonal-rich phase was seen near the metal/oxide interface for both samples. Tetragonal phase near the interface is stabilized from compressive stress and oxygen sub-stoichiometry. The relaxed-tetragonal phase was observed in the bulk of the Zr oxide, while it was not observable in high concentrations in the bulk of the Zr-2.65Nb oxide. The relaxed-tetragonal phase is stabilized by oxygen sub-stoichiometry, voided of compressive stress to support stability. Some of the tetragonal phase seen in the bulk of the Zr oxide had a corresponding compressive stress seen by monoclinic zirconia (M_2) peak shift to lower wavenumbers. Therefore, tetragonal phase stabilized with support from compressive stress was seen in the bulk of the Zr oxide. This stress-induced tetragonal phase seen in the bulk Zr oxide was likely supported by nearby crack propagation, creating new stress tensors in surrounding oxide.

Co-localization of SKPFM, Raman mapping, and SEM/EDS allowed correlation of different oxide and metal characteristics. For Zr, a broad Raman peak in the 200−250 cm^{-1} range spatially correlated to the cathodic particle seen with SKPFM. This particle is likely iron-rich, due to the shouldering direction of the characteristic peak and its correlation to the peaks seen in the Raman spectrum of hematite (Fe_2O_3). Raman laser damage removed the opportunity to observe N and Fe EDS counts to confirm the elemental makeup of the cathodic particle. However, when Raman mapping and related laser damage are omitted, correlations between VPD and elemental makeup of particles can be observed, as confirmed by observation of the pre-breakaway Zr sample. Here, the cathodic secondary particles seen with SKPFM were confirmed as iron-rich with EDS.

For SKPFM/Raman mapping correlations, tetragonal-rich zirconia at the metal/oxide interface correlated to lower VPD than the neighboring zirconium metal and monoclinic zirconia. Raman spectra revealed a thick tetragonal-rich region near the metal/oxide interface, that also had a lower VPD as seen with SKPFM. A small region of higher VPD was seen in the Zr oxide, correlating to the start of the bulk monoclinic-rich zirconia. This was confirmed with co-localized SKPFM and percent tetragonality mapping of the Zr-2.65Nb sample, where a slight drop in VPD seen at the metal/oxide interface correlates to the thin tetragonal-rich zirconia seen with Raman mapping. Therefore, in addition to the barriers produced by the coolant/oxide and oxide/metal interfaces, the establishment of a p-n junction between the tetragonal and monoclinic zirconia provides another required step in the oxidation mechanism of the metal substrate. This supports the theory that the tetragonal-rich layer at the metal/oxide interface is a protective barrier to further oxidation. SKPFM is a useful characterization technique to support the understanding of cladding oxidation mechanisms. This high-resolution, non-destructive technique can be used in the future for hydride detection and growth, oxide stoichiometry and phase distribution, secondary phases' role in cladding oxidation mechanisms, and irradiation effect of the cladding's electronic properties. When combined with complementary characterization techniques, the methods reported establish novel experimental advancements that can provide new insight into cladding degradation processes.

7.5 Acknowledgments

This work was supported in part through the Department of Energy (DOE) In-Pile Instrumentation program under DOE Idaho Operations Office Contract DE-AC07-

05ID14517. The glovebox AFM used for this work was funded through the National Science Foundation Grant No. 1727026 and accessed through the Boise State Surface Science Laboratory. The Hitachi SEM used for this work was supported by the Department of Energy [National Nuclear Security Administration] under Award Number DE-NE0000338. Paul H. Davis of Boise State University is thanked for his support with the Horiba Raman and Bruker AFM systems. The authors also acknowledge the departmental support from Boise State's Micron School of Materials Science and Engineering. The views and opinions of authors expressed herein do not necessarily state or reflect those of the U.S. Government or any agency thereof. The raw/processed data required to reproduce these findings can be shared upon request to corresponding author at coreyefaw@u.boisestate.edu.

CHAPTER 8 – A CLOSED-HOST BI-LAYER DENSE/POROUS SOLID ELECTROLYTE INTERPHASE FOR ENHANCED LITHIUM-METAL ANODE STABILITY

8.1 Introduction

The drastic costs of global warming, both environmentally and economically, are driving the necessity to diminish a dependency on oil and gas for energy applications. Alternative clean energy reliance has been at the forefront of global investment for a more sustainable future. Part of this transitional effort is focused on energy storage via a rechargeable battery. Lithium metal is often considered the "Holy Grail" of rechargeable battery technology, due to its high theoretical capacity (3,860 mAh/g) and low electrochemical potential (-3.04 V vs. SHE), which has the practical capability of achieving a specific energy above 500 Wh/kg when paired with a high-theoretical capacity sulfur or high-voltage Ni-rich $LiNi_{1-y-z}Mn_yCo_zO_2$ (NMC) cathode [62, 66, 248-253].

However, there are key issues that limit the commercialization of rechargeable Li-metal batteries (LMBs), including poor cycling performance or safety concerns from short circuiting. The poor performance of lithium metal arises from its unavoidably heterogeneous surface (Figure 8.1a). The innate variability in mechanical and electrochemical properties of lithium's native film of oxides and carbonates initiates a cascading effect of heterogeneity into the solid-electrolyte interphase (SEI), ending with an uneven electric field and Li^+ flux distribution [254]. The susceptibility of increased Li^+

flux at thermodynamically favorable sites (e.g., dislocations, grain boundaries, crystallographic and topographic heterogeneities, etc.) caused by phenomena such as the "tip effect" [99, 255] leads to dendrite formation, causing rapid failure via short circuiting. Meanwhile, dendrites with high specific surface area spontaneously react with the electrolyte, rendering accumulation of resistive SEI and formation of isolated lithium (i.e., "dead Li") during lithium stripping, thereby driving continuous loss of active material (LAM) at the anode side as well as increased cell impedance [62, 253, 256]. To minimize dendrite growth and LAM, a robust and stable SEI that permits uniform Li^+ flux must be formed on the Li-metal anode.

The ideal SEI should be dense, mechanically and electrochemically stable to hinder side reactions, electronically insulating to prevent lithium deposition on the SEI, ionically conductive to improve diffusion kinetics, and homogeneous to support uniform Li^+ flux and suppress dendrite growth [78, 79, 91, 256, 257]. The spontaneously formed traditional organic-inorganic mixed SEI has poor mechanical strength and loosely formed structure, and thus struggles to tolerate the big volume variation of the electrode during (dis)charging [71, 91]. The inability to control the specific components of the *in situ* formed SEI could cause non-uniform Li^+ flux and ramify deposition, as well as continuously consume active materials, leading to poor reversibility and shortened cycle life.

Rational design of the electrolyte is of great importance to obtain a high-performance SEI. For example, it was observed that the addition of fluoroethylene carbonate (FEC) to a carbonate-based solvent shifted the SEI from a mosaic (i.e., mixed amorphous and crystalline) to a multilayered (i.e., layered amorphous and crystalline)

structure. The variability in crystalline grain distribution has a severe impact on ionic flux distribution [91]. Others have shown that additives such as $LiNO_3$ improve the cyclability of Li||S batteries by forming a stabilized SEI, in addition to lessening the polysulfide shuttling effect [250, 251, 258, 259]. An electrolyte with salt aggregation and limited solvation to Li^+, such as high-concentration electrolytes (HCE) and localized high-concentration electrolytes (LHCE), can increase the salt's reduction potential and render a salt-reduced SEI layer (e.g., inorganic LiF-rich) rather than a solvent-reduced SEI layer (e.g., mixed organic-inorganic) [260-263]. Such salt-driven inorganic SEI, in general, has a lower affinity to lithium than a solvent-driven SEI, and thus can withstand structural damage over repeated volume fluctuations during the cell's lifetime.

Comparing with the *in situ* formed SEI via electrolyte optimization, the composition and structure of a pre-treated artificial SEI on lithium is more controllable. An inorganic SEI (e.g., LiF) is promising due to its wide electrochemical stability window, low solubility, and low adhesion to Li metal [95, 97, 264, 265]. However, a traditional dense inorganic SEI is generally brittle, and cracks appear over cycling due to the non-uniform lithium deposition caused by an unavoidably heterogeneous or non-conformal SEI (Figure 8.1b) [97, 264]. Hence, new methodologies to form a reliable SEI is highly desirable. For example, Mai and co-workers proposed a lithiophilic/lithiophobic gradient interfacial layer design, which can realize gradient Li^+ distribution to increase Li^+ concentration far from the separator side, thus decreasing the risk of short circuit. An underlying lithiophilic ZnO/carbon nanotubes (CNTs) layer stabilized the SEI and simultaneously inhibited dendrite growth, while the upper lithiophobic CNTs layer with a high modulus suppressed mossy dendrites from piercing the separator [83]. Xie et al.

found that controlling the electric field distribution can help to localize Li^+ flux. Coating the side of the separator facing the lithium anode with an electron-conducting functionalized nanocarbon or ultrathin copper film could regulate bidirectional dendrite growth on both separator and anode to avoid short circuit [266]. In addition, the design of hosting lithium inside a mixed ion and electron conductive scaffold or matrix has been extensively utilized [99, 267, 268]. The high specific surface area of the 3-D scaffold decreases the local current density and thus minimizes dendrite formation, based on Sand's formula in the "Space Charge Model" [82, 269]. The resultant host provides confined space to accommodate Li plating/stripping, thus lessening electrode volume changes. However, for the designs mentioned above, lithium is still exposed directly to the electrolyte, and thus parasitic reaction cannot be easily mitigated [82]. Therefore, a closed host is critically important for stabilizing the Li-metal anode.

Accordingly, we propose a closed-host bi-layer SEI structure on lithium metal (Figure 8.1c). The following are our design principles for such an SEI structure. The outer SEI layer should be ionically conductive and relatively dense to mitigate consumption of active materials. Beneath the dense layer, an inorganic-rich and porous structure in contact with lithium metal can help mechanically inhibit SEI fracture, guide Li^+ flux and ensure uniform Li plating/stripping. The porous SEI must at least be ionically conductive and the pores should be interconnected. In this case, the lithium can only be plated at the Li/SEI or current collector/SEI interface, while the electron involved in the redox reaction transports through deposited Li metal. The material of the porous structure should be lithiophobic with high interfacial energy against Li to maintain a stable porous structure over cycling. If the porous material also exhibits electronic

conduction, the interconnectivity is not necessary, and lithium is able to nucleate at the available pore sites in the frame structure. In this work, we demonstrated such a bi-layer SEI structure, consisting of an interconnected, porous LiF-rich artificial SEI and a dense inorganic-rich *in situ* formed SEI, which was verified to improve cycling performance.

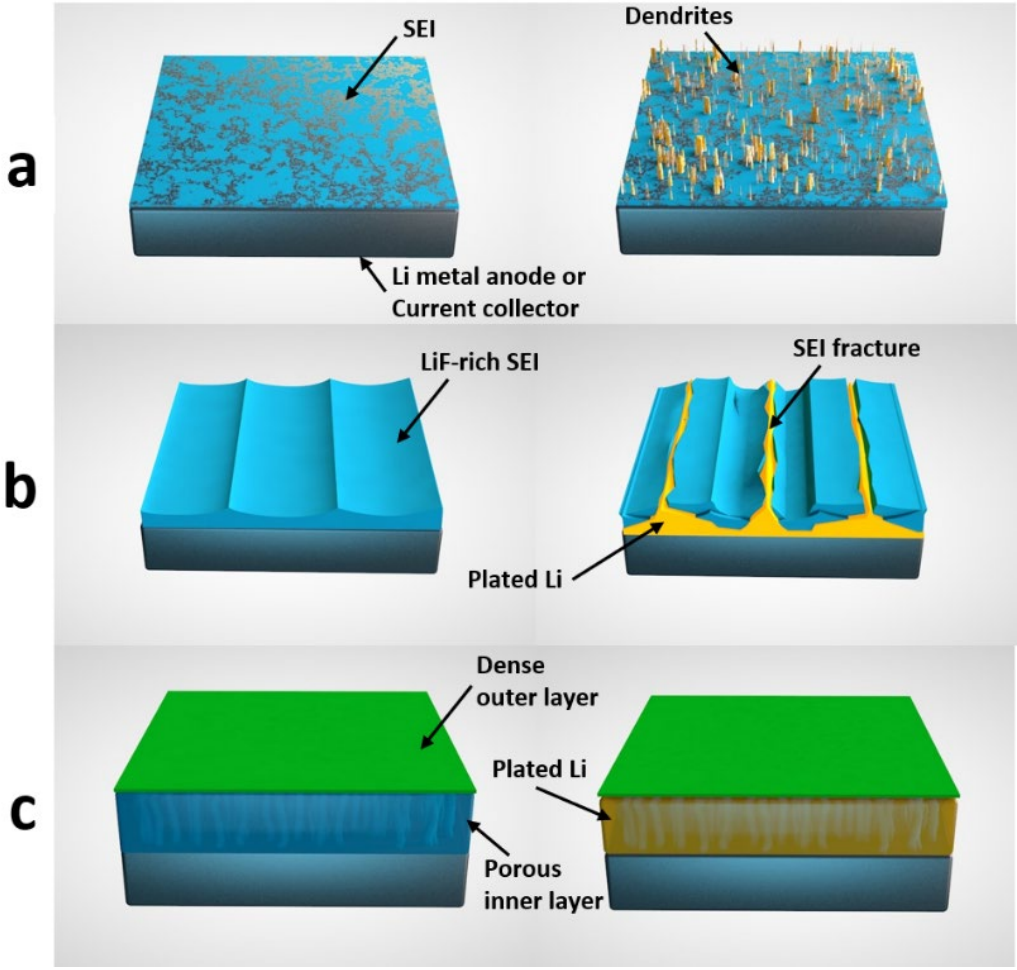

Figure 8.1. Schematic showing the initial structure and failure mechanism for (a) Li-metal and (b) dense LiF artificial SEI, as well as (c) the plating mechanism for a bi-layer dense/porous artificial SEI.

8.2 Materials and methods

8.2.1 Materials Synthesis

Lithium foil (170 μm, MTI Corporation) is punched into ~1.43 cm diameter disks and rolled onto spacers. The samples are then gently polished at two perpendicular

directions for 5 seconds each way to remove native film. A mixed SEI film of LiI and LiF is produced from reaction of polished lithium and a precursor solution. The precursor solution was made by adding 50 mg of polyvinylidene fluoride (PVDF, Sigma-Aldrich, MW~534,000) and 66 mg of iodine (Fisher Scientific) to 10 mL N,N-dimethylformamide (DMF, Sigma-Aldrich). Elementally, this describes the 1:3 I:F ratio solution; varying the amount of iodine in the precursor produces different I:F ratios (22 mg for 1:9 I:F, 40 mg for 1:5 I:F, and 198 mg for 1:1 I:F). Similar deposition of a dense LiF artificial SEI is done by excluding iodine in the precursor solution [79]. The artificial SEI is deposited by placing a ~1.59 cm diameter Celgard® 2325 separator wetted with the precursor solution onto the polished lithium foil for 3-5 seconds [79]. Removal of LiI from the artificial SEI and formation of the porous LiF SEI is done by rinsing the surface with equal parts 1,3-dioxolane (DOL, Sigma-Aldrich) and dimethoxyethane (DME, Sigma-Aldrich) solvent, followed by drying in a glovebox.

8.2.2 Cathode Preparation

The sulfur cathode was produced by mixing 1.28 g sulfur (Fisher Scientific, 99.5%) with 0.52 g super P (EQ-Lib-SuperP, MTI Corporation) conductive agent. This mixture was ball milled and further heat treated at 155°C in an autoclave. 0.2 g PVDF binder mixed in 1-methyl-2-pyrrolidone (NMP, Sigma-Aldrich, ≥99%) solution is added to the S-C mix with an additional 5 g of NMP solvent, mixed with three 5 mm diameter zirconia balls in an ARE-310 Thinky Mixer for 5 minutes, resulting in 64% active mass. The slurry was rolled onto a 20 μm carbon-coated Al current collector (MTI Corporation) and dried in a furnace with dry air flow at 80°C for three days. The resultant electrode has 3 mg/cm^2 of active sulfur weight with a porosity of 80-90%. The practical capacity for

1C of this sulfur is defined as 1000 mA/g (i.e., 3 mAh/cm^2). $LiFePO_4$ (LFP) cathode was purchased from BASF. An active mass of 85 wt.% is confirmed, with inclusion of 7.5% PVDF binder and 7.5% carbon black. Practical capacity of LFP is defined as 2.4 mAh/cm^2, with a mass loading of 13.97 mg/cm^2 (~172 mA/g). Both cathodes were punched into 1.27 cm diameter disks and dried in vacuum prior to loading into glovebox for cell construction.

8.2.3 Electrochemical Measurements

Galvanostatic cycling of symmetric coin cells was done with a MACCOR Model 2200 (Maccor, Inc.). 32 µL of 1M lithium bis(trifluoromethanesulfonyl)imide (LiTFSI, BASF) and 2 wt.% of lithium nitrate ($LiNO_3$, Sigma-Aldrich) mixed in 1:1 DOL:DME was used as the electrolyte in each symmetric cell. $LiNO_3$ was also excluded from symmetric cells to observe the effect of the additive on the formation of the bi-layer SEI structure.

Galvanostatic cycling of Li||S was done between 1.8 and 2.6 V operating at a C/5 rate following two C/20 formation cycles, with an electrolyte to sulfur ratio of 10 µL/mg. For Li||LFP, cycling was done between 2.5 and 4.2 V operating at C/2 rate following three C/5 formation cycles, with 36 µL electrolyte per cell. Rate performance testing (RPT) of both systems was done at different C-rates (5 cycles per rate), examining cycle durability with a final 10 cycles at C/2 rate. Electrochemical impedance spectroscopy (EIS) was used to analyze impedance spectra for symmetric cells. 10 µA perturbation was used to acquire impedance spectra within a range of 1 MHz - 0.1 Hz. At least 4 coins cells for each condition were repeated. Majority showed similar performance.

8.2.4 Characterization

Different characterization techniques were utilized both after treatments and after cycling. Post-mortem samples were disassembled in a glovebox, rinsed with 1:1 DOL:DME, and dried in vacuum prior to analysis. A PHI-5600 XPS (Physical Electronics) with an Al (Kα) source was used to provide surface analysis, along with an Ar^+ ion gun (2 kV, 1.2 μA) for sputter depth profiling. A FEI Teneo FESEM was used to observe morphology and elemental make-up (via energy dispersive X-ray spectroscopy, EDS). FEI Scios DualBeam FIB-SEM system was used to conduct the cryo-FIB-SEM characterization. All samples were transferred from glovebox to the FIB-SEM chamber with an air-tight transfer holder to minimize air exposure. The sample was cooled to -180℃ with liquid nitrogen using the built-in cooling pipeline to minimize the beam damage to the sample. Gallium ion beam with a voltage of 30 kV, current of 7 nA and dwell time of 100 ns was used to roughly mill down the cross-section of the deposited lithium followed by a cleaning process with ion beam at 1 nA. The SEM images of the cross-section were taken using Everhart-Thornley Detector (ETD) at 5 kV and 0.1 nA. Atomic force microscopy (AFM) techniques were used to acquire maps of nanoscale properties of polished Li. Quantitative nanomechanical mapping (QNM) was used to quantify mechanical properties such as adhesion, modulus, and deformation, calibrated with a nominally 8-nm Sb-doped Si probe (Bruker Corporation). Scanning Kelvin probe force microscopy (SKPFM) provided simultaneous maps of surface topography and electronic properties (i.e., Volta potential difference). This is employed in a dual pass, frequency modulated (FM), PeakForce (PF, Bruker Corporation) method to acquire spatially resolved Volta potentials, operating in a pseudo capacitor-like method at a

constant lift height of 100 nm above the surface. A nominally 5-nm, Si-based probe with an Al-coated cantilever (Bruker Corporation) was used for SKPFM acquisition, calibrated with a relatively inert gold standard for repeatable results [122]. Both techniques were done on a Bruker Dimension Icon AFM equipped with a 64-bit NanoScope V controller, inside an inert glovebox (MBraun, <0.1 ppm O_2 and H_2O).

8.2.5 Computational Details

Large-scale Atomic/Molecular Massively Parallel Simulator (LAMMPS) [270] code was used to perform all molecular dynamics (MD) simulations. Ovito tool was used to perform all atomic trajectory visualization [271]. Further specifics to each simulation are provided below.

8.2.5.1 The Role of DMF to form LiF-rich SEI

The PVDF molecule solvation/de-solvation processes in DMF and N,N-dimethylacetamide (DMA) solvents were investigated, ensued by the examination of the PVDF migration and stabilization near the Li–DMF and Li–DMA interfaces. A stabilized PVDF near the Li-solvent interface could be beneficial in enhancing Li-PVDF electrochemical interaction, and a formation of the LiF artificial structure.

The initial Li/DMF/PVDF and Li/DMA/PVDF molecular geometry constructions, and the subsequent pcff+ forcefield assignment were performed in the MedeA simulation environment [272]. The pcff+ force field, which comprised of the bond, angle, dihedral, improper, Coulombs, and Lennard-Jones (LJ) 6-9 interactions, was used to model the Li/DMF/PVDF and Li/DMA/PVDF atomic interactions. The pppm algorithm was used to calculate the long-range Coulombic interactions. Lithium-metal was treated as rigid without any atomic charges. A more refined and sophisticated forcefield (e.g., MEAM

[273] or ReaxFF [274]) can be used to obtain a refined simulation result. A canonical (NVT) ensemble with a periodic boundary condition was used with a timestep of 0.1 fs, total simulation time of 1 ns, and frequency of saving the atomic trajectory information every 1 picosecond (ps).

8.2.5.2 The Stability of LiF and LiI Interface

Embedded ion method (EIM) [275] was used to validate the accuracy of the EIM potential to model LiF and LiI phases. Subsequently, a combined LiI-LiF system was investigated in an isobaric-isothermal (NPT) ensemble with periodic conditions at 1 atm and 300 K, with a timestep of 1 fs for a 25 ps length of simulation for individual LiF and LiI phases and 500 ps for the combined LiI-LiF interface with atomic trajectory information collected every 1 ps.

8.2.5.3 Li^+ Transport Energy Barriers

Li-Li interaction in any Li crystal was described by the MEAM force field [273]. The Li-Li, F-F, and Li-F interaction in a LiF crystal, as well as between Li and LiF crystals were all described in a universal force field [276]. Energy barriers of Li^+ transport through bulk LiF, along LiF surface, and between a Li-LiF interface were observed. LiF(001) and Li(001) have the lowest surface energy [277], and thus were chosen to build the Li-LiF interface. A 7x7x7 Li supercell and 6x6x6 LiF supercell were combined to construct the Li(001)-LiF(001) interface, giving only 0.2% mismatch in the lattice parameters. For comparison, a 6x6x12 LiF supercell was produced in an individual simulation. The charge of Li^+ and F^- in LiF were set to ±0.8, according to previous research [278].

8.2.5.4 Stress-Strain Testing

The as built LiF and Li-LiF simulation cells were first ran in an NPT ensemble for 500 ps for equilibration. The equilibrated density of LiF is 2.52 g/cm^3, which is close to experimental data. After that, the equilibrated structures were put into a tensile testing simulation. Stretch strain was performed under a constant strain rate of 0.05 ps^{-1} until strain reached 20%. The compression strain of the other two directions were applied according to a Poisson's ratio of 0.326 [279].

8.3 Results and Discussion

A proof-of-concept closed-host bi-layer dense/porous SEI on Li-metal anode surface was demonstrated in this work. LiF was selected for the porous frame structure, due to its wide electrochemical stability window against Li, low solubility in electrolytes, and superior mechanical properties [78, 79, 95, 97, 259, 264, 265]. In addition, LiF has a high interfacial energy against Li (i.e., lithiophobic), which can suppress dendrite nucleation and growth inside LiF, based on the Butler-Volmer model [59, 97, 253]. Nevertheless, the biggest issue for LiF as SEI is its low ionic conductivity, but Li ion transport along Li/LiF interfaces can be greatly enhanced, which will be discussed later. As mentioned in the introduction, the LiF-rich pores should be interconnected, as LiF is electronically insulating. Here, through a simple method of producing a mixed LiI-LiF surface composite by reaction of polished lithium metal with a precursor solution of polyvinylidene fluoride (PVDF) and iodine (I_2) dissolved in N,N-dimethylformamide (DMF) [79], followed by a solvent rinse (equal parts 1,3-dioxolane, DOL and dimethoxyethane, DME) to dissolve the LiI, a porous LiF-rich artificial SEI structure is produced. Comparing with dimethylacetamide (DMA), DMF as the precursor solvent

was found to promote the reaction between PVDF and Li-metal, since a stabilized PVDF near the Li–solvent interface could be beneficial in an enhancement of the Li–PVDF electrochemical interaction and stabilization of the artificial LiF SEI structure. The DMF solvent is vital for promoting the initial reaction, as evidenced by a molecular dynamics (MD) simulation where PVDF mobility in DMF is superior when compared to PVDF in DMA (See details in Figure S8.1).

Figure 8.2 presents the surface and cross-sectional morphology, as well as X-ray photoelectron spectroscopy (XPS) of the resultant LiI-LiF composite. As is displayed in XPS results, LiF and LiI are successfully formed. These peaks remain as a function of depth, suggesting relatively uniform distribution throughout the ~ 4 μm thick composite, although a small number of pores were still observed in its cross-section, due to slight dissolution of formed LiI in the DMF solvent. Seen with EDS mapping, there is an intermingling of iodine and fluorine (Figure S8.2f). According to MD simulation, intermixing of LiI and LiF does not occur, confirming LiI-LiF interfaces present within the composite (Figure S8.3e). LiI phase easily dissolves into DOL:DME solvent, leaving behind a porous LiF-rich artificial SEI structure (Figure 8.2e-h). XPS depth profiling confirms the absence of LiI after rinsing, while LiF is retained throughout the artificial SEI. The absence of LiI along the depth direction implies that interconnected pores are constructed, which is a must for an electronically insulating LiF-rich structure. The interconnectedness of the SEI allows Li plating and stripping in the pores and electronic transportation through the plated Li. The resultant porous artificial SEI is ~4-5 μm thick with an interconnected network of pores varying in size, ranging 100s of nanometers. For comparison, exclusion of I_2 in the precursor solution results in formation of a denser LiF-

rich SEI layer with a thickness of less than 1 μm (Figure S8.2b, Figure S8.4). The dissolution of LiI from DMF during the initial reaction, led to available Li sites for further reaction, resulting in subsequently thicker LiI-LiF composite layer or porous LiF artificial SEI.

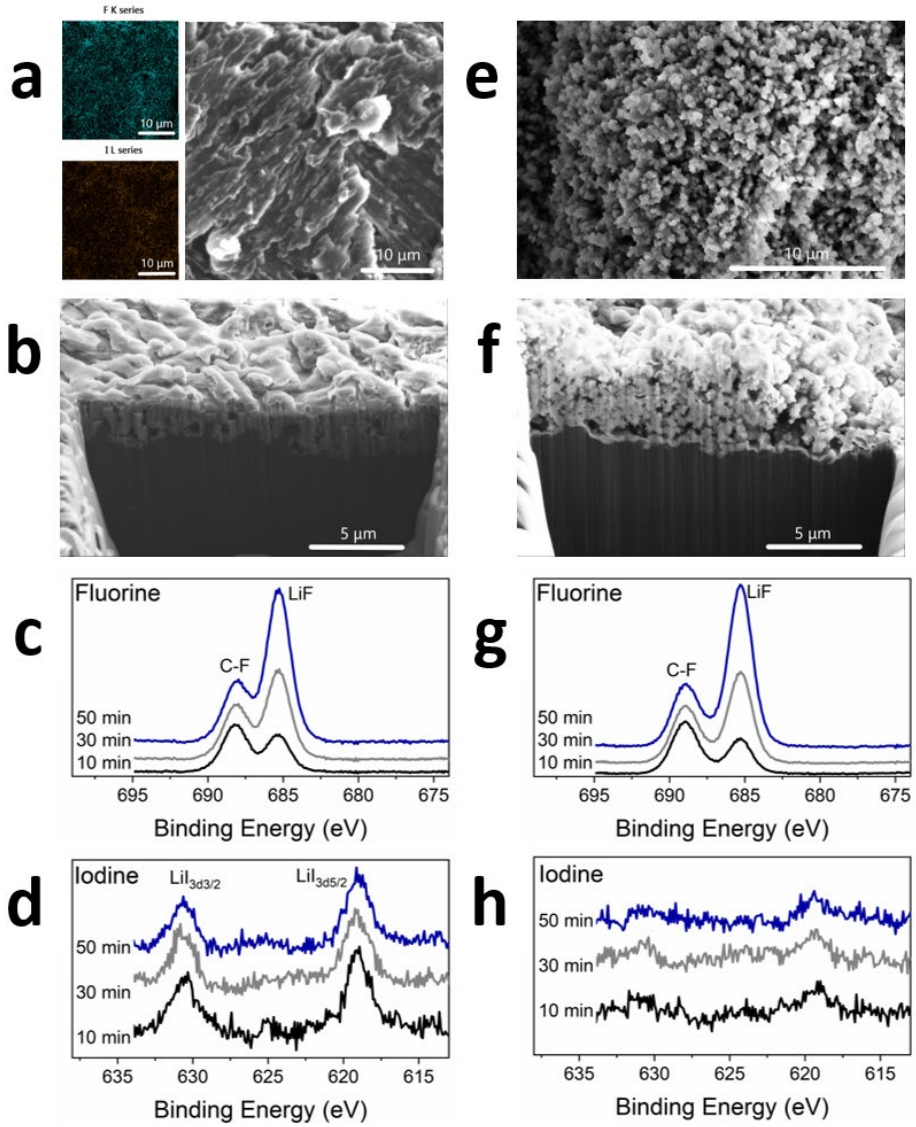

Figure 8.2. (a) FESEM and EDS, (b) cross-sectional cryo-FIB-SEM, (c) fluorine and (d) iodine XPS depth profile of the mixed LiI-LiF composite film. (e) Surface and (f) cross-sectional cryo-FIB-SEM, (g) fluorine and (h) iodine XPS depth profile of the porous LiF artificial SEI after rinse with DOL:DME.

The open-frame porous structure is not designed to restrict parasitic side reactions between lithium and the electrolyte, therefore a relatively dense SEI layer should be formed either ex-situ or *in situ* on top of the porous structure to realize the design of a closed host (Figure 8.3a). The top dense SEI layer prefers to be *in situ* formed; otherwise, the bottom porous structure would be easily destroyed (e.g. pores being filled) by ex-situ process, such as physical vapor deposition, chemical vapor deposition and so on. In this work, the approach of an *in situ* SEI was adopted by reaction with an additive in the electrolyte, such as FEC in carbonate-based solvents [280-284] or $LiNO_3$ in ether-based solvents [250, 258, 259]. Additives such as these have shown to form a passive inorganic-rich SEI layer to protect the Li-metal anode. Further, the material of open-frame porous structure prefers to be electrically insulating (e.g. LiF-rich) rather than traditional mixed ion and electron conductive (e.g. carbon-based). Otherwise, lithium will nucleate at the available pore sites in the mixed-conductive frame structure and SEI will be *in situ* formed anywhere within the pores, rather than only on the top of porous structure. Since optimizing electrolyte additives is not the focus of this work, 2 wt.% $LiNO_3$ was used in addition to 1M lithium bis(trifluoromethanesulfonyl)imide (LiTFSI) in a 1:1 DOL:DME ether-based electrolyte as an example to demonstrate the closed-host bi-layer design.

The electrochemical testing of symmetric cells, assembled as Li||Li, LiF||LiF and porous LiF||porous LiF was conducted with different current densities and areal capacities (Figure 8.3b-c and Figure S8.5). Figure 8.3d shows the corresponding evolution of different anode surface morphologies over cycling, which were characterized with Field Emission-Scanning Electron Microscope (FESEM). The

presence of chemical and topographic heterogeneities (Figure S8.2a, Figure S8.6, Figure S8.7) drives the growth of dendrites on polished lithium metal (Figure 8.3d). Correspondingly, evidence of dendrite growth is clearly seen in the symmetric cell voltage profile as a "soft" short circuit (after 31 and 9 cycles, respectively to Figure 8.3b-c), where an aggregate of lithium dendrites press into the separator but don't penetrate to make contact with the opposite electrode [285]. This is also evident at higher current densities (Figure S8.5).

When a dense LiF-rich artificial SEI is formed on the polished lithium, susceptibility to dendrite growth is reduced, if not completely removed. Rather, the failure mechanism shifts to continuous Li loss. Evidenced with post-mortem FESEM analysis, the surface morphology shifts from granular for polished lithium to a single component-like structure for LiF in the early cycles, suggesting lithium growth under the insulating SEI layer and early stability (Figure 8.3d). As cycling continues, the large volume fluctuations during Li plating/stripping and non-uniform Li^+ flux leads to high local stress and fracture of the dense LiF-based SEI, surfacing fresh sites for new SEI to form via consumption of lithium and electrolyte. Over time, this consumption leads to a more resistant ionic pathway, resulting in the increased overpotential as cycling progresses (Figure 8.3b-c and Figure S8.5). With the chemical treatment described here, as well as by others [79], the retention of native species can still be present (Figure S8.2c), causing non-uniform Li^+ flux and susceptibility to SEI fracture. The removal of native species in the interphase and formation of a conformal SEI is very challenging to accomplish.

However, a porous SEI structure directly in contact with lithium can minimize the influence of native species. As shown in Figure 8.3d, the post-mortem analysis reveals a relatively uniform surface without dendrites or cracking over extended cycles. A dense, uniform SEI is present as a bi-layer, where an *in situ* SEI forms over the top of the porous artificial SEI, stabilizing the closed-host design and drastically reducing active consumption of underlying lithium. That agrees well with much improved symmetric cell cyclability, as minimal voltage hysteresis is maintained when compared to the dense LiF artificial SEI (Figure 8.3b-c and Figure S8.5).

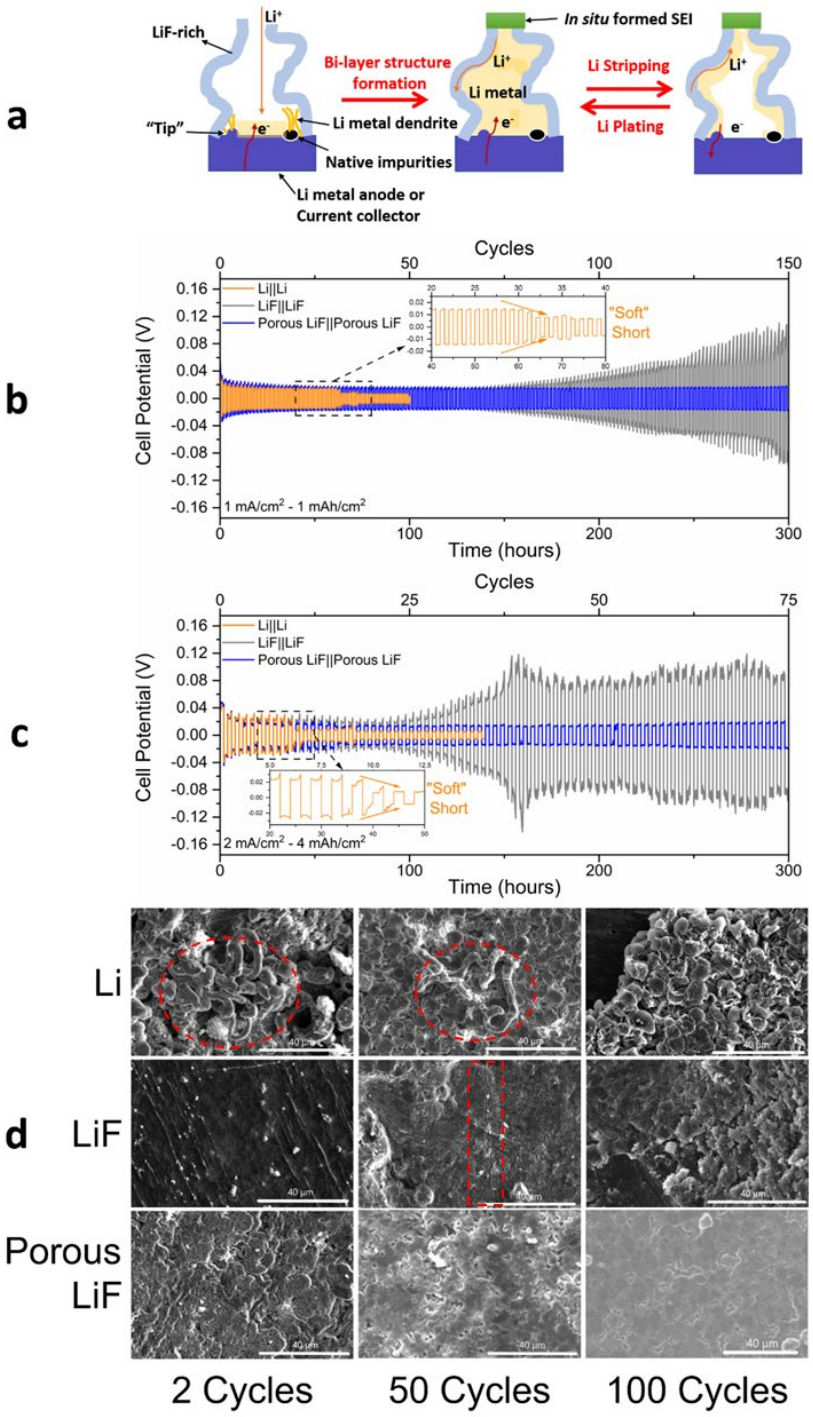

Figure 8.3. (a) Schematic showing the development and retention of the bi-layer SEI structure. (b-c) Symmetric cell cycling of different anode treatments at (b) low (1 mA/cm^2, 1 mAh/cm^2) and (c) high (2 mA/cm^2, 4 mAh/cm^2) current density and areal capacity, with (d) post-mortem FESEM of 1 mAh/cm^2 lithiated electrodes at increasing cycles.

The underlying mechanisms resulting in the longer lifespan based on a bi-layer SEI structure was deeply investigated (Figure 8.3a). The dendritic growth driven by the presence of chemical or topographical heterogeneities can be suppressed in a process of lithium metal percolating through the tortuous and interconnected pores. The pore walls will not be penetrated or damaged, retaining the interconnected porous structure, due to high interfacial energy between LiF and Li [265, 286]. As metallic lithium grows through the pores during the plating process, the exposed upper region of the plated Li metal in the porous structure is consumed via reaction with electrolyte, forming a relatively dense, inorganic-rich protective SEI layer, drastically reducing continuous reaction between Li and electrolyte. The top SEI layer has no native species and is relatively homogeneous, which would benefit uniform Li^+ flux. As cycling continues, the pathway for fast Li^+ transport is through the interconnected LiF|Li interfaces (Figure 8.3a), as evidenced with MD simulations (Figure 8.4a-b). Here, the LiF|Li interface has a drastically lower energy barrier for Li^+ transport (0.60 eV) when compared to ionic transport through bulk LiF (1.30 eV) and along LiF surface (1.23 eV). Therefore, the increased thickness of the porous LiF layer (Figure 8.2f) compared to the dense LiF layer (Figure S8.4b) should not cause a drastic increase in impedance, as LiF|Li interface is more ionically conductive, which agrees well with rate performances of full cell and will be discussed later. Additionally, the porous structure provides more interfaces between SEI and plated Li, where plating and stripping takes place, thus reducing the local volume fluctuations. Upon the pores being filled, the resultant composite of brittle LiF and ductile Li can further resist SEI cracking. As for the Li/LiF interface in Figure 8.4c, there are two sudden drops in stress at 9% and 17.5% strain. However, no obvious sudden drops in the

curve of potential energy vs. strain and the well-maintained atomic structure at 15% strain differ from the pure LiF crystal with visible structural fracturing (Figure 8.4d). The orientation of LiF and Li is visibly shifted while under 15% strain, which caused the drop in stress. Accordingly, the porous LiF structure, supplying improved Li/LiF interfaces when lithiated, undergoes a reorientation when under strain rather than fracture like pure LiF, therefore lessening the issue of SEI fracture.

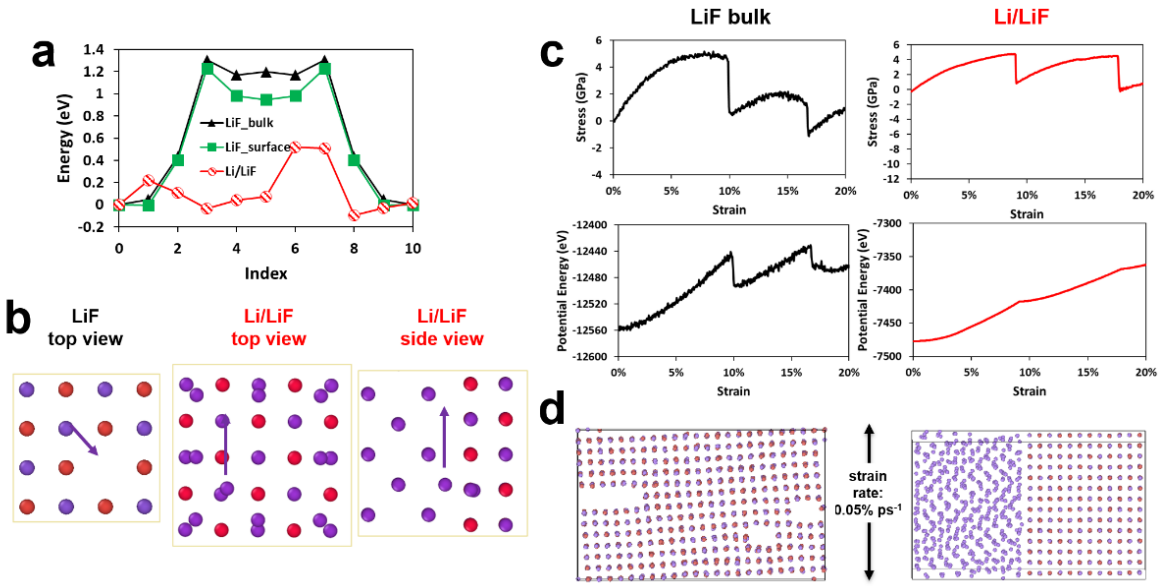

Figure 8.4. (a) MD energy barrier simulation of Li^+ through bulk LiF, the surface of LiF, and along a Li/LiF interface, with (b) LiF crystal and Li/LiF interface pathway schematics. (c) MD stress-strain simulation of (left) LiF crystal and (right) Li/LiF interface, with (top) stress-strain plot, (middle) potential energy-strain plot, and (d) crystal structure at 15% strain. Li and F atoms are shown as purple and red in (b) and (d), respectively.

Of note, the interconnected pore structure and closed-host design both play an important role and are indispensable. For the closed-host, $LiNO_3$ stabilizes the *in situ* formed SEI through oxidation of sulfur species. This has been confirmed by previous work [250, 258], as it has in this work. Electrodes observed post-mortem with XPS revealed a decrease in the amount of polysulfides (Li_2S_x) while increasing the higher

oxidation states of sulfur (Li_xSO_y) when $LiNO_3$ is included (Figure S8.8). These polysulfides can play a role even when sulfur cathode is excluded from the cell, where they are obtainable by the decomposition of LiTFSI salt in the electrolyte. The combination of LiTFSI and $LiNO_3$ salts is necessary to produce an insoluble, electrically insulating SEI with passive Li_xSO_y species, which can minimize further reaction between Li metal and electrolyte [250, 258]. This prompts that focus should not only be placed on producing a feasible porous artificial SEI, but also in choosing an optimal electrolyte chemistry to form a stable *in situ* SEI layer. In this case, the use of $LiNO_3$ supported the formation of a stable bi-layer structure, consisting of a porous LiF-rich inner layer and a dense *in situ* formed outer layer.

When there is no $LiNO_3$ in the electrolyte (i.e., 1M LiTFSI in 1:1 DOL:DME), an unstable, porous SEI with more polysulfides will be formed (Figure S8.8b), which influences the instability of the bi-layer structure, as observed with symmetric cell cycling (Figure 8.5a). Regardless of anode treatment (polished Li, dense LiF artificial SEI, porous LiF artificial SEI), the absence of $LiNO_3$ leads to ultimate failure of symmetric cell via increasing cell resistance, suggesting the formation of dead Li or severe SEI build-up. However, after 150 cycles, the porous LiF symmetric cell exhibits lower voltage hysteresis (200 mV) than the other anode treatments (455 mV for polished Li, 420 mV for dense LiF). Also, consistent with the cycling performances, post-mortem FESEM reveals less mossy Li, as well as less surface fracture over cycling for the porous LiF treatment (Figure S8.9). This suggests that the porous structure promotes a more uniform deposition of Li at the early stage of growth, thus lessening internal cell resistance at later cycles comparatively to dense LiF or polished Li. However, the closed-

host design is not accomplished when $LiNO_3$ in removed from the electrolyte, thus allowing consumption of active materials to occur.

The porous LiF anode treatment was further observed with cryo-FIB-SEM after a single 1 mAh/cm^2 lithiation, where $LiNO_3$ was included or excluded from the symmetric cell (Figure 8.5b-e). Assuming uniform Li^+ flux, the 1 mAh/cm^2 capacity would result in ~5 μm of plated lithium. The thickness of the porous SEI is nearly 5 μm, which means the growth of metallic lithium will inevitably penetrate the porous layer, plating some under the porous layer. Continuous parasitic reaction will happen if there is no protection of a stable, electrically insulating top SEI layer. The porous LiF electrode without $LiNO_3$ formed an extremely porous, thick SEI after lithiation, where a large amount of lithium was consumed, which is consistent with the presence of polysulfides confirmed with XPS depth profiling (Figure S8.8a-b). When $LiNO_3$ is included, the resulting SEI after lithiation is incredibly compact (Figure 8.5c). The pores of the artificial SEI appear to be filled with plated lithium. After subsequent delithiation, the porous structure is visibly retained (inset of Figure 8.5c and Figure S8.10a). After further cycling, the *in situ* thin SEI layer was observed with the thickness of ranging 100s of nanometers, which suppresses further Li loss (inset of Figure 8.5c and Figure S8.10b), agreeing well with the absence of polysulfides beneath the SEI layer (Figure S8.8). The stabilization of the bi-layer structure is further supported by collecting EIS spectra as a function of rest without cycling (Figure S8.11) when compared to cells with and without $LiNO_3$ after cycling (Figure 8.5f-g). The Nyquist plots presented are fit with an equivalent circuit consisting of SEI resistance (R_s) and charge-transfer resistance (R_{ct}) in parallel with constant phase elements (CPE), as well as electrolyte resistance (R_e) (Figure 8.5g, inset) [69, 77, 287,

288]. Complete resistance data for equivalent circuit fits is provided in Table S8.1. In the case of resting without cycling, the bi-layer structure has yet to be realized (i.e., open-host), and therefore the SEI resistance continues to increase over time. After cycling and the closed host has formed, a low SEI resistance is maintained (~1.6 Ω at each time interval), while an increase in SEI impedance from 0 to 8 hours resting is seen when $LiNO_3$ is excluded from the electrolyte (52.6 Ω to 67.3 Ω). Additionally, the initial SEI resistance of the symmetric cell without $LiNO_3$ at 0-hour rest is exceptionally greater than the impedance seen for the cell with $LiNO_3$ (52.6 Ω versus 1.6 Ω) due to severe electrolyte loss (side reaction) and SEI build-up after 100 cycles. This reveals that the dense *in situ* SEI formation fulfills the closed-host design. In summary, such a bi-layer structure will allow uniform Li plating/stripping, suppress Li dendrite growth, and minimize parasitic reaction while also reducing the stress placed on SEI and subsequent fracture that plagues the dense LiF artificial SEI.

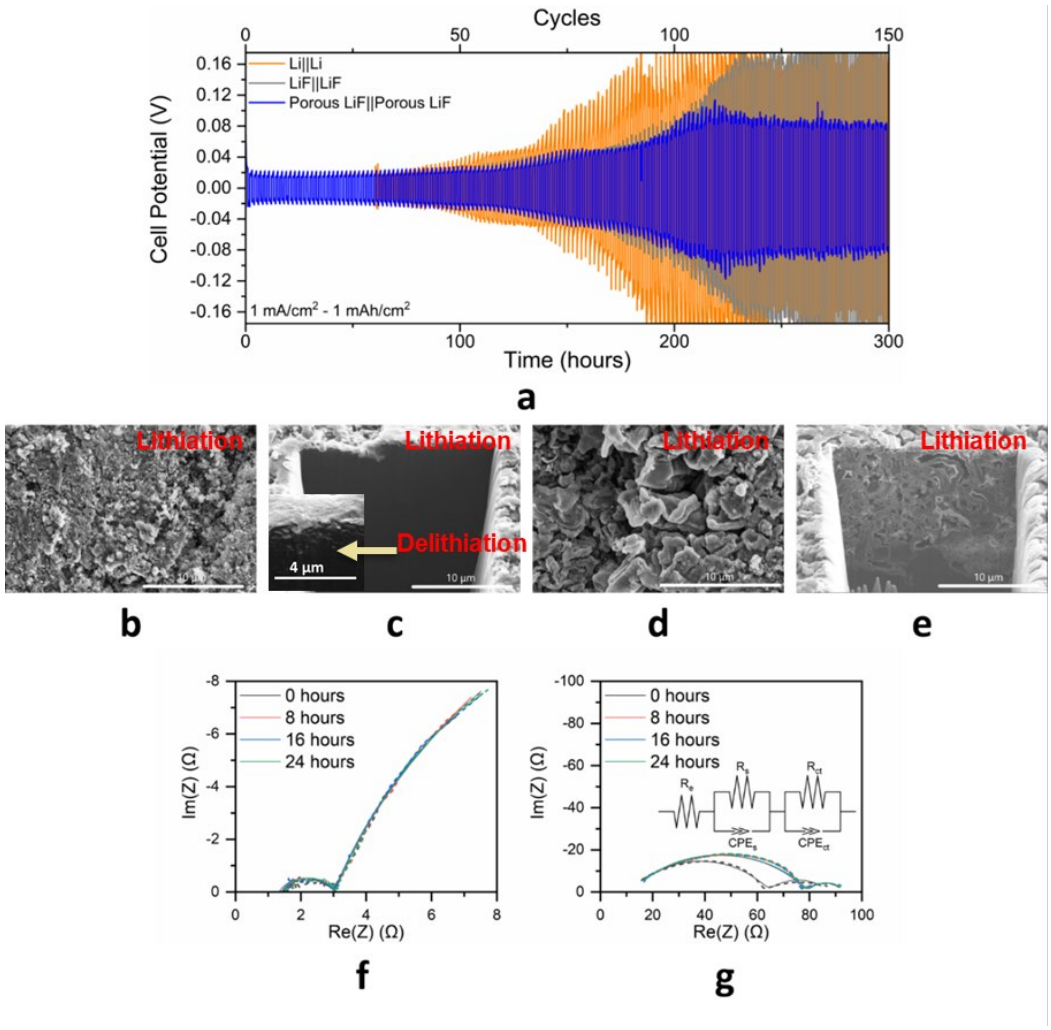

Figure 8.5. (a) Symmetric cell cycling of different anode treatments without $LiNO_3$ in the electrolyte. (b, d) Surface and (c, e) cross-section cryo-FIB-SEM of porous LiF anode after a single lithiation cycle in a symmetric cell (b, c) with $LiNO_3$ and (d, e) without $LiNO_3$. (f-g) The inset in Figure (c) shows cross-section cryo-FIB-SEM of porous LiF anode after delithiation with $LiNO_3$. EIS spectra of porous LiF symmetric cells (f) with $LiNO_3$ and (g) without $LiNO_3$, as a function of time at rest after cycling (>100 cycles), with the equivalent circuit model and fits included (raw data as dashes, equivalent circuit fits as solid lines).

In the approach to make the porous layer, tailoring the amount of I_2 (elemental iodine to fluorine, i.e., I:F ratio) in the precursor solution has an effect on cell performance, likely driven by a direct correlation to the porosity or tortuosity of the artificial SEI (Figure S8.12). The 1:3 I:F ratio was chosen as the optimized concentration in the precursor, showing the lowest stabilized voltage hysteresis under 30 mV, which

ultimately defined the superior SEI porosity or tortuosity to be used in full-cell testing with both sulfur and $LiFePO_4$ (LFP) cathodes.

The improvement of lithium anode with a bi-layer SEI consisting of porous LiF artificial SEI and dense *in situ* SEI is further confirmed with sulfur-based cathode full-cell testing. Cyclic voltammograms maintained similar peak location and intensity with different anode treatments (Figure S8.13a) [289]. For cycling performance, initial formation cycles at a C/20 rate support the construction of the bi-layer structure, being used to stabilize the anode. After the formation cycles, the porous LiF outperformed dense LiF and polished Li anodes, shown in Figure 8.6a-c. With galvanostatic cycling at a C/5 rate (Figure 8.6a), the capacity of the porous LiF cell was maintained above 820 mAh/g after 50 cycles with little to no capacity fading, while the dense LiF and polished Li cells provided lower capacities of 515 and 355 mAh/g, respectively. Along with lower capacities, the dense LiF and polished Li suffered early cycle capacity fade (Figure 8.6b-c). This reveals the enhanced stability of the anode with bi-layer structure that allows increased capacity and capacity retention after 50 cycles. Further evidence of a stable anode is shown with post-mortem FESEM (Figure S8.14), where the anode treated with the bi-layer SEI retained a dense SEI with lower sulfur-content when compared to the polished Li and dense LiF anode. The relatively similar surface morphologies of cathodes before and after cycling also suggests that surface chemistry did not drastically change, thus corresponding to the reduced polysulfide shuttling effect due to stable SEI.

To exclude the shuttling effect on cyclability in Li-S cells, the stable LFP cathode with areal capacity of 2.4 mAh/cm^2 was also used to further exhibit the feasibility of the novel bi-layer porous/dense SEI. After formation cycles at a C/5 rate, galvanostatic

cycling at a C/2 rate revealed extended cycle life due to the construction of the bi-layer SEI structure on the anode surface (Figure 8.6f). Following similar initial formation cycle capacities (~145-150 mAh/g, Figure 8.6g-i), the initial aging capacity for polished Li was drastically lower than the artificial SEI treatments and faded rapidly after ~30 cycles. The cell with bi-layer SEI maintained a capacity of 138 mAh/g with 98.7% CE% and 99.2% of capacity retention as well as a highly compact and uniform surface (Figure S8.15) after 125 cycles. Comparatively, dense LiF had less stable capacity retention, showing fade after ~55 cycles and resulting with a capacity of 95 mAh/g and 60% CE% as well as anode surface fracture (Figure S8.15) after 100 cycles. The full cell testing results are in a good agreement with symmetric cell results.

Further, we found the bi-layer SEI design did not sacrifice rate performance. When observing the charge-discharge curves (Figure 8.6g-i), the polarization (i.e., difference between charge and discharge voltage plateaus) is lower for porous LiF than polished Li and dense LiF. The rate capacities for Li-S and Li-LFP full cells are summarized in Figure 8.6e and j, respectively. Similarly, the cell anode with bi-layer SEI design depicts the highest rate performances. This relates back to the increase in LiF|Li interfaces and the improved Li^+ conductivity along the LiF|Li interface due to significantly reduced energy barrier for Li^+ transport (0.6 eV) (Figure 8.4a). In addition, the closed-host bi-layer structure can be applied in the high-voltage Li-metal batteries with high Ni-NMC as the cathode. However, the electrolyte, such as carbonate-based electrolyte with FEC as the additive [78, 284, 290], which can resist high voltage, should be used in place of the one (DOL:DME) used in this work. Alternatively, the relatively

dense top SEI layer can be ex-situ formed, which will be studied later. Nevertheless, the current work as the proof-of-concept is sufficient.

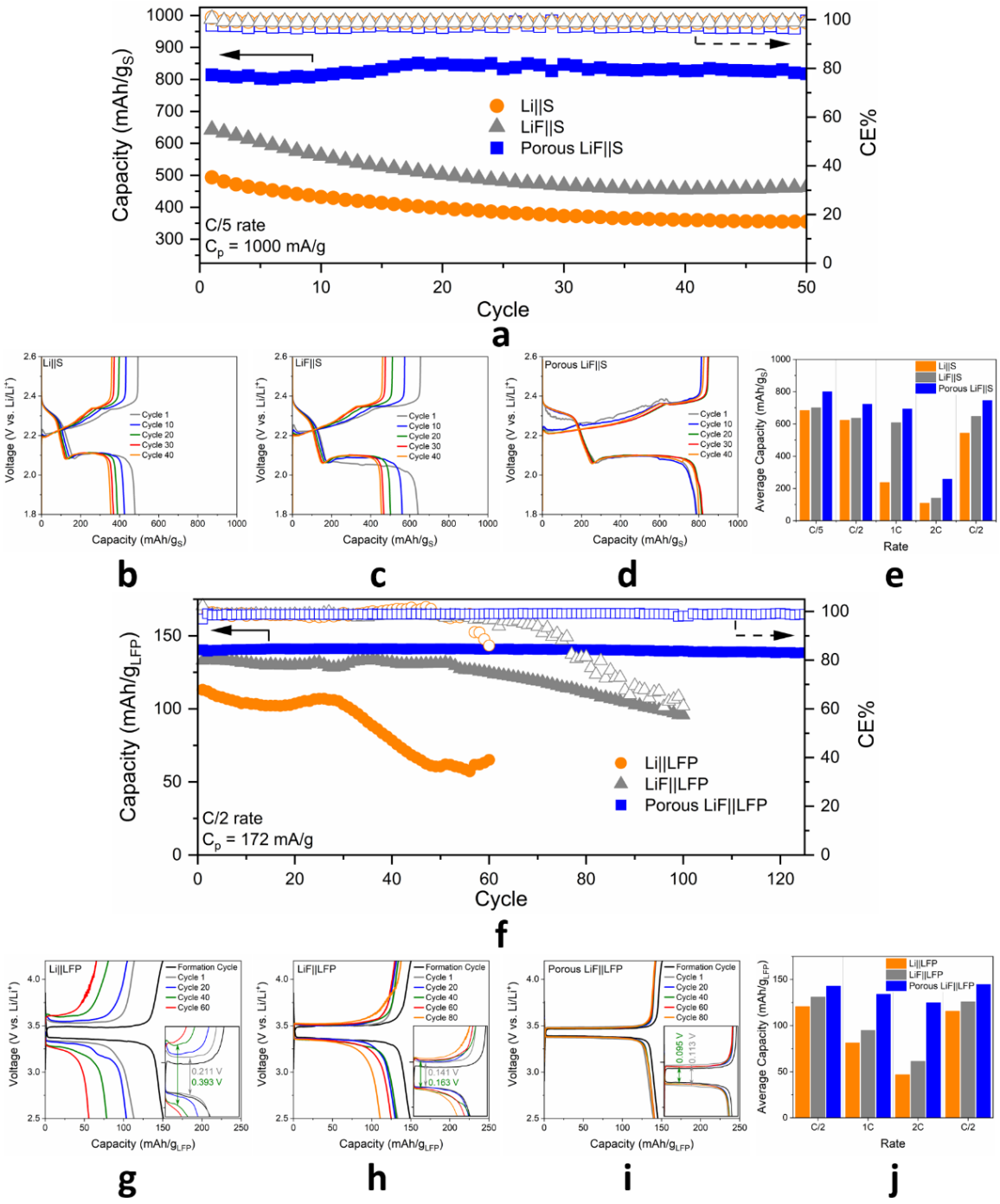

Figure 8.6. (a) Li-S cell galvanostatic cycling at C/5 rate with (b-d) charge-discharge curves for (b) Li, (c) LiF, and (d) porous LiF anode cell, as well as (e) rate performance testing. (f) Li-LFP cell galvanostatic cycling at C/2 rate with (g-i) charge-discharge curves for (g) Li, (h) LiF, and (i) porous LiF anode cell, as well as (j) rate performance testing.

8.4 Conclusions

We demonstrated a bi-layer structure, constructed of an interconnected, tortuous, porous LiF-rich layer in contact with lithium and a dense *in situ* formed inorganic-rich layer on top of the porous structure, showing enhanced anode stability. This was produced through a facile method of forming a composite LiI-LiF coating, followed by dissolving the LiI with a solvent rinse. The resulting artificial SEI was a LiF-rich, porous structure, where an increased number of Li/LiF interfaces for lithium nucleation are made available, thus reducing local volume fluctuations, improving the flexibility of the SEI, as well as decreasing anode resistance due to faster Li^+ diffusion along such interface. Additionally, the interconnected and tortuous pores improve the Li^+ flux distribution and mechanically suppresses dendrite growth, which usually occurred due to chemical or topographical heterogeneities on the Li-metal surface. In early cycling, lithiated sites near the electrolyte are consumed to form a dense, electrically insulating upper layer of inorganic-rich SEI, thus realizing the closed-host bi-layered structure. This top layer reduces the side reaction, allowing extended cyclability on the Li-metal side. This was validated with symmetric cell cycling at different rates and areal capacities, as well as with full-cell testing using both sulfur and LFP cathodes. The design of a closed-host bi-layer structure, consisting of an electrically insulating dense top layer and porous bottom layer, opens the new opportunity to improve the stability of the Li-metal anode and unlock a plausible route for high-energy metal-based batteries, such as Li, Na and K metals.

8.5 Author Contributions

B. Li and C. Efaw conceived the idea of the study and wrote the paper. C. Efaw prepared anode materials and conducted the electrochemical, SEM, XPS and AFM experiments. B. Lu conducted cryo-FIB-SEM experiments. Y. Lin and G. Pawar performed MD simulations. P.R. Chinnam prepared sulfur cathode. B. Li, E. Dufek, M. Hurley and S.Y. Meng supervised the projects. All the authors contributed to the discussion and interpretation of the results.

8.6 Acknowledgments

Research has been supported by the Assistant Secretary for Energy Efficiency and Renewable Energy, Office of Vehicle Technologies of the U.S. Department of Energy through the Advanced Battery Materials Research Program (Battery500 Consortium). INL is operated by Battelle Energy Alliance under Contract Nos. DE-AC07-05ID14517 for the U.S. Department of Energy. The U.S. Government retains and the publisher, by accepting the article for publication, acknowledges that the United States Government retains a nonexclusive, paid-up, irrevocable, world-wide license to publish or reproduce the published form of this manuscript, or allow others to do so, for U.S. Government purposes. The glovebox AFM used in this work was funded through the National Science Foundation Grant No. 1727026 and accessed through the Boise State Surface Science Laboratory. The authors acknowledge the Atomic Films Laboratory at Boise State University for the use of the PHI-5600 XPS system. The authors would like to thank JD Hues, Nicholas Bulloss, and Paul H. Davis of Boise State University for support with XPS, FESEM, and AFM, respectively, and thank Charles C. Dickerson, Yulun Zhang,

and Ningshengjie Gao of Idaho National Laboratory for help with electrochemical testing.

8.7 Supporting Information

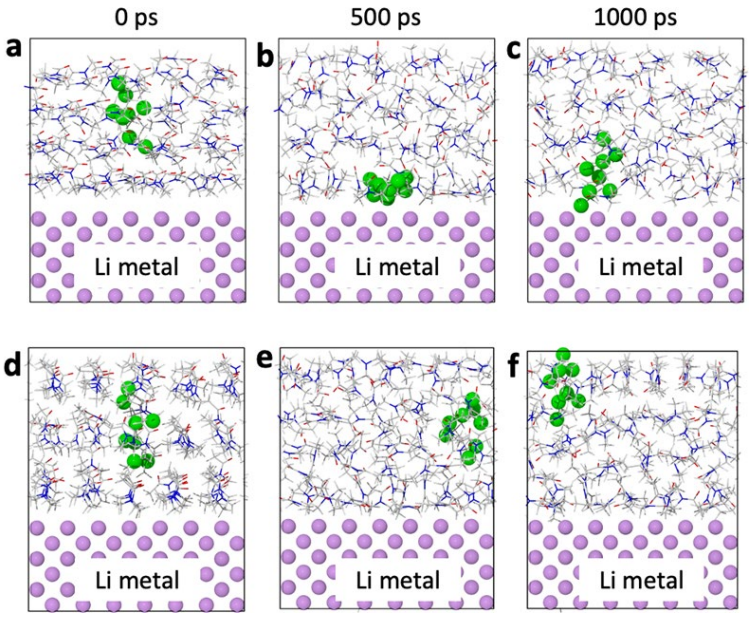

Figure S8.1. A temporal evolution of PVDF in DMF solution with snapshots taken at (a) 0 ps, (b) 500 ps, and (c) 1000 ps. A temporal evolution of PVDF in DMA solution with snapshots taken at (d) 0 ps, (e) 500 ps, and (f) 1000 ps. The simulation box size in all simulations is 24.5703 × 24.5703 × 30 Å^3.

Figure S8.1 illustrates a temporal evolution of the PVDF molecule in DMF and DMA solvents. The PVDF molecule evolved differently in DMF and DMA solvents, where in DMF the PVDF molecule migrated and stabilized near the Li-metal surface. The variability in the PVDF solvation and de-solvation kinetics plays a vital role and dictates the PVDF residence time (the average time that PVDF molecule spent in each solvent solvation shell before migrating to the next solvent solvation shell) in the solvents. The PVDF molecule was highly mobile in the DMF and rapidly underwent a series of solvation and de-solvation steps before reaching to the Li-metal surface (Figure S8.1b-c). The residence time of the PVDF molecule in DMF solvent solvation shells was very

small (~10s of ps); therefore, enabling a rapid migration and stabilization of PVDF molecule on Li-metal where the PVDF molecule spent extended time (300-400 ps). Such extended interaction between PVDF molecule and Li-metal surface could be sufficient to facilitate a typical PVDF degradation and formation of a stable LiF SEI structure.

On the other hand, the PVDF molecule in DMA solvent displayed a localized mobility with a significantly higher residence time (~350 ps). In other words, the PVDF molecule was strongly bounded to the DMA solvent solvation shells. Consequently, the PVDF molecule displayed a significantly slow migration towards the Li-metal surface (Figure S8.1f) within the simulated timeframe. Therefore, such slower solvation and desolvation kinetics may not be beneficial to promote the Li–PVDF interaction and form a stable LiF SEI structure. Overall, various aforementioned evidence clearly demonstrates the critical role of DMF solvent in a formation and stabilization of the LiF SEI structure.

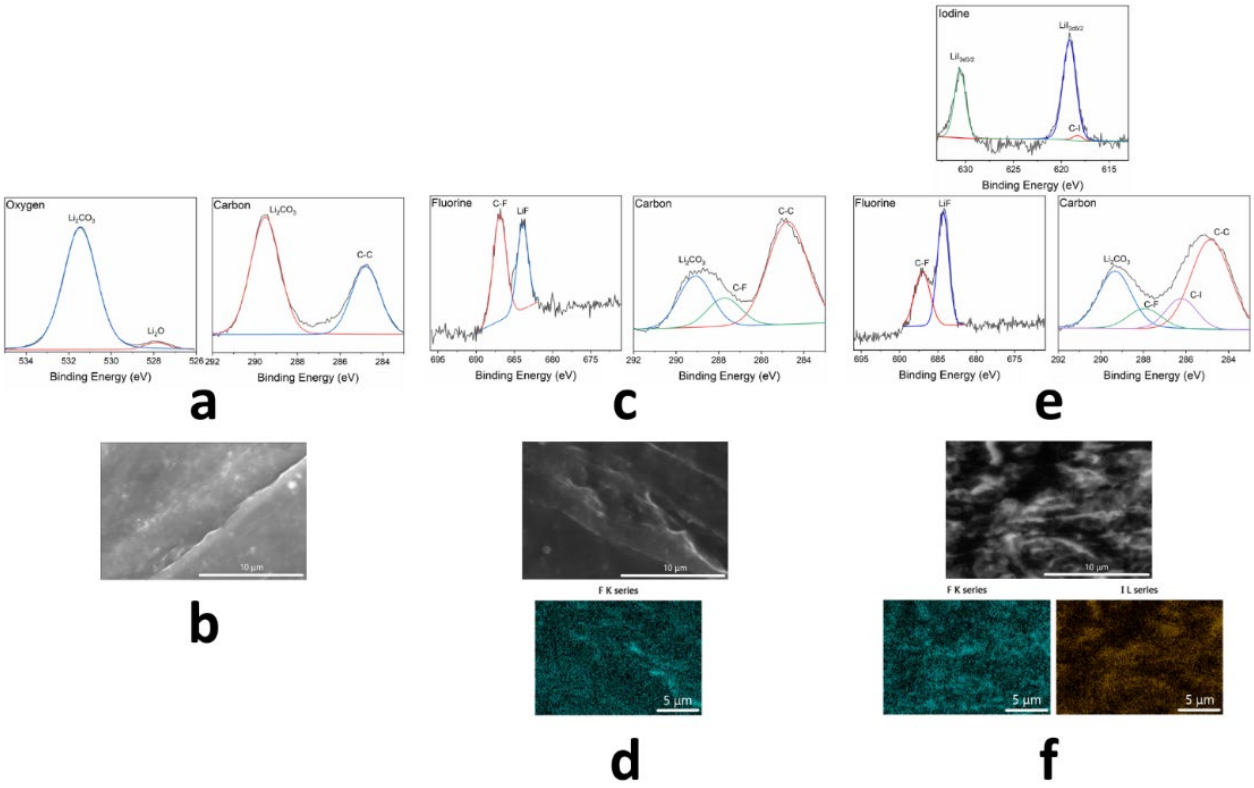

Figure S8.2. (a, c, e) High-resolution XPS with peaks labeled and (b, d, f) FESEM and EDS of (a, b) polished Li, (c, d) LiF artificial SEI, and (e, f) LiI-LiF composite layer.

XPS and FESEM-EDS were used to confirm make-up and distribution of surface components (Figure S8.2). Carbon and oxygen peaks with XPS reveal the presence of native film species (e.g., Li_2O and Li_2CO_3) [102, 105, 291-293] on polished lithium (Figure S8.2a). Pre-treatments of differing complexity attempt to lessen the concentration of native species [72, 94, 294]. Dense LiF artificial SEI is confirmed with XPS and EDS (Figure S8.2b-c). Two peaks are seen in the F1s peak range, which correspond to C-F and LiF [79, 105, 293]. According to the EDS results, the fluorine distribution is not uniform. Therefore, the waterfall effect initiated by the heterogeneous initial lithium surface led to non-uniform reactivity between lithium and PVDF. The carbon-rich organic regions, along with topographic ridges, are sites of greater Li^+ conductivity that readily react with PVDF to form fluoride-rich regions. This facile method of producing an artificial SEI is

prone to intrinsic variability from an initially heterogeneous lithium surface [97]. Similar C-F and LiF binding energy peaks are seen for the LiI-LiF artificial SEI sample, in addition to C-I and LiI peaks [291, 292, 295] (Figure S8.2e). The C-I peak (~618.4 eV) may have been retained after rinsing with DOL:DME solvent, with a slight shift in noise at that range seen in Figure 8.2h. This organoiodine bond appears to not be as readily dissolvable as the LiI compound from the initial composite structure, resulting in slight retention after rinsing.

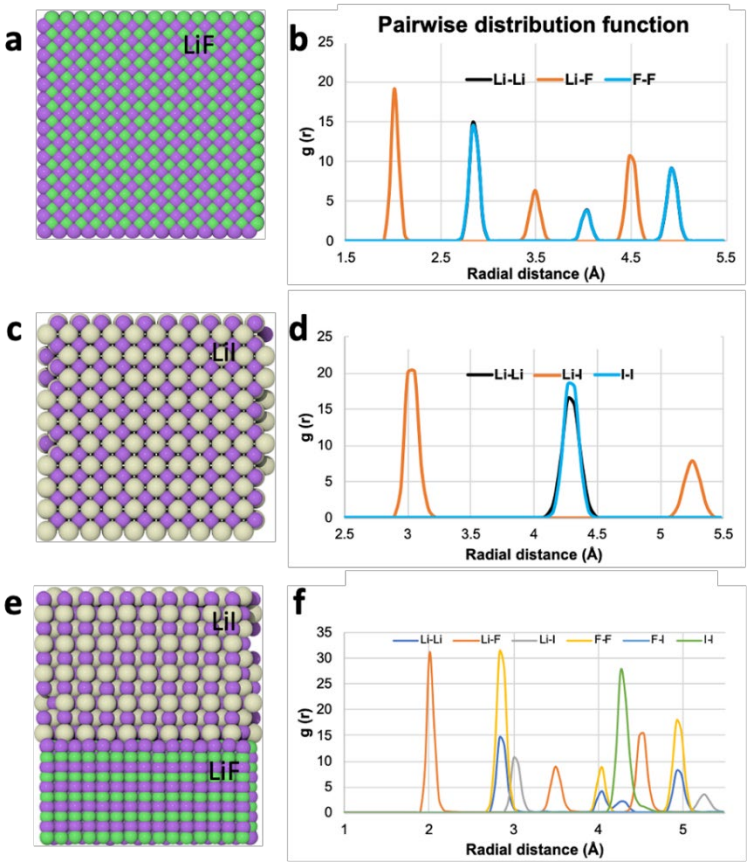

Figure S8.3. (a) LiF structure and (b) a pairwise distribution function of LiF structure after 25 ps. (c) LiI structure and (d) a pairwise distribution function of LiI structure after 25 ps. (e) LiF–LiI structure and (f) a pairwise distribution function of LiF–LiI structure after 500 ps.

Figure S8.3 shows the MD validation results for the individual LiF (Figure S8.3a) and LiI (Figure S8.3c) phases after 25 ps, and an evolution of a combined LiF-LiI (Figure

S8.3e) after 500 ps. A good agreement between mass density ($LiF_{simulation}$ = 2.63 g/cm^3 and $LiF_{experiment}$ = 2.64 g/cm^3 ; $LiI_{simulation}$ = 3.98 g/cm^3 and $LiI_{experiment}$ = 4.08 g/cm^3) and pairwise distribution function (g(r), locations of the Li-Li, Li-F, and Li-I peaks) were consistent with results reported in literature. [296] The LiI and LiF phases remain, creating an interface between them without strong bonding between the phases (Figure S8.3e-f). Thus, the removal of LiI will produce pores that surpass atomic scale, evidenced with cross-sectional cryo-FIB-SEM, where pores vary in size on the scale of 100s of nanometers (Figure 8.2e-f).

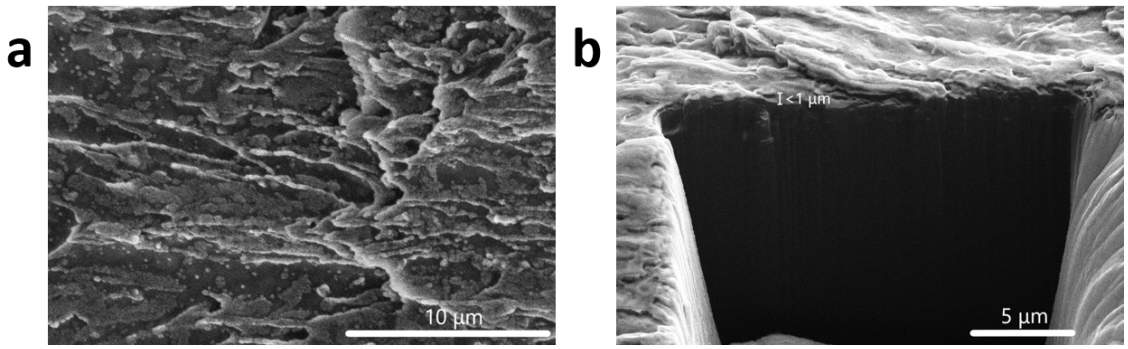

Figure S8.4. (a) Surface and (b) cross-section cryo-FIB-SEM of dense LiF artificial SEI

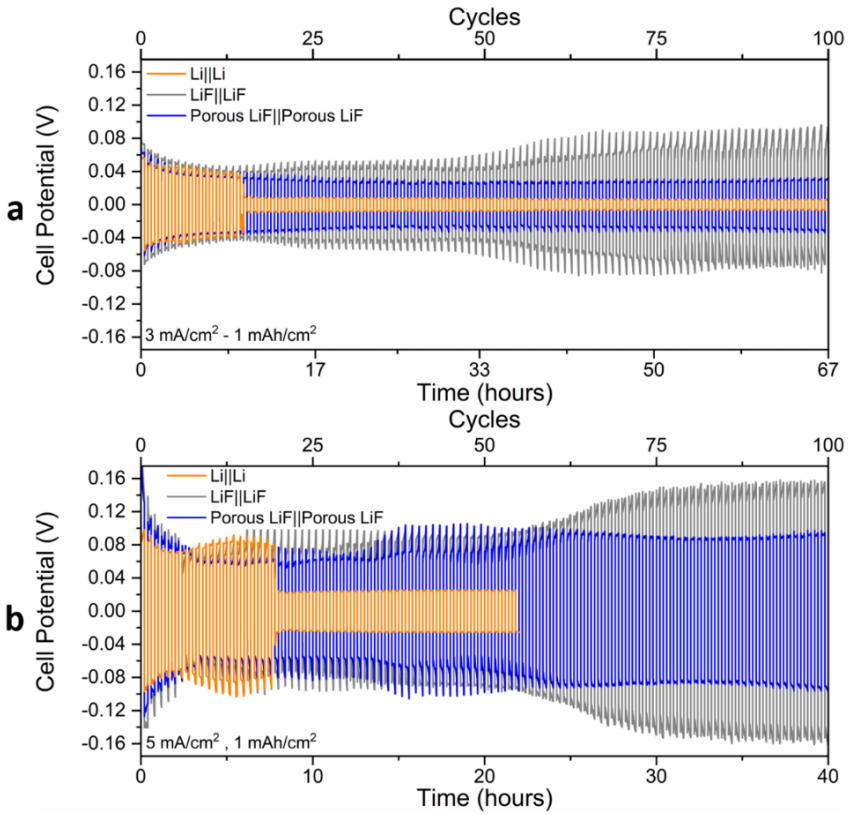

Figure S8.5. (a) 3C and (b) 5C rate symmetric cell cycling at low areal capacity (1 mAh/cm^2) for bare Li, dense LiF, and porous LiF treatments.

Different high rate, low loading symmetric cell tests are shown in Figure S8.5. At 3C rate (3 mA/cm^2, 1 mAh/cm^2), polished Li underwent a soft short circuit after 15 cycles, where voltage hysteresis drastically dropped from 80 mV to under 20 mV range. Dense LiF showed stable voltage hysteresis of 90 mV until cycle 23, where a steady increase in voltage hysteresis ended at 170 mV after 100 cycles. Porous LiF maintained stable voltage hysteresis of 70 mV over 100 cycles. For the higher 5C rate (5 mA/cm^2, 1 mAh/cm^2), a soft short for polished Li occurred after 20 cycles. Voltage prior to short was 190 mV in full range, dropping to under 50 mV after short. Dense LiF had a stable voltage hysteresis of 185 mV for 55 cycles, after which the resistance increased until 315 mV hysteresis was reached after 100 cycles. Porous LiF increased from 160 mV hysteresis to 180 mV after 35 cycles, stabilizing at this value for the 100 cycles.

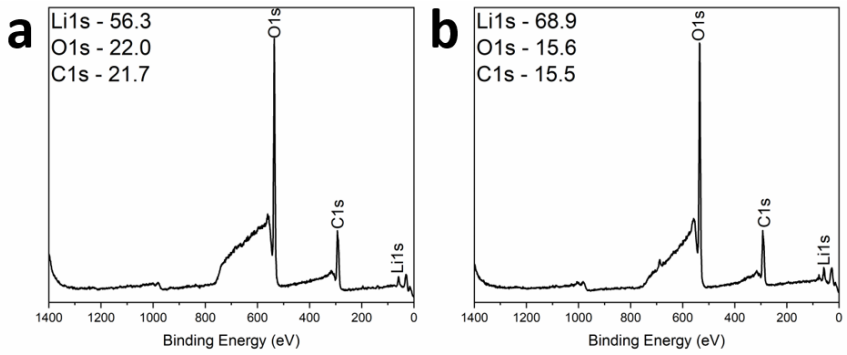

Figure S8.6. XPS survey scan of (a) untreated, rolled Li foil and (b) polished Li foil, with peak identifications presented. Weight percentages for each identified element is included.

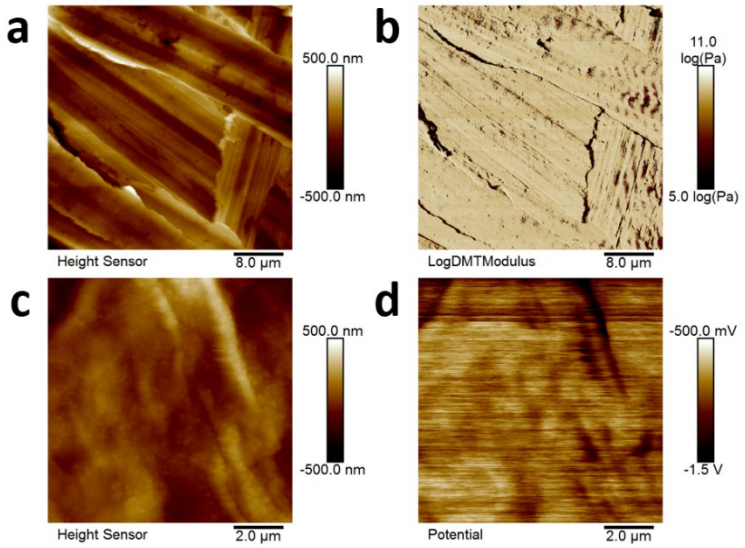

Figure S8.7. AFM techniques of polished Li, with (top) QNM of (a) topography and (b) log DMT Modulus, as well as (bottom) SKPFM of (c) topography and (d) Volta potential, showing a correlation of peaks and valleys, as well as chemical heterogeneities, to variations in mechanical and electronic properties, respectively by technique.

Carbon and oxygen peaks with XPS (Figure S8.2a) reveal the presence of native film species (Li_2O and Li_2CO_3) on polished lithium, which contributes to the issue of heterogeneity on the surface of lithium metal. Pre-treatments of differing complexity attempt to lessen the concentration of native species, especially focusing on removing carbides. Carbides have been observed as “hot spots” for increased ionic flux, contributing to the issue of heterogeneity and instability of LMBs. However,

topographical heterogeneities also contribute to the localized hot spot propagation [72]. Polishing of lithium, while it does reduce oxide and carbide content (Figure S8.6), it also creates nucleation sites at topographical peaks and valleys from the surface roughening [72], further confirmed with atomic force microscopy (AFM) techniques (Figure S8.7). Here, both mechanical (modulus, Figure S8.7b) and electronic (Volta potential, Figure S8.7d) mapping of polished Li reveal correlations between topographical and plausibly chemical variations with shifts in corresponding properties. These differences in surface properties lead to non-uniform Li^+ flux, increasing at specific "hot spots" (dislocations, grain boundaries, crystallographic and topographic heterogeneities, etc.) and undergoing rapid dendrite growth.

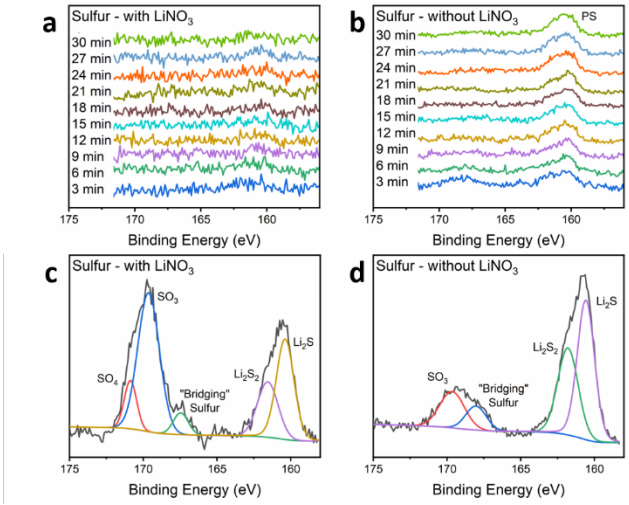

Figure S8.8. Sulfur XPS spectra of lithiated porous LiF electrode (left) with and (right) without $LiNO_3$ in the electrolyte, examined after (a-b) 2 cycles as a function of depth profiling in minutes of sputtering, and (c-d) the electrode surface after 100 cycles.

After 2 cycles in a symmetric cell, the lithiated porous LiF artificial SEI electrode was examined with XPS depth profiling. When $LiNO_3$ is included, the bi-layer structure is formed and prevents consumption of lithium metal. Therefore, no sulfur-based peaks

are present beneath the SEI (Figure S8.8a). When $LiNO_3$ is excluded, the porous layer is not protected by the dense upper layer, and thus the LiTFSI salt decomposes and reacts with available lithium to form polysulfides (labeled as PS in Figure S8.8b). A thick, highly porous SEI is the result of continuous consumption of lithium, further evidenced with cryo-FIB-SEM in Figure 8.5. $LiNO_3$ stabilizes the SEI through oxidation of polysulfides. Porous LiF artificial SEI treated lithium electrodes observed after 100 cycles with XPS revealed an increase in the amount of Li_2S and Li_2S_2 when $LiNO_3$ is excluded (Figure S8.8d). When $LiNO_3$ is included, the amount of polysulfides is decreased (Figure S8.8c), corresponding to an increase in higher sulfur oxidation states (i.e., Li_xSO_y species and bridging sulfur) [250]. The presence of $LiNO_3$ reduces to form insoluble Li_xNO_y, while sulfide species oxidize to passive Li_xSO_y species. It is evident that as cycling continues, the presence of polysulfides increases, regardless of the inclusion of $LiNO_3$. However, the inclusion of this additive reduces the consumption of active Li from oxidation with polysulfides in solution [250]. This is of particular importance when operating with abundant sulfur species in solution, either from electrolyte (e.g., LiTFSI salt) or cathode material (e.g., S cathode).

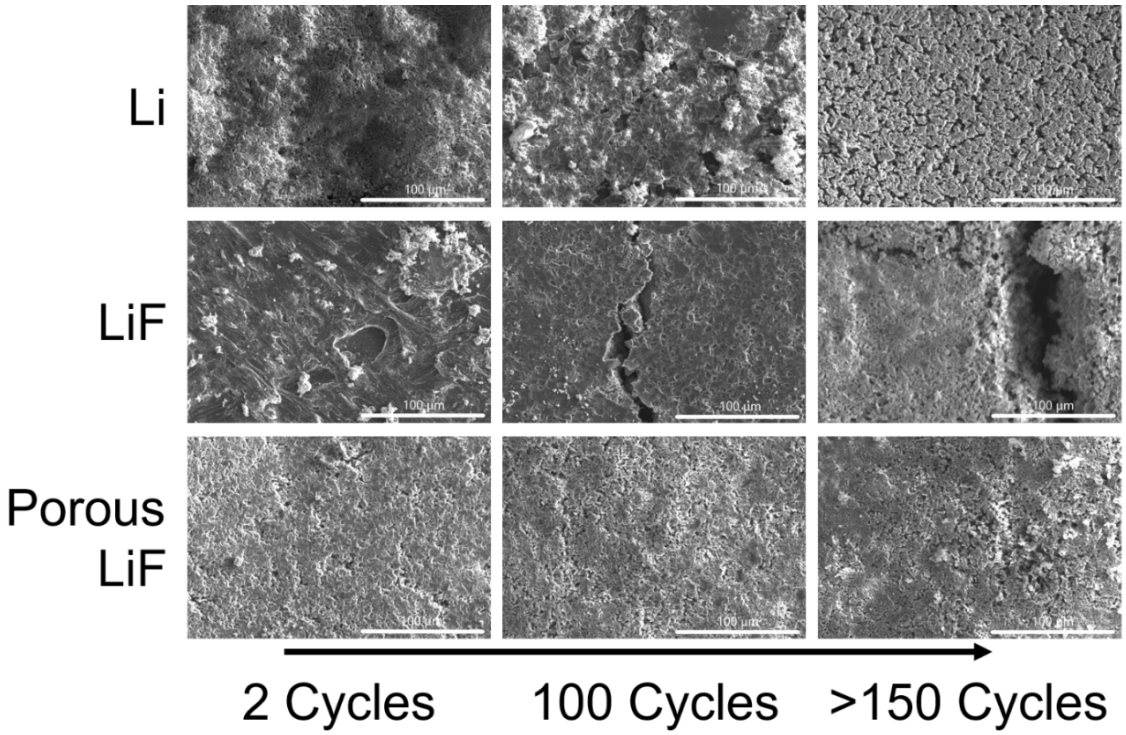

Figure S8.9. Post-mortem FESEM of different anode treatments (all lithiated electrodes) in a symmetric cell over increasing cycles operating at low current density (1 mA/cm^2) and areal capacity (1 mAh/cm^2) without $LiNO_3$ in the electrolyte (1M LiTFSI in 1:1 DOL:DME).

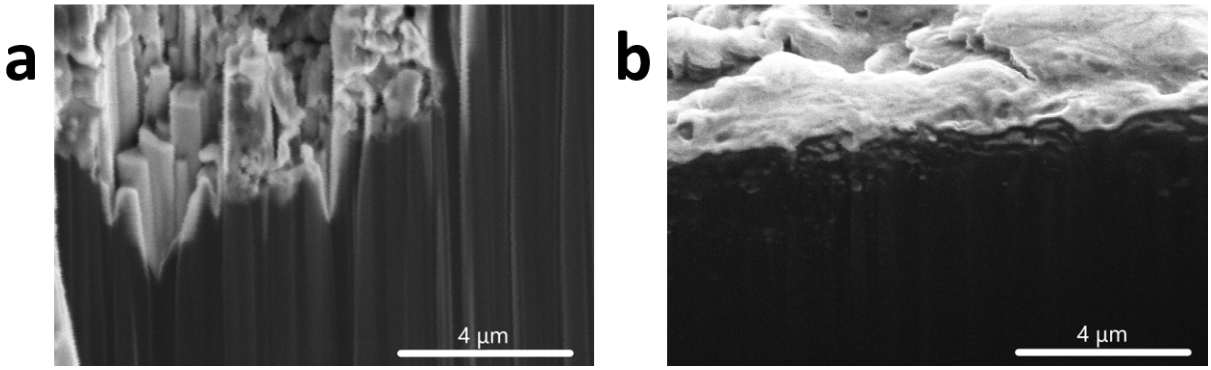

Figure S8.10. Cross-section cryo-FIB-SEM of porous LiF artificial SEI electrode after (a) first stripping cycle, revealing retention of porous structure, and after (b) second stripping cycles, revealing formation of dense top layer, with semi-porous inner layer visible.

Table S8.1. Resistances (electrolyte resistance, R_e; SEI resistance, R_s; charge-transfer resistance, R_{ct}) for equivalent circuit EIS fits of porous LiF symmetric cells at rest (a) without cycling, with $LiNO_3$ (Figure S8.11), (b) after cycling, with $LiNO_3$ (Figure 8.5f), and (c) after cycling, without $LiNO_3$ (Figure 8.5g).

With $LiNO_3$	R_e (Ω)	R_s (Ω)	R_{ct} (Ω)
8 hours	1.70	24.87	8.03
16 hours	1.71	26.76	8.59
24 hours	1.74	31.07	8.37
32 hours	1.71	34.56	8.92
40 hours	1.73	36.72	9.21

a

With $LiNO_3$	R_e (Ω)	R_s (Ω)	R_{ct} (Ω)	Without $LiNO_3$	R_e (Ω)	R_s (Ω)	R_{ct} (Ω)
0 hours	1.44	1.56	42.37	0 hours	11.68	52.61	23.12
8 hours	1.40	1.61	42.79	8 hours	12.00	67.3	13.35
16 hours	1.33	1.69	36.73	16 hours	12.30	66.83	13.88
24 hours	1.41	1.64	37.49	24 hours	11.81	68.07	13.57

b **c**

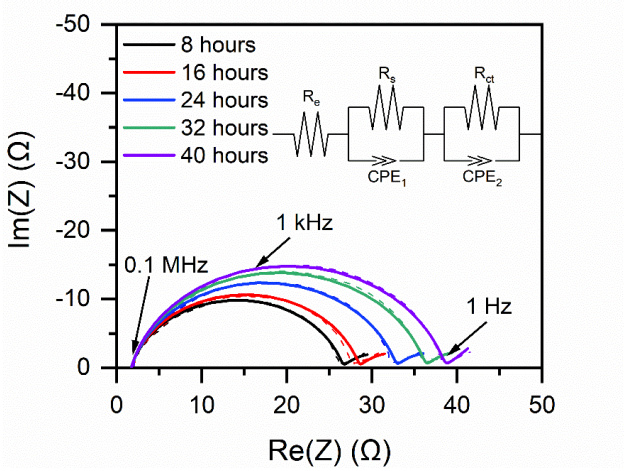

Figure S8.11. EIS spectra of a symmetric porous LiF cell as a function of time at rest, without any cycling, with the equivalent circuit model and fits included (raw data as dashes, equivalent circuit fits as solid lines).

The SEI resistance (R_s) is substantially higher prior to cycling than the resistance seen after cycling for the porous LiF symmetric cell (Figure 8.5f). The higher R_s is driven

by the insulating nature of the native species and LiF present in the SEI. Additionally, the open-host structure allows continuous SEI formation, leading to an increasing resistance over time at rest.

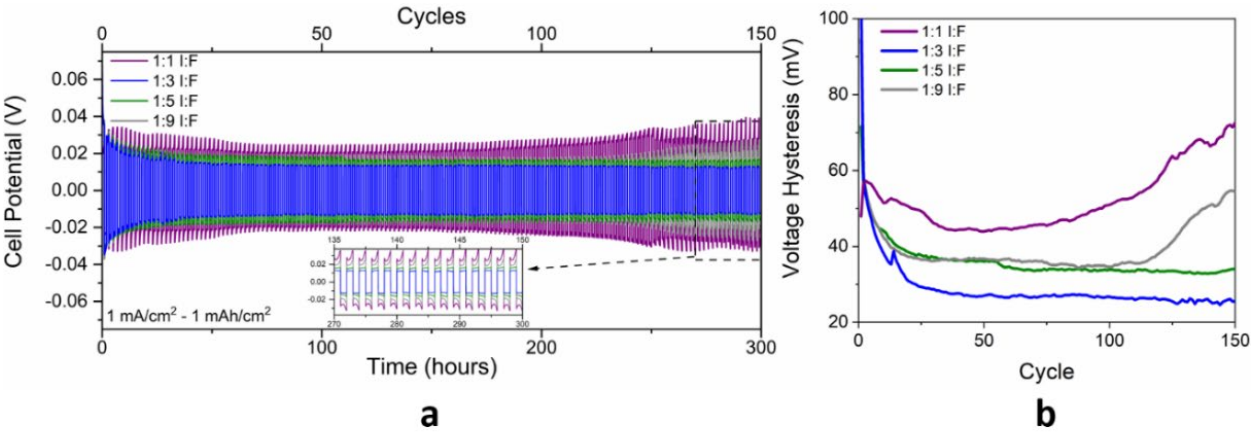

Figure S8.12. (a) Symmetric cell cycling of varied LiF porosity, as correlated to iodine concentration in the precursor solution. (b) Voltage hysteresis (i.e., cell potential range for each cycle) for each symmetric cell.

With low amounts of iodine in the precursor (1:9 elemental iodine to fluorine, i.e., I:F ratio), the voltage hysteresis is similar to that of dense LiF, revealing that there is little change in SEI porosity and thus is susceptible to the same issue of SEI fracture. Increasing the amount of iodine to a 1:5 I:F ratio, the voltage hysteresis stabilizes under 40 mV. Increasing to a 1:3 I:F ratio, and thus increasing porosity, leads to a lower stabilized voltage hysteresis under 30 mV. However, with further increasing the ratio, the tortuosity might decrease, leading to Li metal dendrite growth and more dead Li formed thus an immediate increase in voltage hysteresis.

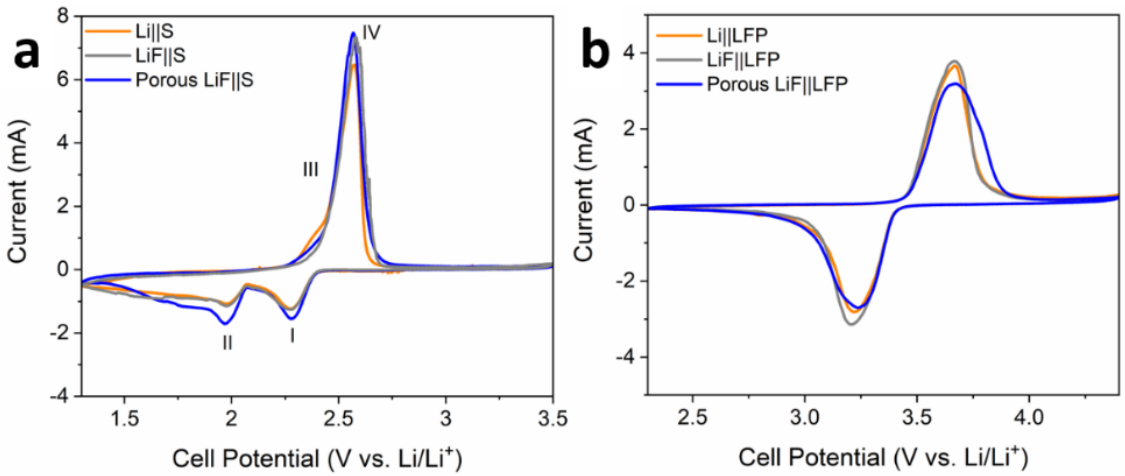

Figure S8.13. Cyclic voltammograms for (a) sulfur cathode and (b) LFP cathode, with different anode treatments.

Cyclic voltammograms were collected for each anode treatment after peak stability was accomplished (cycle 5). For sulfur cathode, the cathodic peaks (III-IV) at 2.3-2.4 V and 2.57 V coordinate with reduction of lithium polysulfides (Li_2S_8 to Li_2S_n to Li_sS_2 / Li_2S), while the anodic peaks (I-II) at 2.30 V and 1.90 V are associated with oxidation of the Li_2S to lithium polysulfide and back to Li_2S_8 [289]. The peak positions and currents are similar for all anode treatments with LFP cathode, where the cathodic peak is at 3.7 V and the anodic peak is at 3.2 V.

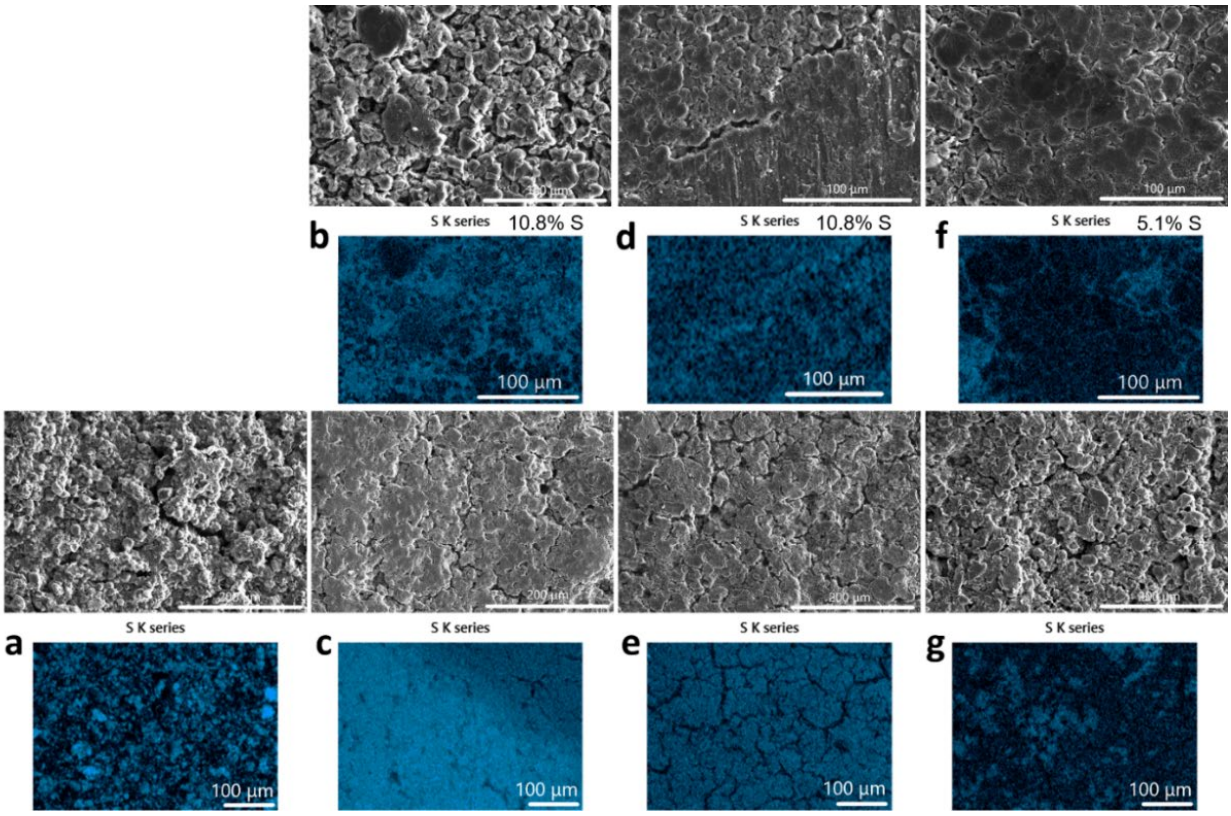

Figure S8.14. (a) FESEM of as-prepared sulfur cathode with sulfur EDS map. Post-mortem FESEM with sulfur EDS map for (b, d, f) anode and (c, e, g) sulfur cathode, respectively with anode treatment of (b, c) polished Li, (d, e) dense LiF artificial SEI and (f, g) porous LiF artificial SEI. Sulfur weight percentages are included for the EDS maps on the anode side.

Post-mortem FESEM and EDS of Li||S (Figure S8.14b-c), LiF||S (Figure S8.14d-e), and porous LiF||S (Figure S8.14f-g) reveals differences in both morphology and sulfur distribution. On the anode-side, bare Li reveals a roughened, granular morphology, showing susceptibility to dendrite growth and formation of dead Li (Figure S8.14b). Dense LiF has a fractured surface, driven by non-uniform ionic flux and failure of SEI, leading to rapid consumption of active Li and increasingly resistive ionic pathway (Figure S8.14d). Porous LiF anode surface is highly compact, dense SEI with minimal sulfur content present (Figure S8.14f). As discussed before, the bi-layer structure cannot form without the presence of $LiNO_3$ in the electrolyte, which oxidizes polysulfides and

creates a stable SEI film. Here, with the reduced sulfur content and surface distribution, it is seen that the polysulfide shuttling effect is reduced on porous LiF when compared to the polished Li and dense LiF anodes. This is further exemplified when observing the cathodes. For comparison, the as-prepared sulfur cathode (Figure S8.14a) shows a roughened surface of distributed S-rich regions. The sulfur cathode across from polished Li was highly compacted, with excessive sulfur uniformly distributed on the surface. The change in morphology is related to a shift in chemical make-up to soluble polysulfides (Figure S8.14c). The cathode across from dense LiF is also compacted in morphology, with relatively uniform distribution of polysulfide species (Figure S8.14e). As for the cathode across from porous LiF, the surface morphology is similar to that of the as-received cathode, with closely related sulfur distribution in the EDS maps (Figure S8.14g). The relatively similar structure means that surface chemistry did not drastically change, corresponding to the reduced polysulfide shuttling effect.

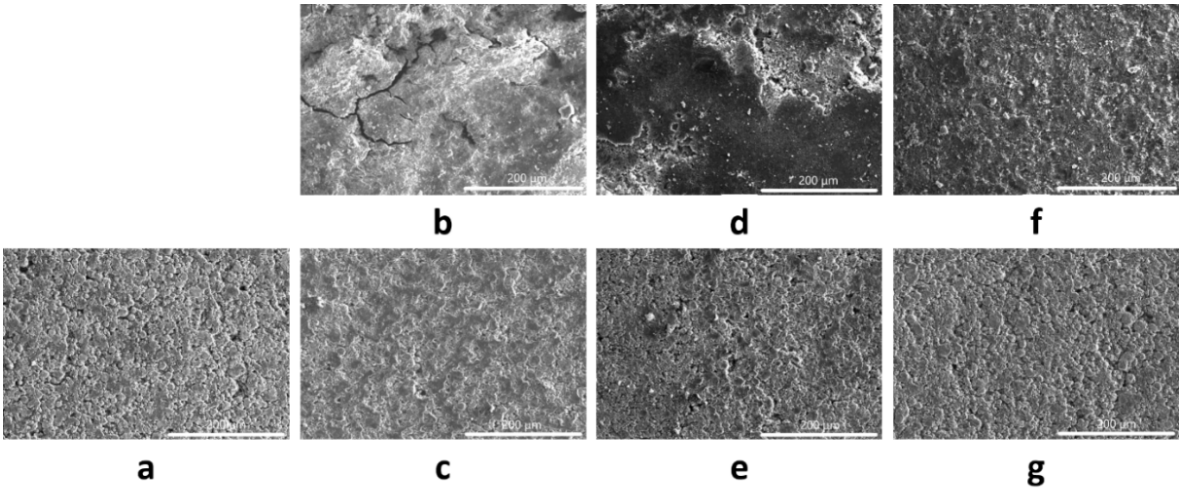

Figure S8.15. (a) FESEM of as-received LFP cathode. Post-mortem FESEM of anode and LFP cathode, respectively, of (b, c) polished Li (d, e) LiF artificial SEI, and (f, g) porous LiF artificial SEI cells.

Figure S8.15a presents the as-received LFP cathode. Post-mortem FESEM of Li||LFP (Figure S8.15b-c), LiF||LFP (Figure S8.15d-e) and porous LiF||LFP (Figure S8.15f-g) reveal surface morphology of both anode and cathode. Observing the cathode-side, there is not much change in surface morphology, revealing that failure is not driven by the cathode (Figure S8.15c, e, g). On the anode-side, polished Li reveals SEI fracture, driven by non-uniform kinetics and brittle SEI formation (Figure S8.15b). Dense LiF has large SEI fracture, providing sites for further LAM and formation of a more resistive pathway (Figure S8.15d). As for porous LiF, the surface is highly compact and uniform, revealing that the high stability of the bi-layer SEI structure prevented constant consumption of active materials, maintaining stability for extended cycles (Figure S8.15f).

CHAPTER 9 – CONCLUSIONS AND FUTURE WORK

In summary, electrochemically driven degradation of materials limits the expansion and sustainability of many clean energy technologies, including nuclear energy and batteries. There is a notable intersectionality between these two fields, where degradation processes occur through reaction with relatively extreme environments at the interface and consumption of active materials. In order to advance these fields, we must expand our understanding of fundamental science, design novel technologies to address the key fundamental issues, and determine how to get those technologies to a level of readiness where they may be utilized in real-world applications. Advanced characterization techniques should continue to be developed so we may expand our understanding of the interplay among crystallographic structures, thermodynamic states, and kinetic mechanisms. Developing novel interfaces and methods of monitoring reactions *in situ* or in-pile may provide future pathways for increased energy-dense and resilient systems. With new technologies, based in a fundamental understanding of materials, an expansion to large-scale, real-world applications can foster a new future based on cleaner, more sustainable, and ethical energy.

Along with these efforts, a holistic, diverse approach must be pursued to reach the lofty goal of a decarbonized society that combats human-driven environment destruction. This means tracking and reducing harsh environmental and socioeconomical practices throughout the lifecycle of materials and energy technologies (Figure 9.1). For example, focus should not only be placed on improving the usability of lithium-metal batteries; we

must also diversify from our environmentally taxing materials, such as cobalt and lithium, to other materials like sulfur or sodium. Extraction should also be a point of focus, such as choosing regions and methods of extraction that are ethically responsible. At the end of battery life, finding reuse applications or developing recycling methods will help secure a supply chain, as well as reduce our overall carbon footprint. As is the case in many facets of life, diversity is also a good protocol for decarbonization. We cannot purely rely on one single technology, but rather simultaneously advance many pathways to reach a sustainable, net-zero emission future.

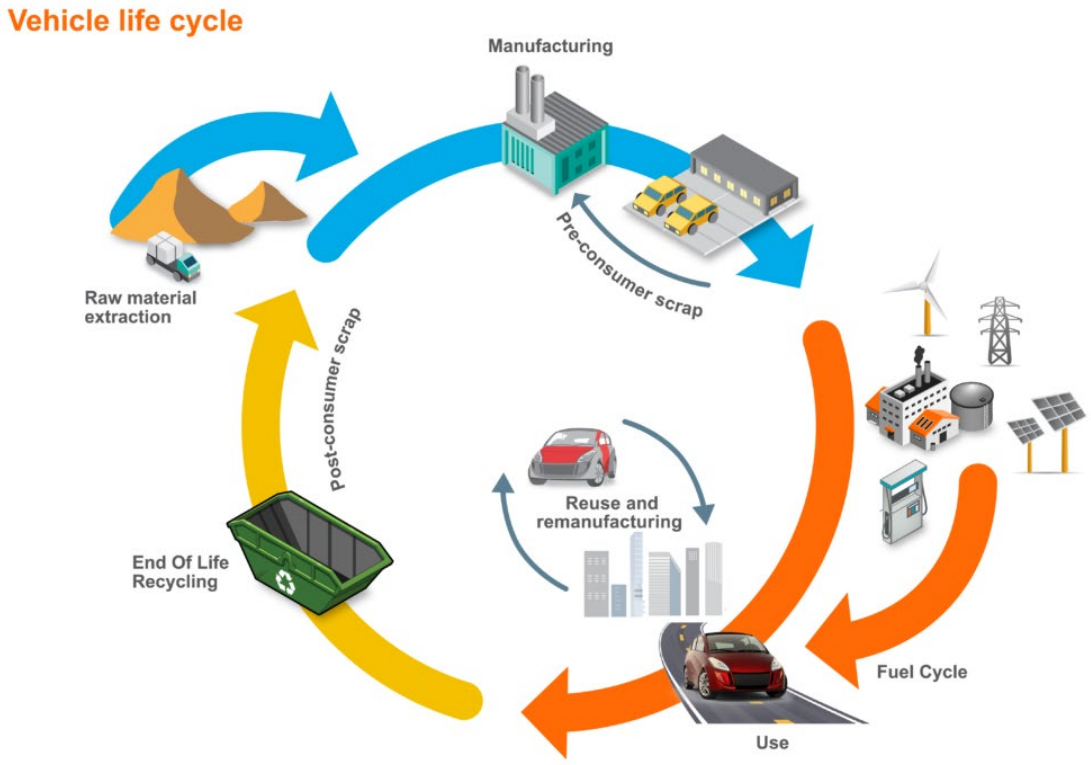

Figure 9.1. From ahssinsights.org, "Vehicle Life Cycle Assessment (LCA) encompasses all phases of the product cycle, from raw material extraction to end of life recycling and disposal."

For future work, general efforts may be focused into the two key applications of this dissertation, one being sensor development for monitoring cladding degradation in a

nuclear reactor, the other in anode treatments for the advancement of high-energy lithium-based batteries. Possible future work is also specified for each of my first author publications.

Nuclear Cladding Sensors

Sensor development is focused on monitoring the state of degradation of cladding materials in-pile, so that users may be able to operate the reactor in a more efficient and safer manner. An EIS monitor was tested and developed at Boise State University to eventually correlate equivalent circuit models to corrosion mechanisms determined from high-resolution post-mortem characterization. Initial focus was set on comparing EIS-predicted oxide thickness with post-mortem SEM at pre- and post-breakaway oxidation states (Figure 9.2). A relatively accurate estimation of oxide thickness was confirmed for pre-breakaway oxidation state 1, (OS1); however, after breakaway occurred (OS2-OS4, confirmed with a transition to linear mass growth from TGA), the estimation of oxide thickness from EIS dramatically diverged from actual oxide thickness. This points to a difference in mechanism, and thus a new equivalent circuit should be used [297]. Further efforts into monitoring oxide thickness and other markers of cladding integrity with EIS should be continued, so as to provide novel sensors in actual nuclear reactors.

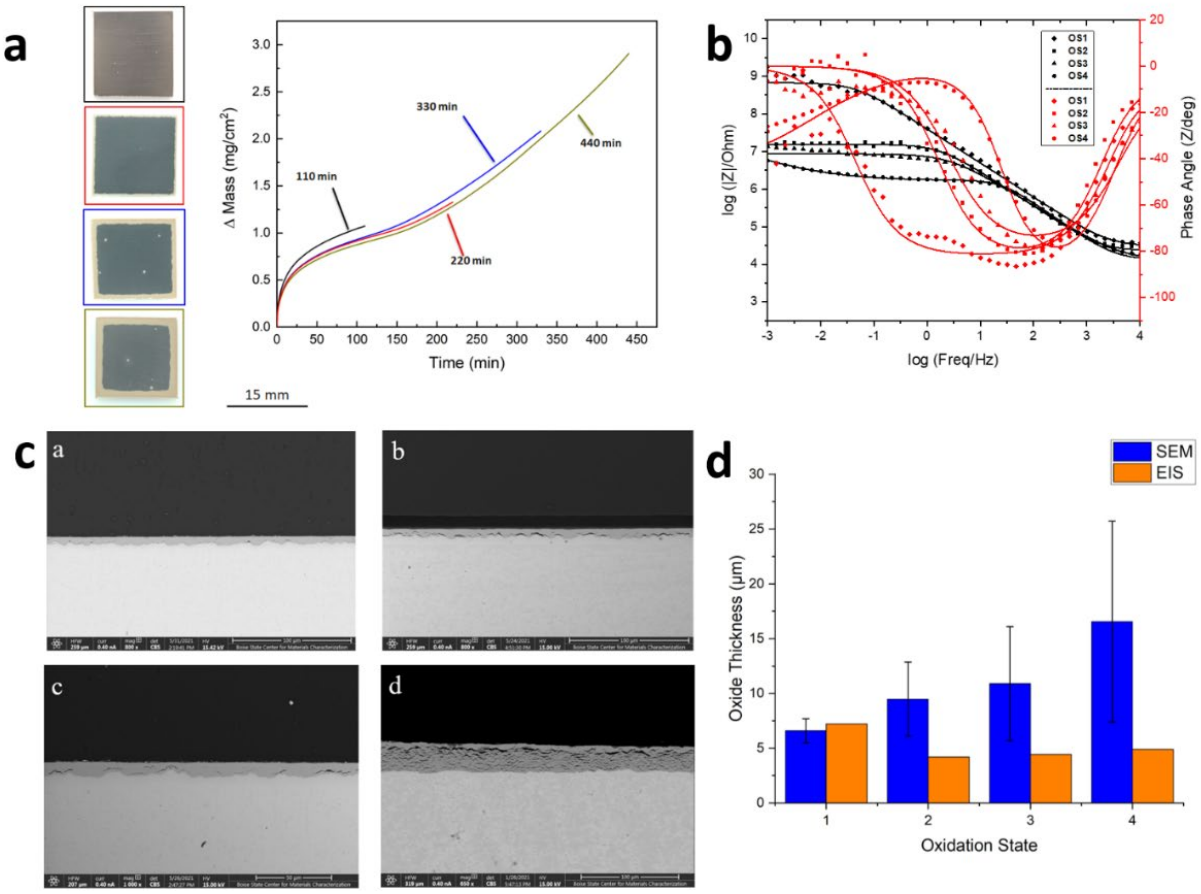

Figure 9.2. Adapted from Reynolds [297]: Correlation of EIS and post-mortem SEM oxide thickness measurement for Zry-4 alloy exposed to 700°C simulated air (80% N_2 + 20% O_2). (a) Thermogravimetric analysis with oxidation states (OS) increasing from 1 to 4 with increasing exposure time. (b) EIS Bode plots at each OS. (c) post-mortem cross-sectional SEM at OS1-4, from a-d respectively. (d) Comparison of oxide thickness from EIS and SEM at each OS.

Further testing methods are also available within the suite of characterization at Boise State University. In particular, *in situ* Raman can provide observation of zirconia growth mechanisms. A high-temperature (HT) Raman stage has been set up at Boise State (Figure 9.3) to observe the oxidation of zirconium and its alloys *in situ*, furthering our capabilities to analyze the oxidation mechanisms as a function of time.

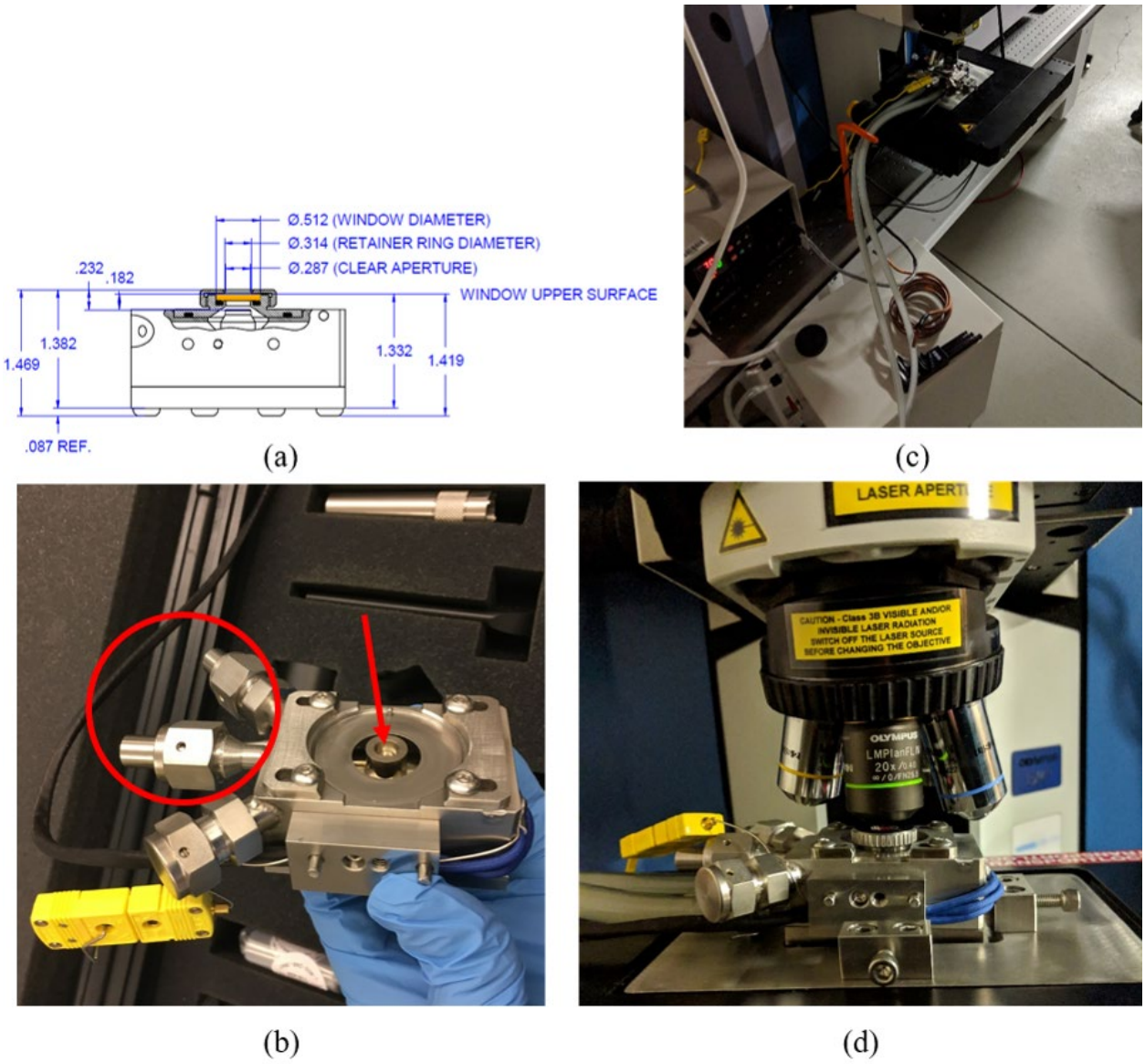

Figure 9.3. From Hu et al. [110]: "(a) Dimensional rendering of the HT Raman sample holder, via Harrick. (b) Raman HT Raman sample holder, with arrow pointing out sample cup and circle noting availability for gas or electrolyte inlet and outlet. (c) BSU's HT Raman stage set-up, including high temperature controller (HTC) and coolant. (d) HT Raman sample holder mounted on stage and set up for Raman spectroscopy with a 20x objective."

Lithium-Metal Batteries

For lithium-metal batteries, parameterization of early-onset SEI structure is an interesting future focus of work. Varying external parameters, such as temperature, can affect the solvation structure of the electrolyte (Figure 9.4), thus rendering a different SEI structure during redox and desolvation near the lithium-metal anode surface. It has been observed that varying the electrolyte, as well as the temperature of the electrolyte during the initial formation cycles can lead to differences in cycle life when operating under similar aging conditions. Other parameters, such as cell pressure, could play a role in electrode stability (e.g., plating/stripping pathways, electrode density, SEI integrity, etc.) that would influence both capacity utilization and cycle life.

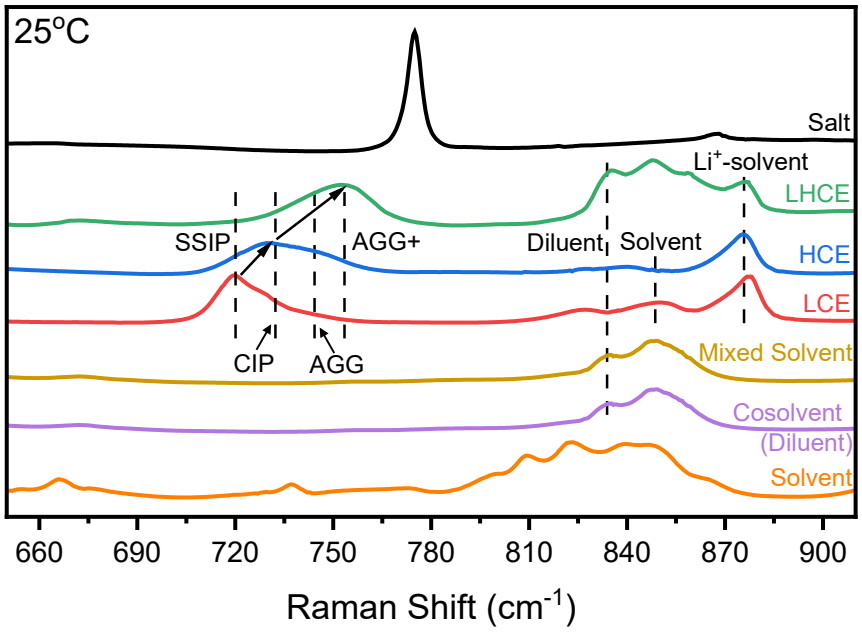

Figure 9.4. Raman spectra of different electrolytes and their components. From bottom to top: (orange) common solvent with peaks between 800-860 cm^{-1}, (purple) diluent cosolvent with peaks between 830-850 cm^{-1}, (gold) mixed solvent with primary peaks dominated by the diluent, (red) LCE electrolyte, with cation-anion interactions (SSIP and CIP) between 710-730 cm^{-1} and Li^+-solvent interaction at 875 cm^{-1}, (blue) HCE electrolyte with a blue-shift of cation-anion interactions to 730-750 cm^{-1} (SSIP, CIP, and AGG), (green) LHCE electrolyte with a further blue-shift of cation-anion interactions to 740-760 cm^{-1} (CIP, AGG, and AGG+), and (black) solid salt with prominent peak at ~775 cm^{-1}.

Further understanding of lithium foil surface treatments is necessary to produce a surface of increased uniformity, both topographically and chemically. One pathway is by using polycyclic aromatic hydrocarbons (PAHs), non-polar molecules commonly found in fossil fuels, to undergo controlled reaction with lithium foil to remove its native film. Research has been conducted on simulating the charge-transfer mechanism between PAHs and lithium, finding that two lithium atoms are inclined to adsorb onto various PAH types [298-300]. Further, an experimental study utilized 0.1M naphthalene ($C_{10}H_8$), the simplest PAH in the family, mixed in high electrochemically stable tetrahydrofuran as a precursor solution to chemically etch lithium metal [94]. However, a link between theoretical calculations and experimental evidence has yet to be determined; in other words, the mechanism by which PAHs react to remove the native oxide has yet to be discerned. Additionally, the role of tetrahydrofuran in the reaction mechanism is also unknown. Studies into different PAHs, along with the solvent by which the salt is dissolved and allowed to react should be conducted. Initial results showed a variation in visual extent of reaction compared to the 2018 study from Singapore (Figure 9.5) [94]. This could be driven by a difference in materials (e.g., initial lithium and its native film components) or variations in exposure environment (e.g., sealed vial or unsealed vial, physical agitation occurring or not, etc.).

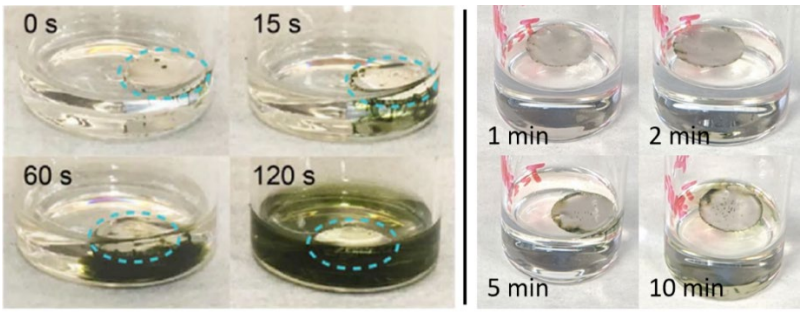

Figure 9.5. (Left) From Tang et al. [94]: "Time-lapsed digital photos to show the polishing process of lithium foil by naphthalene in tetrahydrofuran." (Right) Same process of time-lapse photos of lithium foil by 0.1M naphthalene in tetrahydrofuran.

Other directions of work worth noting are the design and testing of anode-free batteries and all-solid-state-batteries. In the case of anode-free batteries, a pre-lithiated cathode (i.e., lithium already stored in the cathode) supplies the full cell charge prior to cycling. In this design, the removal of excess lithium required to operate a lithium-metal battery allows a reduction in battery mass and volume, simplified cell fabrication, and reduced cost, while maintaining a high energy density. Here, finding a current collector material or surface that has high lithiophilicity (i.e., attraction to lithium plating) and a reduced activation energy for plating could facilitate relatively more uniform ionic distribution, thus reducing the detrimental effects of dendrites and active material consumption.

As for all-solid-state-batteries, a transition from liquid electrolytes to solid electrolytes has been of interest, due to reduced electrolyte flammability (i.e., improved safety upon short circuiting), improved thermal, mechanical, and electrochemical stability, enabled metal anode and high voltage operation due to reduced active consumption at the anode-side, and reduced excess material for packing in large-scale cells, therefore rendering higher pack-level energy densities. However, large solid-solid interfacial impedances are common, along with design of solid electrolytes with high

ionic conductivity and parameterized defect density. The diffusion mechanism through solids is driven through defects; however, larger voids and excessive grain boundaries make the charge-transfer pathway more tortuous as well as susceptible to dendritic growth. Fundamentally, the charge-transfer mechanism is similar to that of ion transport through the SEI in a liquid electrolyte (Figure 9.6). Further research into designing quality solid electrolytes and reducing interfacial impedances could enable the expansion of all-solid-state-batteries in electric vehicle and grid energy markets [57, 58].

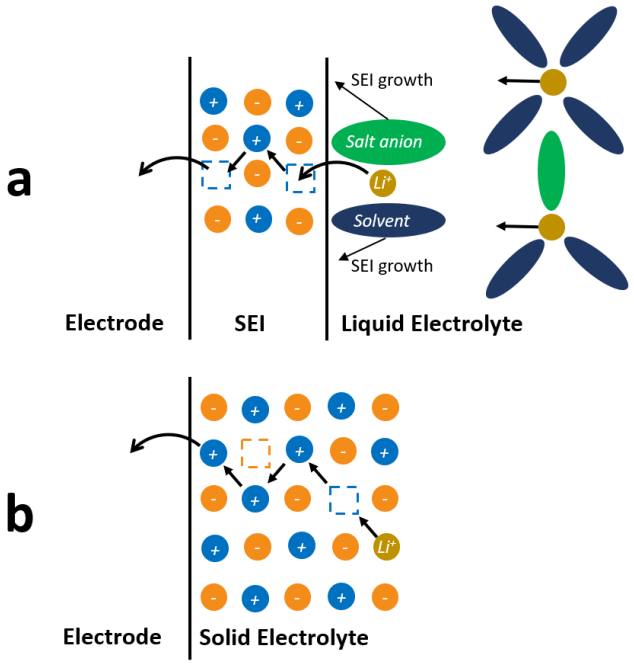

Figure 9.6. Comparison of charge-transfer mechanisms of lithiation for (a) liquid and (b) solid electrolytes. (a) For liquid electrolytes, transport is driven by (electro)chemical potential gradients. Upon approach of the SEI, desolvation occurs, followed by Li^+ transport through SEI by vacancy and interstitial "hopping" mechanism. At the electrode surface, another charge-transfer step occurs. (b) For solid electrolytes, transport is driven by charge mobility and concentration. In the electrolyte, transport of Li^+ occurs by vacancy and interstitial "hopping", followed by a charge-transfer at the electrode surface.

Chapter 5 – SKPFM

First, a methodology should be utilized, such as calibrating the probe with an inert material (e.g., gold), to have more quantifiable measurements provided with SKPFM for research in specific fields such as corrosion or batteries. One example is using calibrated measurements to compare "snapshots" of a material after exposure to a corrosive environment or after/during cycling in a battery [135, 137, 138, 140]. With improved calibration, quantifying VPDs for small material features, such as grain boundaries, defects, sub-stoichiometry [111], etcetera should be attempted so that we may better understand the driving forces to electrochemical reactions seen in bulk measurements.

Chapter 6 – Raman of Zirconium Alloys

Raman mapping should be expanded to corrosive systems of more complexity beyond a O_2-N_2 mixture. From here, we may start to observe hydride formation or other species that could play a role in the oxidation mechanism. Bulk analysis shows little change in the pathway, but any observed microscale differences such as interface-tetragonal phase thickness at progressive oxidation states. Correlation between post-mortem Raman analysis to *in situ* EIS measurements of the same material could expand our knowledge of when to fit with accurate equivalent circuits. This may be difficult, as low-temperature corrosion does not lead to thick oxides, and therefore could be difficult to resolve with cross-sectional Raman. However, either rapid degradation at extreme temperatures, or long-term exposure studies could provide an insight that allows oxide progression mechanisms to be accurately correlated to equivalent circuit models.

Chapter 7 – Co-localization of Oxidized Zirconium

Same as Chapter 6, the suite of characterization tools should be utilized to accurately portray different mechanisms of corrosion to equivalent circuit models described with EIS. Observation of more complex systems with the characterization tools can be accomplished; this could include different oxidizing chemistries, different alloy types, etcetera, so we could build a database of information that may not have been well recognized in the field before.

Co-localization of these high-resolution techniques may start by quantifying baseline values of zirconium and its alloys with co-localized SKPFM and SEM/EDS. Variations in VPD values may be utilized as a predictive measure on how different additives affect performance. For instance, iron forms SPPs immediately when included in zirconium [301], while tin and niobium mix with zirconium for some atomic percent [302, 303]. How do these inclusions affect the VPD measurement across the initial zirconium alloy, and how could this drive the corrosion mechanism in a specific environment? This would be a great starting point for expansion of our understanding of the corrosion mechanisms by collecting interval data of various alloys in various environments.

Chapter 8 – Bi-Layer SEI Structure

To start, formation of a more controllable artificial SEI should be investigated. This includes achieving consistent porosity of the layer, as well as thickness. Similarly, a more controllable methodology of depositing the artificial SEI should be developed. The simplistic method of a wetted separator material followed by rinse has a poor tolerance to human error. Designing a method that can expand to a manufacturing-ready level would

be ideal; an example to investigate is a simple spin coating with a controlled precursor solution exposure, followed by an automated, repeatable rinsing step. Quality control measurements could be performed to ensure repeatability – this would require extensive usage of characterization tools. An example would be to use FIB-SEM and XPS to confirm structural and chemical repeatability, respectively.

Expansion of the porous artificial SEI to larger capacity cells (e.g., single-layer pouch cells) should also be initiated. This gives opportunity to see if this design is scalable and usable in a future application such as electric vehicles. Again, quality control efforts to ensure repeatability should be incorporated.

REFERENCES

1. Ceballos, G. and P.R. Ehrlich, *The misunderstood sixth mass extinction.* Science, **360** (6393), 1080-1081 (2018), DOI: 10.1126/science.aau0191.

2. Shivanna, K.R., *The Sixth Mass Extinction Crisis and its Impact on Biodiversity and Human Welfare.* Resonance-Journal of Science Education, **25** (1), 93-109 (2020), DOI: 10.1007/s12045-019-0924-z.

3. Fahrenkamp-Uppenbrink, J., *The Sixth Extinction: An Unnatural History.* Science, **346** (6214), 1176-1177 (2014),

4. Huang, B.Y., et al., *Extended Reconstructed Sea Surface Temperature, Version 5 (ERSSTv5): Upgrades, Validations, and Intercomparisons.* Journal of Climate, **30** (20), 8179-8205 (2017), DOI: 10.1175/Jcli-D-16-0836.1.

5. Menne, M.J., et al., *The Global Historical Climatology Network Monthly Temperature Dataset, Version 4.* Journal of Climate, **31** (24), 9835-9854 (2018), DOI: 10.1175/Jcli-D-18-0094.1.

6. Foote, E.N., *Circumstances Affecting the Heat of the Sun's Rays.* American Journal of Science and Arts, **22** 382-383 (1856),

7. van Loenhout, J., R. Below, and D. McClean, (2019), *Human cost of disasters: An overview of the last 20 years (2000-2019),* https://reliefweb.int/sites/reliefweb.int/files/resources/Human%20Cost%20of%20Disasters%202000-2019%20Report%20-%20UN%20Office%20for%20Disaster%20Risk%20Reduction.pdf.

8. Deutch, J., *Is Net Zero Carbon 2050 Possible?* Joule, **4** (11), 2237-2240 (2020), DOI: 10.1016/j.joule.2020.09.002.

9. IEA, (2021), *Net Zero by 2050,* Paris, https://www.iea.org/reports/net-zero-by-2050.

10. Zhang, Y.Y., Y. Zhang, and J. Zhang, *Environmental Impacts of Carbon Capture, Transmission, Enhanced Oil Recovery, and Sequestration: An Overview.* Environmental Forensics, **14** (4), 301-305 (2013), DOI: 10.1080/15275922.2013.843616.

11. Kahn, M.E., *Cheap and Clean How Americans Think About Energy in the Age of Global Warming.* Science, **347** (6219), 238-238 (2015), DOI: 10.1126/science.aaa1579.

12. Diaz, L.A. and T.E. Lister, *Economic evaluation of an electrochemical process for the recovery of metals from electronic waste.* Waste Management, **74** 384-392 (2018), DOI: 10.1016/j.wasman.2017.11.050.

13. Diaz, L.A., et al., *Comprehensive process for the recovery of value and critical materials from electronic waste.* Journal of Cleaner Production, **125** 236-244 (2016), DOI: 10.1016/j.jclepro.2016.03.061.

14. Diaz, L.A., et al., *Electrochemical-assisted leaching of active materials from lithium ion batteries.* Resources Conservation and Recycling, **161** (2020), DOI: 10.1016/j.resconrec.2020.104900.

15. Kesler, S.E., et al., *Global lithium resources: Relative importance of pegmatite, brine and other deposits.* Ore Geology Reviews, **48** 55-69 (2012), DOI: 10.1016/j.oregeorev.2012.05.006.

16. Callister, W.D. and D.G. Rethwisch, *Materials Science and Engineering, an Introduction*. 8th ed. 2010, Hoboken, NJ: John Wiley & Sons.

17. Jones, D.A., *Principles and Prevention of Corrosion*. 2nd ed. 1996, Upper Saddle River, NJ: Prentice-Hall, Inc.

18. Stojilovic, N., E.T. Bender, and R.D. Ramsier, *Surface chemistry of zirconium.* Progress in Surface Science, **78** (3-4), 101-184 (2005), DOI: 10.1016/j.progsurf.2005.07.001.

19. Couet, A., et al., *In-situ electrochemical impedance spectroscopy measurements of zirconium alloy oxide conductivity: Relationship to hydrogen pickup.* Corrosion Science, **119** 1-13 (2017), DOI: 10.1016/j.corsci.2016.12.008.

20. Cox, B., *Some thoughts on the mechanisms of in-reactor corrosion of zirconium alloys.* Journal of Nuclear Materials, **336** (2-3), 331-368 (2005), DOI: 10.1016/j.jnucmat.2004.09.029.

21. Cox, B., *The Oxidation and Corrosion of Zirconium and Its Alloys .5. Mechanism of Oxide Film Growth and Breakdown on Zirconium and Zircaloy-2.* Journal of the Electrochemical Society, **108** (1), 24-30 (1961), DOI: 10.1149/1.2428005.

22. Proff, C., S. Abolhassani, and C. Lemaignan, *Oxidation behaviour of zirconium alloys and their precipitates - A mechanistic study.* Journal of Nuclear Materials, **432** (1-3), 222-238 (2013), DOI: 10.1016/j.jnucmat.2012.06.026.

23. Wei, J., et al., *The effect of Sn on autoclave corrosion performance and corrosion mechanisms in Zr-Sn-Nb alloys.* Acta Materialia, **61** (11), 4200-4214 (2013), DOI: 10.1016/j.actamat.2013.03.046.

24. Ni, N., et al., *How the crystallography and nanoscale chemistry of the metal/oxide interface develops during the aqueous oxidation of zirconium cladding alloys.* Acta Materialia, **60** (20), 7132-7149 (2012), DOI: 10.1016/j.actamat.2012.09.021.

25. Douglass, D.L., *Oxide plasticity in the oxidation mechanism of zirconium and its alloys.* Corrosion Science, **5** (4), 255-262 (1965), DOI: 10.1016/S0010-938x(65)90592-5.

26. Vandegrift, J.L., et al., *Oxidation Behavior of Zirconium, Zircaloy-3, Zircaloy-4, Zr-1Nb, and Zr-2.65Nb in Air and Oxygen.* Nuclear Materials and Energy, (2019), DOI: 10.1016/j.nme.2019.100692.

27. Motta, A.T., A. Couet, and R.J. Comstock, *Corrosion of Zirconium Alloys Used for Nuclear Fuel Cladding.* Annual Review of Materials Research, **45** 311-343 (2015), DOI: 10.1146/annurev-matsci-070214-020951.

28. Couet, A., A.T. Motta, and A. Ambard, *The coupled current charge compensation model for zirconium alloy fuel cladding oxidation: I. Parabolic oxidation of zirconium alloys.* Corrosion Science, **100** 73-84 (2015), DOI: 10.1016/j.corsci.2015.07.003.

29. Bradhurst, D.H. and P.M. Heuer, *Influence of Oxide Stress on Breakaway Oxidation of Zircaloy-2.* Journal of Nuclear Materials, **37** (1), 35-+ (1970), DOI: 10.1016/0022-3115(70)90180-7.

30. Chong, K.B. and M.E. Fitzpatrick, *Evolution of stress fields and phase content in corroded zirconium cladding materials.* Surface & Coatings Technology, **324** 140-145 (2017), DOI: 10.1016/j.surfcoat.2017.05.072.

31. Zielinski, A. and S. Sobieszczyk, *Hydrogen-enhanced degradation and oxide effects in zirconium alloys for nuclear applications.* International Journal of Hydrogen Energy, **36** (14), 8619-8629 (2011), DOI: 10.1016/j.ijhydene.2011.04.002.

32. Duriez, C., D. Drouan, and G. Pouzadoux, *Reaction in air and in nitrogen of pre-oxidised Zircaloy-4 and M5 (TM) claddings.* Journal of Nuclear Materials, **441** (1-3), 84-95 (2013), DOI: 10.1016/j.jnucmat.2013.04.095.

33. Duriez, C., et al., *Zircaloy-4 and M5 (R) high temperature oxidation and nitriding in air.* Journal of Nuclear Materials, **380** (1-3), 30-45 (2008), DOI: 10.1016/j.jnucmat.2008.07.002.

34. Lasserre, M., et al., *Qualitative analysis of Zircaloy-4 cladding air degradation in O-2-N-2 mixtures at high temperature.* Materials and Corrosion-Werkstoffe Und Korrosion, **65** (3), 250-259 (2014), DOI: 10.1002/maco.201307078.

35. Lasserre, M., et al., *Modelling of Zircaloy-4 accelerated degradation kinetics in nitrogen-oxygen mixtures at 850 degrees C.* Journal of Nuclear Materials, **462** 221-229 (2015), DOI: 10.1016/j.jnucmat.2015.03.052.

36. Guerain, M., et al., *Review of stress fields in Zirconium alloys corrosion scales.* Corrosion Science, **95** 11-21 (2015), DOI: 10.1016/j.corsci.2015.03.004.

37. Kurpaska, L., et al., *In-situ stress analysis of the Zr/ZrO2 system as studied by Raman spectroscopy and deflection test in monofacial oxidation techniques.* Applied Surface Science, **385** 106-112 (2016), DOI: 10.1016/j.apsusc.2016.05.074.

38. Kurpaska, L., et al., *Raman spectroscopy analysis of air grown oxide scale developed on pure zirconium substrate.* Journal of Nuclear Materials, **466** 460-467 (2015), DOI: 10.1016/j.jnucmat.2015.06.005.

39. Kurpaska, L., et al., *On the determination of growth stress during oxidation of pure zirconium at elevated temperature.* Applied Surface Science, **446** 27-35 (2018), DOI: 10.1016/j.apsusc.2018.02.215.

40. Kurpaska, L., et al., *Zirconia Layer Formed by High Temperature Oxidation of Pure Zirconium: Stress Generated at the Zirconium/Zirconia Interface.* Oxidation of Metals, **79** (3-4), 261-277 (2013), DOI: 10.1007/s11085-012-9348-9.

41. Kurpaska, L., et al., *Stress analysis of zirconia studied by Raman spectroscopy at low temperatures.* Spectrochimica Acta Part a-Molecular and Biomolecular Spectroscopy, **131** 691-695 (2014), DOI: 10.1016/j.saa.2014.05.023.

42. Idarraga, I., et al., *Potentialities of Raman Imaging for the Analysis of Oxide Scales Formed on Zircaloy-4 and M5 (R) in Air at High Temperature.* Oxidation of Metals, **79** (3-4), 289-302 (2013), DOI: 10.1007/s11085-012-9331-5.

43. Idarraga, I., et al., *Raman investigation of pre- and post-breakaway oxide scales formed on Zircaloy-4 and M5 (R) in air at high temperature.* Journal of Nuclear Materials, **421** (1-3), 160-171 (2012), DOI: 10.1016/j.jnucmat.2011.11.071.

44. Barberis, P., et al., *Raman spectra of tetragonal zirconia: powder to zircaloy oxide frequency shift.* Journal of Nuclear Materials, **288** (2-3), 241-247 (2001), DOI: 10.1016/S0022-3115(00)00727-3.

45. Barberis, P., T. MerleMejean, and P. Quintard, *On Raman spectroscopy of zirconium oxide films.* Journal of Nuclear Materials, **246** (2-3), 232-243 (1997), DOI: 10.1016/S0022-3115(97)00038-X.

46. Duriez, C., et al., *Separate-effect tests on zirconium cladding degradation in air ingress situations.* Nuclear Engineering and Design, **239** (2), 244-253 (2009), DOI: 10.1016/j.nucengdes.2008.10.017.

47. Steinbruck, M., *Prototypical experiments relating to air oxidation of Zircaloy-4 at high temperatures.* Journal of Nuclear Materials, **392** (3), 531-544 (2009), DOI: 10.1016/j.jnucmat.2009.04.018.

48. Steinbruck, M. and M. Bottcher, *Air oxidation of Zircaloy-4, M5 (R) and ZIRLO (TM) cladding alloys at high temperatures.* Journal of Nuclear Materials, **414** (2), 276-285 (2011), DOI: 10.1016/j.jnucmat.2011.04.012.

49. Steinbruck, M., N. Ver, and M. Grosse, *Oxidation of Advanced Zirconium Cladding Alloys in Steam at Temperatures in the Range of 600-1200 degrees C.* Oxidation of Metals, **76** (3-4), 215-232 (2011), DOI: 10.1007/s11085-011-9249-3.

50. Oskarsson, M., E. Ahlberg, and K. Pettersson, *Oxidation of Zircaloy-2 and Zircaloy-4 in water and lithiated water at 360 degrees C.* Journal of Nuclear Materials, **295** (1), 97-108 (2001), DOI: 10.1016/S0022-3115(01)00480-9.

51. Olander, D.R., et al., *Chemical processes in defective LWR fuel rods.* Journal of Nuclear Materials, **248** 214-219 (1997), DOI: 10.1016/S0022-3115(97)00172-4.

52. Michel, B., et al., *3D fuel cracking modelling in pellet cladding mechanical interaction.* Engineering Fracture Mechanics, **75** (11), 3581-3598 (2008), DOI: 10.1016/j.engfracmech.2006.12.014.

53. Nikulin, S.A. and A.B. Rozhnov, *Corrosion cracking of zirconium cladding tubes. A review. 2. Effect of external factors, structure, and properties of the alloys.* Metal Science and Heat Treatment, **47** (9-10), 427-433 (2005), DOI: 10.1007/s11041-006-0006-1.

54. Jenssen, H.K., et al., (2017), *PIE results and mechanistic interpretation on on-line EIS data from the cladding corrosion test IFA-731, HWR-1156,* OCECD Halden Reactor Project,

55. Wang, C.H., et al., *All-solid-state lithium batteries enabled by sulfide electrolytes: from fundamental research to practical engineering design.* Energy & Environmental Science, **14** (5), 2577-2619 (2021), DOI: 10.1039/d1ee00551k.

56. Zheng, Y., et al., *A review of composite solid-state electrolytes for lithium batteries: fundamentals, key materials and advanced structures.* Chemical Society Reviews, **49** (23), 8790-8839 (2020), DOI: 10.1039/d0cs00305k.

57. Zhao, Q., et al., *Designing solid-state electrolytes for safe, energy-dense batteries.* Nature Reviews Materials, **5** (3), 229-252 (2020), DOI: 10.1038/s41578-019-0165-5.

58. Wang, L.G., et al., *Fundamentals of Electrolytes for Solid-State Batteries: Challenges and Perspectives.* Frontiers in Materials, **7** (2020), DOI: 10.3389/fmats.2020.00111.

59. Ji, X., et al., *Solid-State Electrolyte Design for Lithium Dendrite Suppression.* Advanced Materials, (2020), DOI: 10.1002/adma.202002741.

60. Schnell, J., et al., *All-solid-state lithium-ion and lithium metal batteries - paving the way to large-scale production.* Journal of Power Sources, **382** 160-175 (2018), DOI: 10.1016/j.jpowsour.2018.02.062.

61. Whittingham, M.S., *Electrical Energy Storage and Intercalation Chemistry.* Science, **192** (4244), 1126 (1976), DOI: 10.1126/science.192.4244.1126.

62. Lin, D.C., Y.Y. Liu, and Y. Cui, *Reviving the lithium metal anode for high-energy batteries.* Nature Nanotechnology, **12** (3), 194-206 (2017), DOI: 10.1038/Nnano.2017.16.

63. Liu, C.F., Z.G. Neale, and G.Z. Cao, *Understanding electrochemical potentials of cathode materials in rechargeable batteries.* Materials Today, **19** (2), 109-123 (2016), DOI: 10.1016/j.mattod.2015.10.009.

64. Winter, M., B. Barnett, and K. Xu, *Before Li Ion Batteries.* Chemical Reviews, **118** (23), 11433-11456 (2018), DOI: 10.1021/acs.chemrev.8b00422.

65. J.-K., P., *Principles and Applications of Lithium Secondary Batteries*. 2012.

66. Liu, J., et al., *Pathways for practical high-energy long-cycling lithium metal batteries.* Nature Energy, **4** (3), 180-186 (2019), DOI: 10.1038/s41560-019-0338-x.

67. Mukhopadhyay, A. and M.K. Jangid, *Li metal battery, heal thyself.* Science, **359** (6383), 1463-1463 (2018), DOI: 10.1126/science.aat2452.

68. Takehara, Z., *Future prospects of the lithium metal anode.* Journal of Power Sources, **68** (1), 82-86 (1997), DOI: Doi 10.1016/S0378-7753(96)02546-3.

69. Aurbach, D., et al., *New insights into the interactions between electrode materials and electrolyte solutions for advanced nonaqueous batteries.* Journal of Power Sources, **81** 95-111 (1999), DOI: 10.1016/S0378-7753(99)00187-1.

70. Peled, E., *The Electrochemical-Behavior of Alkali and Alkaline-Earth Metals in Non-Aqueous Battery Systems - the Solid Electrolyte Interphase Model.* Journal of the Electrochemical Society, **126** (12), 2047-2051 (1979), DOI: 10.1149/1.2128859.

71. Peled, E. and S. Menkin, *Review-SEI: Past, Present and Future.* Journal of the Electrochemical Society, **164** (7), A1703-A1719 (2017), DOI: 10.1149/2.1441707jes.

72. Meyerson, M.L., et al., *The effect of local lithium surface chemistry and topography on solid electrolyte interphase composition and dendrite nucleation.* Journal of Materials Chemistry A, **7** (24), 14882-14894 (2019), DOI: 10.1039/c9ta03371h.

73. Ding, F., et al., *Dendrite-Free Lithium Deposition via Self-Healing Electrostatic Shield Mechanism.* Journal of the American Chemical Society, **135** (11), 4450-4456 (2013), DOI: 10.1021/ja312241y.

74. Wu, F.X., et al., *Lithium Iodide as a Promising Electrolyte Additive for Lithium-Sulfur Batteries: Mechanisms of Performance Enhancement.* Advanced Materials, **27** (1), 101-108 (2015), DOI: 10.1002/adma.201404194.

75. Shi, P.C., et al., *A highly concentrated phosphate-based electrolyte for high-safety rechargeable lithium batteries.* Chemical Communications, **54** (35), 4453-4456 (2018), DOI: 10.1039/c8cc00994e.

76. Zheng, J.M., et al., *Electrolyte additive enabled fast charging and stable cycling lithium metal batteries.* Nature Energy, **2** (3), (2017), DOI: 10.1038/nenergy.2017.12.

77. Kazyak, E., K.N. Wood, and N.P. Dasgupta, *Improved Cycle Life and Stability of Lithium Metal Anodes through Ultrathin Atomic Layer Deposition Surface Treatments.* Chemistry of Materials, **27** (18), 6457-6462 (2015), DOI: 10.1021/acs.chemmater.5b02789.

78. Lin, D.C., et al., *Conformal Lithium Fluoride Protection Layer on Three-Dimensional Lithium by Nonhazardous Gaseous Reagent Freon.* Nano Letters, **17** (6), 3731-3737 (2017), DOI: 10.1021/acs.nanolett.7b01020.

79. Lang, J.L., et al., *One-pot solution coating of high quality LiF layer to stabilize Li metal anode.* Energy Storage Materials, **16** 85-90 (2019), DOI: 10.1016/j.ensm.2018.04.024.

80. Liu, W., et al., *Core-Shell Nanoparticle Coating as an Interfacial Layer for Dendrite Free Lithium Metal Anodes.* Acs Central Science, **3** (2), 135-140 (2017), DOI: 10.1021/acscentsci.6b00389.

81. Lu, Q.W., et al., *Dendrite-Free, High-Rate, Long-Life Lithium Metal Batteries with a 3D Cross-Linked Network Polymer Electrolyte.* Advanced Materials, **29** (13), (2017), DOI: 10.1002/Adma.201604460.

82. Wang, C.Z., et al., *Controlling Li Ion Flux through Materials Innovation for Dendrite-Free Lithium Metal Anodes.* Advanced Functional Materials, **29** (49), (2019), DOI: 10.1002/adfm.201905940.

83. Zhang, H.M., et al., *Lithiophilic-lithiophobic gradient interfacial layer for a highly stable lithium metal anode.* Nature Communications, **9** (2018), DOI: 10.1038/s41467-018-06126-z.

84. Efaw, C.M., et al., *A closed-host bi-layer dense/porous solid electrolyte interphase for enhanced lithium-metal anode stability.* Materials Today, **In Press** (2021), DOI: 10.1016/j.mattod.2021.04.018.

85. Cao, X., et al., *Review-Localized High-Concentration Electrolytes for Lithium Batteries.* Journal of the Electrochemical Society, **168** (1), (2021), DOI: 10.1149/1945-7111/abd60e.

86. Ren, X.D., et al., *Localized High-Concentration Sulfone Electrolytes for High-Efficiency Lithium-Metal Batteries.* Chem, **4** (8), 1877-1892 (2018), DOI: 10.1016/j.chempr.2018.05.002.

87. Zheng, Y., et al., *Localized high concentration electrolyte behavior near a lithium-metal anode surface.* Journal of Materials Chemistry A, **7** (43), 25047-25055 (2019), DOI: 10.1039/c9ta08935g.

88. Cao, X., et al., *Monolithic solid-electrolyte interphases formed in fluorinated orthoformate-based electrolytes minimize Li depletion and pulverization.* Nature Energy, **4** (9), 796-805 (2019), DOI: 10.1038/s41560-019-0464-5.

89. Holoubek, J., et al., *Tailoring electrolyte solvation for Li metal batteries cycled at ultra-low temperature.* Nature Energy, **6** (3), 303-313 (2021), DOI: 10.1038/s41560-021-00783-z.

90. Holoubek, J., et al., *An All-Fluorinated Ester Electrolyte for Stable High-Voltage Li Metal Batteries Capable of Ultra-Low-Temperature Operation.* Acs Energy Letters, **5** (5), 1438-1447 (2020), DOI: 10.1021/acsenergylett.0c00643.

91. Li, Y.Z., et al., *Correlating Structure and Function of Battery Interphases at Atomic Resolution Using Cryoelectron Microscopy.* Joule, **2** (10), 2167-2177 (2018), DOI: 10.1016/j.joule.2018.08.004.

92. Wang, X.F., Y.J. Li, and Y.S. Meng, *Cryogenic Electron Microscopy for Characterizing and Diagnosing Batteries.* Joule, **2** (11), 2225-2234 (2018), DOI: 10.1016/j.joule.2018.10.005.

93. Wang, X.F., et al., *Glassy Li metal anode for high-performance rechargeable Li batteries.* Nature Materials, **19** (12), 1339-+ (2020), DOI: 10.1038/s41563-020-0729-1.

94. Tang, W., et al., *Chemically polished lithium metal anode for high energy lithium metal batteries.* Energy Storage Materials, **14** 289-296 (2018), DOI: 10.1016/j.ensm.2018.05.009.

95. Chen, L., et al., *Novel ALD Chemistry Enabled Low-Temperature Synthesis of Lithium Fluoride Coatings for Durable Lithium Anodes.* Acs Applied Materials & Interfaces, **10** (32), 26972-26981 (2018), DOI: 10.1021/acsami.8b04573.

96. Gao, Z.G., et al., *Protection of Li metal anode by surface-coating of PVDF thin film to enhance the cycling performance of Li batteries.* Chinese Chemical Letters, **30** (2), 525-528 (2019), DOI: 10.1016/j.cclet.2018.05.016.

97. Ko, J. and Y.S. Yoon, *Recent progress in LiF materials for safe lithium metal anode of rechargeable batteries: Is LiF the key to commercializing Li metal batteries?* Ceramics International, **45** (1), 30-49 (2019), DOI: 10.1016/j.ceramint.2018.09.287.

98. Tan, J., et al., *A Growing Appreciation for the Role of LiF in the Solid Electrolyte Interphase.* Advanced Energy Materials, **11** (16), (2021), DOI: 10.1002/aenm.202100046.

99. Cheng, X.B., et al., *Dendrite-Free Lithium Deposition Induced by Uniformly Distributed Lithium Ions for Efficient Lithium Metal Batteries.* Advanced Materials, **28** (15), 2888-2895 (2016), DOI: 10.1002/adma.201506124.

100. Shah, D., et al., *Tutorial on interpreting x-ray photoelectron spectroscopy survey spectra: Questions and answers on spectra from the atomic layer deposition of Al2O3 on silicon.* Journal of Vacuum Science & Technology B, **36** (6), (2018), DOI: 10.1116/1.5043297.

101. Shi, L.L., et al., *Reaction heterogeneity in practical high-energy lithium-sulfur pouch cells.* Energy & Environmental Science, **13** (10), 3620-3632 (2020), DOI: 10.1039/d0ee02088e.

102. Verma, P., P. Maire, and P. Novak, *A review of the features and analyses of the solid electrolyte interphase in Li-ion batteries.* Electrochimica Acta, **55** (22), 6332-6341 (2010), DOI: 10.1016/j.electacta.2010.05.072.

103. Xu, K., *Electrolytes and Interphases in Li-Ion Batteries and Beyond.* Chemical Reviews, **114** (23), 11503-11618 (2014), DOI: 10.1021/cr500003w.

104. Kang, S.J., et al., *Unraveling the role of LiFSI electrolyte in the superior performance of graphite anodes for Li-ion batteries.* Electrochimica Acta, **259** 949-954 (2018), DOI: 10.1016/j.electacta.2017.11.018.

105. Sun, B., et al., *At the polymer electrolyte interfaces: the role of the polymer host in interphase layer formation in Li-batteries.* Journal of Materials Chemistry A, **3** (26), 13994-14000 (2015), DOI: 10.1039/c5ta02485d.

106. Zhao, Y.M., et al., *Stable Li Metal Anode by a Hybrid Lithium Polysulfidophosphate/Polymer Cross-Linking Film.* Acs Energy Letters, **4** (6), 1271-1278 (2019), DOI: 10.1021/acsenergylett.9b00539.

107. Baer, D.R., et al., *Introduction to topical collection: Reproducibility challenges and solutions with a focus on guides to XPS analysis.* Journal of Vacuum Science & Technology A, **39** (2), (2021), DOI: 10.1116/6.0000873.

108. Efaw, C.M., et al. *Determination of Zirconium Oxide Chemistry Through Complementary Characterization Techniques*. in *GLOBAL 2019 - International Nuclear Fuel Cycle Conference and TOP FUEL 2019 - Light Water Reactor Fuel Performance Conference*. 2019. Seattle, WA: American Nuclear Society.

109. Nagasaki, M., K. Nishikawa, and K. Kanamura, *Deterioration Analysis of Lithium Metal Anode in Full Cell during Long-Term Cycles.* Journal of the Electrochemical Society, **166** (12), A2618-A2628 (2019), DOI: 10.1149/2.1151912jes.

110. Hu, H., et al., (2019), *Development of an Electrochemical Impedance Instrument for Monitoring Corrosion Formation (Oxide and Hydride) on Cladding Materials,* US DOE Office of Nuclear Energy, OSTI Identifier 1605005, https://www.osti.gov/biblio/1605005-development-electrochemical-impedance-instrument-monitoring-corrosion-formation-oxide-hydride-cladding-materials.

111. Efaw, C.M., et al., *Characterization of zirconium oxides part II: New insights on the growth of zirconia revealed through complementary high-resolution mapping techniques.* Corrosion Science, **167** (2020), DOI: 10.1016/j.corsci.2020.108491.

112. Efaw, C.M., et al., *Characterization of zirconium oxides part I: Raman mapping and spectral feature analysis.* Nuclear Materials and Energy, **21** (2019), DOI: 10.1016/j.nme.2019.100707.

113. Naumenko, A.P., et al., *Vibrational Analysis and Raman Spectra of Tetragonal Zirconia.* Physics and Chemistry of Solid State, **9** (1), 121-125 (2008),

114. Kurpaska, L., *Structural properties of zirconia - in-situ high temperature XRD characterization.* Journal of Molecular Structure, **1163** 287-293 (2018), DOI: 10.1016/j.molstruc.2018.03.010.

115. Jiang, L.L., et al., *Inhibiting Solvent Co-Intercalation in a Graphite Anode by a Localized High-Concentration Electrolyte in Fast-Charging Batteries.* Angewandte Chemie-International Edition, **60** (7), 3402-3406 (2021), DOI: 10.1002/anie.202009738.

116. Xu, K., et al., *Recent development of PeakForce Tapping mode atomic force microscopy and its applications on nanoscience.* Nanotechnology Reviews, **7** (6), 605-621 (2018), DOI: 10.1515/ntrev-2018-0086.

117. Pittenger, B., N. Erina, and C. Su, (2010), *Quantitative mechanical property mapping at the nanoscale with PeakForce QNM,*

118. Davis, P.H., et al., *Localized deformation in Ni-Mn-Ga single crystals.* Journal of Applied Physics, **123** (21), (2018), DOI: 10.1063/1.5026572.

119. Reinhold, M., et al., *Transformation twinning of Ni-Mn-Ga characterized with temperature-controlled atomic force microscopy.* Journal of Applied Physics, **107** (11), (2010), DOI: 10.1063/1.3429090.

120. Bui, H., et al. *Atomic force microscopy of DNA self-assembled nanostructures for device applications*. in *International Semiconductor Device Research Symposium*. 2009. College Park, MD, USA: IEEE.

121. Kvryan, A., et al., *Corrosion Initiation and Propagation on Carburized Martensitic Stainless Steel Surfaces Studied via Advanced Scanning Probe Microscopy.* Materials, **12** (6), (2019), DOI: 10.3390/ma12060940.

122. Efaw, C.M., et al., *Toward Improving Ambient Volta Potential Measurements with SKPFM for Corrosion Studies.* Journal of the Electrochemical Society, **166** (11), C3018-C3027 (2019), DOI: 10.1149/2.0041911jes.

123. Krok, F., et al., *Lateral resolution and potential sensitivity in Kelvin probe force microscopy: Towards understanding of the sub-nanometer resolution.* Physical Review B, **77** (23), 235427 (2008), DOI: 10.1103/Physrevb.77.235427.

124. Sadewasser, S., et al., *New Insights on Atomic-Resolution Frequency-Modulation Kelvin-Probe Force-Microscopy Imaging of Semiconductors.* Physical Review Letters, **103** (26), (2009), DOI: 10.1103/PhysRevLett.103.266103.

125. Hoppe, H., et al., *Kelvin probe force microscopy study on conjugated polymer/fullerene bulk heterojunction organic solar cells.* Nano Letters, **5** (2), 269-274 (2005), DOI: 10.1021/nl048176c.

126. Sadewasser, S., et al., *Kelvin probe force microscopy for the nano scale characterization of chalcopyrite solar cell materials and devices.* Thin Solid Films, **431** 257-261 (2003), DOI: 10.1016/S0040-6090(03)00267-0.

127. Hurley, M.F., et al., *Volta Potentials Measured by Scanning Kelvin Probe Force Microscopy as Relevant to Corrosion of Magnesium Alloys.* Corrosion, **71** (2), 160-170 (2015), DOI: 10.5006/1432.

128. Kvryan, A., et al., *Microgalvanic Corrosion Behavior of Cu-Ag Active Braze Alloys Investigated with SKPFM.* Metals, **6** (4), 91 (2016), DOI: 10.3390/Met6040091.

129. Ornek, C. and D.L. Engelberg, *SKPFM measured Volta potential correlated with strain localisation in microstructure to understand corrosion susceptibility of cold-rolled grade 2205 duplex stainless steel.* Corrosion Science, **99** 164-171 (2015), DOI: 10.1016/j.corsci.2015.06.035.

130. Ornek, C., et al., *Characterization of 475 degrees C Embrittlement of Duplex Stainless Steel Microstructure via Scanning Kelvin Probe Force Microscopy and Magnetic Force Microscopy.* Journal of the Electrochemical Society, **164** (6), C207-C217 (2017), DOI: 10.1149/2.0311706jes.

131. Pan, T.Y., *Corrosion behavior of a duplex stainless steel under cyclic loading: a scanning Kelvin probe force microscopy (SKPFM) based microscopic study.* Journal of Applied Electrochemistry, **42** (12), 1049-1056 (2012), DOI: 10.1007/s10800-012-0479-0.

132. Benzing, J.T., et al., *Impact of grain orientation and phase on Volta potential differences in an additively manufactured titanium alloy.* Aip Advances, **11** (2), (2021), DOI: 10.1063/5.0038114.

133. Schmutz, P. and G.S. Frankel, *Characterization of AA2024-T3 by scanning Kelvin probe force microscopy.* Journal of the Electrochemical Society, **145** (7), 2285-2295 (1998), DOI: 10.1149/1.1838633.

134. Schmutz, P. and G.S. Frankel, *Corrosion study of AA2024-T3 by scanning Kelvin probe force microscopy and in situ atomic force microscopy scratching.* Journal of the Electrochemical Society, **145** (7), 2295-2306 (1998), DOI: 10.1149/1.1838634.

135. Zhu, X.H., R.I. Revilla, and A. Hubin, *Direct Correlation between Local Surface Potential Measured by Kelvin Probe Force Microscope and Electrochemical Potential of LiNi0.80Co0.15Al0.05O2 Cathode at Different State of Charge.* Journal of Physical Chemistry C, **122** (50), 28556-28563 (2018), DOI: 10.1021/acs.jpcc.8b10364.

136. Nagpure, S.C., B. Bhushan, and S.S. Babu, *Surface potential measurement of aged Li-ion batteries using Kelvin probe microscopy.* Journal of Power Sources, **196** (3), 1508-1512 (2011), DOI: 10.1016/j.jpowsour.2010.08.031.

137. Masuda, H., et al., *Internal potential mapping of charged solid-state-lithium ion batteries using in situ Kelvin probe force microscopy.* Nanoscale, **9** (2), 893-898 (2017), DOI: 10.1039/c6nr07971g.

138. Masuda, H., et al., *Dynamically visualizing battery reactions by operando Kelvin probe force microscopy.* Communications Chemistry, **2** (2019), DOI: 10.1038/s42004-019-0245-x.

139. Luchkin, S.Y., et al., *Li distribution in graphite anodes: A Kelvin Probe Force Microscopy approach.* Journal of Power Sources, **268** 887-894 (2014), DOI: 10.1016/j.jpowsour.2014.06.143.

140. Wu, J.X., et al., *Multi-characterization of LiCoO2 cathode films using advanced AFM-based techniques with high resolution.* Scientific Reports, **7** (2017), DOI: 10.1038/s41598-017-11623-0.

141. Kitta, M. and H. Sano, *Real-Time Observation of Li Deposition on a Li Electrode with Operand Atomic Force Microscopy and Surface Mechanical Imaging.* Langmuir, **33** (8), 1861-1866 (2017), DOI: 10.1021/acs.langmuir.6b04651.

142. Bard, A.J., et al., *Scanning Electrochemical Microscopy - Introduction and Principles.* Analytical Chemistry, **61** (2), 132-138 (1989), DOI: 10.1021/ac00177a011.

143. Engstrom, R.C. and C.M. Pharr, *Scanning Electrochemical Microscopy.* Analytical Chemistry, **61** (19), A1099-+ (1989), DOI: 10.1021/ac00194a002.

144. Kwak, J. and A.J. Bard, *Scanning Electrochemical Microscopy - Apparatus and Two-Dimensional Scans of Conductive and Insulating Substrates.* Analytical Chemistry, **61** (17), 1794-1799 (1989), DOI: 10.1021/ac00192a003.

145. Kwak, J. and A.J. Bard, *Scanning Electrochemical Microscopy - Theory of the Feedback Mode.* Analytical Chemistry, **61** (11), 1221-1227 (1989), DOI: 10.1021/ac00186a009.

146. Sun, P., F.O. Laforge, and M.V. Mirkin, *Scanning electrochemical microscopy in the 21st century.* Physical Chemistry Chemical Physics, **9** (7), 802-823 (2007), DOI: 10.1039/b612259k.

147. Nonnenmacher, M., M.P. Oboyle, and H.K. Wickramasinghe, *Kelvin Probe Force Microscopy.* Applied Physics Letters, **58** (25), 2921-2923 (1991), DOI: 10.1063/1.105227.

148. Weaver, J.M.R. and D.W. Abraham, *High-Resolution Atomic Force Microscopy Potentiometry.* Journal of Vacuum Science & Technology B, **9** (3), 1559-1561 (1991), DOI: 10.1116/1.585423.

149. Rohwerder, M. and F. Turcu, *High-resolution Kelvin probe microscopy in corrosion science: Scanning Kelvin probe force microscopy (SKPFM) versus classical scanning Kelvin probe (SKP).* Electrochimica Acta, **53** (2), 290-299 (2007), DOI: 10.1016/j.electacta.2007.03.016.

150. Leng, Y., et al., *Atomic Ordering of Gainp Studied by Kelvin Probe Force Microscopy.* Applied Physics Letters, **66** (10), 1264-1266 (1995), DOI: 10.1063/1.113257.

151. Lee, N.J., et al., *The interlayer screening effect of graphene sheets investigated by Kelvin probe force microscopy.* Applied Physics Letters, **95** (22), 222107 (2009), DOI: 10.1063/1.3269597.

152. Sadewasser, S., N. Nicoara, and S.D. Solares, *Artifacts in time-resolved Kelvin probe force microscopy.* Beilstein Journal of Nanotechnology, **9** 1272-1281 (2018), DOI: 10.3762/bjnano.9.119.

153. Slobodian, O.M., et al., *Low-Temperature Reduction of Graphene Oxide: Electrical Conductance and Scanning Kelvin Probe Force Microscopy.* Nanoscale Research Letters, **13** (2018), DOI: 10.1186/S11671-018-2536-Z.

154. Campestrini, P., et al., *Relation between microstructural aspects of AA2024 and its corrosion behaviour investigated using AFM scanning potential technique.* Corrosion Science, **42** (11), 1853-1861 (2000), DOI: 10.1016/S0010-938x(00)00002-0.

155. Andreatta, F., H. Terryn, and J.H.W. de Wit, *Effect of solution heat treatment on galvanic coupling between intermetallics and matrix in AA7075-T6.* Corrosion Science, **45** (8), 1733-1746 (2003), DOI: 10.1016/S0010-938x(03)00004-0.

156. Andreatta, F., H. Terryn, and J.H.W. de Wit, *Corrosion behaviour of different tempers of AA7075 aluminium alloy.* Electrochimica Acta, **49** (17-18), 2851-2862 (2004), DOI: 10.1016/j.electacta.2004.01.046.

157. Larignon, C., et al., *Combined Kelvin probe force microscopy and secondary ion mass spectrometry for hydrogen detection in corroded 2024 aluminium alloy.* Electrochimica Acta, **110** 484-490 (2013), DOI: 10.1016/j.electacta.2013.02.063.

158. Ornek, C. and D.L. Engelberg, *Correlative EBSD and SKPFM characterisation of microstructure development to assist determination of corrosion propensity in grade 2205 duplex stainless steel.* Journal of Materials Science, **51** (4), 1931-1948 (2016), DOI: 10.1007/s10853-015-9501-3.

159. Yan, Y., et al., *Study of the tribocorrosion behaviors of albumin on a cobalt-based alloy using scanning Kelvin probe force microscopy and atomic force microscopy.* Electrochemistry Communications, **64** 61-64 (2016), DOI: 10.1016/j.elecom.2016.01.015.

160. Jin, Y., et al., *First-Principle Calculation of Volta Potential of Intermetallic Particles in Aluminum Alloys and Practical Implications.* Journal of the Electrochemical Society, **164** (9), C465-C473 (2017), DOI: 10.1149/2.0191709jes.

161. Ornek, C., et al., *Volta Potential Evolution of Intermetallics in Aluminum Alloy Microstructure Under Thin Aqueous Adlayers: A combined DFT and Experimental Study.* Topics in Catalysis, **61** (9-11), 1169-1182 (2018), DOI: 10.1007/s11244-018-0939-9.

162. Nazarov, A.P. and D. Thierry, *Scanning Kelvin probe study of metal/polymer interfaces.* Electrochimica Acta, **49** (17-18), 2955-2964 (2004), DOI: 10.1016/j.electacta.2004.01.054.

163. Frankel, G.S., et al., *Potential control under thin aqueous layers using a Kelvin Probe.* Corrosion Science, **49** (4), 2021-2036 (2007), DOI: 10.1016/j.corsci.2006.10.017.

164. Ozkanat, O., et al., *Scanning Kelvin Probe Study of (Oxyhydr)oxide Surface of Aluminum Alloy (vol 116, pg 1805, 2012).* Journal of Physical Chemistry C, **116** (10), 6505-6505 (2012), DOI: 10.1021/jp301959u.

165. Afshar, F.N., et al., *Scanning Kelvin probe force microscopy as a means of predicting the electrochemical characteristics of the surface of a modified AA4xxx/AA3xxx (Al alloys) brazing sheet.* Electrochimica Acta, **88** 330-339 (2013), DOI: 10.1016/j.electacta.2012.10.051.

166. Cook, A.B., et al., *Calibration of the scanning Kelvin probe force microscope under controlled environmental conditions.* Electrochimica Acta, **66** 100-105 (2012), DOI: 10.1016/j.electacta.2012.01.054.

167. Jia, J.X., et al., *Simulation of galvanic corrosion of magnesium coupled to a steel fastener in NaCl solution.* Materials and Corrosion-Werkstoffe Und Korrosion, **56** (7), 468-474 (2005), DOI: 10.1002/maco.200403855.

168. de Wit, J.H.W., *Local potential measurements with the SKPFM on aluminium alloys.* Electrochimica Acta, **49** (17-18), 2841-2850 (2004), DOI: 10.1016/j.electacta.2004.01.045.

169. Sathirachinda, N., R. Pettersson, and J.S. Pan, *Depletion effects at phase boundaries in 2205 duplex stainless steel characterized with SKPFM and TEM/EDS.* Corrosion Science, **51** (8), 1850-1860 (2009), DOI: 10.1016/j.corsci.2009.05.012.

170. Sathirachinda, N., et al., *Scanning Kelvin probe force microscopy study of chromium nitrides in 2507 super duplex stainless steel-Implications and limitations.* Electrochimica Acta, **56** (4), 1792-1798 (2011), DOI: 10.1016/j.electacta.2010.08.038.

171. Schaller, R.F. and J.R. Scully, *Spatial determination of diffusible hydrogen concentrations proximate to pits in a Fe-Cr-Ni-Mo steel using the Scanning Kelvin Probe.* Electrochemistry Communications, **63** 5-9 (2016), DOI: 10.1016/j.elecom.2015.12.002.

172. Schaller, R.F. and J.R. Scully, *Measurement of effective hydrogen diffusivity using the Scanning Kelvin Probe.* Electrochemistry Communications, **40** 42-44 (2014), DOI: 10.1016/j.elecom.2013.12.025.

173. Davoodi, A., et al., *Integrated AFM and SECM for in situ studies of localized corrosion of Al alloys.* Electrochimica Acta, **52** (27), 7697-7705 (2007), DOI: 10.1016/j.electacta.2006.12.073.

174. Frumkin, A. and A. Gorodetzkaja, *Capillary electric phenomena in amalgams. I Thallium amalgams.* Zeitschrift Fur Physikalische Chemie--Stochiometrie Und Verwandtschaftslehre, **136** (6), 451-472 (1928), DOI: 10.1515/zpch-1928-13634.

175. Melitz, W., et al., *Kelvin probe force microscopy and its application.* Surface Science Reports, **66** (1), 1-27 (2011), DOI: 10.1016/j.surfrep.2010.10.001.

176. Stratmann, M., *The Investigation of the Corrosion Properties of Metals, Covered with Adsorbed Electrolyte Layers - a New Experimental-Technique.* Corrosion Science, **27** (8), 869-872 (1987), DOI: 10.1016/0010-938x(87)90043-6.

177. Stratmann, M. and H. Streckel, *On the Atmospheric Corrosion of Metals Which Are Covered with Thin Electrolyte Layers .2. Experimental Results.* Corrosion Science, **30** (6-7), 697-714 (1990), DOI: 10.1016/0010-938x(90)90033-2.

178. Stratmann, M. and H. Streckel, *On the Atmospheric Corrosion of Metals Which Are Covered with Thin Electrolyte Layers .1. Verification of the Experimental-Technique.* Corrosion Science, **30** (6-7), 681-696 (1990), DOI: 10.1016/0010-938x(90)90032-Z.

179. Stratmann, M., et al., *On the Atmospheric Corrosion of Metals Which Are Covered with Thin Electrolyte Layers .3. The Measurement of Polarization Curves on Metal-Surfaces Which Are Covered by Thin Electrolyte Layers.* Corrosion Science, **30** (6-7), 715-734 (1990), DOI: 10.1016/0010-938x(90)90034-3.

180. Guillaumin, V., P. Schmutz, and G.S. Frankel, *Characterization of corrosion interfaces by the scanning Kelvin probe force microscopy technique.* Journal of the Electrochemical Society, **148** (5), B163-B173 (2001), DOI: 10.1149/1.1359199.

181. Kvryan, A., et al., *Microgalvanic Corrosion Behavior of Cu-Ag Active Braze Alloys Investigated with SKPFM.* Metals, **6** (4), (2016), DOI: 10.3390/met6040091.

182. Coy, A.E., et al., *Susceptibility of rare-earth-magnesium alloys to micro-galvanic corrosion.* Corrosion Science, **52** (12), 3896-3906 (2010), DOI: 10.1016/j.corsci.2010.08.006.

183. Vieira, L., et al., *Scratch testing for micro- and nanoscale evaluation of tribocharging in DLC films containing silver nanoparticles using AFM and KPFM techniques.* Surface & Coatings Technology, **260** 205-213 (2014), DOI: 10.1016/j.surfcoat.2014.06.065.

184. Mallinson, C.F., A. Harvey, and J.F. Watts, *Characterization of Carbide Particles in S-65 Beryllium by Scanning Kelvin Probe Force Microscopy.* Journal of the Electrochemical Society, **164** (7), C342-C348 (2017), DOI: 10.1149/2.0271707jes.

185. Birbilis, N., et al., *In situ measurement of corrosion on the nanoscale.* Corrosion Science, **51** (8), 1569-1572 (2009), DOI: 10.1016/j.corsci.2009.05.009.

186. Afshar, F.N., et al., *A combined electron probe micro analysis and scanning Kelvin probe force microscopy study of a modified AA4xxx/AA3xxx aluminium brazing sheet.* Electrochimica Acta, **104** 48-63 (2013), DOI: 10.1016/j.electacta.2013.04.080.

187. Alvarez-Pampliega, A., et al., *Scanning Kelvin force microscopy study at the cut-edge of aluminum rich metal coated steel.* Materials and Corrosion-Werkstoffe Und Korrosion, **66** (1), 16-22 (2015), DOI: 10.1002/maco.201307145.

188. Arrabal, R., et al., *Role of alloyed Nd in the microstructure and atmospheric corrosion of as-cast magnesium alloy AZ91.* Corrosion Science, **97** 38-48 (2015), DOI: 10.1016/j.corsci.2015.04.004.

189. Anantha, K.H., et al., *Correlative Microstructure Analysis and In Situ Corrosion Study of AISI 420 Martensitic Stainless Steel for Plastic Molding Applications.* Journal of the Electrochemical Society, **164** (4), C85-C93 (2017), DOI: 10.1149/2.0531704jes.

190. Sarvghad-Moghaddam, M., et al., *Establishing a correlation between interfacial microstructures and corrosion initiation sites in Al/Cu joints by SEM-EDS and AFM-SKPFM.* Corrosion Science, **79** 148-158 (2014), DOI: 10.1016/j.corsci.2013.10.039.

191. Yu, Q.F. and T.Y. Pan, *Microstructural Modeling of Pitting Corrosion in Steels Using an Arbitrary Lagrangian-Eulerian Method.* Metallurgical and Materials Transactions a-Physical Metallurgy and Materials Science, **48A** (5), 2618-2632 (2017), DOI: 10.1007/s11661-017-4018-9.

192. Nazarov, A., et al., *Effect of Mechanical Stress on the Properties of Steel Surfaces: Scanning Kelvin Probe and Local Electrochemical Impedance Study.* Journal of the Electrochemical Society, **164** (2), C66-C74 (2017), DOI: 10.1149/2.1311702jes.

193. Back, G., A. Nazarov, and D. Thierry, *Localized corrosion of heat-treated and welded stainless steel studied using a scanning Kelvin probe.* Corrosion, **61** (10), 951-960 (2005),

194. Jonsson, M., D. Thierry, and N. LeBozec, *The influence of microstructure on the corrosion behaviour of AZ91D studied by scanning Kelvin probe force microscopy and scanning Kelvin probe.* Corrosion Science, **48** (5), 1193-1208 (2006), DOI: 10.1016/j.corsci.2005.05.008.

195. Nazarov, A., N. Le Bozec, and D. Thierry, *Assessment of steel corrosion and deadhesion of epoxy barrier paint by scanning Kelvin probe.* Progress in Organic Coatings, **114** 123-134 (2018), DOI: 10.1016/j.porgcoat.2017.09.016.

196. Nazarov, A., et al., *Scanning Kelvin Probe Investigation of Corrosion Under Thick Marine Paint Systems Applied on Carbon Steel.* Corrosion, **68** (8), 720-729 (2012), DOI: 10.5006/0551.

197. Nazarov, A., F. Vucko, and D. Thierry, *Scanning Kelvin Probe for detection of the hydrogen induced by atmospheric corrosion of ultra-high strength steel.* Electrochimica Acta, **216** 130-139 (2016), DOI: 10.1016/j.electacta.2016.08.122.

198. Lacroix, L., et al., *Statistical study of the corrosion behavior of Al2CuMg intermetallics in AA2024-T351 by SKPFM.* Journal of the Electrochemical Society, **155** (1), C8-C15 (2008), DOI: 10.1149/1.2799089.

199. Sun, D.Q., et al., *Influence of atom termination and stacking sequence on the theta '/Al interfaces from first-principles calculations.* Superlattices and Microstructures, **94** 215-222 (2016), DOI: 10.1016/j.spmi.2016.04.026.

200. Lu, H., et al., *Electron work function-a promising guiding parameter for material design.* Scientific Reports, **6** (2016), DOI: 10.1038/srep24366.

201. Kohn, W. and L.J. Sham, *Quantum Density Oscillations in an Inhomogeneous Electron Gas.* Physical Review, **137** (6A), 1697- (1965),

202. Hohenberg, P. and W. Kohn, *Inhomogeneous Electron Gas.* Physical Review B, **136** (3B), B864-+ (1964), DOI: 10.1103/PhysRev.136.B864.

203. Tanem, B.S., G. Svenningsen, and J. Mardalen, *Relations between sample preparation and SKPFM Volta potential maps on an EN AW-6005 aluminium alloy.* Corrosion Science, **47** (6), 1506-1519 (2005), DOI: 10.1016/j.corsci.2004.07.029.

204. Yasakau, K.A., et al., *Volta Potential of Oxidized Aluminum Studied by Scanning Kelvin Probe Force Microscopy.* Journal of Physical Chemistry C, **114** (18), 8474-8484 (2010), DOI: 10.1021/jp1011044.

205. Li, C., et al., (2013), *PeakForce Kelvin Probe Force Microscopy,*

206. Leblanc, P. and G.S. Frankel, *A study of corrosion and pitting initiation of AA2024-T3 using atomic force microscopy.* Journal of the Electrochemical Society, **149** (6), B239-B247 (2002), DOI: 10.1149/1.1471546.

207. Sachtler, W.M., G.J.H. Dorgelo, and A.A. Holscher, *Work Function of Gold.* Surface Science, **5** (2), 221-& (1966), DOI: 10.1016/0039-6028(66)90083-5.

208. Jette, E.R. and F. Foote, *Precision determination of lattice constants.* Journal of Chemical Physics, **3** (10), 605-616 (1935), DOI: 10.1063/1.1749562.

209. Kresse, G. and J. Furthmuller, *Efficient iterative schemes for ab initio total-energy calculations using a plane-wave basis set.* Physical Review B, **54** (16), 11169-11186 (1996), DOI: 10.1103/PhysRevB.54.11169.

210. Kresse, G. and D. Joubert, *From ultrasoft pseudopotentials to the projector augmented-wave method.* Physical Review B, **59** (3), 1758-1775 (1999), DOI: 10.1103/PhysRevB.59.1758.

211. Perdew, J.P., K. Burke, and M. Ernzerhof, *Generalized gradient approximation made simple.* Physical Review Letters, **77** (18), 3865-3868 (1996), DOI: 10.1103/PhysRevLett.77.3865.

212. Perdew, J.P. and W. Yue, *Accurate and Simple Density Functional for the Electronic Exchange Energy - Generalized Gradient Approximation.* Physical Review B, **33** (12), 8800-8802 (1986), DOI: 10.1103/PhysRevB.33.8800.

213. Momma, K. and F. Izumi, *VESTA 3 for three-dimensional visualization of crystal, volumetric and morphology data.* Journal of Applied Crystallography, **44** 1272-1276 (2011), DOI: 10.1107/S0021889811038970.

214. Colchero, J., A. Gil, and A.M. Baro, *Resolution enhancement and improved data interpretation in electrostatic force microscopy.* Physical Review B, **64** (24), (2001), DOI: 10.1103/Physrevb.64.245403.

215. Mallinson, C.F. and J.F. Watts, *Communication-The Effect of Hydrocarbon Contamination on the Volta Potential of Second Phase Particles in Beryllium.* Journal of the Electrochemical Society, **163** (8), C420-C422 (2016), DOI: 10.1149/2.0471608jes.

216. Singh-Miller, N.E. and N. Marzari, *Surface energies, work functions, and surface relaxations of low-index metallic surfaces from first principles.* Physical Review B, **80** 235407 (2009), DOI: 10.1103/Physrevb.80.235407.

217. Hyla, A.S., et al., *Work function reduction by a redox-active organometallic sandwich complex.* Organic Electronics, **37** 263-270 (2016), DOI: 10.1016/j.orgel.2016.06.034.

218. Cornil, D. and J. Cornil, *Work-function modification of the (111) gold surface upon deposition of self-assembled monolayers based on alkanethiol derivatives.* Journal of Electron Spectroscopy and Related Phenomena, **189** 32-38 (2013), DOI: 10.1016/j.elspec.2013.06.004.

219. Kurpaska, L., et al., *Shift in low-frequency vibrational spectra measured in-situ at 600 degrees C by Raman spectroscopy of zirconia developed on pure zirconium and Zr-1%Nb alloy.* Journal of Molecular Structure, **1126** 186-191 (2016), DOI: 10.1016/j.molstruc.2016.03.001.

220. Kim, Y. and D.E. Luzzi, *Purification of pulsed laser synthesized single wall carbon nanotubes by magnetic filtration.* Journal of Physical Chemistry B, **109** (35), 16636-16643 (2005), DOI: 10.1021/jp0522359.

221. Cox, B., *Pellet Clad Interaction (Pci) Failures of Zirconium Alloy Fuel Cladding - a Review.* Journal of Nuclear Materials, **172** (3), 249-292 (1990), DOI: 10.1016/0022-3115(90)90282-R.

222. Bouvier, P., J. Godlewski, and G. Lucazeau, *A Raman study of the nanocrystallite size effect on the pressure-temperature phase diagram of zirconia grown by zirconium-based alloys oxidation.* Journal of Nuclear Materials, **300** (2-3), 118-126 (2002), DOI: 10.1016/S0022-3115(01)00756-5.

223. Ishigame, M. and T. Sakurai, *Temperature-Dependence of Raman-Spectra of Zro2.* Journal of the American Ceramic Society, **60** (7-8), 367-369 (1977), DOI: 10.1111/j.1151-2916.1977.tb15561.x.

224. Phillippi, C.M. and K.S. Mazdiyasni, *Infrared and Raman Spectra of Zirconia Polymorphs.* Journal of the American Ceramic Society, **54** (5), 254-+ (1971), DOI: 10.1111/j.1151-2916.1971.tb12283.x.

225. Godlewski, J., et al. *Stress Distribution Measured by Raman Spectroscopy in Zirconia Films Formed by Oxidation of Zr-Based Alloys*. in *Zircnoium in the Nuclear Industry: Twelfth International Symposium*. 2000. West Conshohocken, PA: ASTM STP.

226. *O-Zr Phase Diagram*, in *ASM Int., Diagram No. 101191*. 2009.

227. Block, S., J.A.H. Dajornada, and G.J. Piermarini, *Pressure-Temperature Phase-Diagram of Zirconia.* Journal of the American Ceramic Society, **68** (9), 497-499 (1985), DOI: 10.1111/j.1151-2916.1985.tb15817.x.

228. Iltis, X., F. Lefebvre, and C. Lemaignan, *Microstructural Study of Oxide Layers Formed on Zircaloy-4 in Autoclave and in-Reactor .2. Impact of the Chemical Evolution of Intermetallic Precipitates on Their Zirconia Environment.* Journal of Nuclear Materials, **224** (2), 121-130 (1995), DOI: 10.1016/0022-3115(95)00069-0.

229. Sundell, G., M. Thuvander, and H.O. Andren, *Tin clustering and precipitation in the oxide during autoclave corrosion of Zircaloy-2.* Journal of Nuclear Materials, **456** 409-414 (2015), DOI: 10.1016/j.jnucmat.2014.10.003.

230. Li, P., I.W. Chen, and J.E. Pennerhahn, *Effect of Dopants on Zirconia Stabilization - an X-Ray-Absorption Study .1. Trivalent Dopants.* Journal of the American Ceramic Society, **77** (1), 118-128 (1994), DOI: 10.1111/j.1151-2916.1994.tb06964.x.

231. Yan, C.G., et al., *Effects of Ion Irradiation on Microstructure and Properties of Zirconium Alloys-a Review.* Nuclear Engineering and Technology, **47** (3), 323-331 (2015), DOI: 10.1016/j.net.2014.12.015.

232. Renciukova, V., et al., *Corrosion of zirconium alloys demonstrated by using impedance spectroscopy.* Journal of Nuclear Materials, **510** 312-321 (2018), DOI: 10.1016/j.jnucmat.2018.08.005.

233. Bagotsky, V.G., *Fundamental of Electrochemistry, second ed.* 2006, Hoboken, New Jersey.

234. Senoz, C., et al., *Scanning Kelvin Probe as a highly sensitive tool for detecting hydrogen permeation with high local resolution.* Electrochemistry Communications, **13** (12), 1542-1545 (2011), DOI: 10.1016/j.elecom.2011.10.014.

235. Evers, S., C. Senoz, and M. Rohwerder, *Hydrogen detection in metals: a review and introduction of a Kelvin probe approach.* Science and Technology of Advanced Materials, **14** (1), (2013), DOI: 10.1088/1468-6996/14/1/014201.

236. Lafouresse, M.C., et al., *A Kelvin probe force microscopy study of hydrogen insertion and desorption into 2024 aluminum alloy.* Journal of Alloys and Compounds, **722** 760-766 (2017), DOI: 10.1016/j.jallcom.2017.06.143.

237. Oger, L., et al., *Hydrogen diffusion and trapping in a low copper 7xxx aluminium alloy investigated by Scanning Kelvin Probe Force Microscopy.* Materials Science and Engineering a-Structural Materials Properties Microstructure and Processing, **706** 126-135 (2017), DOI: 10.1016/j.msea.2017.08.119.

238. Hua, Z.L., et al., *Scanning Kelvin probe force microscopy study on hydrogen distribution in austenitic stainless steel after martensitic transformation.* Materials Letters, **245** 41-44 (2019), DOI: 10.1016/j.matlet.2019.02.089.

239. Sadewasser, S., et al., *High-resolution work function imaging of single grains of semiconductor surfaces.* Applied Physics Letters, **80** (16), 2979-2981 (2002), DOI: 10.1063/1.1471375.

240. Kikukawa, A., S. Hosaka, and R. Imura, *Silicon Pn Junction Imaging and Characterizations Using Sensitivity Enhanced Kelvin Probe Force Microscopy.* Applied Physics Letters, **66** (25), 3510-3512 (1995), DOI: 10.1063/1.113780.

241. Novik, N.N., V.G. Konakov, and I.Y. Archakov, *Zirconia and Ceria Based Ceramics and Nanoceramics - a Review on Electrochemical and Mechanical Properties.* Reviews on Advanced Materials Science, **40** (2), 188-207 (2015),

242. Polatidis, E., et al., *Residual stresses and tetragonal phase fraction characterisation of corrosion tested Zircaloy-4 using energy dispersive synchrotron X-ray diffraction.* Journal of Nuclear Materials, **432** (1-3), 102-112 (2013), DOI: 10.1016/j.jnucmat.2012.07.025.

243. Kratochvilova, I., et al., *Nanosized polycrystalline diamond cladding for surface protection of zirconium nuclear fuel tubes.* Journal of Materials Processing Technology, **214** (11), 2600-2605 (2014), DOI: 10.1016/j.jmatprotec.2014.05.009.

244. Williams, F.J. and C.M. Aldao, *On the origin of metal film work function changes under electrochemical modification.* Surface Science, **425** (1), L387-L392 (1999), DOI: 10.1016/S0039-6028(99)00253-8.

245. Cardell, C. and I. Guerra, *An overview of emerging hyphenated SEM-EDX and Raman spectroscopy systems: Applications in life, environmental and materials sciences.* Trac-Trends in Analytical Chemistry, **77** 156-166 (2016), DOI: 10.1016/j.trac.2015.12.001.

246. deFaria, D.L.A., S.V. Silva, and M.T. deOliveira, *Raman microspectroscopy of some iron oxides and oxyhydroxides.* Journal of Raman Spectroscopy, **28** (11), 873-878 (1997), DOI: 10.1002/(Sici)1097-4555(199711)28:11<873::Aid-Jrs177>3.3.Co;2-2.

247. Ferreira, M.G.S., et al., *Semiconducting properties of oxide and passive films formed on AISI 304 stainless steel and Alloy 600.* Journal of the Brazilian Chemical Society, **13** (4), 433-440 (2002),

248. Seh, Z.W., et al., *Designing high-energy lithium-sulfur batteries.* Chemical Society Reviews, **45** (20), 5605-5634 (2016), DOI: 10.1039/c5cs00410a.

249. Bruce, P.G., L.J. Hardwick, and K.M. Abraham, *Lithium-air and lithium-sulfur batteries.* Mrs Bulletin, **36** (7), 506-512 (2011), DOI: 10.1557/mrs.2011.157.

250. Aurbach, D., et al., *On the Surface Chemical Aspects of Very High Energy Density, Rechargeable Li-Sulfur Batteries.* Journal of the Electrochemical Society, **156** (8), A694-A702 (2009), DOI: 10.1149/1.3148721.

251. Xiong, X.S., et al., *Methods to Improve Lithium Metal Anode for Li-S Batteries.* Frontiers in Chemistry, **7** (2019), DOI: 10.3389/fchem.2019.00827.

252. Xu, W., et al., *Lithium metal anodes for rechargeable batteries.* Energy & Environmental Science, **7** (2), 513-537 (2014), DOI: 10.1039/c3ee40795k.

253. Cheng, X.B., et al., *Toward Safe Lithium Metal Anode in Rechargeable Batteries: A Review.* Chemical Reviews, **117** (15), 10403-10473 (2017), DOI: 10.1021/acs.chemrev.7b00115.

254. Wang, G., et al., *Suppressing dendrite growth by a functional electrolyte additive for robust Li metal anodes.* Energy Storage Materials, **23** 701-706 (2019), DOI: 10.1016/j.ensm.2019.02.026.

255. Enze, L., *The Application of a Surface-Charge Density Distribution Function to the Solution of Boundary-Value Problems.* Journal of Physics D-Applied Physics, **20** (12), 1609-1615 (1987), DOI: 10.1088/0022-3727/20/12/011.

256. Dai, H.L., et al., *Stabilizing lithium metal anode by octaphenyl polyoxyethylene-lithium complexation.* Nature Communications, **11** (1), (2020), DOI: 10.1038/s41467-020-14505-8.

257. Yu, Z.A., et al., *A Dynamic, Electrolyte-Blocking, and Single-Ion-Conductive Network for Stable Lithium-Metal Anodes.* Joule, **3** (11), 2761-2776 (2019), DOI: 10.1016/j.joule.2019.07.025.

258. Xiong, S.Z., et al., *Characterization of the solid electrolyte interphase on lithium anode for preventing the shuttle mechanism in lithium-sulfur batteries.* Journal of Power Sources, **246** 840-845 (2014), DOI: 10.1016/j.jpowsour.2013.08.041.

259. Xu, C.X. and J.J. Jiang, *Designing electrolytes for lithium metal batteries with rational interface stability.* Rare Metals, **40** (2), 243-245 (2021), DOI: 10.1007/s12598-020-01629-5.

260. Chen, S.R., et al., *High-Voltage Lithium-Metal Batteries Enabled by Localized High-Concentration Electrolytes.* Advanced Materials, **30** (21), (2018), DOI: 10.1002/adma.201706102.

261. Chen, S.R., et al., *High-Efficiency Lithium Metal Batteries with Fire-Retardant Electrolytes.* Joule, **2** (8), 1548-1558 (2018), DOI: 10.1016/j.joule.2018.05.002.

262. Ren, X.D., et al., *Enabling High-Voltage Lithium-Metal Batteries under Practical Conditions.* Joule, **3** (7), 1662-1676 (2019), DOI: 10.1016/j.joule.2019.05.006.

263. Wood, S.M., et al., *Predicting Calendar Aging in Lithium Metal Secondary Batteries: The Impacts of Solid Electrolyte Interphase Composition and Stability.* Advanced Energy Materials, **8** (26), (2018), DOI: 10.1002/aenm.201801427.

264. He, M.F., et al., *The intrinsic behavior of lithium fluoride in solid electrolyte interphases on lithium.* Proceedings of the National Academy of Sciences of the United States of America, **117** (1), 73-79 (2020), DOI: 10.1073/pnas.1911017116.

265. Yuan, Y.X., et al., *Porous LiF layer fabricated by a facile chemical method toward dendrite-free lithium metal anode.* Journal of Energy Chemistry, **37** 197-203 (2019), DOI: 10.1016/j.jechem.2019.03.014.

266. Liu, Y.W., et al., *Local Electric Field Facilitates High-Performance Li-Ion Batteries.* Acs Nano, **11** (8), 8519-8526 (2017), DOI: 10.1021/acsnano.7b04617.

267. Chen, K.H., et al., *Efficient fast-charging of lithium-ion batteries enabled by laser-patterned three-dimensional graphite anode architectures.* Journal of Power Sources, **471** (2020), DOI: 10.1016/j.jpowsour.2020.228475.

268. Yan, C., et al., *An Armored Mixed Conductor Interphase on a Dendrite-Free Lithium-Metal Anode.* Advanced Materials, **30** (45), (2018), DOI: 10.1002/adma.201804461.

269. Datta, M.K., et al., *Constitutional under-potential plating (CUP) - New insights for predicting the morphological stability of deposited lithium anodes in lithium metal batteries.* Journal of Power Sources, **467** (2020), DOI: 10.1016/j.jpowsour.2020.228243.

270. Plimpton, S., *Fast Parallel Algorithms for Short-Range Molecular-Dynamics.* Journal of Computational Physics, **117** (1), 1-19 (1995), DOI: 10.1006/jcph.1995.1039.

271. Stukowski, A., *Visualization and analysis of atomistic simulation data with OVITO-the Open Visualization Tool.* Modelling and Simulation in Materials Science and Engineering, **18** (1), (2010), DOI: 10.1088/0965-0393/18/1/015012.

272. MedeA version 3.1; MedeA is a registered trademark of Materials Design, I., San Diego, USA.

273. Cui, Z.W., et al., *A second nearest-neighbor embedded atom method interatomic potential for Li-Si alloys.* Journal of Power Sources, **207** 150-159 (2012), DOI: 10.1016/j.jpowsour.2012.01.145.

274. Wang, X., et al., *Glassy Li metal anode for high-performance rechargeable Li batteries.* Nature Materials, 1-7 (2020),

275. Zhou, X.W. and F.P. Doty, *Embedded-ion method: An analytical energy-conserving charge-transfer interatomic potential and its application to the La-Br system.* Physical Review B, **78** (22), (2008), DOI: 10.1103/PhysRevB.78.224307.

276. Rappe, A.K., et al., *Uff, a Full Periodic-Table Force-Field for Molecular Mechanics and Molecular-Dynamics Simulations.* Journal of the American Chemical Society, **114** (25), 10024-10035 (1992), DOI: 10.1021/ja00051a040.

277. Liu, Z., et al., *Interfacial Study on Solid Electrolyte Interphase at Li Metal Anode: Implication for Li Dendrite Growth.* Journal of the Electrochemical Society, **163** (3), A592-A598 (2016), DOI: 10.1149/2.0151605jes.

278. Benitez, L. and J.M. Seminario, *Ion Diffusivity through the Solid Electrolyte Interphase in Lithium-Ion Batteries.* Journal of the Electrochemical Society, **164** (11), E3159-E3170 (2017), DOI: 10.1149/2.0181711jes.

279. Ao, T., et al., *Strength of lithium fluoride under shockless compression to 114 GPa.* Journal of Applied Physics, **106** (10), (2009), DOI: 10.1063/1.3259387.

280. Huang, A., et al., *Enabling Rapid Charging Lithium Metal Batteries via Surface Acoustic Wave-Driven Electrolyte Flow.* Advanced Materials, **32** (14), (2020), DOI: 10.1002/adma.201907516.

281. Mogi, R., et al., *Effects of some organic additives on lithium deposition in propylene carbonate.* Journal of the Electrochemical Society, **149** (12), A1578-A1583 (2002), DOI: 10.1149/1.1516770.

282. Shen, C., et al., *Direct Observation of the Growth of Lithium Dendrites on Graphite Anodes by Operando EC-AFM.* Small Methods, **2** (2), (2018), DOI: 10.1002/smtd.201700298.

283. Shen, C., et al., *In Situ AFM Imaging of Solid Electrolyte Interfaces on HOPG with Ethylene Carbonate and Fluoroethylene Carbonate-Based Electrolytes.* Acs Applied Materials & Interfaces, **7** (45), 25441-25447 (2015), DOI: 10.1021/acsami.5b08238.

284. Zhang, X.Q., et al., *Fluoroethylene Carbonate Additives to Render Uniform Li Deposits in Lithium Metal Batteries.* Advanced Functional Materials, **27** (10), (2017), DOI: 10.1002/adfm.201605989.

285. Wu, B.B., et al., *The interplay between solid electrolyte interface (SEI) and dendritic lithium growth.* Nano Energy, **40** 34-41 (2017), DOI: 10.1016/j.nanoen.2017.08.005.

286. Chen, J., et al., *Electrolyte design for LiF-rich solid-electrolyte interfaces to enable high-performance microsized alloy anodes for batteries.* Nature Energy, **5** (5), 386-397 (2020), DOI: 10.1038/s41560-020-0601-1.

287. Wang, L.P., et al., *Li metal coated with amorphous Li3PO4 via magnetron sputtering for stable and long-cycle life lithium metal batteries.* Journal of Power Sources, **342** 175-182 (2017), DOI: 10.1016/j.jpowsour.2016.11.097.

288. Bieker, G., M. Winter, and P. Bieker, *Electrochemical in situ investigations of SEI and dendrite formation on the lithium metal anode.* Physical Chemistry Chemical Physics, **17** (14), 8670-8679 (2015), DOI: 10.1039/c4cp05865h.

289. Zhang, Y.L., et al., *Dual Functional Ni3S2@Ni Core-Shell Nanoparticles Decorating Nanoporous Carbon as Cathode Scaffolds for Lithium-Sulfur Battery with Lean Electrolytes.* Acs Applied Energy Materials, **3** (5), 4173-4179 (2020), DOI: 10.1021/acsaem.0c00568.

290. Markevich, E., et al., *Very Stable Lithium Metal Stripping-Plating at a High Rate and High Areal Capacity in Fluoroethylene Carbonate-Based Organic Electrolyte Solution.* Acs Energy Letters, **2** (6), 1321-1326 (2017), DOI: 10.1021/acsenergylett.7b00300.

291. Zhang, H., et al., *Improved Rate Performance of Lithium Sulfur Batteries by In-Situ Anchoring of Lithium Iodide in Carbon/Sulfur Cathode.* Electrochimica Acta, **238** 257-262 (2017), DOI: 10.1016/j.electacta.2017.04.028.

292. Jia, W.S., et al., *Pretreatment of Lithium Surface by Using Iodic Acid (HIO3) To Improve Its Anode Performance in Lithium Batteries.* Acs Applied Materials & Interfaces, **9** (8), 7068-7074 (2017), DOI: 10.1021/acsami.6b14614.

293. Shutthanandan, V., et al., *Applications of XPS in the characterization of Battery materials.* Journal of Electron Spectroscopy and Related Phenomena, **231** 2-10 (2019), DOI: 10.1016/j.elspec.2018.05.005.

294. Becking, J., et al., *Lithium-Metal Foil Surface Modification: An Effective Method to Improve the Cycling Performance of Lithium-Metal Batteries.* Advanced Materials Interfaces, **4** (16), (2017), DOI: 10.1002/admi.201700166.

295. González-Torres, M., et al., *XPS Study of the Chemical Structure of Plasma Biocopolymers of Pyrrole and Ethylene Glycol.* Advances in Chemistry, **2014** (2014), DOI: 10.1155/2014/965920.

296. Zhou, X.W., F.P. Doty, and P. Yang, *Atomistic simulation study of atomic size effects on B1 (NaCl), B2 (CsCl), and B3 (zinc-blende) crystal stability of binary ionic compounds.* Computational Materials Science, **50** (8), 2470-2481 (2011), DOI: 10.1016/j.commatsci.2011.03.028.

297. Reynolds, M.A., *In-Situ Electrochemical Impedance Spectroscopy of Zirconium Oxides for Nuclear Sensing Applications*, in *Micron School of Materials Science & Engineering*. 2021, Boise State University.

298. Baker, T.A. and M. Head-Gordon, *Modeling the Charge Transfer between Alkali Metals and Polycyclic Aromatic Hydrocarbons Using Electronic Structure Methods.* Journal of Physical Chemistry A, **114** (37), 10326-10333 (2010), DOI: 10.1021/jp105864v.

299. Panigrahi, S. and G.N. Sastry, *Reducing polyaromatic hydrocarbons: the capability and capacity of lithium.* Rsc Advances, **4** (28), 14557-14563 (2014), DOI: 10.1039/c3ra47326k.

300. Sadlej-Sosnowska, N., *Ab Initio Study of Charge Transfer between Lithium and Aromatic Hydrocarbons. Can the Results Be Directly Transferred to the Lithium-Graphene Interaction?* Journal of Physical Chemistry A, **118** (34), 7044-7051 (2014), DOI: 10.1021/jp4125292.

301. Bhanumurthy, K. and G.B. Kale, *Modification of Zirconium-Iron Phase-Diagram.* Scripta Metallurgica Et Materialia, **28** (6), 753-756 (1993), DOI: 10.1016/0956-716x(93)90048-W.

302. Arico, S.F., L.M. Gribaudo, and L.A. Roberti, *Equilibrium phases surrounding the alpha Zr solid solution in the Zr-Sn-O system.* Journal of Materials Science, **31** (21), 5587-5591 (1996), DOI: 10.1007/Bf01160802.

303. Beck, H.P. and C. Kaliba, *High-Pressure Investigations on Zro2 Doped with Cr, Fe and Nb.* Materials Research Bulletin, **26** (2-3), 145-152 (1991), DOI: 10.1016/0025-5408(91)90004-6.